AN INVESTIGATION OF 40-50 DAY LARGE SCALE DIVERGENT CIRCULATIONS IN THE TROPICAL TROPOSPHERE

by

HENRY BOX SELKIRK

B.A. The Evergreen State College
(1977)

Submitted to the Department of
Earth, Atmospheric and Planetary Sciences
in Partial Fulfillment of the Requirements
for the Degree of

DOCTOR OF PHILOSOPHY

at the

MASSACHUSETTS INSTITUTE OF TECHNOLOGY

February 1986

Signature of Author _____
Department of Earth, Atmospheric, and
Planetary Sciences, February 28, 1986

Certified by _____
Reginald E. Newell
Thesis Supervisor

Accepted by _____
Chairman, Department Committee on Graduate Students

AN INVESTIGATION OF 40-50 DAY LARGE-SCALE DIVERGENT CIRCULATIONS IN THE TROPICAL TROPOSPHERE

by

HENRY BOX SELKIRK

Submitted to the Department of
Earth, Atmospheric and Planetary Sciences
in Partial Fulfillment of the Requirements for the Degreee of
Doctor of Philosophy in Meteorology
February 1986

ABSTRACT

Intraseasonal fluctuations of the large scale divergent circulation of the tropical troposphere during the one year period December 1, 1978 - November 30, 1979 are examined using analyses prepared by the European Centre for Medium Range Weather Forecasts (ECMWF). It is demonstrated through a number of empirical orthogonal function (EOF) analyses that highly coherent, equatorially symmetric fluctuations in a narrow band of frequencies centered near 45 days dominate the zonally asymmetric variance in both the 200 and 850 mb velocity potential. This 40-50 day variability appears as an eastward-moving anomaly in the velocity potential at each level which is related to local modulations of the Walker circulation on the order of several meters per second. In addition it is shown that local changes in the divergent meridional wind occur in tandem with the zonal wind anomalies.

A primary characteristic of the variability of the divergent circulation is a vertical coherence in which negative anomalies of velocity potential at 200 mb, indicating large scale divergence, tend to be paired with positive anomalies and large scale convergence at 850 mb and vice versa. The role played by convection in the oscillation is examined with an index of highly reflective cloud (HRC). In the Northern Hemisphere, 40-50 day anomalies in this index are seen to propagate eastward and are in phase with the local anomalies of meridional divergent winds reconstructed from the leading modes in the EOF analyses.

The intraseasonal variability in the Hadley circulation is also investigated by analysis of both the zonal average meridional winds and the twice-daily values of the streamfunction of the meridional circulation. EOF analysis shows that the streamfunction has a tendency to oscillate at intraseasonal time scales, but in a somewhat wider band of frequencies than is evident in the Walker circulation. Likewise, the zonally symmetric variability of the HRC index shows no clear 40-50 day signal; 40-50 day variability in convection appears to be restricted primarily to the maritime continent region.

Certain aspects of the dynamical relationship between the zonally asymmetric Walker circulation variations, the Hadley circulation and the very prominent 40-50 day oscillation in the zonal circulation are

examined by twice-daily evaluation of the zonal average zonal momentum budget at 200 mb in the tropics. The forcing terms explicitly calculated are the advection of zonal momentum by both the zonally-averaged meridional and vertical wind fields, the Coriolis torque and the convergence of the horizontal eddy flux of momentum. Residuals are generally equal in magnitude to the net forcing, but correlations indicate that none of the first three terms above is strongly linked to the zonal acceleration. In particular, at the 40-50 day time scale only the eddy flux convergence shows a significant in-phase relationship with the zonal acceleration. These findings thus do not support a zonally symmetric mechanism in the tropics for generating the 40-50 day oscillation in the zonal circulation; rather the oscillation appears to be more closely linked to the basic asymmetry of tropical convection which is manifested in the 40-50 day variation of the Walker circulation.

Thesis Supervisor: Reginald E. Newell
Title: Professor of Meteorology

To Susan

ACKNOWLEDGEMENTS

To Reginald Newell, my friend, advisor and teacher, I would like to extend my sincerest thanks for his unwavering trust and enthusiasm which have enabled this project to come to fruition.

My introduction to the dynamics of the tropical atmosphere and ocean, which is the foundation upon which this dissertation is based, has been enriched by the exchange of ideas with both teachers and fellow students at M.I.T., including John Anderson, Wesley Ebisuzaki, Dave Gutzler, Steve Zebiak, Mark Cane, Ed Sarachik, Randy Dole and Ed Harrison. In this respect, this thesis has been a cooperative effort.

Most of the computations used in this study were performed on the computer systems at the National Center for Atmospheric Research (NCAR). I am especially grateful to Michel Verstraete, Akira Kasahara, Roland Madden, Dennis Shea and Ken Hansen, all of NCAR, for their help and advice. And to Oswaldo Garcia of NOAA/CIRES in Boulder for his hospitality and the opportunity to use his unique data set.

During the final preparation of the manusript, I received invaluable insights and guidance from Rick Rosen and Randy Dole. Ellen Silverberg's editing helped untangle my sometimes knotted syntax. Susan Ary and Susan Black provided copious technical and moral assistance.

Support for this research has been provided by the Climate Dynamics Section of the National Science Foundation under grants ATM-8211645 and ATM-8517107, the Stratosphere-Troposphere Exchange Project of the National Aeronautics and Space Administration under grant NAGW-703 and the Department of Energy under contract DE-AC-02-76EV12195.

TABLE OF CONTENTS

I. Introduction

The climate of the tropical atmosphere is distinguished by large scale circulation systems which develop on long time scales. At the planetary scale, these circulations redistribute heat meridionally (the Hadley circulation) as well as zonally (the Walker circulation). In the seasonal cycle of the Hadley circulation, annual periodicity is externally imposed by the seasonal cycle of the incoming solar radiation over the globe. In the case of the changes in the Walker and Hadley circulations observed with the Southern Oscillation, the time scales seem to be determined by interactions between the atmosphere and the equatorial ocean (Zebiak, 1985). Spatial scales in both instances are determined to some degree by the organizing tendency of latent heating: upward motion occurs in strong convective and mesoscale updrafts in relatively confined regions of surface moisture convergence while downward motion is found over much wider regions. At these time scales, the development of highly persistent anomalies in the surface boundary conditions also plays a significant role in the organization of the circulation systems.

At "short" time scales, which in the tropics we might consider as anything shorter than an advective time scale of 25-30 days for planetary scale disturbances, a wide spectrum of atmospheric waves and circulation systems have been observed. These range from mesoscale circulations forced by the diurnal cycle of solar heating (Houze et al., 1981), to easterly waves which derive their energy from a combination of barotropic and baroclinic instabilities (Norquist et al., 1977) and on up to planetary-scale disturbances resembling idealized normal modes of

the equations of motion (Madden, 1978; Ahlquist, 1982). This study focuses on coherent circulations in the tropical atmosphere with time scales longer than the above but shorter than the time scales linked to the annual cycle. As such these "intraseasonal" phenomena presently occupy a gray area in atmospheric dynamics between the theory of waves and that of steady, forced circulations.

The most well-known intraseasonal phenomenon is the 40-50 day oscillation in the tropical zonal winds originally documented by Madden and Julian (1971, 1972); it provides the central focus of this work. They found significant horizontal and vertical coherence of the upper (150 mb) and lower (850 mb) tropospheric zonal winds and surface pressures at 40-50 day periods at a number of upper air stations in the tropics. As there was little coherence in the meridional wind at these frequencies, they suggested that the upper and lower tropospheric zonal wind anomalies together could be considered as the horizontal components of a zonally-oriented overturning similar to the Walker circulation. These wind anomalies seemed to originate over East Africa and the western reaches of the equatorial Indian Ocean, progress eastward and intensify over the Indonesia and New Guinea region and western equatorial Pacific where they would either enhance or depress the mean pattern of the Walker circulation. [After Ramage (1968) we will refer to the equatorial region encompassing the Indonesian archipelago and New Guinea as the "maritime" continent. This region stretches approximately from 100°E to 150°E.]

Implicit in Madden and Julian's (1972) schematic picture of the circulation (reproduced here as Fig. 1.1) is the intensified forcing of the anomaly as it propagates through the maritime continent and the

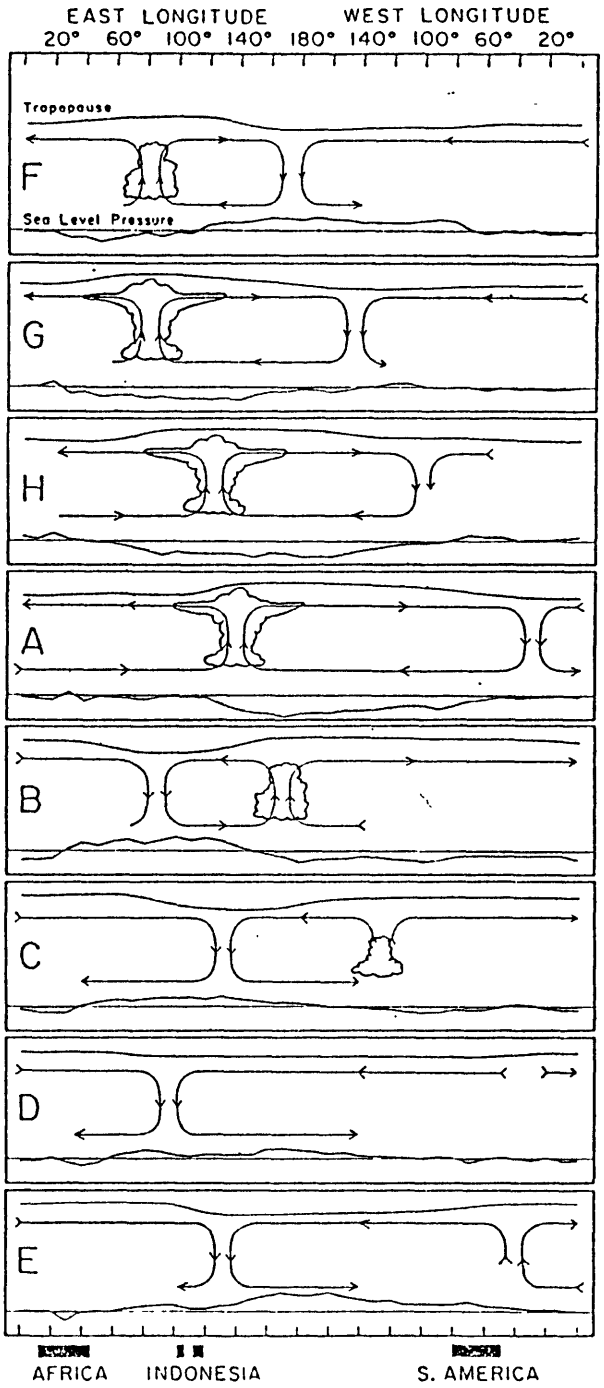

FIG. 16. Schematic depiction of the time and space (zonal plane) variations of the disturbance associated with the 40–50 day oscillation. Dates are indicated symbolically by the letters at the left of each chart and correspond to dates associated with the oscillation in Canton's station pressure indicated in Fig. 11. The mean pressure disturbance taken from Fig. 12 is plotted at the bottom of each chart with negative anomalies shaded. The circulation cells are based on the mean zonal wind disturbance presented in Fig. 13. Regions of enhanced large-scale convection are indicated schematically by the cumulus and cumulonimbus clouds. The relative tropopause height is indicated at the top of each chart.

Fig. 1.1 Empirical model of the 40-50 day oscillation from Madden and Julian (1972).

western Pacific regions. The decay of the "wave" over the central and eastern Pacific Ocean was thought to be due to the lack of convective forcing in those regions. In addition, Madden and Julian did not observe a similar 40-50 day variability over the South American continent and did not include it in their picture.

Madden and Julian (1972) described the 40-50 day variations in zonal wind and temperature in terms of an eastward propagating modulation of the Walker cell. However, Anderson and Rosen (1983) have produced strong evidence of intraseasonal variability in the global relative angular momentum; Fig. 1.2 is a time series of this quantity for the year of the First Global Atmospheric Reasearch Programme Global Experiment (FGGE), December 1, 1978 through November 30, 1979, in both raw and bandpass filtered form. [The zonally averaged zonal winds used in the calculation of the angular momentum here were derived from the FGGE III-b analysis data set produced by the European Centre for Medium Range Weather Forecasts (ECMWF). Pertinent details of this data set, which is the main data source for the study reported here, will be discussed in Chapter 3.] Anderson and Rosen (1983) used 5 years of zonal winds from the NMC operational analysis and identified perturbations on the zonal mean zonal wind field that propagate poleward and downward from the upper equatorial troposphere. They suggested that this phenomenon is the reflection in the zonal mean wind field of the enhancement of the centers of tropical circulation by the eastward propagation of the Madden and Julian "Walker cell" wave. They argue that transient variations of the zonal mean meridional wind field are a dominant component in the phenomenon, giving rise to Coriolis torques which in turn alter the subtropical jet streams.

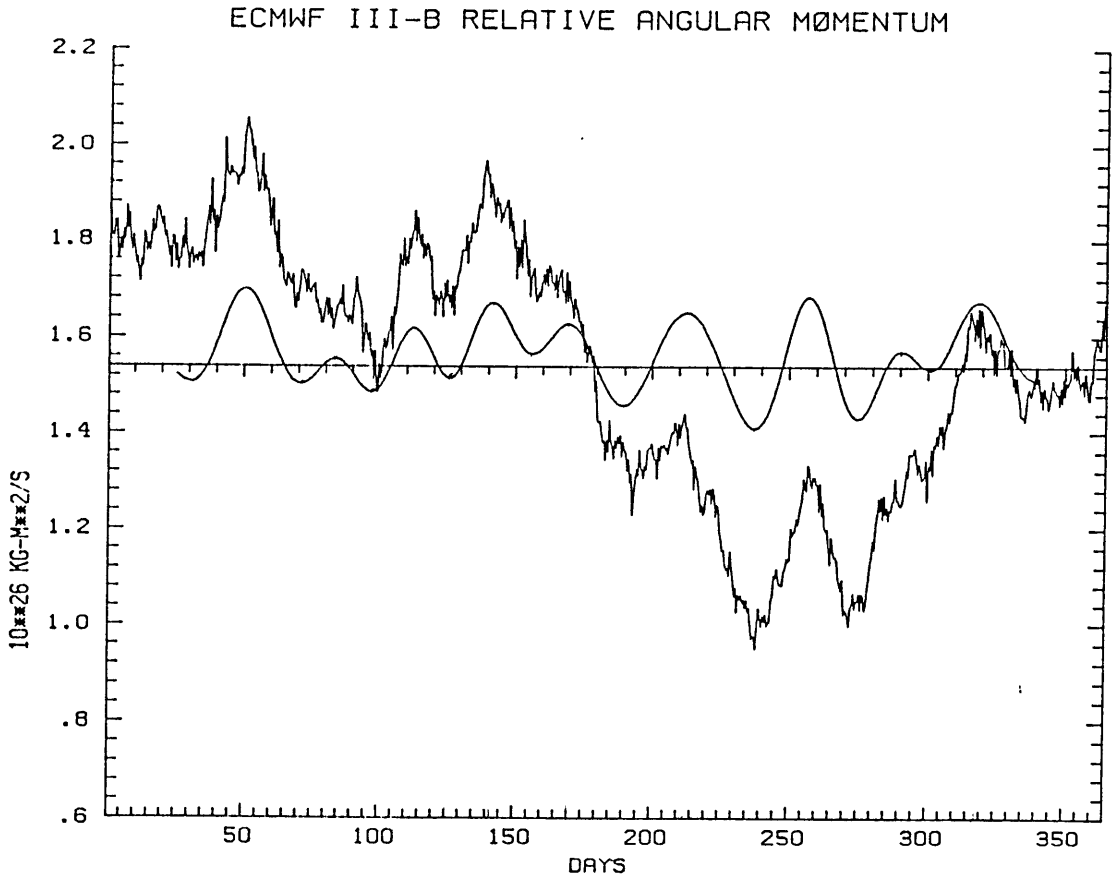

Fig. 1.2 40-day filtered and raw time series of FGGE year global relative angular momentum. Details of calculation in Chapter 6.

During the last few years a number of studies have extended the description of global aspects of the 40-50 day oscillation begun by Madden and Julian. Weickmann (1983) examined 5-day averaged fields of both 250 mb streamfunction and outgoing longwave radiation (OLR) over the Northern Hemisphere and the tropics for six northern winters. He found considerable large-scale variability in both the middle latitude circulation and the tropical OLR fields in the intraseasonal band from 28-72 days. In most of the years examined the intraseasonal variability in the OLR appeared as an eastward propagating phenomenon centered at the equator. The variability in the global circulation fields was dominated by extensions and contractions of the Asian and American upper level jets. Weickmann et al. (1985) investigated in more detail the eastward propagation of OLR anomalies in the 28-72 day band and their relationship to variations in the upper tropospheric circulation. They found definite eastward propagation of OLR anomalies in the equatorial region from 60° to 160°E and a tendency for anomalies over South America and Africa to precede those farther east. From their cross-spectral and composite analyses they suggested that during the period when intensified convection is moving through the Indian Ocean and maritime continent region, the tropical and subtropical flow over most of the tropics is distinguished by a series of upper level anticyclones paired across the equator; during this time tropical upper level troughing is restricted to the central and western Pacific region. Later on, when the intensified cloudiness has reached the western Pacific and considerably slowed in its eastward progress, the low latitude circulation is more wavenumber one in character with a tendency for westerly anomalies in the upper level western hemisphere tropics. A

particularly interesting result was a strong coherence between tropical outgoing longwave radiation and middle latitude circulation changes a quarter to a third of the globe downstream, possibly due to remote forcing by planetary scale wave propagation (cf. Hoskins and Karoly, 1981; Branstator, 1983.)

Lau and Chan (1985) also have examined the intraseasonal variability of outgoing longwave radiation, paying particular attention to the development and motions of anomalies over the Indian Ocean, maritime continent and the western Pacific. As in Weickmann's work and in their earlier studies on interannual variability of OLR (Lau and Chan, 1983a; 1983b), the striking characteristic of tropical OLR variations is the consistent occurrence of east-west oriented anomaly dipoles over the Indian Ocean, maritime continent and the western Pacific with a longitudinal scale of 60-90°. Thus for example when convection is enhanced over the eastern Indian Ocean, it tends to be suppressed in the region to the east of New Guinea. Lau and Chan (1985) found that the eastward propagation of OLR anomalies at 40-50 days can be characterized by relatively swift ($\sim$5 m/s) movement across the Indian Ocean region and a much slower progression eastward across the maritime continent ($\sim$1 m/s) where the anomalies appear to intensify.

The 40-50 day oscillation is an important mode of variability in the more localized patterns of weather associated with the monsoon circulations of Asia and Australia. Sikka and Gadgil (1980), Yasunari (1979, 1980, 1981) and Krishnamurti and Subrahmanyam (1983), among others, have documented significant variability of cloud cover and winds over the Indian subcontinent and surrounding ocean regions during the Southwest Monsoon at time scales up to 40-50 days. Over India the

Intertropical Convergence Zone (ITCZ), which appears as a zonally-oriented band of intense cloudiness, seems to move northward from the equatorial Indian Ocean to the base of the Himalayas, alternately enhancing and suppressing convection in the regions it passes over. There is some evidence from Julian and Madden (1981) that the timing of the start of the ITCZ's northward progression is linked to the passage of the equatorial disturbance discussed in their earlier work.

An eastward progression of 40-50 day disturbances in the divergent wind field on the planetary scale identified by Madden and Julian (1972) was established by Lorenc (1984). Using empirical orthogonal function (EOF) analyses on the global velocity potential fields at 200 and 850 mb, he found that the dominant nonseasonal variance was in the form of an eastward propagating wave at approximately zonal wavenumber one. (As in the study to be reported here, velocity potential fields were derived by Lorenc from the FGGE III-b analysis data set from ECMWF). In the Indian Ocean region, he also found northward propagating bands of divergence and convergence, in agreement with the results of Krishnamurti and Subrahmanyam (1983). Figure 1.3 is taken from Lorenc's work and represents an idealized half-cycle of the 40-50 day oscillation in the 200 mb velocity potential and divergence during the northern summer.

Lorenc's study was limited to the FGGE year, and Weickmann's (1983) results strongly suggest that certain years, the FGGE year in particular, can have stronger amplitudes in this frequency band than others. Anderson et al. (1984) have shown that the amplitude and dominant frequency of intraseasonal variability in the global angular momentum varies significantly from one year to the next. However, the

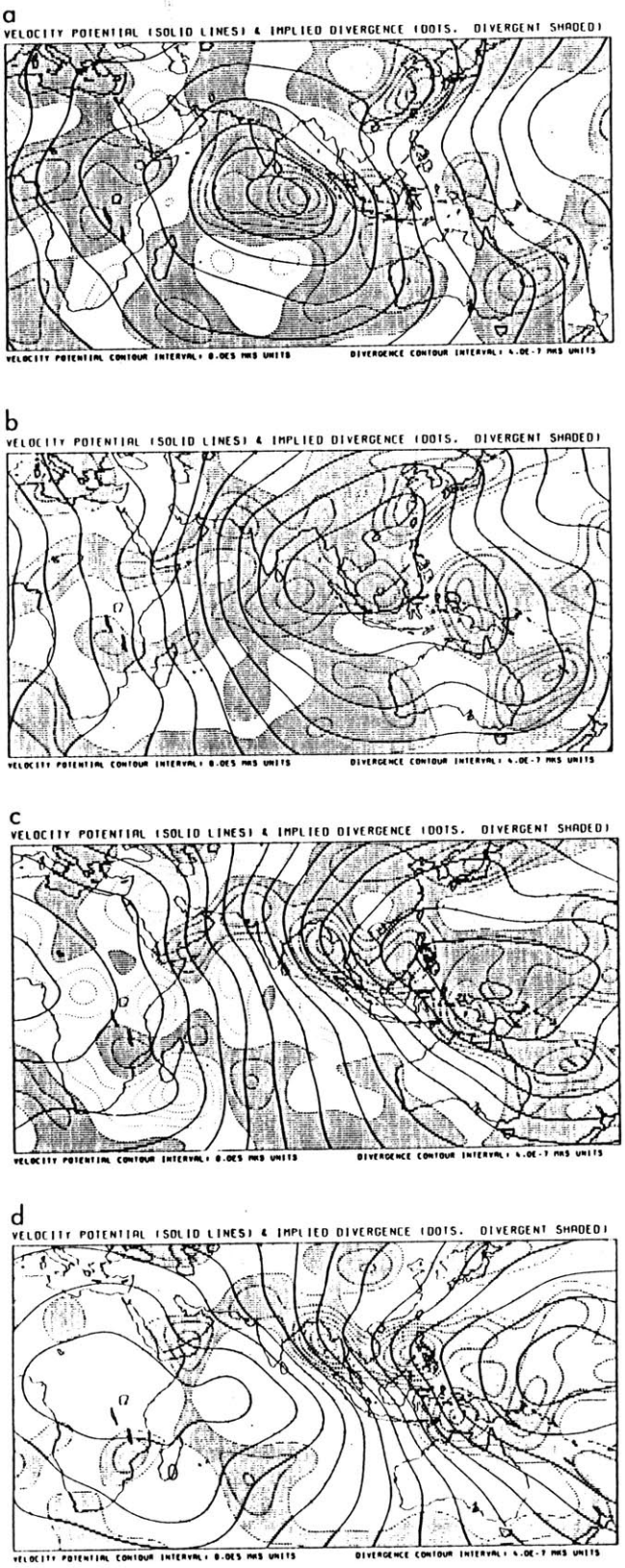

Fig. 1.3 Four stages in an idealized half-cycle of the 40-50 day oscillation in the 200 mb velocity potential and divergence during northern summer. From Lorenc (1984).

40-50 day signal in the divergent flow is much stronger than in the streamfunction patterns revealed in the EOF analysis by Weickmann (1983), which suggests that the year-to-year varibility of the former is of less consequence.

Murakami et al. (1984) have investigated the phase propagation of the 40-50 day oscillation in the total upper and lower tropospheric winds over the region 30°E - 150°W during the northern summer of the FGGE year. At 200 mb, they found a tendency for 40-50 day anomalies of the zonal wind to propagate eastward across the Indian Ocean but then to spread both northeastward and southward from the maritime continent region east of 100°E. At 850 mb the predominant motion is northward over the South Asian and western Pacific region. Also in this region, they found evidence for eastward propagation of wave packets at speeds between 5 and 10 m/s within the generally westward phase propagation of transient disturbances in the 850 mb meridional wind field.

Using longitudinal averages from 60°E to 150°E, Murakami et al. (1984) also studied the behavior of the 40-50 day oscillation over the monsoon region as a whole. They found that the variance of the longitudinal mean of the 850 mb zonal wind near 10°N was dominated by a 40-50 day oscillation with an amplitude of up to 4 m/s; these anomalies propagated northward to the vicinity of 25°N with somewhat smaller amplitude. In composites drawn from the four 40-50 day cycles in the period May through September, the most important contribution to the zonal momentum tendency between the equator and 15°N was the ageostrophic component of the Coriolis torque; further north the balance is more complicated as both the advective, eddy, and residual terms became more important. Their results also indicate that eddy flux convergence and

advective effects were essential in the northward propagation of the anomalies in the longitudinal mean flow.

The observations of 40-50 day variations in outgoing longwave radiation by Weickmann (1983), Lau and Chan (1985) and others leave little doubt that cumulus convection plays an important role in the 40-50 day oscillation. There are likely complex interactions at sub-planetary scales between cumulus convection, moisture supply and sensible heating which determine the regional character of the 40-50 day oscillation. For example, in Webster's (1983) model of an idealized land-ocean monsoon system, sensible heating plays an important role in the destabiliztion of the planetary boundary layer ahead of northward advancing convective zones at two week time scales. At the planetary scale, cumulus convection in one region may sustain the 40-50 day oscillation elsewhere. Murakami et al. (1984) examined the role of vertical motions correlated with cumulus convection in the generation of the 40-50 day wind anomalies during the 1979 summer monsoon season. Their longitudinal means over the monsoon region show that there was substantial midtropospheric conversion of potential energy to kinetic energy north of the equator within the monsoon region as well as in the subtropics of the Southern Hemisphere. In Murakami and Nakazawa (1985) it appears that once the 40-50 day disturbance travels out into the Pacific, the 40-50 day perturbations are maintained by lateral wave energy flux at upper levels which then radiates downward to the lower levels.

Chang (1977) offered an explanation of the 40-50 day zonal wind phenomenon discovered by Madden and Julian in terms of equatorial wave theory. Chang pointed out that the inviscid Kelvin wave theory of

Holton and Lindzen (1968) applied to the Madden and Julian doppler-shifted phase speeds of $\sim$15 m/s would yield a vertical wavelength of 8-9 km, significantly shorter than the observed value of at least 15 km. By the introduction of Rayleigh friction and Newtonian cooling into the linearized equations of motion on the equatorial beta plane, he obtained vertically-trapped solutions which can approximate the observed vertical structure of the 40-50 day wave as well as the mean Walker circulation; the 40-50 day solution required a thermal and radiative damping time near 5 days. Stevens and White (1979) noted that Chang's frictional mode is extremely sensitive to the thermal damping time and that a more realistic 20 day thermal damping time would yield a phase speed below the range allowed by the observations. These comments do not however invalidate Chang's conclusion that the apparent tropospheric trapping of slowly evolving and stationary tropical disturbances is due to the frictional effects of cumulus convection.

The evidence of 40-50 day variability in the zonally symmetric zonal wind field from Anderson and Rosen (1983) has raised the possibility that the Hadley circulation not only is related to the generation of the 40-50 day oscillation in the angular momentum but is also coupled to changes in the Walker circulation. Anderson (1984) has investigated the behavior of the zonally symmetric slow modes in a tropical atmosphere which has both meridional and zonal winds as a basic state and has found that they can have non-zero frequency. This contrasts sharply with systems with vanishing meridional winds in the basic state where the frequencies of the zonally symmetric Rossby normal modes are identically zero (see for example Lindzen, 1967). This sensitivity of the slow linear modes to the presence of a Hadley cell

suggests that the advective character of the Hadley wind field might be an important factor in the dynamics of the oscillation.

The lack of coupling of the slow, relatively nondivergent zonally symmetric Rossby modes to the convection which is the driving force in the Hadley circulation is an unsatisfactory aspect of Anderson's zonally symmetric perturbation analysis. Goswami and Shukla (1984) have alternatively suggested that the interaction of moisture convergence with the Hadley circulation is important. They observed slow oscillations in a zonally symmetric version of the GLAS general circulation model which allowed a dynamic interaction of the moisture field with the convective parameterization scheme. The slow oscillations in their model arise from changes in the moisture supply to, and the convective instability of, the Hadley circulation. They argue that the convergence of dry air in the Hadley circulation would have a time scale based upon the transit of an individual air parcel through the system which they estimate at 42 days. Moist convection will only be maintained so long as the atmosphere remains convectively unstable. Once the atmosphere becomes convectively neutral, it remains for dynamical and radiative processes on longer time scales to destabilize the circulation enough to sustain moist convection once again.

Anderson (1984) also argues that changes in convective instability of the Hadley rising motion is a key ingredient: a burst of Hadley rising motion will continue only so long as the large-scale tropical troposphere remains unstable. In an integration of a model in which he introduces a time-varying forcing, the heating of the upper equatorial troposphere stabilizes the atmosphere and acts to turn off the convection. The other crucial factor is the thermally-balanced upper

tropospheric zonal wind fields that result from the heating of the upper tropical troposphere; they prevent a quick redistribution of the excess of potential energy in the tropics. It would remain for the ageostrophic Hadley circulation to accomplish this mass adjustment by advecting the warm perturbation in the upper troposphere northward, a process limited by the typical mean amplitudes of the Hadley winds. During this poleward advective process, the actual Coriolis torque on the zonally-averaged zonal wind would change with the Hadley overturning.

We must point out here that the mechanisms responsible for the slow oscillations found by Anderson (1984), Goswami and Shukla (1984) and also Webster (1983) may well apply to localized circulation systems smaller than the strictly defined Hadley circulation. We will presume that these mechanisms could apply to quasi-symmetric flow conditions, for example when a major portion of a particular latitude band displays nearly uniform cloudiness. On the other hand, it is dangerous to consider a "local Hadley cell" as a circulation existing in relative isolation from the rest of the tropical belt. In the upper air over the subtropics in particular, the aforementioned advective time scale of 25-30 days would undoubtedly contribute to longitudinal mixing of thermodynamic properties such as mixing ratio.

Is the 40-50 day phenomenon seasonally dependent? This question has important ramifications for understanding the mechanisms important in the oscillation. In particular, a wave explanation would need to accomodate the rather different seasonal mean flows characteristic of the equatorial troposphere. Over the eastern Pacific and to a lesser extent over the Atlantic Ocean, the time mean upper level zonal winds

are westerly during the northern winter season but in northern summer there is an unbroken equatorial belt of easterlies (Selkirk, 1984).

So far there has been conflicting evidence for seasonal dependence of the oscillation, and to some extent the answers are dependent upon what measure of the phenomenon is chosen. Anderson et al. (1984), using a long time series from Truk, found that the frequency of the 40-50 day oscillation in zonal wind is not sensitive to time of year. This suggests that the considerable differences between the monsoon circulations and background flows of the northern summer and winter seasons are not crucial in the maintenance of the oscillation.

The intensity of the oscillation does appear to vary seasonally. In a large group of individual tropical stations, Madden (1985) found the strongest 40-50 day coherence between the zonal winds at 850 and 150 mb coincided with the seasonal passage of the ITCZ. In Anderson et al. (1984) there is some evidence that the amplitude of the 40-50 day angular momentum oscillation is somewhat reduced during the northern fall.

Most studies from the FGGE year period have emphasized the 40-50 day oscillation during the summer monsoon period. As suggested by Murakami and Nakazawa (1985) and Krishnamurti et al. (1985) conversion between available potential energy and kinetic energy over the South Asian monsoon regions may be crucial in the maintenance of the regular 40-50 day variations in those regions. However, Quah (1984) has shown a definite 40-50 day variability in both the 200 and 850 mb zonal wind fields in the tropics from the northern winter of that year. He did not however observe over Indonesia and Australia a meridional propagation of

convergence and divergence zones similar to that observed over the Indian subcontinent in northern summer.

The following is an investigation of the tropical circulation during the FGGE year, when the global observing systems were particularly well suited to defining the state of the tropical atmosphere on the large scale, especially with respect to the divergent circulations produced by latent heating. Some of the initial findings on the 40-50 day oscillation in the Walker circulation reported here are also contained in results from the independent work by Lorenc (1984); in this study we examine this phenomenon as one facet in a complex of intraseasonal variations. Our emphasis in this study is on the variations that occur in the Hadley and Walker circulations on the time scales resolvable in a year-long data set which are longer than the variations traditionally attributed to tropical and planetary-scale waves. We will attempt to identify the morphology of the variations as well as their causes. Particular attention will be paid to the interaction between the Hadley and Walker circulations and to their relationship to the 40-50 day oscillation in atmospheric angular momentum.

This work is divided into 7 chapters. Chapter 2 is a review of the observational data on the structure and maintenance of the Walker and Hadley circulations as well as a discussion of the physical mechanisms governing their seasonal and interannual variations which may be relevant to this study. Chapter 3 is a description of the primary data source we have employed in the thesis which is the set of global analyses for the FGGE year prepared at the European Centre. In addition, some attention is paid to the suitability of the ECMWF analysis

for our stated tasks. We also make use in this work of an index of highly reflective clouds (HRC) as an indicator of deep convective clouds. After some discussion of the FGGE year mean and monthly average fields of the divergent circulation as well as the highly reflective cloud, Chapter 4 is devoted to a description of the results of exploratory analyses of the long period variations of the large scale divergent as well as rotational circulations present in the analysis. Chapter 5 is an examination of the eastward propagation of the Walker circulation. We also consider the zonally asymmetric anomalies of the divergent wind field and changes in highly reflective cloud. Chapter 6 is an investigation of the variability of the zonal mean circulation during the year, and of its relationship to variations in the zonally asymmetric tropical circulation. Chapter 7 summarizes the findings of the work; it also suggests fruitful directions for further research.

2. The Time Mean Structure of the Walker and Hadley Circulations

Before discussing the behavior of the Hadley and Walker circulations at intraseasonal time scales, we will briefly review the time mean structure of these two components of the tropical circulation and the roles they play in the general circulation of the atmosphere as a whole and within the tropics alone. The present investigation of the intraseasonal fluctuations of the Walker and Hadley circulations will emphasize the day-to-day variability of these circulations rather than their monthly time means, for example. It is important for the discussions to follow that we carefully define our terms.

Following Lorenz (1967), we will use the term "meridional circulation" to refer to the zonal average of the meridional wind v. At times we will make references to the streamfunction of the meridional circulation as simply the meridional circulation. This implies no separate definition of the term since in this work we derive the streamfunction directly from the zonal average meridional wind field. "Zonal circulation" will be used interchangeably with the zonal average of the zonal wind component u. Brackets will be used to distinguish zonal averages (when necesary) and overbars will indicate time averages. The term "mean meridional circulation," which is widely used in the general circulation literature, will refer to the time mean of that zonal average. The "Hadley circulation" is understood to be the thermally direct, tropical component of the meridional circulation. When we are considering the overturning within the tropics, meridional circulation and Hadley circulation will be used interchangeably.

A number of researchers use the term "local Hadley cell" to refer to regions of relatively strong poleward flow in the upper troposphere associated with one of the several large scale regions of intense tropical convection. (The term has probably most often been applied to the East Asian region to the north of Indonesia during northern winter.) In this work we will restrict our usage of the terms "Hadley circulation" and "Hadley cell" specifically to the zonal mean meridional wind, although the results in succeeding chapters provide ample support for the view that the latter quantity is most often the sum of a few relatively isolated local extrema in the divergent meridional wind field which are clearly located near centers of large-scale diabatic heating. We take this position to avoid additional subdivision of the general circulation, recognizing that the impermanent nature of "local" Hadley circulations would make the subdivision in certain seasons somewhat arbitrary.

2.1 The Mean Meridional Circulation and the Maintenance of the Mean Zonal Circulation

In the monthly-averaged and Eulerian framework in which the general circulation is traditionally described, the poleward transports of dynamical quantities are often divided into three components: the mean (or time average) meridional circulation (MMC), the stationary eddies, and the transient eddies. The MMC is defined by the zonally-averaged meridional and vertical wind fields, and the Hadley and Ferrel cells are respectively the thermally direct and indirect components of the MMC. Defined as it is in an Eulerian context, the MMC cannot be interpreted

as a material circulation, although in the rising portion of the Hadley cell where the eddy circulation is relatively weak it does bear some resemblance to one. Energetically speaking, thermally direct refers in the case of the Hadley circulation to a zonal average conversion of available potential energy to kinetic energy; this is accomplished by low latitude rising motion and subtropical subsidence. Although the upward motion in the Hadley circulation is clearly connected to forcing by diabatic heating and upward movement of air parcels, the subsidence connected with the descending branch of the Hadley cell and the equatorward branch of the Ferrel cell is largely eddy-induced.

The meridional circulation is conveniently expressed in terms of the zonal average of the meridional wind by the streamfunction

$$\Psi_{MC} = 2\pi a \cos\phi \int_{P_t}^{p} [v(\phi,p')]dp'/g \tag{2.1}$$

where a is the average radius of the earth (6371 km), ϕ is latitude and g is the gravitational acceleration. P_t is a suitably chosen upper level (usually in the stratosphere) where it can be assumed that the vertical velocity is effectively zero. The mean meridional circulation streamfunction $\overline{\Psi}_{MC}$ can be differentiated to recover the time averages of the zonally averaged meridional and vertical winds:

$$[\bar{v}(\phi,p)] = (g/2\pi a \cos\phi)\frac{\partial \overline{\Psi}_{MC}}{\partial p} \tag{2.2a}$$

$$[\bar{\omega}(\phi,p)] = -(g/2\pi a^2 \cos\phi)\frac{\partial \overline{\Psi}_{MC}}{\partial \phi} \tag{2.2b}$$

As discussed by Newell et al. (1972), Eq.(2.1) requires that the mass flux F across a given latitude ϕ_j vanish. This

quantity is written in terms of the estimates of the zonal mean meridional winds:

$$F(\phi) \equiv 2\pi a \cos\phi \int_{P_t}^{P_s} [v(\phi,p)] \, dp/g. \tag{2.3}$$

where P_s is the zonal average surface pressure. At a given moment in time, F will in general not vanish, due to the inherent inaccuracies in the measurements of the meridional circulation as well as the real flow of mass across latitude circles. In the Northern Hemisphere, for example, it is related to the zonal average surface pressure tendency of the polar cap north of the latitude by the following polar cap integral:

$$F(\phi) = (2\pi a^2/g)\int_{\phi}^{\pi/2} \frac{\partial P_s}{\partial t} \cos\phi' d\phi'. \tag{2.4}$$

Over the course of the seasonal cycle there are small meridional mass fluxes due to the slow changes in the mean surface pressure over the various latitude belts. In the Northern Hemisphere, Trenberth (1981) finds an area-averaged difference of 2.65 mb in the surface pressure due to dry air alone from January to July. This is equivalent to a cross-equatorial mass flux of 4.37×10^8 kg/s and gives a vertical average meridional wind equal to ~1 mm/s. Thus subtraction of the mass-weighted vertical average wind from monthly or seasonally averaged data will not greatly change the picture of the meridional circulation.

On a day-to-day basis the vertical average of the meridional wind in an analysis at any one latitude will likely be much larger, both due to the inaccuracies of the analysis and to actual mass fluxes. Although the European Centre's FGGE analysis data set, for example, includes

twice-daily global fields of sea level pressure, surface pressure analyses are not generally available from which one could reliably estimate the time dependence of the mass of the atmosphere, either as a whole or within individual latitude belts. We will see in Chapter 6 that the typical instantaneous net meridional motions computed from the ECMWF III-b are quite large, on the order of 10-20 cm/s, and imply hemispheric scale surface pressure changes of several millibars per day. Thus as the real mass fluxes are being lost in analysis noise, setting F=0 even on a day-to-day basis appears to be a reasonable approach. In this study we will calculate the streamfunction of the meridional circulation on a daily basis by means of this adjustment.

Fig. 2.1 (taken from Oort, 1983) displays cross-sections of time mean Ψ_{MC} for the three month seasons December - February and June - August. In these seasons the Hadley cells are dominated by a cross-equatorial cell with rising motion in the summer hemisphere and "sinking" in the winter hemisphere. Fig. 2.2 shows the corresponding cross-sections of the meridional wind from which Ψ_{MC} fields in Fig. 2.1 were derived. The most significant meridional wind motions associated with these cross-equatorial cells occur in the upper troposphere above 300 mb where magnitudes peak near 3 m/s.

The usual separation between time-averaged motions and transients is useful only when the averaging period is sufficiently longer than the typical lifetimes of the transient disturbances. Rosen and Salstein (1982) have demonstrated that the magnitudes of the stationary eddy fluxes of heat and momentum tend to increase as the averaging period is lengthened from 5 to 10 days; on the other hand, they change very little as the time period is extended to one month. With respect to the

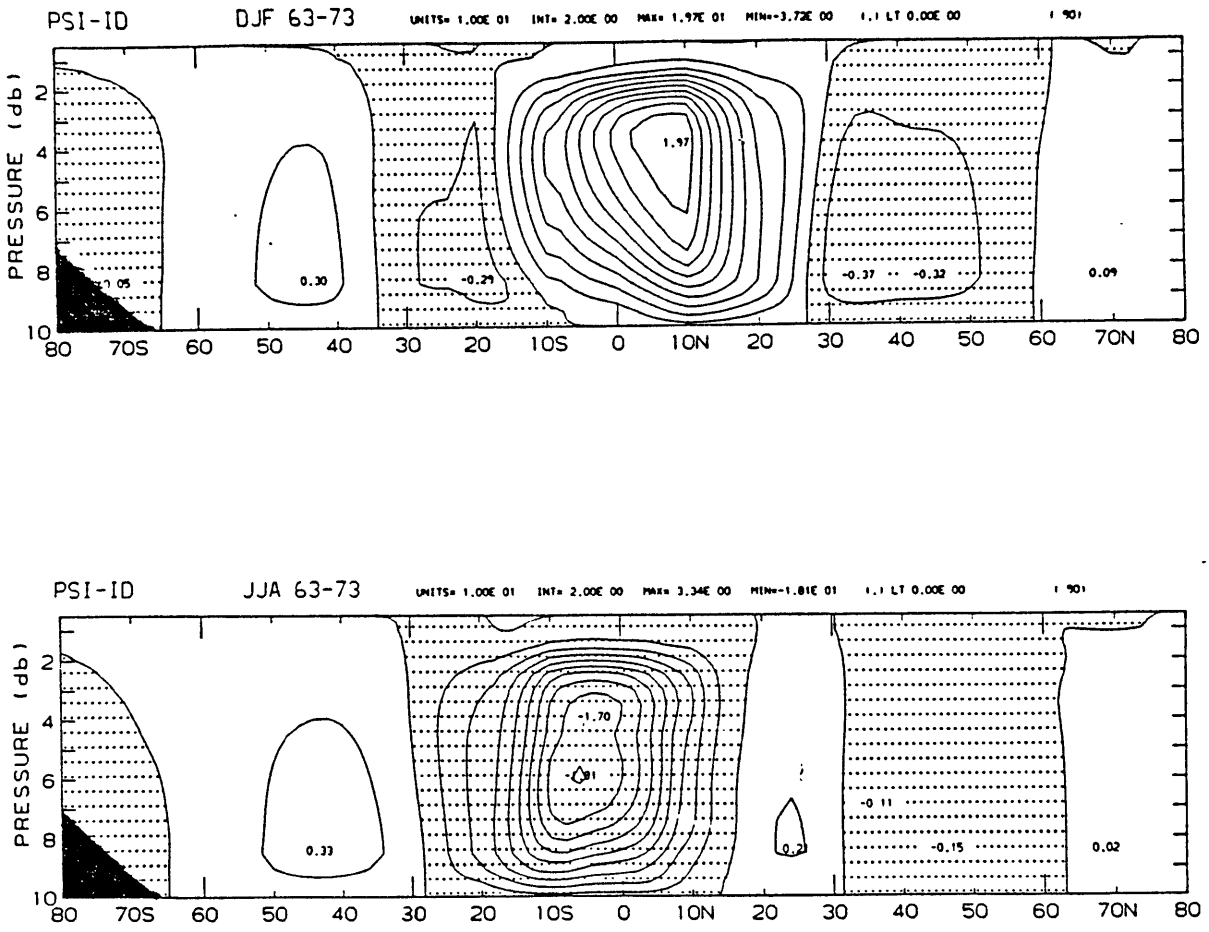

Fig. 2.1 Time average meridional-height cross-sections of Ψ_{MMC} from Oort(1983), contour interval 10^{10} kg/s. December-February 1963-1973 (upper) and June-August 1963-1973.

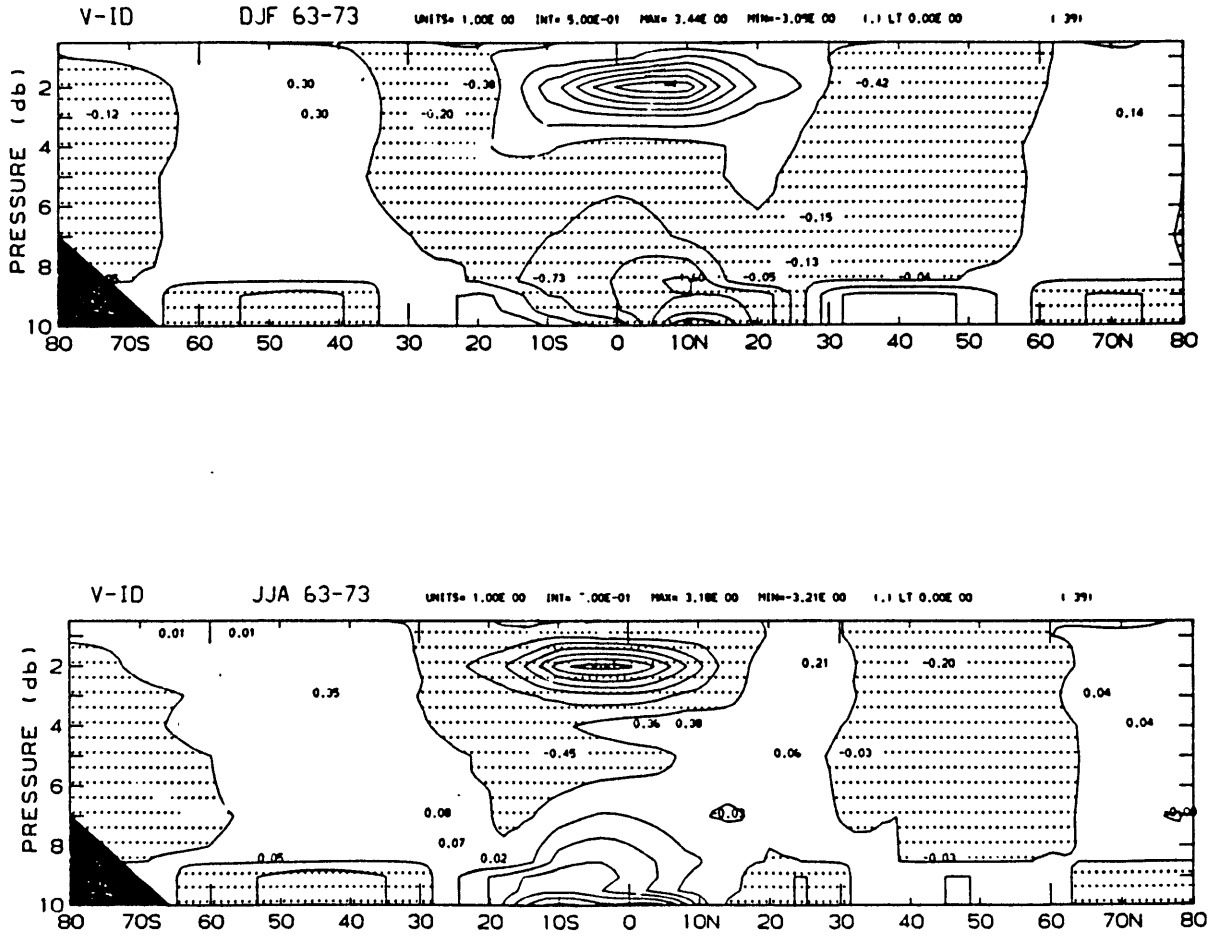

Fig. 2.2 As in 2.1, but for $[\bar{v}]$, contour intervals 1 m/s.

meridional circulation itself, however, the reduction of random errors by a factor of five in monthly averaging can be critical. In fact, as is pointed out by Newell et al. (1972), among others, a mid-latitude direct zonal average of station monthly mean meridional winds is not likely to be statistically different from zero. In the subtropics and higher latitudes, the mean meridional circulation $[\bar{v}]$ can be derived indirectly by balancing the Coriolis torque $f[\bar{v}]$ against other terms in the tendency equation for the time mean zonal circulation. In the free atmosphere, the balance is dominated by the convergence of the horizontal eddy flux of relative angular momentum, the mountain torque and the time tendency of the zonal momentum (Newell et al., 1972).

The separation of quadratic quantities into time and zonal means and the respective eddies is also a sensible one when using the station data-based approach in the original general circulation studies carried out by Starr's and Newell's groups at M.I.T. and since expanded by Oort and his collaborators at the Geophysical Fluid Dynamics Laboratory (GFDL). The methods employed an appropriate time averaging, usually monthly, of station and ship data before any spatial averaging or analysis is carried out. The emphasis in these and other general circulation studies has been on the zonal mean circulation; the zonal averages of flux and other quadratic quantities are more accurately estimated. (It is worth noting in passing that the day-to-day fluctuations of the Hadley cell will come under the heading of transient eddies in the traditional framework.)

The meridional circulation and the eddies nearly offset each other in the zonally-averaged budgets of relative angular momentum, temperature and total energy. These budgets are difficult to balance

with observed data even over the averaging length of a season because the observed net changes are generally small in comparison to the magnitude of the individual contributions.

Schneider and Lindzen (1977) and Schneider (1977) have examined the thermal and momentum balances in zonally symmetric tropical circulation without the effects of eddies. In linear calculations (Schneider and Lindzen, 1977) it was found that in the tropics, deep heating from cumulus convection induces horizontal temperature gradients in the subtropics and hence vertical shears in the zonal circulation. Above the boundary layer, a meridional circulation is induced through thermal wind imbalance brought on by frictional damping. In the free atmosphere this is provided by cumulus friction although its role in zonally symmetric calculations such as the above has been the subject of some debate (cf. Held and Hoskins, 1985). In the lowest 2 kilometers this calculation produces a surface boundary layer circulation which is forced by meridional surface temperature gradients and surface friction. This lower layer cell also appears in the nonlinear model in Schneider (1977) which is somewhat more realistic as it permits meridional momentum fluxes.

The lower cell predicted by the Schneider and Lindzen theory is not apparent in most calculations of the meridional circulation. It should be pointed out however that the method employed by Oort (1983) for Fig. 2.2 forces the surface boundary layer to balance any residual meridional flow from the free atmosphere. In Chapter 6 we will investigate the meridional circulation calculated directly from zonal averages of the meridional wind at each level.

Newell et al. (1972) have examined seasonal averages of the balance of zonal mean zonal momentum for the tropics; their findings are summarized in Fig. 2.3. They found that in general in the tropical upper troposphere the zonal circulation is accelerated by the Coriolis torque due to the Hadley circulation. This acceleration is balanced by the upgradient advection of zonal momentum by the meridional circulation. In the lower troposphere the Hadley circulation Coriolis torque is not strongly compensated by flux divergence; they attribute the large imbalance to effects of friction which are extremely difficult to estimate independently. Further poleward in the latitudes of the subtropical jet stream, it is the indirect Ferrel cell which contributes to a deceleration of the zonal flow in the upper troposphere. This tendency is offset by the convergence of momentum flux into the jet by the eddies. As before, the observational data lead to an imbalance in the lower level.

Oort and Peixoto (1983) have summarized the annual cycle of the transports of total energy by the mean meridional circulation and the eddies for the ten-year period 1963-1973. For January the meridional flux of total energy is positive northward from 5°S. In the tropics this transport is accomplished by the Hadley cell. The net northward flux of energy is the relatively small difference between the northward flux of potential energy in the upper branch and southward transport of sensible and latent heat in the lower branch. In the subtropics, the transient eddy flux of sensible and latent heat becomes the dominant component and northward of 35°N a strong sensible heat flux by the standing eddies also becomes important. In middle latitudes, the Ferrel

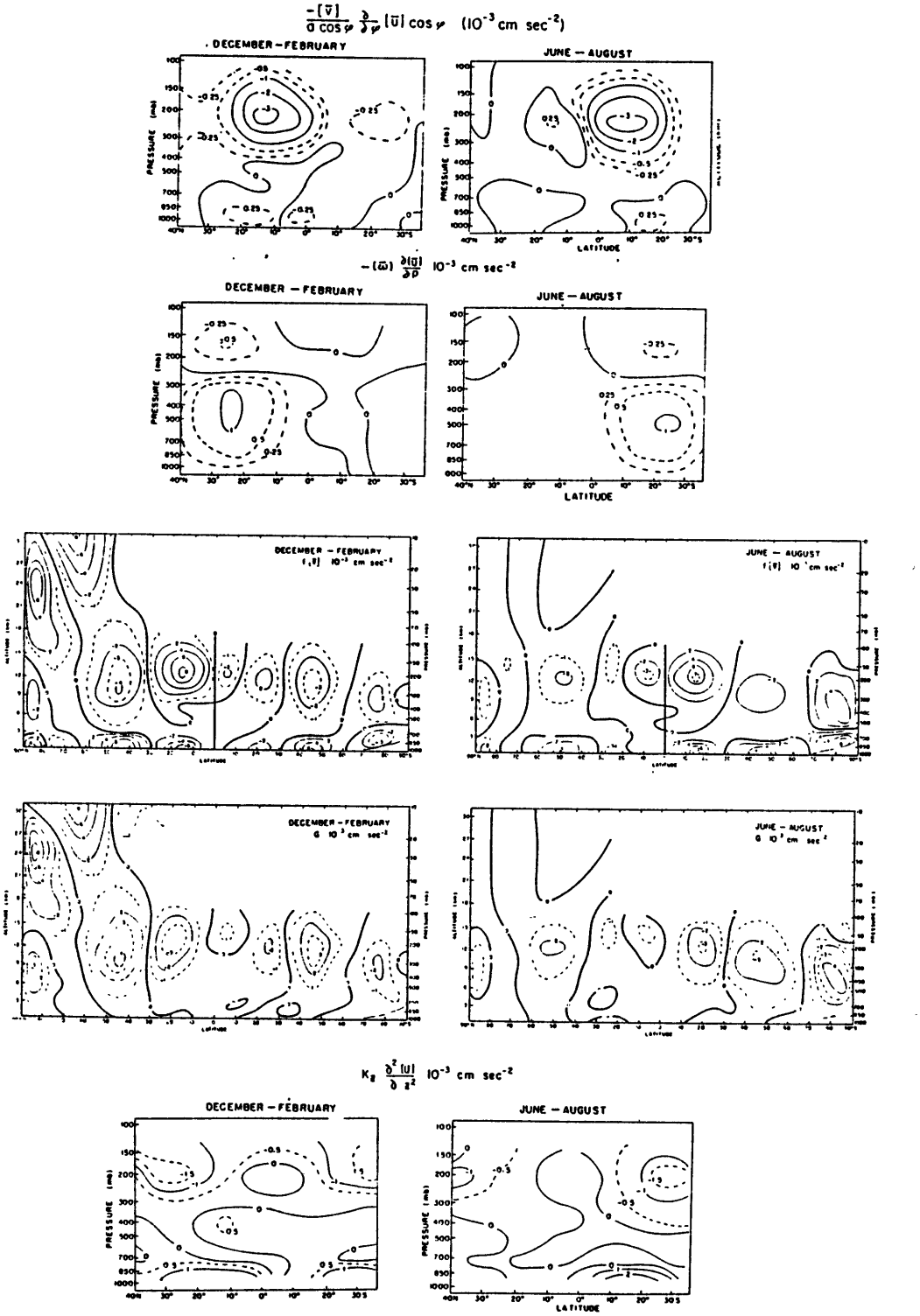

Fig. 2.3 Latitude-height fields of components in the time mean zonal momentum budgets for the seasons December - February and June - August taken from the study of Newell, et al. (1972). The components displayed are (a) the advection of mean zonal momentum by the mean meridional circulation, (b) the vertical advection of zonal momentum, (c) the mean Coriolis torque, (d) the eddy flux convergence of zonal momentum by both standing and transient eddies and (e) the turbulent vertical transfer of momentum.

cell transports potential energy southward and sensible heat northward for a small net southward flux.

The Northern Hemisphere summertime meridional circulation is considerably weaker than its winter counterpart. In general, the weaker summer hemisphere cell of the Hadley circulation and the eddies combine to make a weak poleward flux northward of 5°N. In the baroclinic zones the poleward sensible and latent heat fluxes by the transient eddies begin to predominate. The summertime Ferrel cell is fairly weak.

Oort and Peixoto's results suggest that the Hadley circulation, at least in the Northern Hemsiphere, contributes strongly to the total poleward flux of energy up to 20-25 degrees of latitude in the winter hemisphere and somewhat further equatorward in the summer hemisphere. It should be mentioned of course that the mean meridional circulation we are considering here is an Eulerian diagnostic in isobaric coordinates and does not represent a material circulation. The actual global trajectories of air parcels are more closely approximated by consideration of the isentropic Hadley circulation.

Fig. 2.4 from Townsend and Johnson (1985) depicts isentropic mass streamfunctions for the DJF and JJA seasons in 1979 calculated from the National Meteorological Center's (NMC) FGGE III-a analysis data set. Since vertical motions in isentropic coordinates are possible only through diabatic processes, the total circulation in this analysis reflects the actual global scale differences of heating and consequently stretch from the equator to the pole. As Townsend and Johnson note, the ageostrophic component of the isentropic Hadley cell and the isobaric Hadley cell define nearly the same vertically integrated poleward

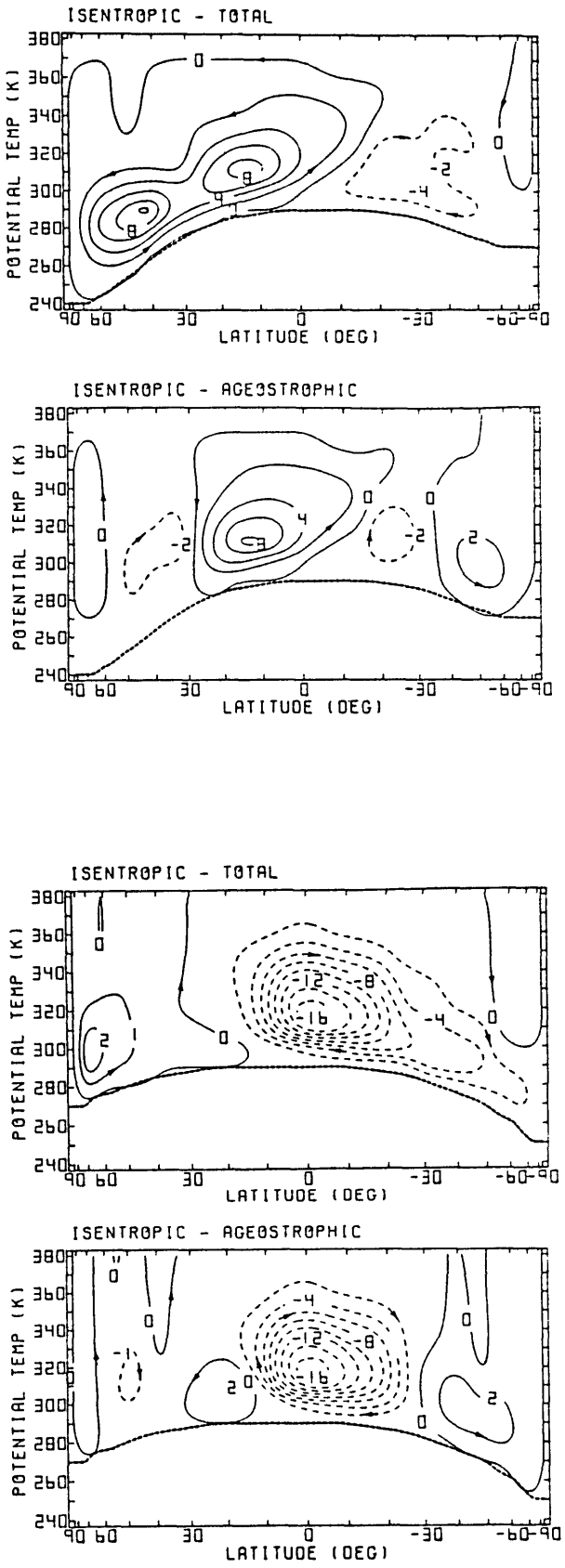

Fig. 2.4 Streamfunctions of the isentropic mean meridional circulation computed from NMC FGGE III-a data by Townsend and Johnson (1985): December 1978-February 1979 (upper) and June-August 1979. Contour intervals 10^{10} kg/s.

transfer of energy; thus it is useful in a monthly time mean to consider the isobaric Hadley cell as an entity unto itself. Furthermore, there may well be coherent modulations of the cell operating at even shorter time scales. As mentioned above we will explore this possibility in a study of the day-to-day fluctuations of the isobaric Hadley cell.

2.2 The Walker Circulation

Bjerknes (1969) named the Walker circulation after Sir Gilbert Walker who was the first to document the global character of the phenomenon he called the Southern Oscillation. [See the summary of Walker's work in Montgomery (1940).] In his studies of global weather patterns, Walker documented an alternation of weather and climate on time scales of several years or more over the subtropics and tropics. He referred to it as the Southern Oscillation because it appeared to be primarily, though by no mean exclusively, a Southern Hemisphere phenomenon. It seemed to take the form of a large scale-swaying of pressure between two centers of action, one in the Indonesian region, the other over western South America.

Since Walker's time the basic conception of the Southern Oscillation has remained unchanged; numerous studies have verified that it is indeed the single most important mode of variance in the tropical climate system at time scales of several years. Troup (1965) and Bjerknes (1966, 1969) proposed that the planetary scale mass exchanges which give rise to the surface pressure fluctuations associated with the Southern Oscillation might operate through toroidal circulations oriented longitudinally in the equatorial zone of the Pacific and

Indonesian regions. Bjerknes proposed that the cooperative interaction of the trade winds and zonal sea surface temperature gradients in the eastern equatorial Pacific act to maintain both strong and weak episodes of the circulation.

The relatively cool ocean surface in the equatorial central and eastern Pacific is maintained by a combination of upwelling and cold westward advection. These two processes are maintained by strong westward surface wind stresses; the trade easterlies here are in part the surface manifestation of the Walker circulation. These easterlies converge in the western Pacific into a sharply demarcated zone of clouds which fluctuates zonally by season, but rarely moves eastward of the dateline, except during El Niño events. In the upper levels, the lower level easterlies are overlain by equatorial westerlies in at least three seasons of the year (Selkirk, 1984). The upper level Walker westerlies converge in the clear air of the eastern Pacific where sinking motion is maintained by radiative cooling.

Beyond the western limits of the Pacific dry zone stretches the so-called monsoon region in which convection occurs at a diversity of time and space scales. In the summer hemisphere, surface westerlies occur here and sustain the convergence and moist convection which drive the respective summer monsoons of the Northern and Southern hemispheres. It is generally not possible to define in a synoptic chart a planetary-scale center of convective heating in the monsoon region, but near the equator the rising motion seems to center in the annual mean over the maritime continent, although there are considerable longitudinal as well as meridional shifts about this mean. The summer hemisphere monsoon circulations are associated with strong surface westerlies or weak

easterlies near the equator. These are in turn overlain at high levels by strong easterlies. Thus, as in the longitude-height diagrams in Fig. 2.5 due to Newell et al. (1974), the characteristic structure of the Walker circulation appears as an eastward overturning to the east of the equatorial heating center and an oppositely directed overturning to the west. (By an "eastward overturning" we will be referring to a circulation pattern in which easterly winds at the surface are overlain by relative westerlies in the upper troposphere; westward overturnings are defined by the inverse.)

During the southern summer when monsoon circulations are occurring over Australasia, the Brazilian rain forest and central southern Africa, there are centers of rising motion over 140°E, 10°E and 70°W. In this season it is confusing to refer to a single Walker circulation; we will instead refer to a complex of eastward and westward overturning Walker 'cells' which together compose a global Walker circulation. In the maps for northern summer, the Walker circulation is dominated by Pacific and Indian Ocean cells diverging near 130°E. In this study we will attempt to avoid confusion in references to the Walker circulation and cells by restricting the term 'circulation' to the global complex of individual 'cells' as a whole. Similarly the Hadley 'circulation' consists of summer and winter hemisphere 'cells'.

Gill (1980) proposed a very simple beta plane model to account for the observed mean patterns of upper and lower tropospheric winds in the tropical Pacific. With a heat source centered at the equator and horizontal scaling consistent with the equivalent depth of latent heat-forced circulations, he obtained a very reasonable pattern of tropical easterlies and westerlies. His model balances advection of planetary

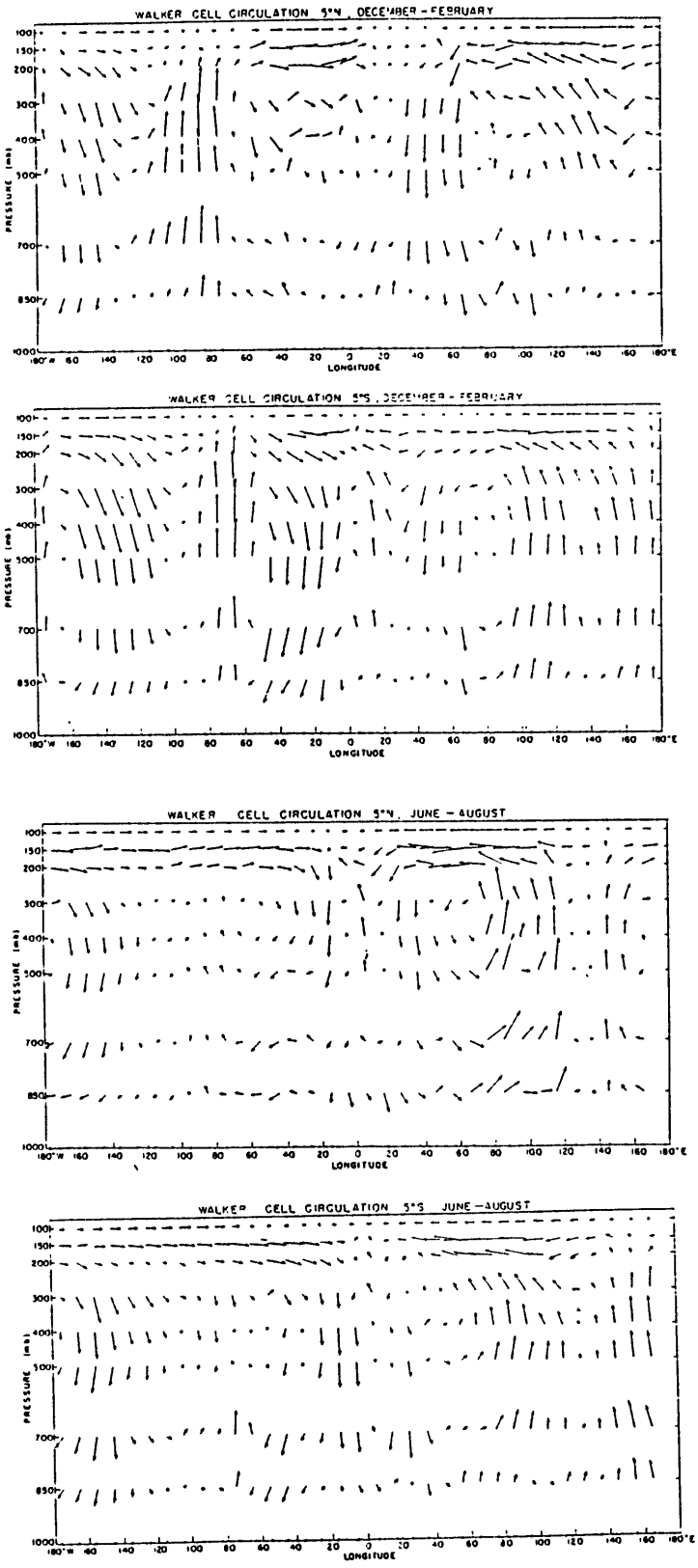

Fig. 2.5 Longitudinal-height profiles of the east-west circulations in the 10° belts centered at 5°N (upper panels) and 5°S. Derived by Newell et al. (1974) from their time average zonal winds for the period 1957-1963 and kinematically-derived vertical velocities, December-January (top); June-August (bottom).

vorticity, vortex stretching and friction. Sardeshmukh and Hoskins (1985), noting that Gill's model fails to account for the exact location of upper tropospheric winds relative to observed heating distributions, suggest that considerably better agreement between the model and observed vorticity at upper levels can be achieved in an inviscid model in which all the steady nonlinear terms are included, viz.

$$\frac{\partial \zeta}{\partial t} + \tilde{V} \cdot \nabla (\zeta + f) = - (\zeta + f) \nabla \cdot \tilde{V} \tag{2.6}$$

Here ζ is the vertical component of the relative vorticity and $\tilde{V}$ is the horizontal wind field.

Cornejo-Garrido and Stone (1977) investigated the maintenance of the Pacific Walker cell, in particular the hypothesis of Bjerknes (1969) that the cell is driven by the sea surface temperature gradient at the equator which maintains an east-west gradient of evaporation and hence moisture supply for convective instability. Although the upward and downward motions in the cell are certainly maintained by latent heating and radiative cooling respectively, they find that evaporation is strong in the eastern equatorial Pacific due to the combination of intense insolation under clear skies and strong surface winds. They suggest that it is the convergence of moisture flux in the western Pacific which anchors deep convection to that region, rather than the sea surface temperature gradient itself. This idea has led to considerable debate, for there exist a number of indications that convective zones during El Niño events will move eastward in concert with sea surface temperature isotherms.

Whatever is the subtle balance of forces which determines the location of rising motion in the western Pacific, the most intense regions of large-scale near-equatorial convection are located over the land masses of South America, Africa and the maritime continent. Although to some extent the seasonal excursions of the 'monsoon' troughs change the details of the local precipitation patterns, the permanent patterns of vegetative cover and orography provide some anchoring of local circulations which in turn influence the large scale. These influence not only the mean circulation, but also the anomalous circulations. For example, the presence of the Andes Mountains prevents the flow of moisture from the east into equatorial disturbances in the eastern Pacific. This region is instead dominated by downward motion from the convergence of the upper levels of the South American and Pacific cells of the Walker circulation. The eastward progression of 40-50 day anomalies which must be sustained by convection is inhibited in this region.

Considerable insight into the Walker circulation can be gained from inspection of diagrams such as Fig. 2.5. An alternative viewpoint which perhaps better reflects the fact that the Walker circulation is maintained by overturnings associated with diabatic heating was first advanced in Krishnamurti (1971) and Krishnamurti et al. (1973). Starting from observed divergence obtained from large scale analyses of the tropics, they derived the velocity potential distribution for the Northern Hemisphere summer and winter monsoons. Krishnamurti's papers introduced the use of the velocity potential and the separation between the divergent and rotational components of the wind to large scale studies of the tropics. A brief discussion of our terminology follows.

The horizontal wind field $\tilde{V}$ can be represented by the sum of a divergent component $\tilde{V}^d$ and a rotational component $\tilde{V}^r$. In order to obtain a decomposition into these two components, one must first derive the scalar fields of vorticity ζ and divergence D. These two fields are related respectively to the velocity potential and the streamfunction by the Poisson equations

$$\nabla^2 \chi = D \tag{2.4a}$$

and

$$\nabla^2 \psi = \zeta. \tag{2.4b}$$

On the sphere, the divergence and vertical component of vorticity are written

$$D = \frac{1}{a\cos\phi}\frac{\partial u}{\partial \lambda} + \frac{1}{a\cos\phi}\frac{\partial}{\partial \phi} v \cos\phi \tag{2.5a}$$

and

$$\zeta = \frac{1}{a\cos\phi}\frac{\partial v}{\partial \lambda} - \frac{1}{a\cos\phi}\frac{\partial}{\partial \phi} u \cos\phi \tag{2.5b}$$

Finally, the divergent and rotational components are derived by the following differentiations

$$\tilde{V}^d = \nabla \chi \tag{2.6a}$$

and

$$\tilde{V}^r = \tilde{k} \times \nabla \psi \tag{2.6b}$$

where $\tilde{k}$ is the unit vertical vector. Divergent winds in this convention will blow across the contours of velocity potential from negative to positive values. Rotational winds will blow along contours with higher values to the right if one is facing eastward.

In the middle latitudes, the total flow on synoptic scales is highly rotational; the vorticity commonly exceeds the divergence by an order of magnitude at synoptic scales. Thus the contours of the streamfunction define the general pattern of the flow quite well. In the tropics, as will be apparent in the mean maps we will present in Chapter 4, the divergence is of more consequence, particularly in the lower levels where total wind speeds are less than 10 m/s. Here the streamfunction can still give a good idea of the basic flow, however.

Boundary conditions represent a problem for the solution of the Poisson equation for the velocity potential on a limited domain. Because of the dominance of the rotational wind field, satisfactory boundary conditions for the streamfunction can often be obtained by using the total, observed wind field or the geostrophic streamfunction $\psi_g = \Phi/f$ where Φ is the geopotential and f is the Coriolis parameter at latitude ϕ. With global wind data the problem is removed, and the solution can be obtained for the entire sphere.

As will be discussed later, there are considerable difficulties associated with diagnosing the divergent wind field in the tropics. The velocity potential, as an integrated divergence, emphasizes the larger scales through weighting by the inverse wavenumber squared; thus velocity potential calculations are fairly robust in their location of large-scale centers of vertical motion.

In this work we will adopt a definition of the Walker circulation that arises from consideration of the planetary scale velocity potential field. Thus we will define it as the large scale <u>divergent</u> east-west circulation in the equatorial zone. The restriction to the divergent circulation links it unambiguously to large scale divergence patterns

and to diabatic heating due to deep convection or to radiative cooling. This diabatic heating tends to induce divergent flow in the upper levels and convergence near the surface, which connects a so-defined Walker cell to the net zonal mass flux, which, although a small residual of eastward flow at one level and westward at another, must ultimately result in the surface pressure changes associated with the Southern Oscillation.

3. The ECMWF III-b Global Analysis: Observational Data Base and Analysis Characteristics

The focal point of this study is the variability of the planetary scale divergent circulations in the tropics. We use as our main data source the FGGE III-b analysis by the European Centre for Medium Range Weather Forecasts (ECMWF). The total wind fields at the 200 and 850 mb levels were decomposed into divergent and rotational components through the calculation of velocity potential and streamfunction fields. After this division was made the variability of the two components could be studied separately. In the present chapter we discuss some general characteristics of the observational data which comprise the FGGE II-b data base and the ECMWF FGGE III-b global analyses derived therefrom. The derivation of velocity potential and streamfunction fields from the III-b analysis wind fields is discussed in Chapter 4.

The European Centre's FGGE III-b data set includes two analyses for each of the calendar days from December 1, 1978 through November 30, 1979. Each 12-hour observation includes analysis fields of geopotential height, zonal wind, meridional wind, temperature and vertical velocity at the fifteen levels 1000, 850, 700, 500, 400, 300, 250, 200, 150, 100, 70, 50, 30, 20 and 10 mb on a 1.875° by 1.875° grid (192 points east-west and 97 points pole-to-pole. Relative humidity is also analyzed, up through the 300 mb level.) There are more than 18,000 grid points over the globe at this resolution, which makes for a rather unwieldy data set of 80 tapes for the full year. For this study we have used a reduced grid data set created by Roy Jenne's group at NCAR which includes only every second grid point in each direction, thus reducing the data volume

by four. This reduction of the grid resolution to 3.75° very likely has had little impact on the synoptic and planetary scale features in the full grid. As we will discuss later in this chapter, the optimum interpolation scheme employed at ECMWF tends to eliminate divergence at scales shorter than approximately 1000 km.

The choice to decompose the total wind field into the component divergent and rotational winds at the two levels 200 and 850 mb was motivated by both theoretical and practical considerations. First of all, it is well known that the primary driving force for the tropical circulation is deep convection, in which near-surface air parcels with high values of moist static energy transform latent heat and internal energy into geopotential energy as they are transported into the high troposphere in vigorous updrafts. Therefore, to a crude approximation, the vertical structure of the divergent circulations is dominated by lower level inflow in the lowest 200 mb and upper level outflow centered near 200 mb.

The second consideration involves the characteristics of the available data and the analysis scheme, both of which are considered in this chapter. Cloud heights are difficult to determine, and wind estimates are commonly applied to a nominal level in either the upper or lower troposphere, usually 200 or 850 mb. Surface winds are also important in the lower level inflow but are difficult to estimate from cloud observations in the middle of the trade wind layer over the ocean.

An important issue is the appropriateness of analyses generated by the forecast-analysis system used by the European Centre in their III-b analyses for the study of the divergent part of the tropical general circulation. This question is raised at the outset because the data

assimilation process used at ECMWF in the III-b analyses (which will be discussed below) tended to underestimate the strength of the Hadley circulation found in, for example, purely station-based data sets (cf. Rosen et al.,1985). On the face of it, such a property would seem to be a serious handicap in the studies reported here. However, as will become clear in the results, this apparent underestimation by no means inhibits analysis of intraseasonal time scale variations.

3.1 The FGGE II-b Data Base: Coverage and Composition

A major goal of FGGE was to integrate on a global scale data obtained from a wide variety of observing platforms outside of the conventional synoptic and upper air network into global observational analyses. Along with an assessment of the impact of an increased observational data base on numerical weather forecasts, particularly in the tropics, the FGGE observational data base has permitted more detailed study of the general circulation in the region.

Many types of observations were only available during the FGGE year. These included *in situ* data gathered remotely by satellites and periodically relayed to central locations. Particularly successful were the drifting buoys released in the Southern Hemisphere which provided vital and unprecedented surface pressure information in remote ocean regions. Guymer and Le Marshall (1981) attribute the unusual number and intensity of surface lows observed over the southern oceans to the impact of these data on the analyses, although Trenberth and van Loon (1981) contend that these differences from more data-sparse years were more a reflection of highly unusual conditions in the Southern

Hemisphere during FGGE rather than a product of increased data coverage. To the extent that interannual variability is an important factor in the meteorology of a remote ocean region, the impact of the single year of FGGE coverage is obviously difficult to assess. As we are concerned here with such regions in the tropics, the conclusions we draw must be tempered with some degree of caution.

Meteorological data collected during FGGE and incorporated into the II-b data set can be divided into five main categories:

(1) Land and ship observations from the FGGE enhancement of the World Weather Watch (WWW) network of synoptic and upper air stations;

(2) single level wind observations from commercial and research aircraft as well as constant level balloons;

(3) drifting buoys released in the southern oceans;

(4) cloud motion winds from the geostationary satellites;

(5) and satellite infrared and microwave soundings from polar orbiting satellites, primarily TIROS-N and NOAA-6.

TIROS-N and NOAA-6 were equipped with a system that enabled data to be gathered from remote balloons, buoys and aircraft. During the Winter MONEX Special Observing Period, January 5 - March 5 (SOP-1) and the Summer MONEX Special Observing Period, May 1-June 30 (SOP-2), additional intensive data gathering on regional scales was carried out. [MONEX is short for **Mon**soon **Ex**periment. Winter MONEX activities spanned the months of December and February, and were chiefly confined to the South China Sea region. Summer MONEX encompassed a wide variety of field experiments from May through August in the Arabian Sea, the Indian subcontinent and the Bay of Bengal.]

Wind measurements were available from a variety of conventional systems and systems enhanced or specifically deployed during FGGE. They include the WWW land-based network of synoptic (SYNOPS) and upper air stations with rawinsondes (RAWINS) or pilot balloons (PIBALS) augmented by the Tropical Wind Observing Ships (TWOS). High- and low-level satellite winds were derived from data from the FGGE-year complement of geostationary satellites which are listed here with their approximate longitudinal locations: Meteosat at 0°, GOES-E at 60°W, GOES-W at 120°W, GMS at 140°E and GOES-Indian Ocean at 60°E. (The latter was available during the Summer MONEX time period only.) These satellites generally provided data over spans of 90-100 degrees of longitude at the equator. Constant level balloons (COLBAS) were launched during Winter and Summer MONEX. During the latter a total of 160 constant level balloons were released starting in late April and early May from Ascension (14°W,8°S), Canton Island (172°W,3°S) and Guam (145°E,14°N) of which 20-40 remained in the tropical belt of the Eastern Hemsiphere. In addition, aircraft dropwindsondes were released from airplanes operating out of Acapulco, Hawaii, Diego Garcia and Ascension Island at various times during the year. Additional details on data coverage and the special data systems can be found in the FGGE Operations Reports on Winter and Summer MONEX (World Meteorological Organization, 1981a; 1981b). In addition to measurements by the FGGE/WWW observational network, temperature data were obtained from satellite IR profiles (SATEM), the drifting buoys (which also monitored surface pressure and sea surface temperature) and dropwindsondes.

Some idea of the coverage and continuity provided by the data utilized in the ECMWF III-b analysis can be obtained by comparison of

the four panels of Fig. 3.1 which are taken from Bjorheim et al. (1981). These show the distribution of III-b assimilated data for January 20, April 20, June 20, and October 20. January 20 and June 20 fell within SOP-1 and SOP-2 during which the observational networks were augmented by special observational efforts. The preponderance of rawinsonde and synoptic data over the Northern Hemisphere continents is immediately evident, yet the drifting buoys seem to provide better oceanic coverage for the Southern Hemisphere. The aircraft reports are primarily confined to the major commercial airline routes in the Northern Hemisphere. Constant level balloons observations appear in the tropics in the January and June maps, and dropwindsondes appear in the January maps as well. Throughout the year the coverage by SATEMs increased; there were a number of days during the first half of the year in which temperature retrievals were limited to one or two orbital swaths.

It is evident that large, normally data-sparse areas of the tropics and the extratropical oceans were sampled by the extra FGGE observations, although some of the improvements in the global observational system during FGGE have become permanent since then, such as the satellite sounding coverage. Low-level cloud winds over the Indian Ocean from GOES-IO are unique to FGGE, as is the coverage provided by the drifting buoys already mentioned. Despite their wide coverage, however, satellite temperature soundings do not seem to be a substitute for radiosondes in data sparse regions such as the subtropical eastern North Pacific. McGuirk et al. (1984) have found that the vertical structure of upper tropospheric cold lows which are a common feature in that region can be completely obscured by the satellite temperature data.

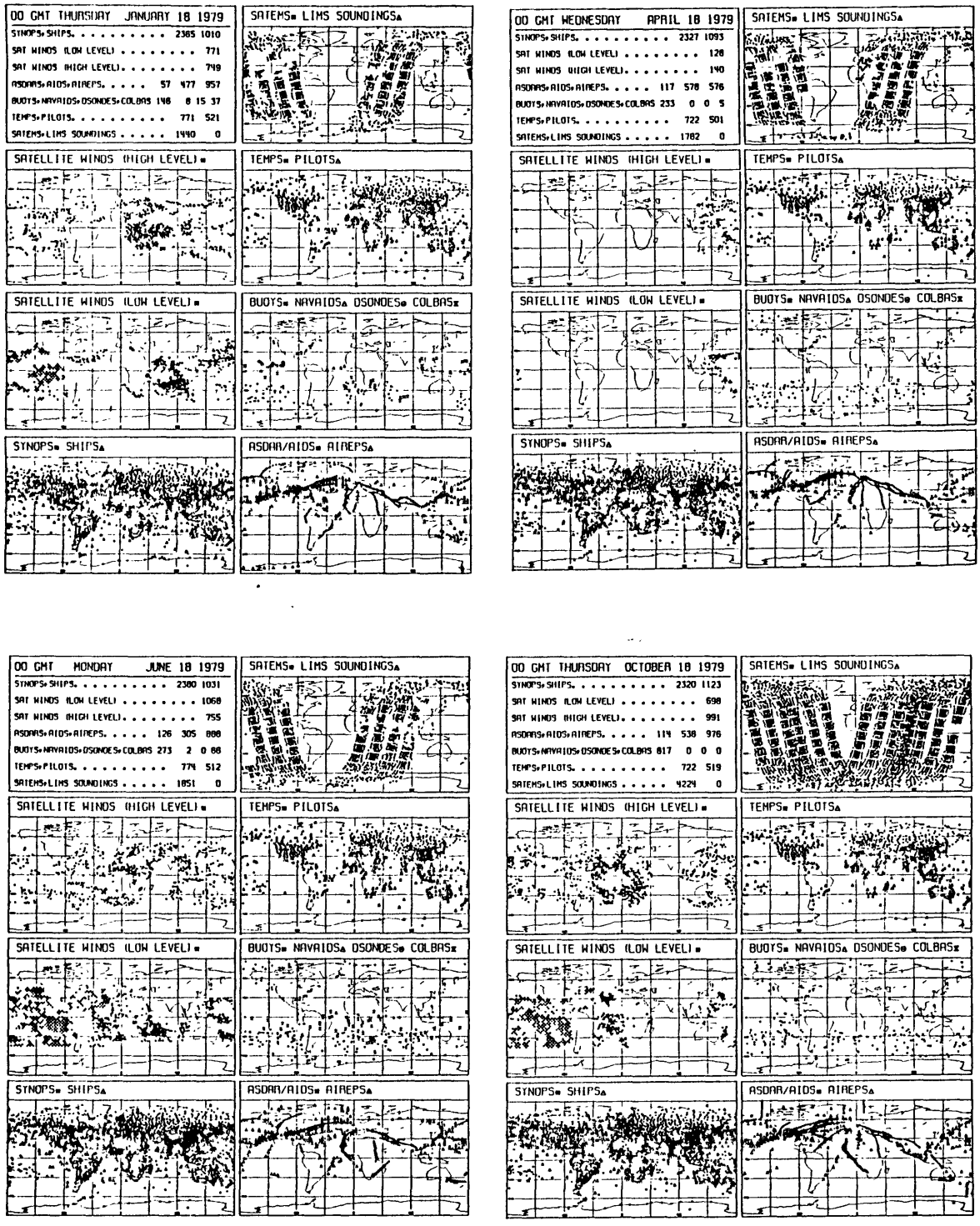

Fig. 3.1 Distributions of data assimilated into the ECMWF FGGE III-b 0Z analyses for January 18 (upper left); April 18 (upper right); June 18 (lower left); and October 18 (lower right). From Bjorheim et al. (1981).

Kallberg et al. (1982) have examined the impact of the FGGE cloud track wind data on the quality of forecasts with the ECMWF model and find that they have a positive impact on 1-3 day tropical forecasts in particular. However, they found a tendency for the cloud track winds to underestimate subtropical jetstreaks compared to other data sources in certain regions. In addition they note that the ECMWF analysis procedure favors internally consistent groups of satellite winds over more high quality radiosondes and aircraft reports. Lorenc and Swinbank (1984), comparing the ECMWF III-b analysis with the MONEX analyses by Krishnamurti et al. (1980), found that the cloud track winds used by the latter analyses systematically underestimated the winds over Indian Ocean upper level winds for the month of July. There is also the inevitable problem of misassignment of cloud heights and consequently spurious mixing of wind speeds in the vertical.

Barwell and Lorenc (1984) have studied the influence of aircraft wind observations on the British Meteorological Office's FGGE analysis. A particularly positive effect of single level aircraft data is better representation of the shape and magnitude of upper tropospheric features such as jet streams than would be obtainable with lower quality data (e.g. cloud track winds). They report increases of up to 20 m/s in jet strengths. High resolution specification of the horizontal wind is essential in these regions of strong horizontal as well as vertical shears.

As already alluded to above, an understanding of the behavior of temperature soundings by satellite infrared and microwave sounders is important for they provide in certain regions virtually the only vertical structure information. Phillips et al. (1979) and Schlatter

(1981) have attempted to assess the reliability of the TOVS profiles produced from TIROS-N retrievals in 1979. While Phillips et al. find the TOVS to be somewhat superior to those from the earlier VTPR instrument, there are biases of up to 2°C in the soundings which appear to be a function of location and degree of cloudiness as well as height with RMS errors between 1° and 2.5°C. Schlatter finds that TIROS-N profiles are generally too warm near the surface and the tropopause, too cool in midtroposphere and that, contrary to the conclusion of Phillips et al., temperature gradients are too weak relative to more reliable data. Both found that cloudy soundings were particularly unreliable.

3.2 The European Centre III-b Analysis Scheme

Two varieties of global analyses were produced during the FGGE year. Level III-a analyses produced at the NMC and the British Meteorological Office were derived from data available within operational cutoff times, usually 6 hours; this data is referred to as level II-a. The level III-b FGGE analysis data sets produced at GFDL, ECMWF and the Goddard Laboratory for Atmospheres (GLA) are each based on some version of the level II-b FGGE data set initially compiled by the designated World Data Centers (WDC's) from the data available within the three-month cutoff date. The ECMWF analysis used in this study is based upon the so-called Main FGGE Level II-b data set; certain observations received by the WDC's since the initial three-month cutoff are not included, mainly data from the regional experiments Winter MONEX, Summer MONEX and WAMEX (Bengtsson et al., 1982). (The presently available GFDL

III-b analysis data set is based on a later version of II-b which includes these data.)

The main aspects of the production of the ECMWF III-b analyses have been reviewed by Bengtsson et al. (1982), so discussion here will be brief. The 6-hour forecast-analysis cycle employed in the production of the III-b analyses consists of three major steps: analysis with optimum interpolation, nonlinear normal mode initialization and forecast. The 6-hour forecast is used as the first guess for the subsequent analysis. ECMWF archived analyses once every twelve hours except for the Special Observing Periods, when each of the six-hour analyses were archived. Once the data assimilation process is complete, the analyzed fields of the dynamical variables are passed through a nonlinear normal mode initialization for the following 6-hour forecast. These steps are outlined in a flow chart which appears in Fig. 3.2 along with a tabulation of the typical observation errors from the various data sources in the FGGE II-b data set.

The ECMWF numerical model used for the first-guess predictions is a 15-level semi-implicit gridpoint model. The basic characteristics of the model are summarized in Figure 3.3 taken from Bengtsson et al. The horizontal resolution is 1.875° (206.25 km at the equator) and the analysis is performed at 15 vertical levels extending from 1000 mb to 10 mb. Prediction is carried out in sigma coordinates necessitating vertical interpolation from the forecast sigma levels back to pressure coordinates before the data assimilation begins.

Before the data actually enter the optimum interpolation process they are subjected to a number of checks for data quality. At this point the observed data are grouped into the analysis boxes used in the

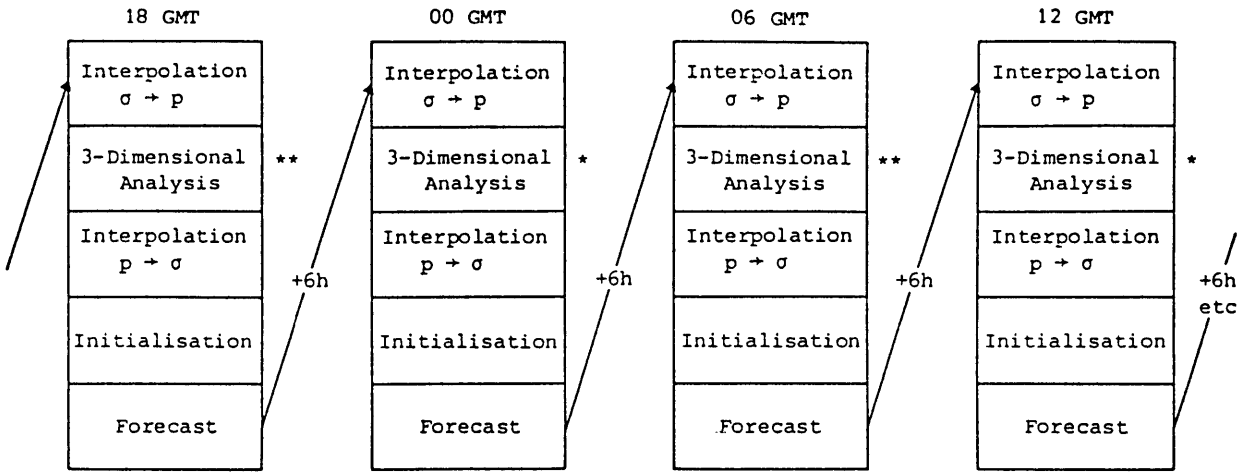

Level (mb)	Temperature (°C)			Wind ($m\ s^{-1}$)			
		TIROS-N		Radiosonde pilot			Clouddrift wind
	Radiosonde	Clear/ partly cloudy	Microwave	ASDAR AIDS	NESS WISCONSIN	ESA LMD	HIMAWARI
10	4.5	2.8	2.8	6	8	8	13
20	3.8	2.6	2.7	6	8	8	13
30	3.2	2.5	2.6	6	8	8	13
50	2.7	2.4	2.5	6	8	8	13
70	2.3	2.2	1.4	6	8	8	13
100	2.1	2.0	1.6	6	8	8	13
150	2.1	2.0	1.7	6	8	8	13
200	2.0	1.9	1.8	6	8	8	13
250	1.8	1.9	1.9	6	8	8	13
300	1.6	1.8	2.0	6	8	8	13
400	1.5	1.8	2.2	5	7	8	10
500	1.2	1.7	2.2	4	7	8	10
700	1.1	1.8	2.5	3	5	8	6
850	1.1	2.0	3.9	2	4	7	6
1000	—	—	—	2	4	7	6

Sea surface pressure: SYNOP/SHIP 1.0 mb; buoy 2.0 mb; COLBA/DROPWINDSONDE/TWOS-NAVAID observation errors are calculated from the level II-b quality information. Temperatures given as layer means.

Fig. 3.2 Flow chart for the ECMWF forecast-analysis-initialization procedure (top) and tabulation of typical observational errors for FGGE II-b data. From Bengtsson et al. (1982).

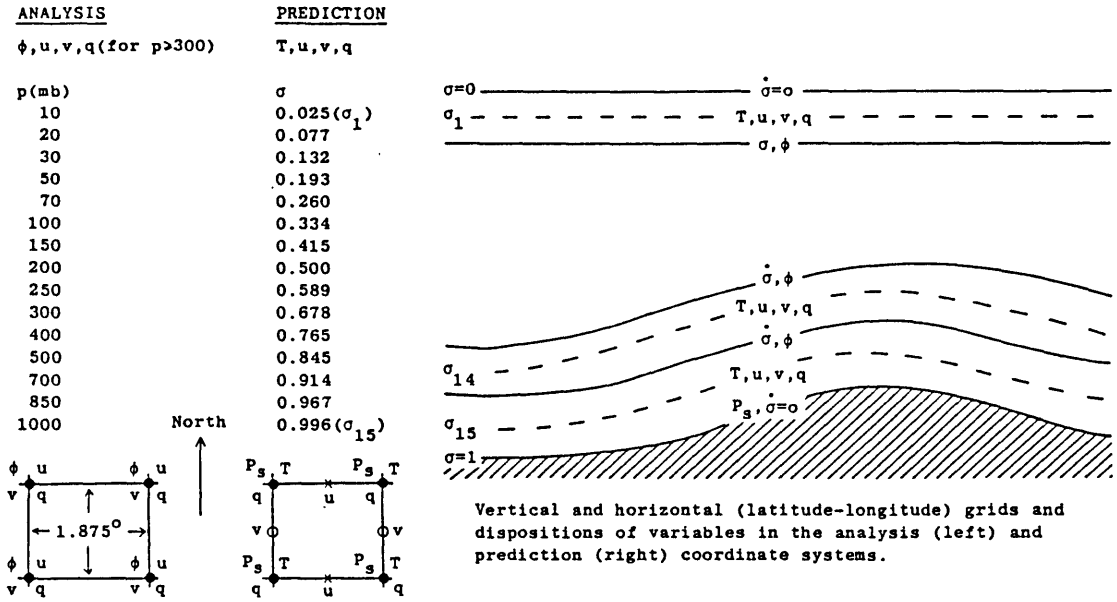

Vertical and horizontal (latitude-longitude) grids and dispositions of variables in the analysis (left) and prediction (right) coordinate systems.

ANALYSIS	
Method	3 dimensional multi-variate (15-analysis levels, see above)
Independent variables	λ, φ, p, t
Dependent variables	ϕ, u, v, q
Grid	Non-staggered, standard pressure levels
First guess	6 hour forecast (complete prediction model)
Data assimilation frequency	6 hour ($\pm$ 3 hour window)
INITIALISATION	
Method	Non-linear normal mode, 5 vertical modes, non-adiabatic
PREDICTION	
Independent variables	λ, φ, σ, t
Dependent variables	T, u, v, q, p_s
Grid	Staggered in the horizontal (Arakawa C-grid). Uniform horizontal (regular lat/lon). Non-uniform vertical spacing of levels (see above).
Finite difference scheme	Second order accuracy
Time-integration	Leapfrog, semi-implicit (Δt = 15 min) (time filter ν = 0.05)
Horizontal diffusion	Linear, fourth order (diffusion coefficient = $4.5 \cdot 10^{15}\ m^4\ s^{-1}$)
Earth surface	Albedo, roughness, soil moisture, snow and ice specified geographically. Albedo, soil moisture and snow time dependent.
Orography	Included, moderately smooth.
Physical parameterisation	(i) Boundary eddy fluxes dependent on roughness length and local stability (Monin-Obukov)
	(ii) Free-atmosphere turbulent fluxes dependent on mixing length and Richardson number
	(iii) Kuo convection scheme
	(iv) Full interaction between radiation and clouds
	(v) Full hydrological cycle
	(vi) Computed land temperature, no diurnal cycle
	(vii) Climatological sea-surface temperature

Fig. 3.3 Summary of the European Centre's 15-level grid point model used in the production of the ECMWF FGGE III-b analyses. From Bengtsson et al. (1982).

optimum interpolation. These measure 6° latitude by 660 km by 300 mb deep; in data sparse regions the depth is extended through the entire vertical domain of the model. During production of the FGGE analysis, the quality control checks included, along with checks for duplicated and mislocated reports, some modifications or exclusions: the TIROS-N microwave soundings over land and in the tropics were excluded as were bad microwave soundings through rainy clouds with clear radiance data, and assigned cloud wind heights were adjusted according to available information on the cloud top temperature or the tropopause. The latter partially compensated for the improper nominal height assignments (usually 850 mb for low level and 200 mb for upper level clouds) in the production elsewhere of cloud driftwinds from the geostationary satellites. Temperature is not analyzed directly and is instead derived from geopotential height differences. This undoubtedly eliminates some significant fine-scale vertical structure in the troposphere, particularly near the surface and the tropopause. This is compounded somewhat by the interpolation from the sigma coordinates of the model to pressure coordinates at assimilation time (Arpe, 1985a).

The details of the optimum interpolation (OI) scheme employed at ECMWF are described by Lorenc (1981). The optimum interpolation calculates adjustments to a forecast first-guess field from a weighted sum of selected observations within a given analysis volume. In the case of the dynamical variables Z, U and V, the selection of data may include any of these three types of data; the separate humidity analysis is univariate.

The interpolation weights are chosen to minimize the squared analysis error at a grid point, given a particular set of observations

distributed throughout the analysis volume within which that grid point lies. The formalism of optimum interpolation recognizes four sources of analysis error: observational errors, covariances between errors in the first guess field, covariances between errors in the observations and covariances between first-guess and observation errors. The latter covariances are assumed to be zero in the ECMWF scheme. Thus the squared analysis error (normalized by the first-guess error variance) at a point k in the analysis volume can be written as a function of the vector $\tilde{w}_k = [w_i]$, the desired interpolation weights for each of the observations i, and the above-mentioned variances and covariances:

$$(e_k^a)^2 = (E_k^a/E_k^p)^2 = 1 - 2\,\tilde{w}_k^T\,\tilde{h}_k + \tilde{w}_k^T\,\mathbf{M}\,\tilde{w}_k$$

where $\tilde{h}_k = [\langle p_k p_i \rangle]$ and $\mathbf{M} = [\langle p_i p_j \rangle + e_i^0 \langle b_i b_j \rangle e_j^0]$, $\langle p_l p_m \rangle$ and $\langle b_l b_m \rangle$ are correlations between first-guess errors and observation errors, respectively, and $e_l^0 = E_l^0/E_l^p$ is the l^{th} observational error normalized by the first-guess variance. First-guess and observational variances are estimates obtained from knowledge of the statistical behavior of these variables. First-guess error covariances are modeled as functional relationships between errors in one variable and place to another. The most important of these from the point of view of divergent winds is the relationship between the error variances of the winds and the geopotential height. Outside the tropics, the relationship is geostrophic; within the tropics, this relationship is relaxed somewhat. In addition, the covariance models employ an isotropic Gaussian damping in distance, the strength of which is specified by a horizontal correlation scale factor. Smaller values of this parameter increase the

resolution of the analysis but also constrain the distance to which extrapolation can reach into data voids.

The net effect of the scale damping factor and the first-guess error covariance models in the III-b analysis was to constrain the corrections to the first guess smaller than about 1000 km to be nondivergent in the tropics and geostrophic outside the tropics. However, large-scale divergence modes did not feel this constraint (Lorenc and Swinbank, 1984) because they are much larger in scale than the analysis boxes; only within the boxes is the analysis constrained to be nondivergent. Figure 3.4, taken from Hollingsworth and Cats (1981) shows a spherical harmonic spectrum of the divergent wind energy at 200 mb for January 1979. Beyond zonal wave 5, even at the largest meridional scales, the divergent energy is small; at the equator a one-quarter wavelength for this harmonic is roughly three analysis boxes in length.

Daley (1985) has experimented with several generalizations of the ECMWF prediction error covariance models to see if the analysis of divergent modes in the tropics could be improved. While the condition of geostrophy is relaxed in the tropics, analysis increments at the scale of the analysis boxes were still constrained in the III-b production system to be nondivergent. He found that a slight relaxation of this constraint, in which the divergence error was allowed to be roughly 1/10 of the total error, produced a much improved divergence analysis without the introduction of "noise." Julian (1984) has proposed a scheme in which the divergent component of the first guess is estimated from the fields of outgoing longwave radiation. Both of these schemes would very likely improve the quality of the divergent wind

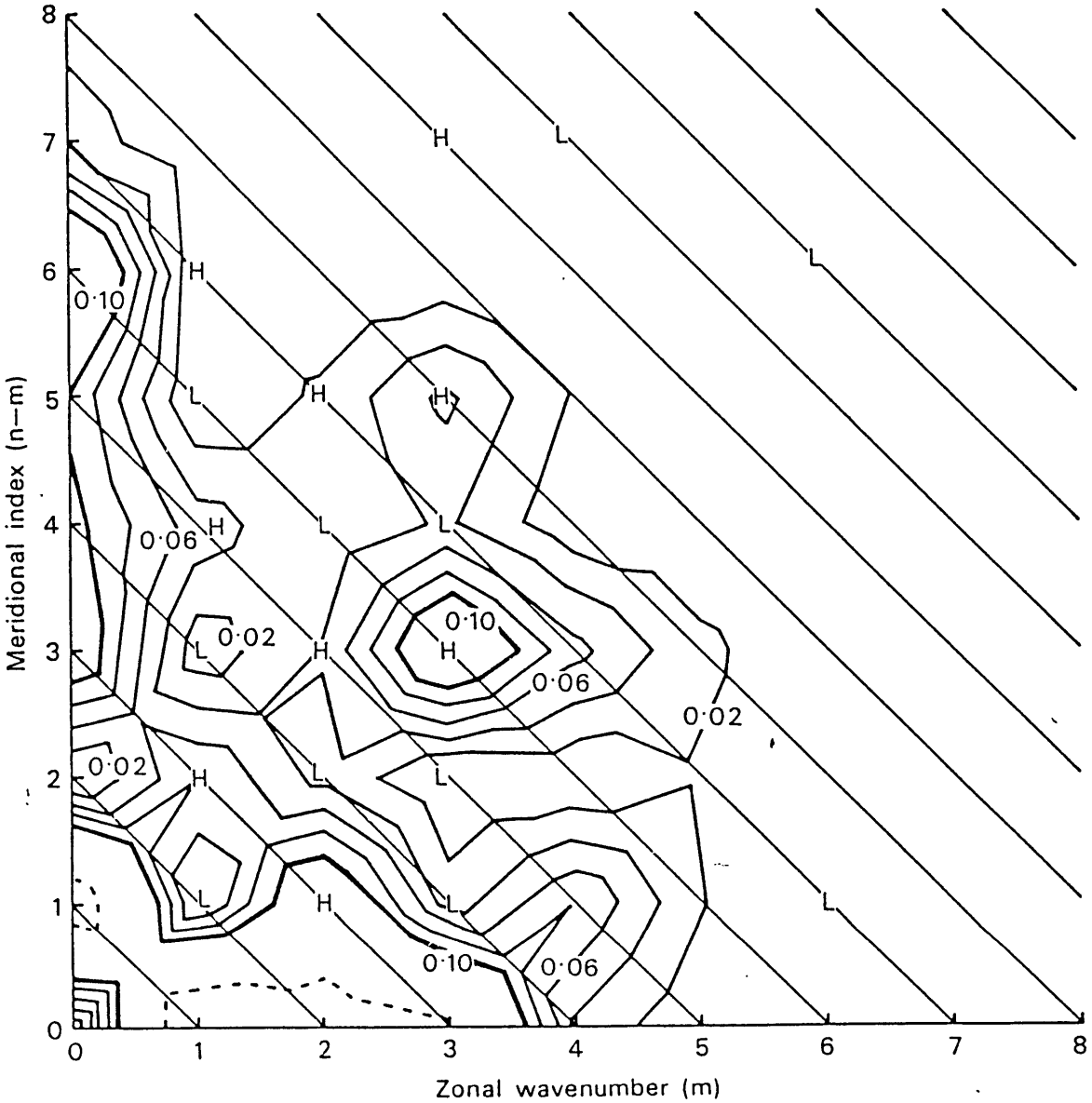

Spherical harmonic spectrum of the kinetic energy of the 200 mb divergent wind for January 1979.

Fig. 3.4 Spherical harmonic spectrum of divergent wind energy at 200 mb in the ECMWF III-b analyses for the month of January. From Hollingsworth and Cats (1981).

analyses from the present III-b archive, the latter scheme being particularly useful in regions of sparse observations.

There have been several studies at the European Centre (Cats and Wergen, 1982; Heckley, 1982; Daley, 1983) suggesting that there are significant problems with estimating model normal modes in the tropics. Daley's (1983) work is the most systematic study. Due to the constraints of the optimum interpolation prediction error covariances mentioned, the greatest problems are found in estimating non-geostrophic modes. In particular the analysis has difficulty with Rossby-gravity and Kelvin waves because of the imposed geostrophy, but there is considerable underestimation of the wind magnitude in modes in which the wind direction is accurately specified. Figure 3.5 compares the results of analyzing the first symmetric Rossby wave (the 5-day wave), the Kelvin wave and the Rossby-gravity wave with their proper magnitudes. These analyses were made with hypothetical 'perfect' observing system and simply demonstrate the difficulties in producing an error-free analysis under ideal conditions. In reality the observations are much sparser and contaminated with errors, compounding the problem further. Cats and Wergen (1982) find considerable aliasing between both horizontal and vertical modes when the optimum interpolation is presented with an augmentation of the normal data by a single input mode; the OI has particular difficulty with internal Kelvin modes.

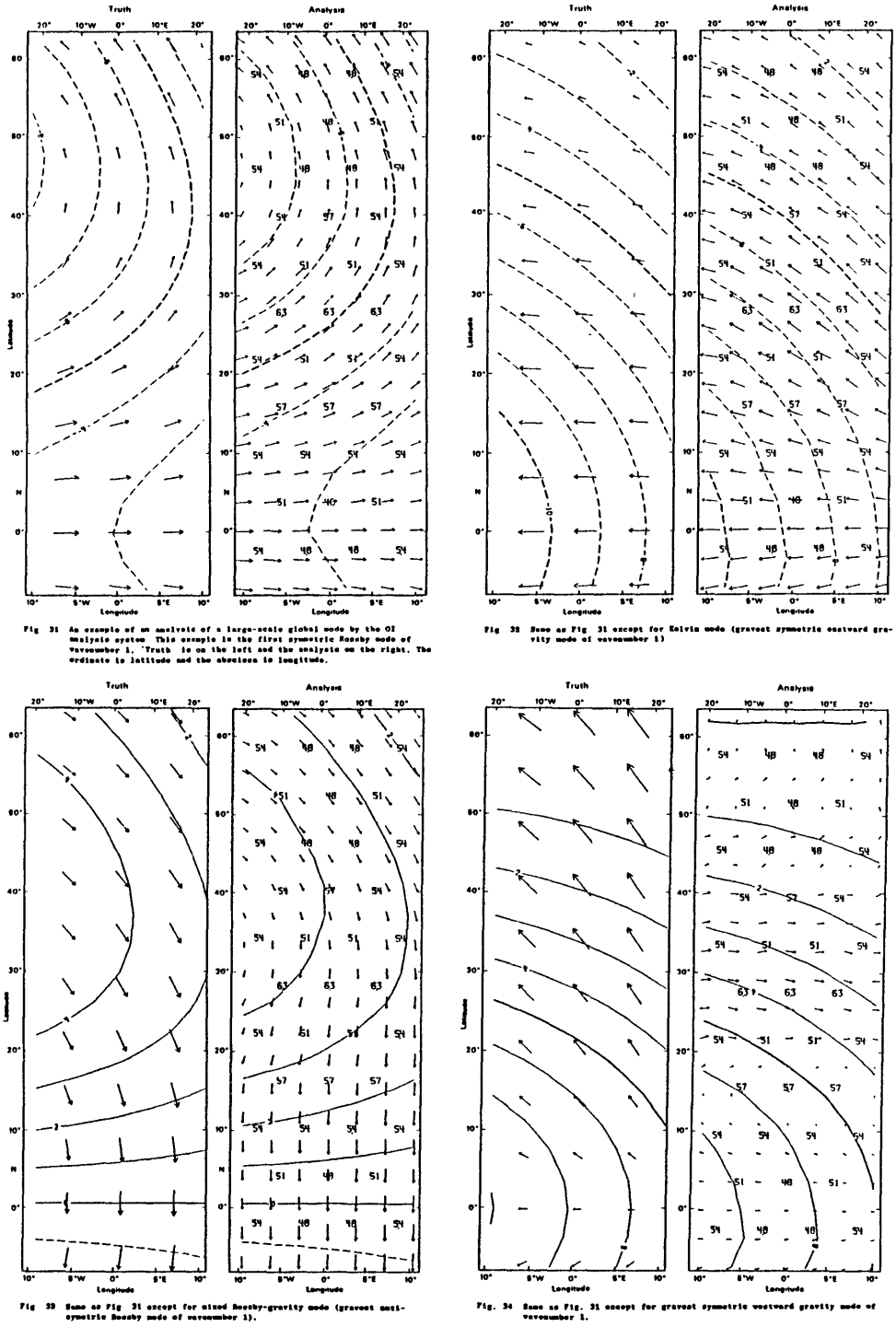

Fig. 3.5 Wind and geopotential height patterns of individual wavenumber one Hough modes (lefthand panels) input to the ECMWF optimum interpolation and the analyses that result (righthand panels), given "perfect" observations: first symmetric Rossby wave (upper left); Kelvin wave (upper right); mixed Rossby-gravity wave (lower left); and gravest symmetric westward gravity wave (lower right). From Daley (1983).

3.3 Normal Mode Initialization for the ECMWF III-b Analyses

The fields of wind and geopotential height which appear in the ECMWF III-b analysis archive are the products of the optimum interpolation procedure described above and as such do not directly reflect the effects of the nonlinear normal mode initialization which precedes each of the forecast runs; only the archived fields of vertical velocity are obtained after initialization. The effects of the nonlinear normal mode initialization on the forecast fields must be considered, however, because these are used in the subsequent analysis/forecast cycle as the optimum interpolation first guess fields. A suppression by the initialization procedure of meteorologically significant large-scale divergent modes forced by latent heating in the tropics might lead to serious underestimation of these modes in the resulting first guess fields 6 hours later. In particular, a number of authors have suggested that this is the case for the zonally symmetric internal modes which represent the Hadley circulation in the European Centre's 15-level model. In the following section we will briefly review the important properties of the Centre's normal mode initialization for the III-b analysis production, its drawbacks with respect to divergent tropical modes that have been discussed in the literature and an assessment of the effects of these problems on this study.

The goal of most initialization procedures for numerical weather prediction models is to eliminate the gravity waves which result from errors in the forecast initial value fields. This goal is usually motivated by a number of concerns, among them the generation of spurious

high frequency mass readjustments as well as unrealistic precipitation events during the initial period of the model integration.

Because of nonlinear interactions between Rossby modes in the primitive equations, a balanced state will include some gravity wave energy. Unlike linear normal mode initialization which sets the gravity mode amplitudes initially to zero, nonlinear normal mode initialization attempts rather to make the time rate of change of gravity wave modal coefficients equal or close to zero. Following Williamson and Temperton (1981) the tendency equation can be written

$$\frac{d}{dt} c(k,l,m) = -i\nu' c(k,l,m) + r(k,l,m) \tag{2.7}$$

where c(k,l,m) is the amplitude of the model gravitational normal mode defined by zonal wavenumber k, latitudinal index l and vertical mode index m. ν' is the associated eigenvalue so that the first term on the righthand side is the linear growth term; the second term is the sum of all the nonlinear modal interactions, including the interactions with the Rossby modes. The basic assumption in the scheme of Machenhauer (1977) is that the r(k,l,m) terms undergo a variation much slower than their corresponding modal coefficients, thereby allowing an iterative procedure to obtain the initialized value for c(k,l,m).

Temperton and Williamson (1981) and Williamson and Temperton (1981) have described in a general context the adiabatic application of Machenhauer's (1977) nonlinear normal mode initialization to multi-level forecast models such as the 15-level model used in the European Centre's III-b analysis. They note that the initialization in the latter model efficiently eliminates contamination of mid-latitude forecasts by gravity waves, although there is little effect upon the Rossby modes. In

the tropics, this reduction of gravity waves is not necessarily beneficial. Puri (1983) has shown that the lowest-frequency model internal gravity modes with equivalent depths of around 250 meters are closely tied to deep convection (these modes tend to have inflow near the surface and outflow in the 300-100 mb region.) In particular, forecast Hadley circulations are primarily maintained by the zonally symmetric internal modes near this equivalent depth.

Hollingsworth and Cats (1981) note that gravity modes are strongly forced by the Rossby modes in the middle latitudes but not in the tropics. Thus, in order to initialize a forecast run with a realistic tropical overturning, the modeler is presented with two alternatives: to include diabatic forcing in the initialization or to exclude some or all of the gravity modes from the initialization. They report on an experiment with the European Centre's forecast model in which they compared the analyses and forecasts for control runs with the first five vertical modes initialized to those from runs in which only the first two modes were initialized. Two figures from their results are reproduced here. Fig. 3.6 displays latitude-height sections of the mean meridional wind after initialization for the control run and the experimental run. It is evident that the filtering of the higher internal modes in the control run suppresses strong cross-equatorial Hadley flows in the upper and lower troposphere. Strong differences in the tropics appear in the initialized velocity potential fields at 150 mb which appear in Fig. 3.7.

With respect to the impact of satellite and rawinsonde coverage on the analysis of divergent wind fields, the January 1981 period used for this experiment was not appreciably inferior to much of the FGGE period,

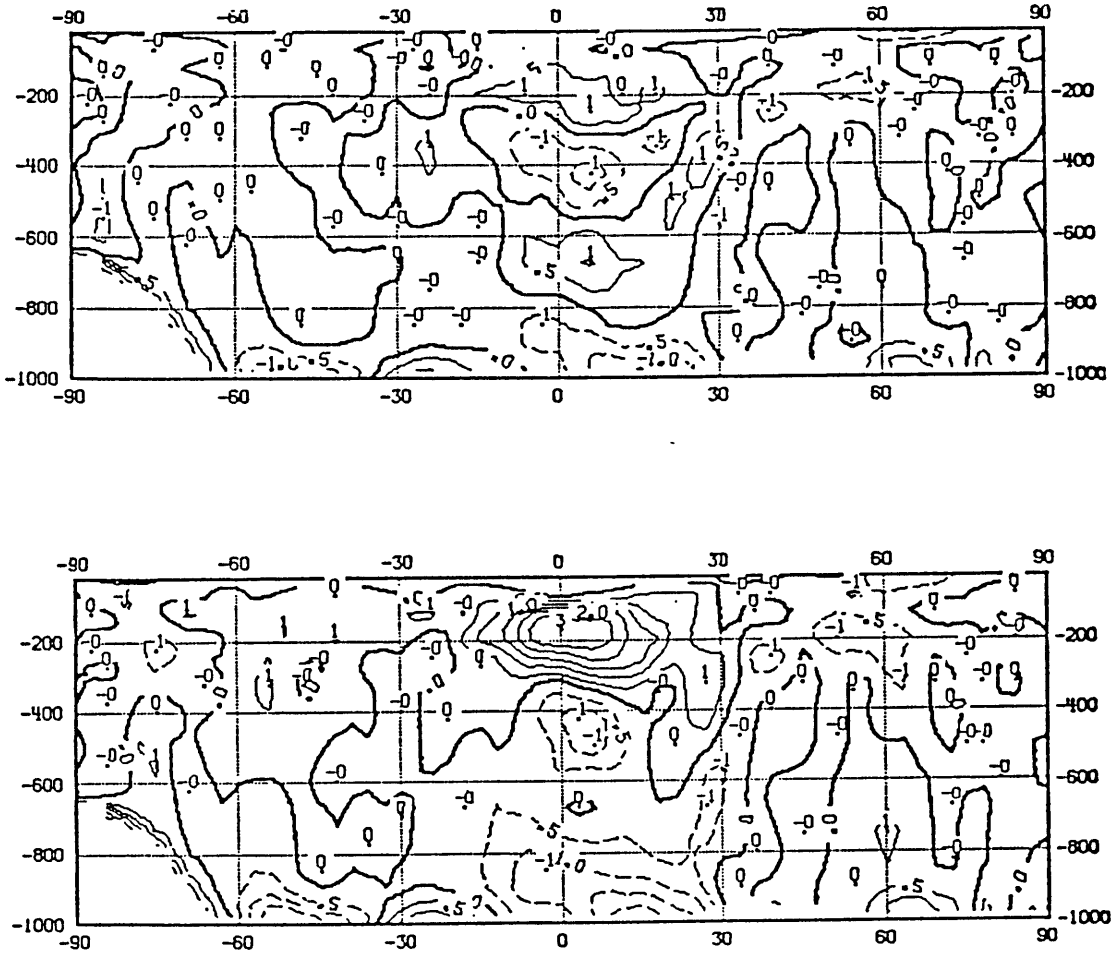

Zonally averaged $[\bar{v}]$ in the initialised analysis in the control run (top) and in the experiment (bottom) after one day of assimilation. Contour interval is 1 m/s.

Fig. 3.6 Meridional height cross-sections of the zonally averaged meridional wind at 24 hours from an initialized control run (top) of the ECMWF model and an experimental run in which only the first two internal gravity modes were initialized (instead of five), contour intervals 1m/s. From Hollingsworth and Cats (1981).

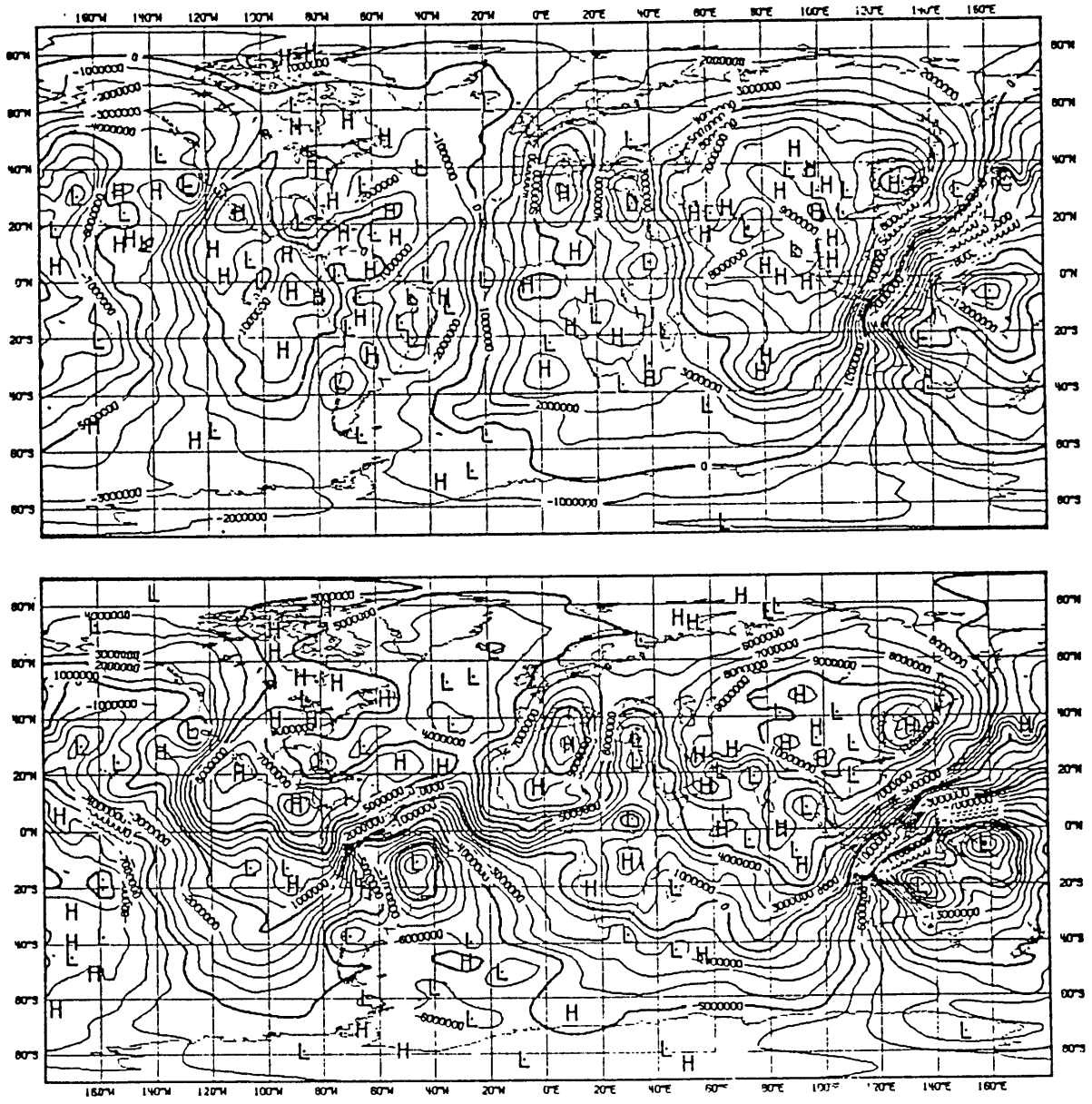

Velocity potential at 150 mb in the control run (top) and the experiment (bottom) after one day of assimilation.

Fig. 3.7 Velocity potential at 150 mb in the control run of 3.5 (top) and the experiment after one day of assimilation, contour intervals $1X10^6$ m^2/s.

so one can usefully ask what are the implications of these differences for the uninitialized analyses which comprise the ECMWF FGGE III-b data set. The impact of the initialization on the uninitialized analysis is felt in the following analysis step 6 hours later. Hollingsworth and Cats present evidence that the convective heating in the filtered, control run does recover somewhat relative to the experimental run during the first 24 hours of the integration. During hours 0-6 the convective heating rate in the control was 82% of the experiment, reaching roughly 100% by the end of 36 hours. The above recovery suggests that the use of the model's 6-hour forecast as a first guess for both the Hadley cell and the zonally asymmetric divergent modes is not gravely hampered by initialization, although the model is likely still spinning up the Hadley cell. This speculation is borne out in results from a study by Heckley (1982). Fig. 3.8 displays the average for March 1981 of the uninitialized velocity potential at 200 mb, the initialized velocity potential and forecasts after 1 and 10 days. Gradients in the initialized analyses are considerably weaker than in the uninitialized analyses as might be expected from the nonlinear normal mode initialization. On the other hand, the gradients in the 1-day forecasts are of the same magnitude or exceed those in the uninitialized analyses. A glaring exception however is over Africa where the forecasts show a much stronger region of outflow than is apparent in the uninitialized analyses. Heckley speculates that the growth of forecast error (i.e. relative to the initialized analyses) could be the result of a number of factors: inadequacy of data over Africa combining with the optimum interpolation and the adiabatic initialization to produce a severe underestimation of the diabatic

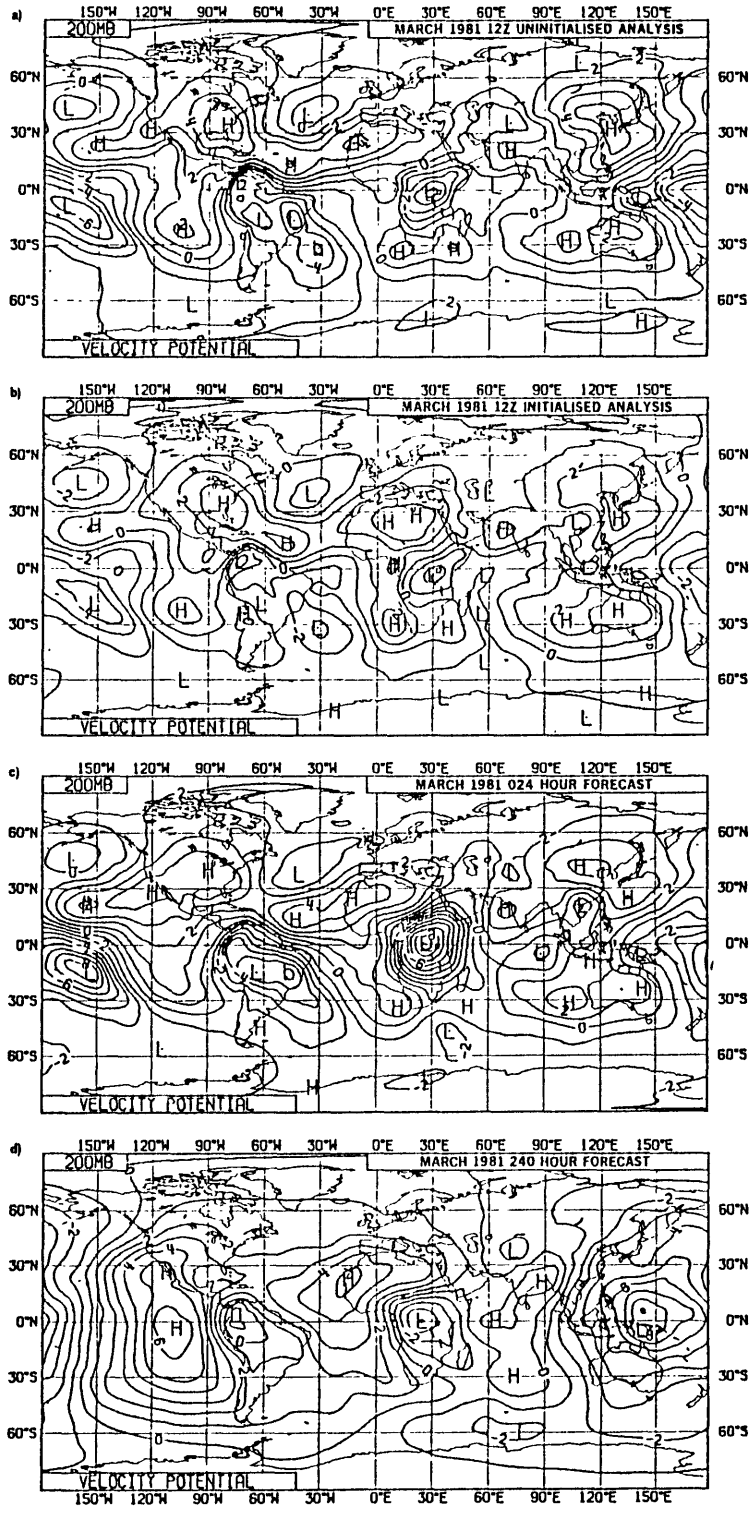

Fig. 3.8 March 1981 averages of 200 mb velocity potential. From top, uninitialized 12Z analyses, initialized 12Z analyses, 1-day forecasts, and 10-day forecasts, contour intervals 1×10^6 m2/s. From Heckley (1982).

circulation over Africa, the aliasing of the diurnal cycle of heating over the continent by the observations as well as the forecast model itself. In the discussion of the results below, we will pay particular attention to lack of data over the African and South American regions where it is known there exist important planetary heat sources.

Perhaps more worrisome are the systematic errors in tropical heating in the European Centre's model which have been examined by Heckley (1985). His results apply to the implementation of the model current in 1983 and 1984 which employed a diabatic initialization. Despite this major difference from the forecast/analysis cycle used in the production of the FGGE III-b analyses, Heckley's remarks are useful in assessing the effects of the model on the large scale divergent circulations in the III-b analysis. Heckley compares 5-day forecasts of the temperature with the uninitialized analyses and finds a warm bias in the tropics confined to a shallow layer centered near 150 mb which reaches more than 4 degrees, or roughly 0.8 K/day excess heating. Below 400 mb and down to the surface the tropical troposphere seems to cool at approximately 0.2-0.5 K/day. He attributes much of this warm/cold bias to known deficiencies in the radiation code of the model, but the increased stability in the upper troposphere probably also affects the Hadley circulation. In addition the analysis tends to be too moist in the lower levels and too dry at upper levels. Heckley suggests that this is partly due to the elimination of small scale divergence by the optimum interpolation scheme; consequently the model has to spend some time spinning up the convection at these scales, resulting in an excess of evaporation over precipitation for the model as a whole for the first 12 hours.

3.4 Comparison of the ECMWF FGGE III-b and GFDL III-b Analyses

As we have seen, the analysis of tropical circulations by the forecast/analysis system used at the European Centre for the FGGE III-b is hampered by the following major problems: insufficient observational coverage, particularly in regions of active convection, constraint of synoptic scale analysis increments to near nondivergence, elimination of low frequency, meterologically significant divergent modes in adiabatic initialization and insufficient convective activity in the initial time periods of model integration. How do these and other deficiencies affect the quality of the analyses with respect to other FGGE global analyses, in particular the GFDL analysis?

The assimilation procedure at GFDL operated quite differently from ECMWF and on the face of it, it would appear that some of the documented problems of the ECMWF approach were avoided by the GFDL analysis. Observations were continuously inserted into the ongoing model integration with optimum interpolation limited to a radius equal to the grid spacing ($\sim$250 km). Initialization was limited to only those modes with frequencies shorter than 6 hours. Comparisons between the two III-b data sets have generally demonstrated that the divergent wind field in the GFDL set is up to 50% stronger than in the ECMWF. Lau (1985a) has produced a compilation of comparative statistics. Figure 3.9 (taken from this study) shows fields of 200 mb velocity potential for the same two periods. The steeper cross-equatorial gradients of velocity potential over the monsoon regions are evidence that the Hadley cell in the GFDL analysis is stronger than in the ECMWF analysis. This can be seen directly in Figure 3.10 which contrasts the

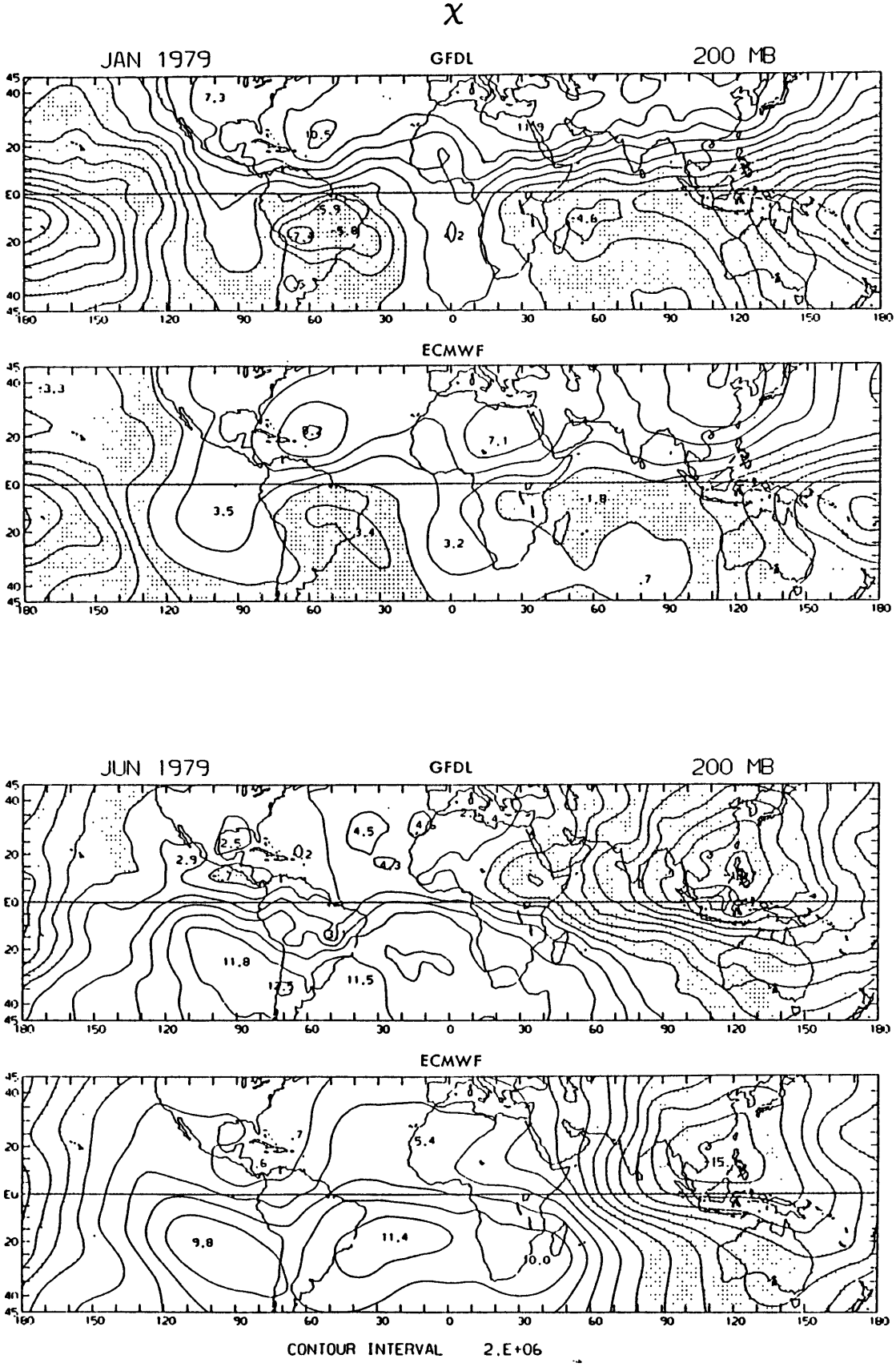

Fig. 3.9 200 mb velocity potential distributions from the FGGE III-b analyses by GFDL and ECMWF: January 1979 (upper panel) and June 1979, contour intervals 2×10^6 m^2/s. From Lau (1985a)

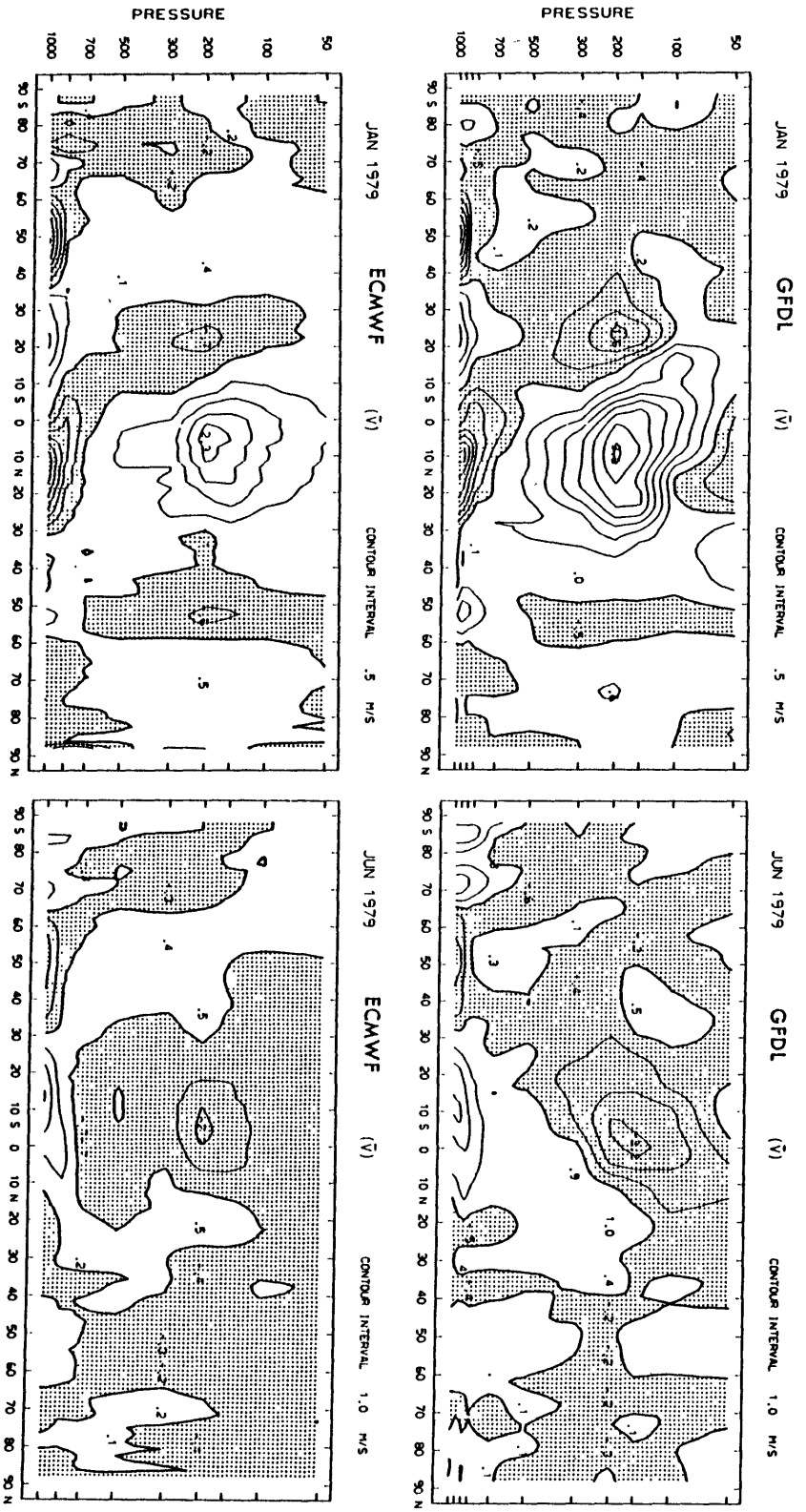

Fig. 3.10 Meridional height cross-sections of the zonally-averaged meridional wind from the the FGGE III-b analyses by GFDL and ECMWF for the months of January 1979 (left panels) and June 1979, contour intervals 1 m/s. From Lau (1985a)

zonal mean meridional wind circulations for the two months January and June 1979.

The relative lack of constraints in the GFDL analysis likely has some drawbacks as has been pointed out in Julian (1985) and Arpe (1985a). They find that the European Centre's analysis is generally more faithful to the total observed wind than GFDL's analysis. Arpe (1985b) has computed comparative RMS differences between observations and analyses between the equator and 21°N for a limited period in SOP-1. At 250 mb the ECMWF analysis has RMS differences from four different observed data types from 3.6 (for PILOTS) to 5.3 m/s (SATOBS). In contrast GFDL differences ranged from 5.4 (TEMPS) to 6.3 m/s (AIREPS). For TEMPS (rawinsondes), the ECMWF RMS difference of 3.7 m/s is definitely superior to GFDL. At other levels the relative agreement with the observed data is similar. Julian (1985) has also made an interesting comparison of the two data sets in spectral groups for three analysis times during SOP-1. He finds that the correlations between the rotational zonal wind u^r in each for waves 1-4 and 5-8 are 0.92 and 0.93 respectively, while for waves 9-16 and 17-30 the correspondence plunges to 0.56 and 0.23. For v^r the correlations are 0.80, 0.83, 0.63, and 0.10. Evidently, the analyses of rotational winds seem to agree much more closely at scales somewhat longer than the size of the European Centre OI analysis bin. The corresponding correlations for u^d (v^d) are expectedly considerably smaller: 0.77 (0.63), 0.34 (0.44), 0.28 (0.06) and -0.20 (-0.04). The much higher divergent wind energy in the higher wave numbers in the GFDL analysis is clearly in evidence here.

Given the analysis problems discussed above and the relative strengths and weaknesses of the ECMWF III-b analysis, general

circulation studies such as the one reported here may be handicapped as far as the magnitude of the divergent circulations are concerned. In connection with the problems of data gaps, interpolation underestimation and aliasing, it is not clear however that other less constrained analysis schemes will do appreciably better, although a properly implemented diabatic initialization may well be superior to adiabatic initialization. Real progress in specification of divergent wind systems may have to wait until the incorporation of proxy data for the location of centers of divergence over ocean and remote continental regions as suggested by Julian (1984). Nonetheless, we will show in this work that there are coherent large-scale divergent circulations in the tropics which emerge from the ECMWF FGGE III-b analysis and which are consistent with independent measures of heating. These appear both as changes in the Walker circulation and in the Hadley circulation, although the former are by far more easily observed.

4. The Dominant Variability of the Large-Scale Divergent Circulation in the Tropics during the FGGE Year

This chapter presents a number of lines of evidence for the existence of remarkably coherent intraseasonal changes during the FGGE year in the large scale divergent circulation, changes which have the 40-50 day period identified in previous works. These fluctuations appear in the dominant modes from empirical orthogonal function analysis of the twice-daily upper and lower tropospheric velocity potential fields generated from the European Centre's analysis set. Velocity potential fields and time series as well as the components of the divergent wind field derived from the velocity potential EOF modes are used to describe the characteristics of these changes.

The slow fluctuations are the strongest in the fields of velocity potential at 200 mb (and thus also in the divergent winds at that height). The lower level divergent wind fields, as represented by EOF modes of the velocity potential at 850 mb, undergo changes that complement the behavior at upper levels, i.e. divergent centers at upper levels are paired with convergence below. Combined EOF analysis of the 850 and 200 mb divergent wind fields yields nearly identical results as the two separate EOF calculations and underlines the importance of mid-tropospheric latent heating in the maintenance of the intraseasonal fluctuations of the Walker Circulation as well as its long-term mean state.

4.1 Derivation of Reduced Grid Data Sets

4.1.1 Calculation of Velocity Potential and Streamfunction and Derivation of Divergent and Rotational Wind Fields

The velocity potential and streamfunction fields for this study were calculated using a direct Poisson equation solver called PHIPSI written by Paul Swartztrauber of NCAR. PHIPSI takes as input the gridded zonal and meridional winds over a latitudinal belt between a chosen pair of meridional boundaries. Streamfunction and velocity potential fields are output on a non-staggered grid whose boundaries are at least one grid latitude farther poleward than the input wind grids. For this study, we chose to employ all the data available in the ECMWF reduced grid between the North and South Poles. Thus the input wind fields spanned the grid latitudes 86.25°S to 86.25°N.

As applied in this study, PHIPSI differs from the more general spherical elliptic equation solver HWSSSP also available at NCAR in that it is not necessary to calculate explicitly the fields of divergence and vorticity. PHIPSI avoids the specification of boundary conditions by finding a set of solutions to the unconstrained problem (i.e. without boundary conditions) which extend at least one grid latitude farther poleward than the input grid of winds. From these is chosen the solution which has the smoothest transition at the boundary (P. Swarztrauber, personal communication.) Comparisions of winds derived from the output velocity potential and streamfunction fields revealed that this approximation procedure is of little consequence for the near-polar boundaries we chose.

Divergent and rotational wind fields can be derived from PHIPSI generated fields of velocity potential χ and streamfunction ψ by means of second-order centered differences:

$$(4.1) \qquad u^d_{i,j} = \frac{1}{a\cos\phi_j}(\chi_{i+1,j} - \chi_{i-1,j})/2\Delta$$

$$(4.2) \qquad v^d_{i,j} = \frac{1}{a}(\chi_{i,j+1} - \chi_{i,j-1})/2\Delta$$

$$(4.3) \qquad u^r_{i,j} = -\frac{1}{a}(\psi_{i,j+1} - \psi_{i,j-1})/2\Delta$$

$$(4.4) \qquad v^r_{i,j} = \frac{1}{a\cos\phi_j}(\psi_{i+1,j} - \psi_{i-1,j})/2\Delta$$

where the superscripts d and r refer to divergent and rotational fields respectively; i,j are zonal and meridional indices, increasing northward and eastward respectively; a is the average radius of the earth; and Δ is the 3.75° grid spacing in units of radians.

PHIPSI solves for velocity potential and streamfunction using a second-order centered difference algorithm. It produces grid values of its solutions at the same points as the input winds. As pointed out, for example, by Dey and Brown (1974), this may lead to considerable underestimation of derived winds in narrow shear zones due to non-compensating truncation errors. However, as PHIPSI solves for both the velocity potential and streamfunction simultaneously, it preserves the energy in the input analysis wind fields to a very good approximation. Time average RMS differences between the analysis winds input to PHIPSI and the wind recomposed from the divergent and rotational components obtained from the velocity potential and streamfunction are small everywhere in the analysis at the 200 mb level where these statistics

were kept. Due to the approximation algorithm PHIPSI employs, the RMS errors for the meridional winds decline monotonically from $O(10^{-1})$ at the poleward boundaries to the equator; equatorward of about 70° latitude the RMS errors were less than 0.01 m/s for the one-year period. Errors in the zonal wind were less than this latter value presumably because of greater precision of the streamfunction estimates near the poleward boundaries.

4.1.2 Daily Highly Reflective Cloud Data: Derivation and Data Reduction

The highly reflective cloud (HRC) data which we use in this study are derived from the $1^{\circ} \times 1^{\circ}$ HRC data continually updated and archived by the group under the direction of Dr. Oswaldo Garcia at NOAA/CIRES in Boulder, Colorado. Dr. Garcia kindly offered us the use of his data for this comparison study.

The HRC data are an index of the distribution of deep convection. The technique for obtaining the data was originally developed by Kilonsky and Ramage (1976). Using daily satellite cloud mosaics in the visible band, each one-degree grid square is checked for the presence of a bright convective cloud systems which are presumed to indicate deep convection. Aside from the criterion that the cloud system must have a scale of 200 km or more, the criteria for distinguishing convective clouds from stratiform and other cloud forms are primarily subjective but fairly easily taught to those involved in the data collection. The coding of the daily data is quite simple. If a one-degree square contains highly reflective cloud, a "1" is entered for that square for that day; if not, a zero. The HRC index is thus essentially a measure

of the frequency of deep convection. It is related to the intensity of the large scale circulation only through time and/or spatial averaging. One major drawback of the data is that they are collected but once daily, and as they rely on the visible photographs this is near local noon. Diurnal variability is thus not resolved.

The $2.5^{\circ} \times 2.5^{\circ}$ grid archive of outgoing longwave radiation (Gruber and Winston, 1978) covers the period from 1974 to the present (with a ten-month gap March-December 1978.) It has been used as an indicator of large-scale anomalies of convection in the tropics by Heddinghaus and Krueger (1981), Lau and Chan (1983a, 1983b, 1985) and Weickmann (1983), among many others.

Both OLR and HRC fields are derived from scanning radiometer measurements on the NOAA polar orbiting satellites in the infrared (IR) and visible channels respectively. As such both data sets are global in character, although the OLR data have the additional advantage of twice daily sampling which can be used to eliminate any aliasing due to diurnal variability of convection. However there are several reasons why we felt the HRC data are a valuable alternative to the OLR for studies of synoptic as well as longer time scale variability of tropical rainfall and convective activity. First of all there are the practical advantages of its higher archived resolution ($1^{\circ} \times 1^{\circ}$ vs. $2.5^{\circ} \times 2.5^{\circ}$) and simple form. Secondly, although there have been a number of estimates of tropical rainfall based upon data from the individual geosynchronous satellites (Griffith et al., 1978; Stout et al., 1979; Arkin, 1979), the OLR data have not been explicitly related to daily or short period variations of rainfall [with the exception of a study by Arkin et al. (1985)]. In contrast, Kilonsky and Ramage (1976) have developed a

regression equation explaining over 50% of the monthly rainfall variance at a set of Pacific coral atolls with monthly HRC totals. In addition, Garcia (1981) found that daily rainfall estimates from the HRC data over the GATE area compare favorably with those using the technique developed by Griffith et al. (1978), although the latter estimates are superior where nighttime rainfall is an important contribution.

For our purposes we have reduced the original $1^{\circ} \times 1^{\circ}$ data to a grid corresponding to the reduced ECMWF grid. This was accomplished by apportioning the one-degree set of 1's and 0's in the daily grids between neighboring $3.75^{\circ} \times 3.75^{\circ}$ grid squares and summing. Partial HRC squares were weighted in the respective ECMWF grid squares by the proportion enclosed in the latter squares. Thus if each of the HRC grid squares at least partially enclosed in an ECMWF grid square indicated the presence of highly reflective cloud, the value for the ECMWF reduced grid square would be 3.75^2 or 14.0625. Since all the figures displaying HRC data in this study employ at least some form of spatial averaging we will employ as the basic unit the "grid-day" which indicates the number of $1^{\circ} \times 1^{\circ}$ grid-squares containing highly reflective cloud within the averaging region on that particular day.

The version of the HRC data set from which we worked in this study was preliminary and reflected certain weaknesses in the TIROS-N photomosaics peculiar to the satellite's first months of operation in 1979. Dr. Garcia has informed us that 40-50 day variability is more clearly indicated in the present version of the data set scheduled for public release in spring 1986.

4.2 The Total, Rotational and Divergent Winds: Annual Mean and Seasonal Behavior

The intraseasonal oscillations we are investigating are set against the backdrop of the seasonal cycle which is the most important mode of variability in the tropics, both in the total and rotational circulations as well as the divergent circulations. In this section are presented annual means and selected monthly means and standard deviations for the 200 and 850 mb wind fields in the ECMWF III-b analysis together with their counterparts for the rotational and divergent wind fields.

4.2.1 Annual Averages and Variability

Fig. 4.1 displays the FGGE-year (12/1/78-11/30/79) 200 mb fields of streamfunction, total zonal wind and standard deviations of the total zonal winds. As is well known, the general pattern of the 200 mb time mean flow in the Northern Hemisphere middle latitudes is much more wavelike than in the Southern Hemisphere; this waviness takes the form of two distinct jet regions, one over eastern Asia, the other over eastern North America. In the Southern Hemisphere, mean winds greater than 20 m/s cover roughly half the hemisphere. There are a number of features to note in the tropics at this level. Strong easterlies (<-10 m/s) prevail across most of the Eastern Hemisphere in a region centered between 10^{o} and 15^{o} N. This undoubtedly reflects the strong easterly jet during the Southwest Monsoon. 200 mb easterlies also are found over South America. It has been speculated that regions of equatorial upper

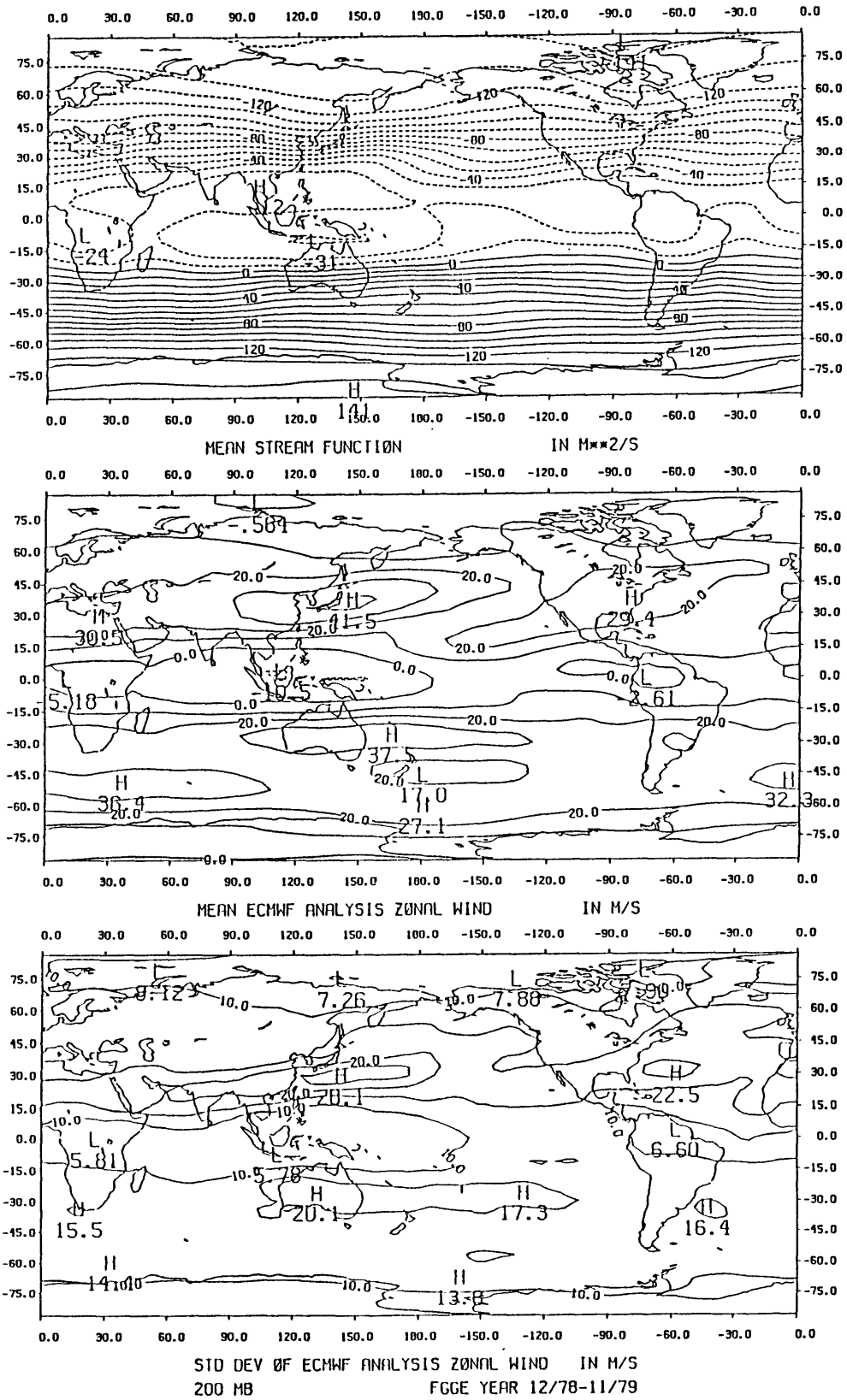

Fig. 4.1 FGGE time averages, 12/1/78-11/30/79, 200 mb streamfunction, contour interval 10×10^6 m^2/s (top); zonal wind from ECMWF III-b analysis, contour interval 10 m/s (center); and standard deviation of zonal wind, contour interval 5 m/s (bottom).

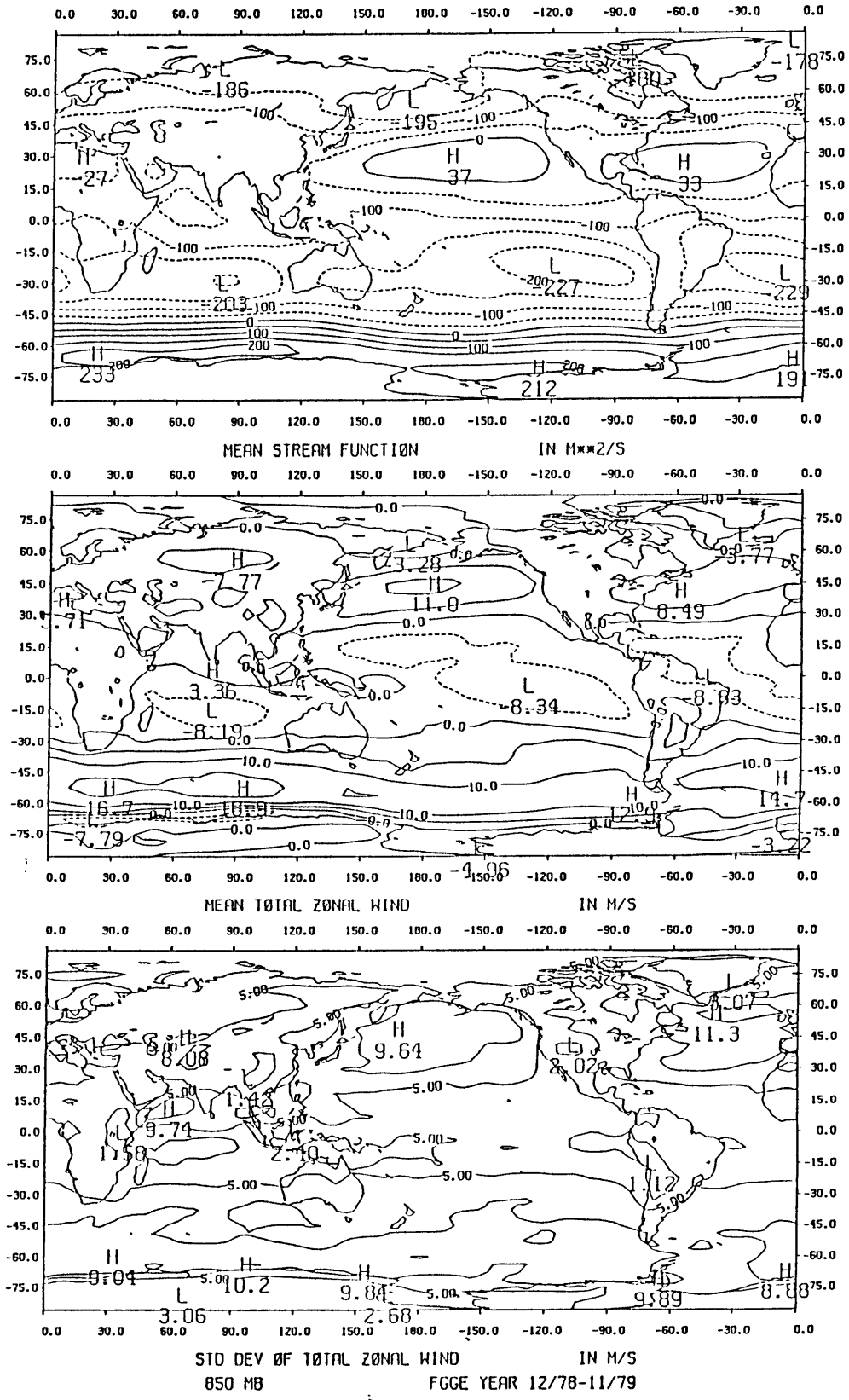

Fig. 4.2 FGGE time averages, 850 mb streamfunction, contour interval 50×10^5 m^2/s (top); zonal wind, contour interval 5 m/s (center); and standard deviation of zonal wind, contour interval 2.5 m/s (bottom).

level westerlies such as those occurring over the eastern Pacific and the Atlantic Ocean offer a means for interhemispheric wave energy transmission (Webster and Holton, 1982).

850 mb means are shown in Fig. 4.2. At this level, the easterly trade winds equatorward of 30 degrees latitude give way to oceanic westerlies further poleward. These are strongest in a wide band nearly encircling the globe between 40°S and 60°S. Westerlies occur at or near the equator in the central Indian Ocean and over the New Guinea region. The strongest average trade winds are in the south central Indian Ocean, and also in bands stretching northwest to southeast across the tropical Pacific and Atlantic oceans.

Standard deviations of the zonal wind at 200 mb (Fig. 4.1, bottom) in the ECMWF III-b analysis are generally higher than in the GFDL III-b analysis [cf. Lau (1985b), p.410]; in the jet regions they correspond to transient zonal kinetic energies greater than GFDL's analysis by nearly a factor of two. The lowest levels of transient kinetic energy at 200 mb appear to be associated with the regions of mean easterlies in the tropics. The same holds at 850 mb (Fig. 4.2, bottom) with the areas in which monsoon westerlies appear showing standard deviations greater than 5 m/s. Meridional wind standard deviations are not shown; at 200 mb they are generally 5 m/s smaller than those of the zonal wind while at 850 they are roughly comparable. The regions of higher variability in the zonal flow at both levels seem to also have higher variability in the meridional flow, with certain exceptions in the monsoon regions which reflect differing locations of seasonally varying maxima in the flow. The rotational flow is defined by the streamfunction; as the rotational winds are by far the dominant component of the total wind

field outside the tropics, presentation of separate maps of rotational winds is somewhat redundant. Fig. 4.3 presents the annual means of the velocity potential, divergent zonal wind and divergent meridional wind at 200 mb. Equatorial symmetry tends to dominate the velocity potential map, and as a result there is little time mean cross-equatorial divergent flow. The one exception is in the eastern Pacific, an area which is dominated by southward divergent flow year round.

Elements of the annual mean divergent circulation at 850 mb are shown in Fig. 4.4. The patterns of divergent winds at 850 mb are not so clearly defined as in the upper troposphere. Overall, the structures we see in these figures are noisier than at 200 mb, undoubtedly reflecting the higher degree of relative uncertainty in the wind measurements at this level, particularly over the ocean. (Note the rather wavy meridional structure of the 850 mb velocity potential in the higher southern latitudes.) Nonetheless, to a great degree, a Walker circulation pattern consistent with that of the upper atmosphere does emerge from the tropical divergent zonal wind figure, i.e. low level divergent easterly flow overlain by westerly flow in the upper level and vice versa.

Krishnamurti (1971) suggested that an equatorial "Walker circulation" is merely one of a complex of east-west divergent circulations which emerge in response to planetary-scale (monsoonal) diabatic heat sources. From Figs. 4.3 and 4.4 it is certainly evident that relatively strong divergent zonal winds are by no means a feature of the tropics alone; furthermore, the basic longitudinal pattern of the mean divergent zonal winds does not seem to change in the higher latitudes. In this annual mean sense, we should say that the Walker circulation, although

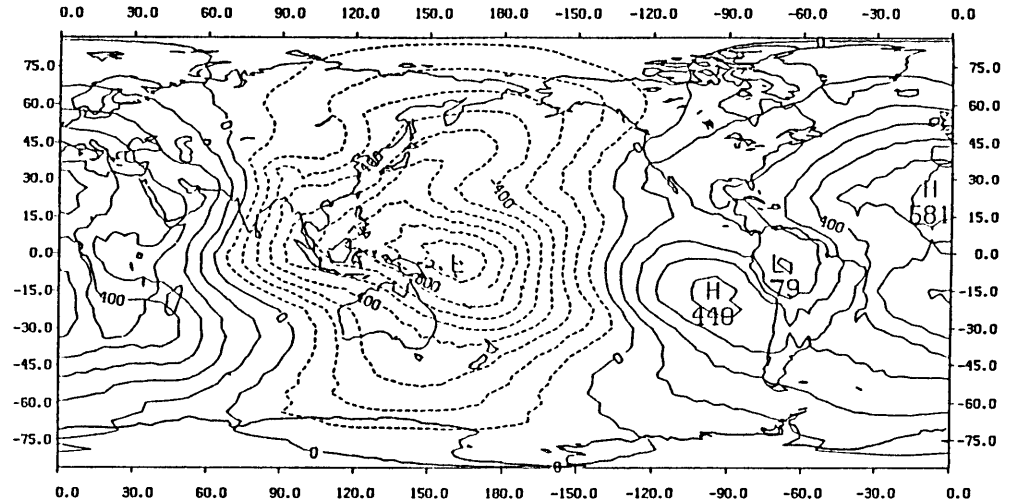

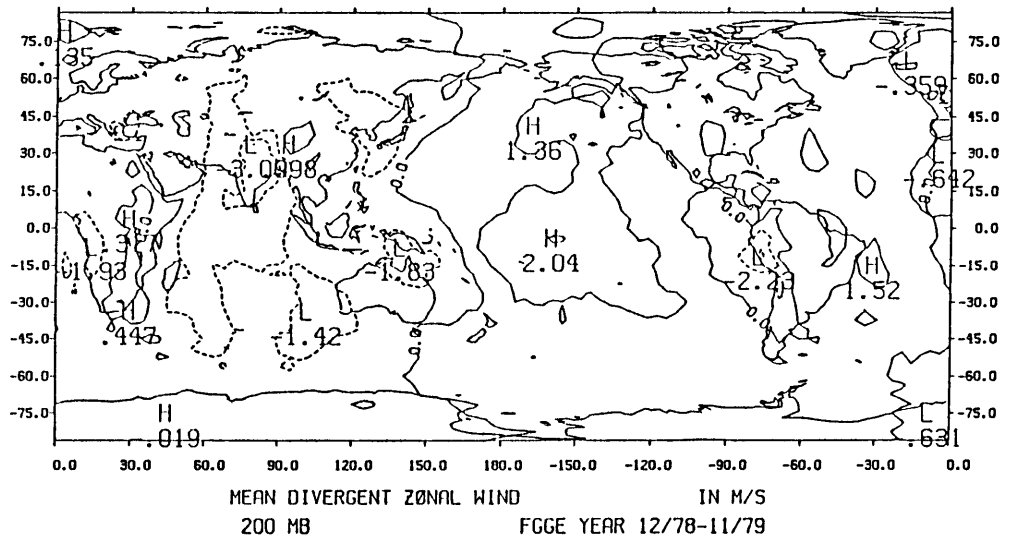

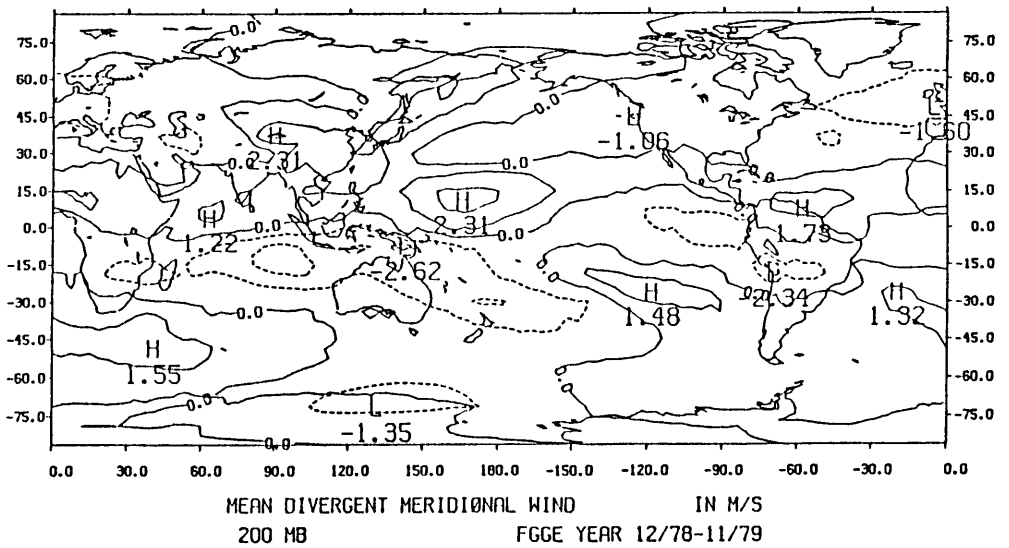

Fig. 4.3 FGGE time averages of 200 mb velocity potential (top), divergent zonal wind and divergent meridional wind.

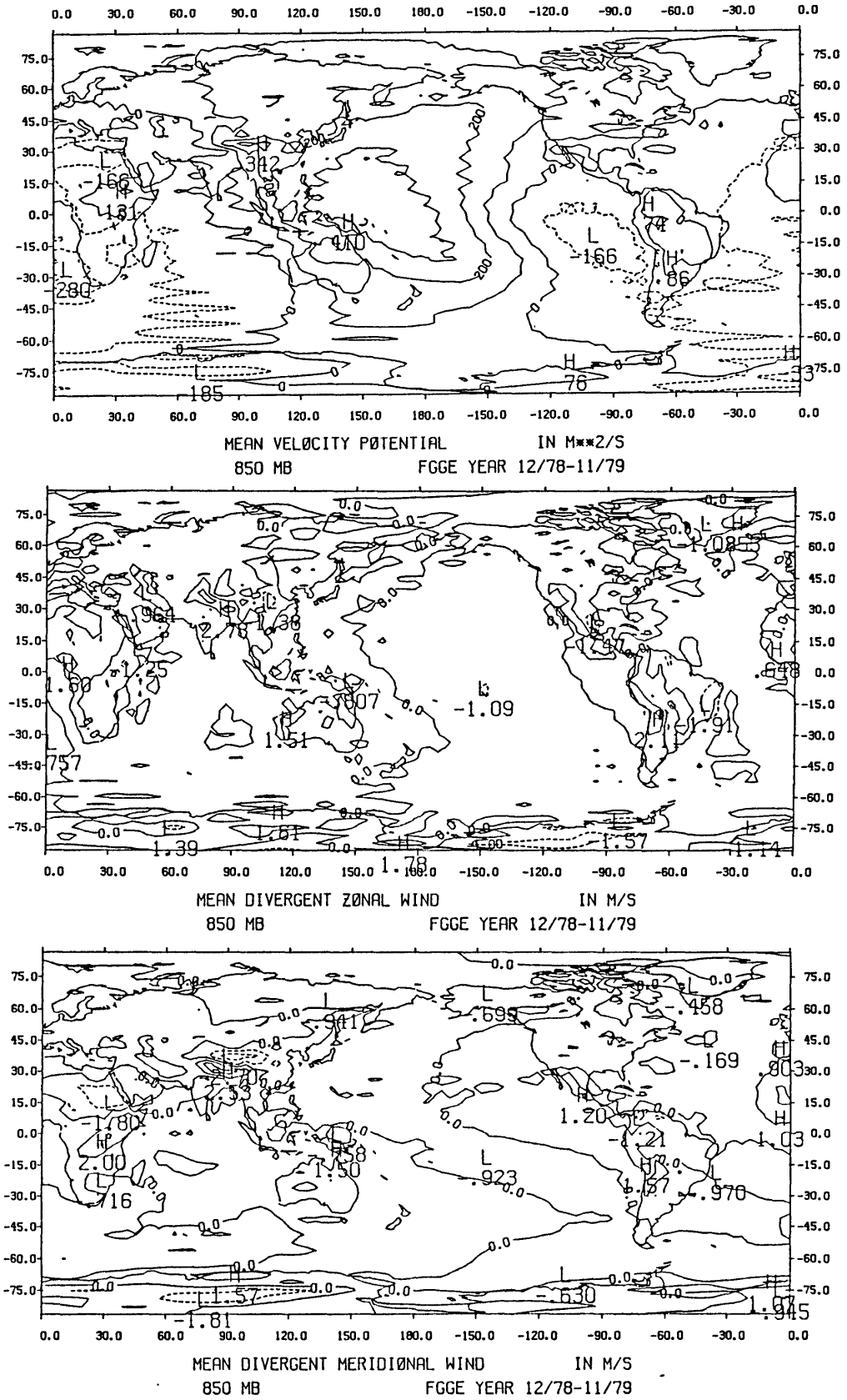

Fig. 4.4 As in 4.3 but for 850 mb.

roughly symmetric with respect to the equator, is definitely not confined there. We will consider in the next section the character of its seasonal behavior.

The meridional uniformity of the divergent zonal wind pattern suggests that averaging the Walker circulation over an equatorial belt of at least several latitudes would not change the sense of the Walker circulation within the belt, and would be useful in gaining a general sense of the net zonal overturning. That is what we have done in Fig. 4.5 where we present superposed 850 and 200 mb longitudinal profiles FGGE time mean tropical band (15°S-15°N) averages of (i) the velocity potential, (ii) the divergent zonal wind field and (iii) the divergence. To derive the latitude-band average divergent zonal winds u^d at grid longitudes i depicted in Fig. 4.5, we first calculated the divergent zonal wind components $u^d_{i,j}$ at the latitudes ϕ_j in the belt from the FGGE time mean velocity potential fields as in Figs. 4.3 and 4.4 and the divergence, D, from the time mean wind fields from the EMCWF analysis by means of

$$(4.5)\quad D_{i,j} = \frac{1}{2\Delta}\left(\frac{1}{a\cos\phi_j}(u_{i+1,j} - u_{i-1,j}) + (v_{i,j+1} - v_{i,j-1})\right) - v_{i,j}\tan\phi_j/a$$

where Δ is the grid spacing of 3.75°. In the case of the divergence, the individual contributions to the band averages were weighted by $\cos\phi_j$ to account for grid box area. The choice of poleward limits is not clearly dictated by sudden changes in the character of the three fields and therefore was somewhat arbitrary. We settled on the choice of a region in which the annual means of the divergence as well as the velocity potential and "Walker circulation" were reasonably representative of values year round. For the belt from 30°S-30°N (not shown) the

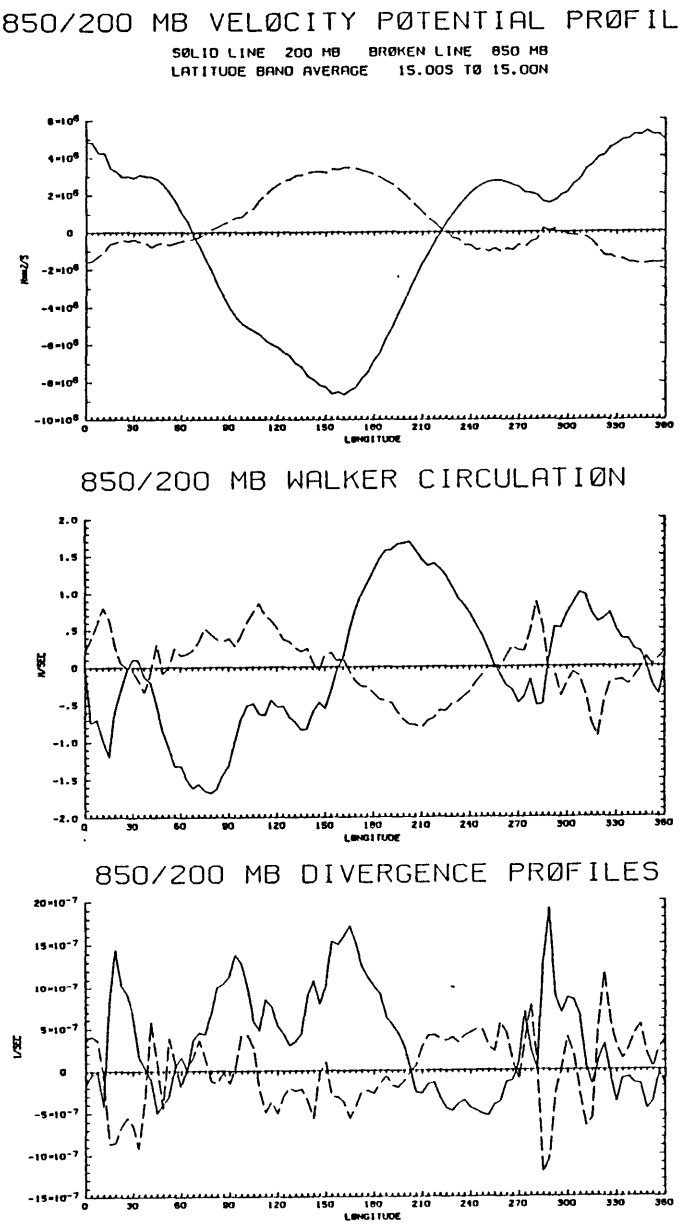

Fig. 4.5 Longitudinal profiles of FGGE time average Walker circulation components at 200 mb (solid) and 850 mb (broken) meridionally averaged from 15°S-15°N. Velocity potential (top), divergent zonal wind (center) and area-weighted divergence (bottom).

velocity potential and Walker profiles are quite similar, but the time mean divergence pattern is far noisier. This was due to the strong winter-to-summer changes in the rising motion over such regions as northern India and southern China.

An alternative method of computing the divergence would have been to compute the divergence directly from the velocity potential field. We have done this, using centered differences, and the results are not noticeably different from the above method, with the exception of rather prominent grid-scale noise. Note also that we have labelled the meridionally averaged divergent zonal winds as the "Walker circulation". This is simply to draw attention to our consideration of the Walker circulation as arising from the divergent part of the zonally asymmetric wind field, and does not imply that the Walker circulation is by definition a meridionally averaged quantity.

The most striking characteristic of the profiles in Figure 4.5 is the strong antisymmetry of the upper and lower levels. This is particularly evident in the divergent zonal winds; zero crossings at 850 and 200 mb coincide almost perfectly. As one would expect, the divergence profiles have considerable small-scale structure, particlarly the 850 mb profile, but there is a great deal of order on the large scale. The 200 mb divergence profile shows the relatively narrow regions of outflow associated with South American and African rising motion and a broader region of outflow extending from the western Indian Ocean to the longitudes of Hawaii and Tahiti. The divergence in this latter region shows two maxima, one just west of the dateline and a second in the eastern Indian Ocean. Convergence is confined to narrow regions in the eastern Pacific, the Atlantic sector and the western Indian Ocean. At

850 mb convergence associated with convective circulations is strongest in the South American and African regions, whereas the convergence over the Asian and Australasian monsoon band is largely confined to the region east of 100^{o}E. Lower level divergence over the eastern Pacific is almost perfectly matched with upper level convergence. These profiles are evidence for strong vertical coupling at large horizontal scales in latent heat-forced tropical circulations, not only in regions of upward motion, but also in regions of downward motion as well. Furthermore, the presence of this vertical coupling in the European Centre's analysis is evidence that at least at these scales the ECMWF III-b analysis method overcomes its nondivergent bias and is correctly interpreting the sense of the divergent circulation.

Interpreting the correspondence between divergence in the upper levels and convergence below and vice versa as evidence of large scale rising motion, it appears that there are two narrow and one very wide region of band-averaged upward motion. The latter extends from the western Indian Ocean eastward to the central Pacific, and the former are located over Africa (15^{o}E-35^{o}E) and South America (75^{o}W-50^{o}W). Within the Indian and Pacific Ocean rising motion there are two centers of upper level divergence, while the two smaller regions are defined by single narrow peaks. The band-average upper divergence in the South American center approaches $2\text{x}10^{-6}$ s^{-1} and is the maximum in the profile.

The equatorial zone upper level divergence profiled in the bottom panel includes both the meridional gradient of the v wind connected to the Hadley circulation and the zonal gradient of the u wind associated with the Walker circulation. Nonetheless we note that the centers of purely zonal divergence or convergence which are located at the points

of steepest gradient along the Walker circulation profiles in the middle panel are also the significant centers of total divergence (or convergence) in the bottom panel. In the sense of the meridional averages we have employed here, it appears that 1) the rising motion is restricted to several regions comprising roughly 3/5 of the equatorial zone; 2) the Hadley circulation arises from the net difference between the poleward divergent meridional flow in these regions and equatorward flow in the regions of sinking motion; and 3) the Walker circulation is due to the zonal imbalances of diabatic heating associated with these same regions of rising and sinking motion.

The concept of a zonal overturning requires that individual Walker cells be composed of lower level divergent flow in one direction and upper level flow oppositely directed, the two branches connected at one end by a center of rising motion and sinking motion at the other. In the middle panel of Figure 4.5 one can clearly identify 5 Walker cells, four of which occur as pairs of oppositely-directed overturnings associated with a single region of upward motion.

The primary feature is the Indian Ocean/Pacific Ocean pair with westward overturning extending across the region between the east coast of Africa and the extreme west Pacific ($\sim 165^{\circ}$E) and eastward overturning from there to 105°W. As mentioned above, there are two upper level divergence peaks within the region spanned by these two cells; it is therefore incorrect to consider the westward overturning as arising entirely from rising motion in the western Pacific region. The westward center is a manifestation of the seasonal movement across the eastern Indian Ocean and Indonesia of the meridionally-averaged center of rising motion due to the Asian monsoon. This movement will be examined in the

next section on the seasonal characteristics of the divergent circulation.

The second pair of Walker cells is located in the South American sector, with the two cells diverging at the sharp, localized peak of rising motion at ~ 70°W, over the upper Amazon basin. The fifth Walker cell is a westward overturning spanning equatorial Africa and the eastern equatorial Atlantic Ocean. We can assume the eastward cell from the African rising motion is canceled by the divergent westerlies of the Indian Ocean Walker cell.

The Pacific Walker cell can be identified with the "Walker circulation" that was proposed first by Troup (1965) and later named by Bjerknes (1969); this cell has received a great deal of attention in the literature on the Southern Oscillation and El Niño. Troup and Bjerknes did not specifically define the Walker circulation in terms of the divergent zonal wind, although we note here that the divergent zonal wind approaches 2 m/s near the velocity maximum of the cell at 150°W and is a substantial portion of the weak total zonal wind field in the central equatorial Pacific region. Thus an unambiguous identification of the Walker circulation with the <u>divergent</u> zonal wind field does not conflict with a looser definition of the Walker circulation, i.e. a zonally-oriented circulation in the tropics due to azonally asymmetric distribution of diabatic heating.

As a check on the physical significance of the divergence profile in Fig. 4.5, we display in Fig. 4.6 the equatorial profile of FGGE mean HRC along with the time mean gridded field of HRC. This profile was obtained by summing across the 13 grid latitudes 22.5°S - 22.5°N at each of the 96 grid longitudes for every day. The yearly grid-day totals

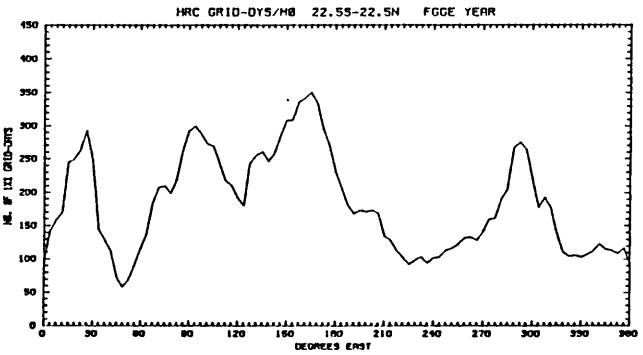

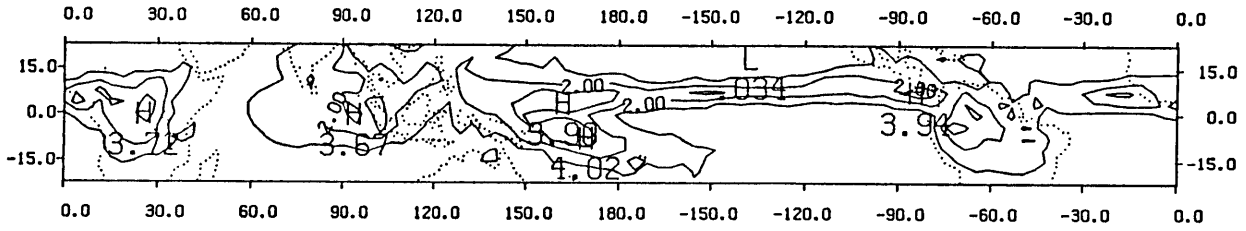

HIGHLY REFLECTIVE CLØUD AVG GRID-DAYS/MØN FGGE YEAR

Fig. 4.6 FGGE year mean HRC profile along the equator for the latitude band 22.5°S - 22.5°N (top) and FGGE year mean HRC in average number of days of highly reflective cloud coverage per 1° x1° grid square per 3i-day month.

were then normalized to grid-days/month by scaling by a factor of 31/365. This will facilitate comparison with the January and July averages we will consider in the next section. The units used in the map are normalized from grid-days per month to the equivalent days per month of HRC for $1^{\circ} \times 1^{\circ}$ squares by dividing by the square of 3.75.

The fit of the yearly "average" HRC profile to the 200 mb divergence profile is quite remarkable. With the single exception of the peak near 30°E the locations of the maxima in both profiles agree to the actual ECMWF grid longitude. In addition to fairly close agreement in relative magnitudes between peaks, many of the smaller scale features are visible in both series. The map in Fig. 4.6 as well is in excellent agreement with the time mean velocity potential distribution, not only in longitude and in time. The agreement of the HRC with elements of the divergent circulation is strong support for the accuracy of at least the large scale ECMWF analysis. Also it makes an unambiguous connection between the time mean Walker circulation and four clearly demarcated regions of convection. The reality of the double peak of divergence over the eastern Indian Ocean region and the far western Pacific is particularly well supported.

4.2.2 January and July Averages

As is evident in the annual cycles of the monsoon wind systems, the changes of the seasons bring about marked changes in the distribution of heating in the tropics, particularly over the tropical continents. The seasonal cycle in the divergent wind fields is a very sensitive indicator of the shifts of the heating centers. These changes are discussed here in terms of the monthly averages for the months of January and July 1979. It might be argued that seasonal averages would have been more appropriate than monthly averages, as the latter are subject to aliasing from 40-50 day variations. However, as the EOF analyses of Section 4.3 will demonstrate, the seasonal cycle is considerably larger in amplitude than individual 40-50 day oscillations and is thus well represented by the contrast between January and July conditions.

Fig. 4.7 presents the January and July 1979 averages of velocity potential at 200 mb. The outstanding change from January to July is the northwestward movement of the velocity potential minimum in the southwestern tropical Pacific to the vicinity of the Philippines. A similar change is apparent over the Americas. Strong meridional gradients in the velocity potential which give rise to zonally elongated regions of divergent flow into the winter hemisphere are located westward of the minima in the western Pacific, the Americas and over Africa. There are somewhat more confined regions of flow towards the summer pole.

The 850 mb velocity potential means are presented in Fig. 4.8. The seasonal movement in the 850 mb velocity potential minima is even greater than that at 200 mb. We should note here that considerable portions of the Tibetan plateau, to name just one region, lie above 850

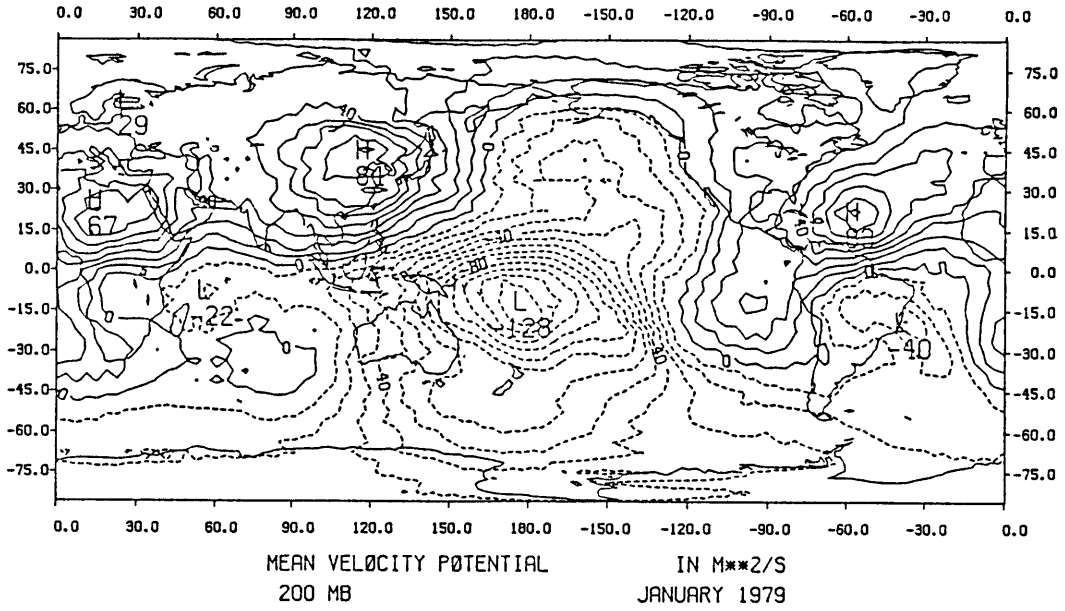

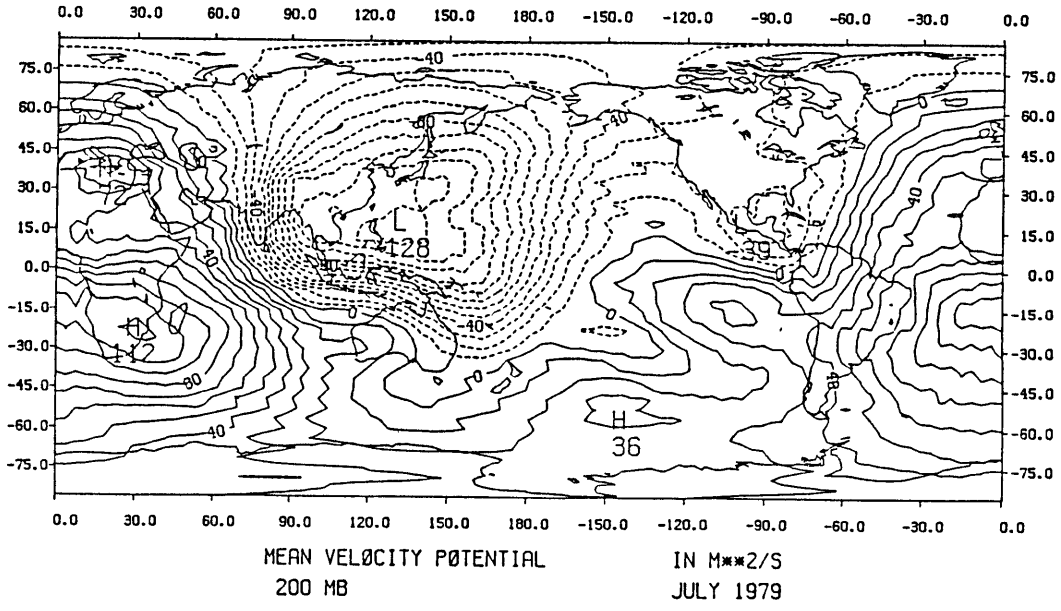

Fig. 4.7 January 1979 (top) and July 1979 average 200 mb velocity potential, contour interval, 10×10^5 m^2/s.

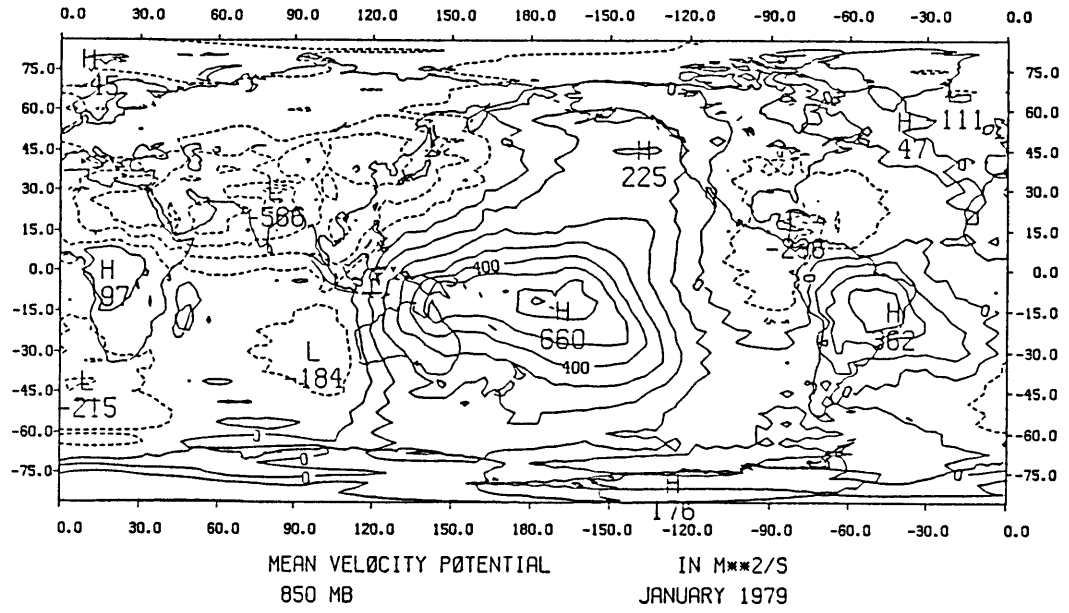

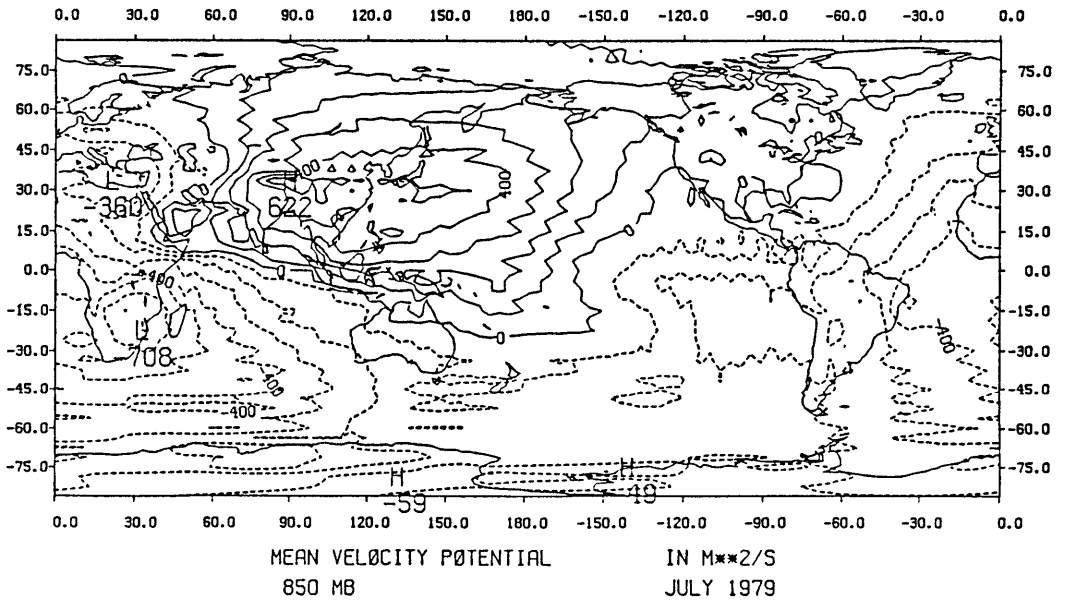

Fig. 4.8 January 1979 (top) and July 1979 average 850 mb velocity potential, contour interval 100×10^4 m^2/s.

mb. Fig. 4.9 is adapted from Oort (1983) and is a rough outline of the intersection of 850 mb surface with the surface. It might be expected that the fine scale features in the vicinity of Tibet in the July map is somewhat fictitious, though northward divergent flow over the Indian subcontinent is certainly likely in the light of the monsoonal convection over the southern flanks of the Himalayas. We present in Fig. 4.10 the January and July means of the highly reflective clouds. There appears to be good agreement in the general pattern of January HRC with the 200 mb velocity potential over the eastern hemisphere. However in the July maps, the small but intense maximum of HRC activity over the western Pacific indicates a rather small center of divergence and thus affects the 200 mb velocity potential analysis only weakly, with a local minimum located somewhat to the east of the HRC maximum. This may be due to the filtering effects of the Poisson solution; a more likely explanation however is that the analysis does not have sufficient data in the region to resolve this intense feature.

The individual components of the divergent wind field can be derived from the mean velocity potential fields in Figures 4.7 and 4.8. These illustrate the relationship between the velocity potential extrema and the Hadley and Walker circulations. We demonstrated in Figure 4.5 that the remarkable vertical coherence between the upper and lower level divergent zonal wind fields in the equatorial region permits the interpretation of longitudinal profiles of the wind in terms of a Walker circulation. Vertical coherence is also a property of the fields of divergent meridional wind. To emphasize the vertical structure of both the Hadley circulation as well as the Walker circulation, we present the two levels of the January and July zonal and meridional divergent wind

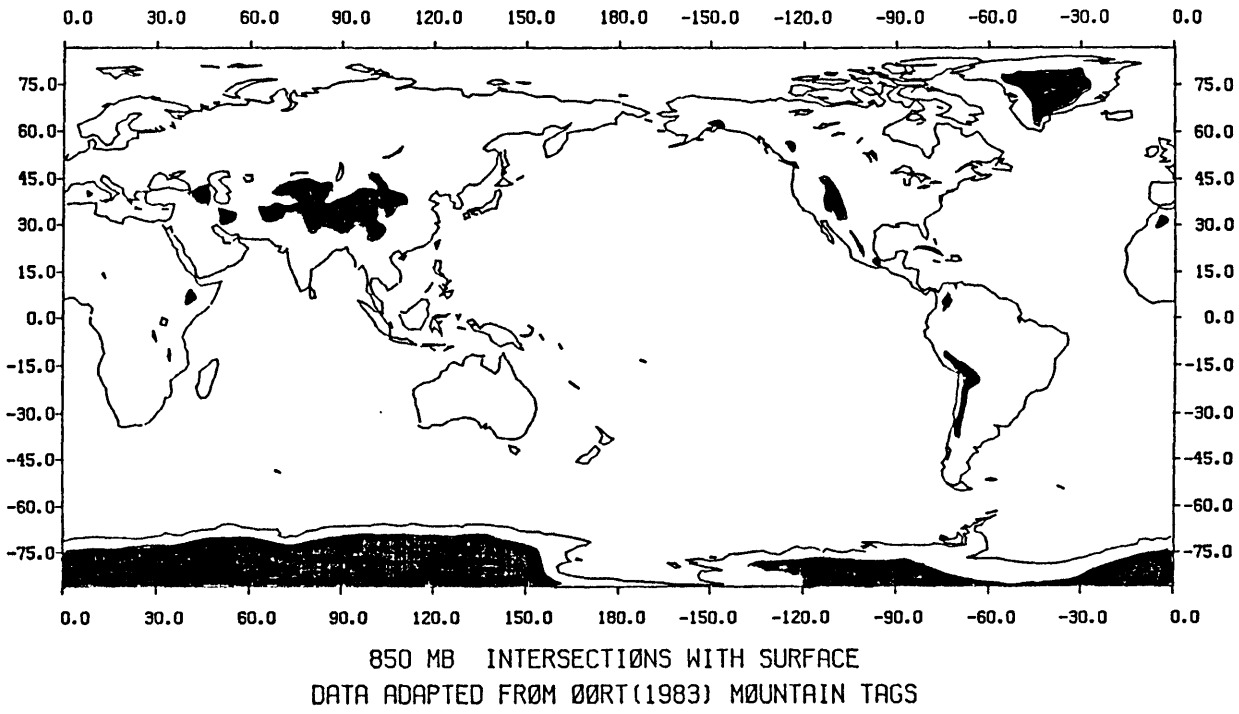

Fig. 4.9 Intersection of the earth's surface with the 850 mb level. From Oort (1983).

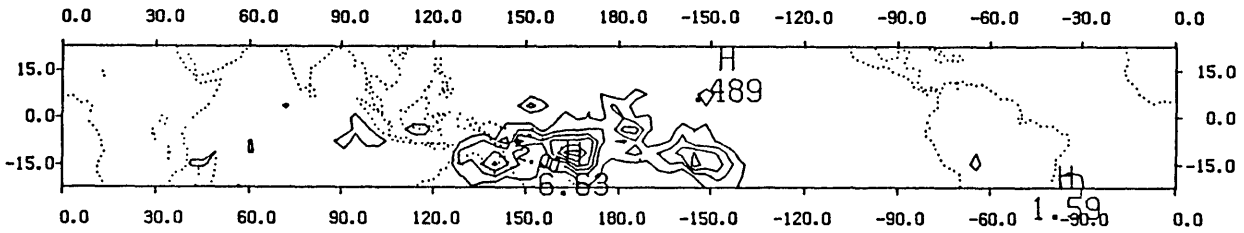

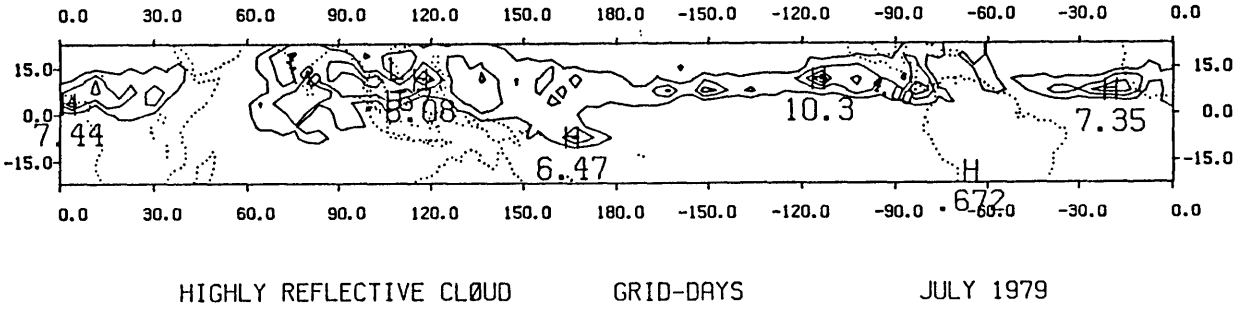

Fig. 4.10 As in Fig. 4.6 (lower) but for January 1979 (top) and July 1979 HRC.

components together in the following four figures. We have derived the zonal divergent wind components at each level from the velocity potential using Eq. 4.1. Similarly, the meridional divergent wind components are derived using Eq. 4.2.

The January 200 and 850 mb zonal divergent wind components appear in Fig 4.11. During this month the Pacific and South American cells of the Walker circulation appear to be primarily in the Southern Hemisphere. The zonal divergent wind at 200 mb peaks at nearly 5 m/s over the central South Pacific at 30^{o} latitude. The zero line separating the Indonesian and Pacific Walker cells appears to be near the 90^{o}E at 200 mb. Fig. 4.12 displays the same fields for the month of July. In this month the center of the Pacific Walker cell has moved to the western equatorial Pacific where 200 mb divergent westerlies exceed 2.5 m/s. Just to the west of this region the sign changes and there is a strong maximum in the easterly 200 mb flow. There also appears a strong easterly region over the Central American sector north of the equator. At 850 mb during this month the prominent features are highly localized, but the general pattern of easterlies in the lower branch of the Pacific Walker cell is present.

Divergent meridional winds for the month of January appear in Fig. 4.13. We have highlighted the tropical maxima and minima at each of the two levels which are paired with extrema of the opposite sign in the other level. The wide region of divergence encompassing the rising portions of the Indian Ocean and Pacific Walker cells appears in this figure as a zonally-elongated region of relatively uniform 200 mb meridional flow centered just south of the equator. At 850 mb the flow converging from the south is mostly confined to the east of Australia in

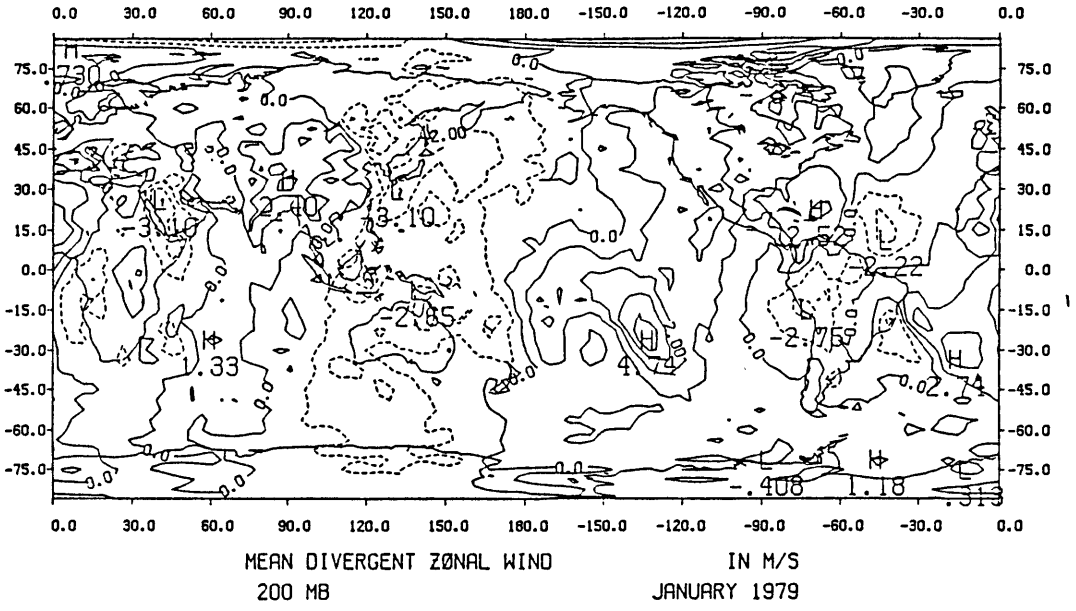

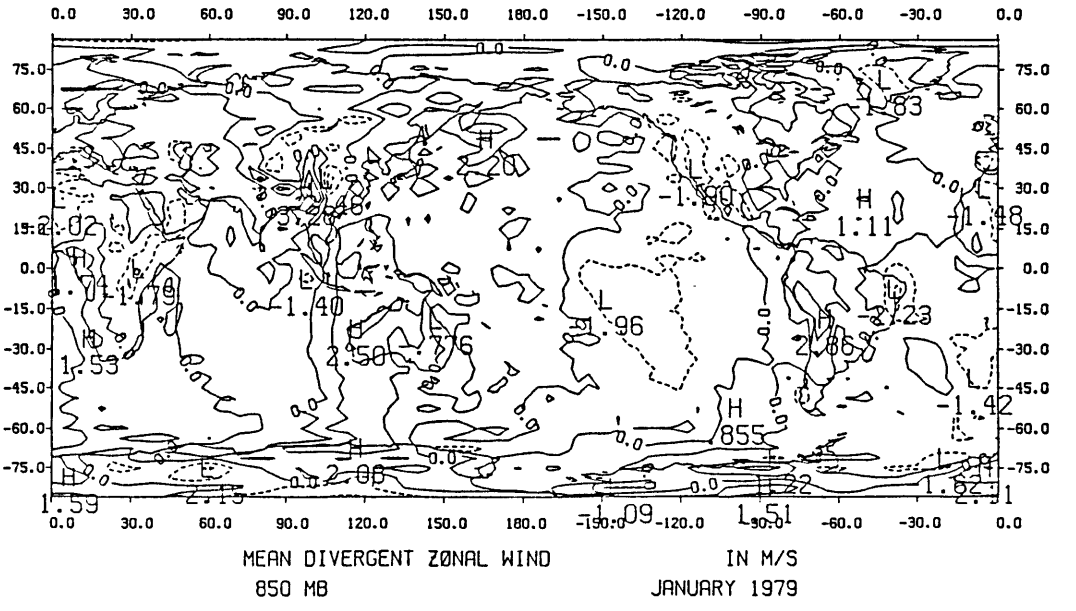

Fig. 4.11 January 1979 200 mb (top) and 850 mb divergent zonal wind fields, contour interval 1 m/s.

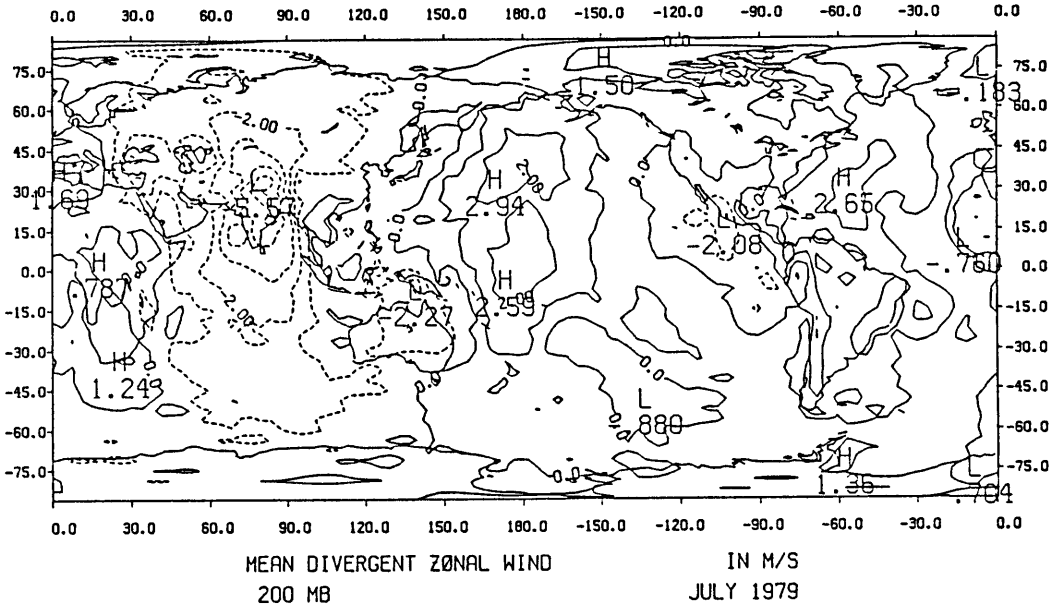

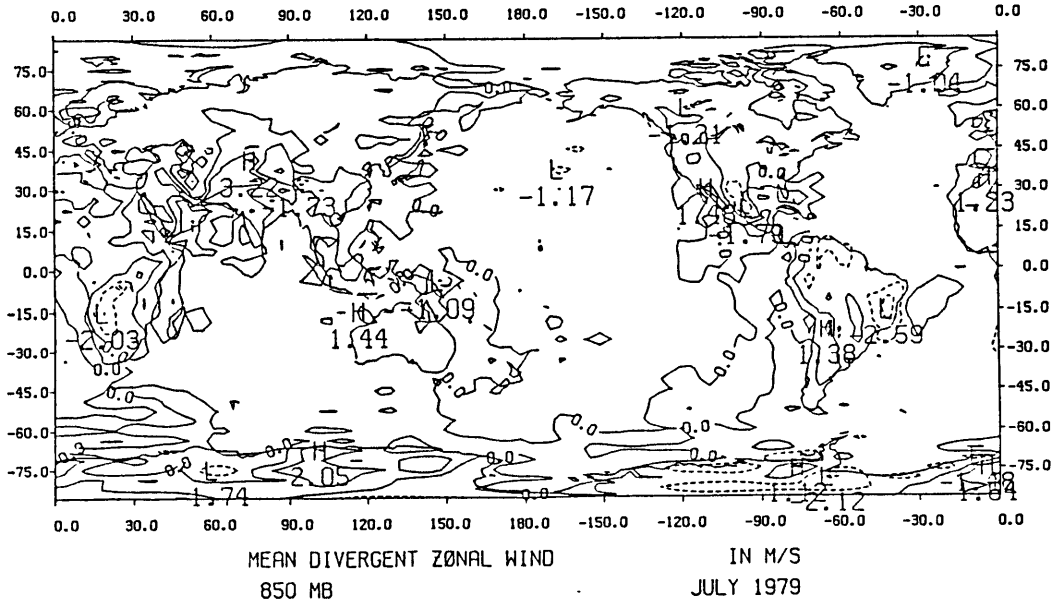

Fig. 4.12 As in Fig. 4.11, but for July 1979.

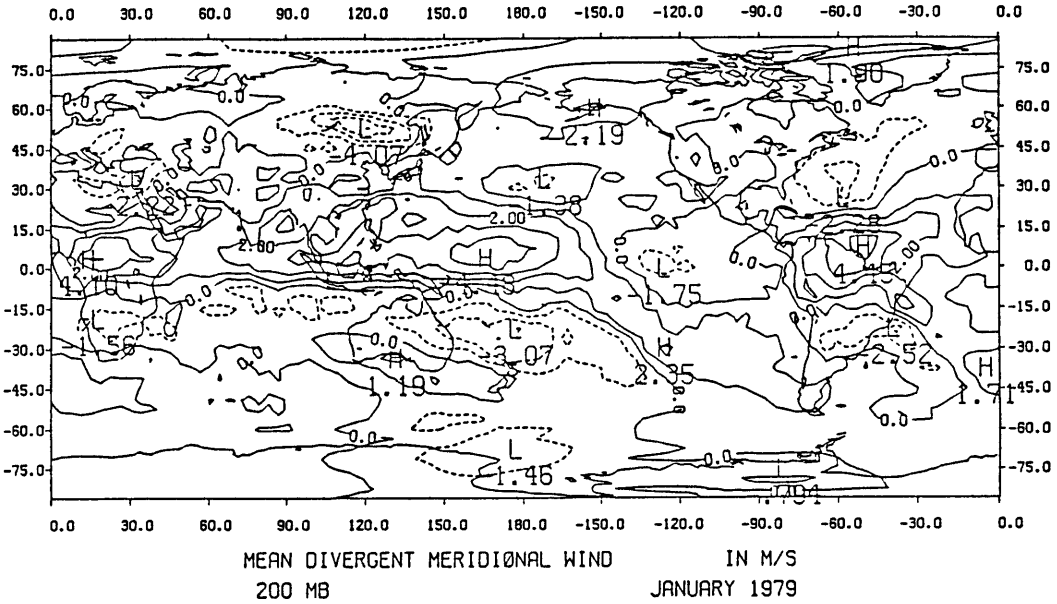

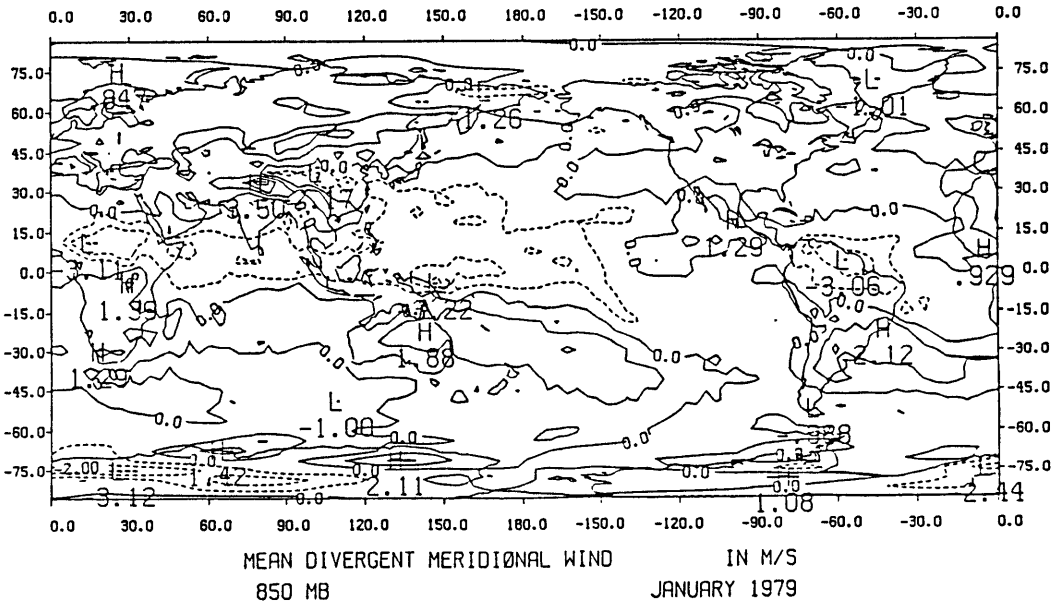

Fig. 4.13 As in Fig. 4.11, but for the divergent meridional wind.

the southwestern Pacific. The other two regions of convergence at 850 mb and divergence at 200 mb do not show the same zonal spans as in the maritime continent region.

This picture changes somewhat in the month of July, the divergent meridional wind fields for which are shown in Fig. 4.14. The strong southward upper level flow associated with the Hadley cell is spread over a wide range of longitudes. At 850 mb, the intense low-level flow in the Somali jet region is a particularly notable feature of the strong southwest monsoon flow. Because of the orientation of these local contributions to the Hadley circulation with respect to the velocity potential minima, the strongest cross-equatorial flow generally occurs in the easterly divergent wind regime. (These easterly divergent winds at 200 mb are located within the regions of easterly total winds as well.)

We present in Figs. 4.15 and 4.16 meridional averages of the Walker circulation and the divergence for the months of January and July respectively. Instead of the single $15^{\circ}S$-$15^{\circ}N$ equatorial belt employed in Figure 4.5, each month is represented by averages over bands from $30^{\circ}S$-0° and 0°-$30^{\circ}N$. This presentation emphasizes the differences between the two hemsipheres in the locations and intensity of the centers of rising motion.

It is immediately apparent that in both months the summer hemisphere has a preponderence of upper level divergence and lower level convergence and the winter hemisphere the reverse. At 200 mb, the divergence and convergence tend to be concentrated to a few centers, the Northern Hemisphere divergence center at $90^{\circ}E$ in July being the most prominent example. The westward position of this feature with respect

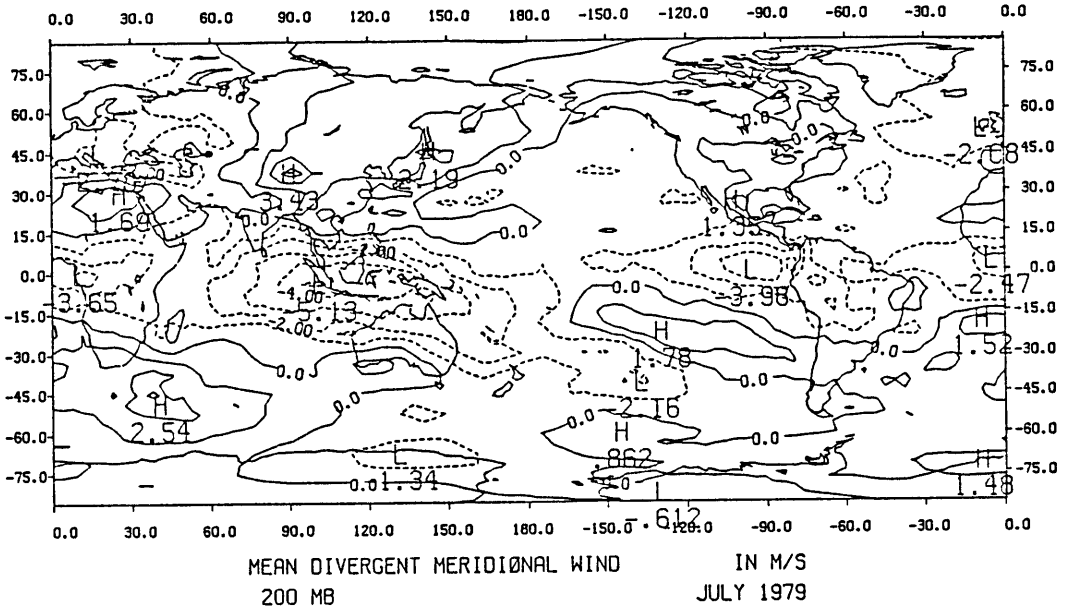

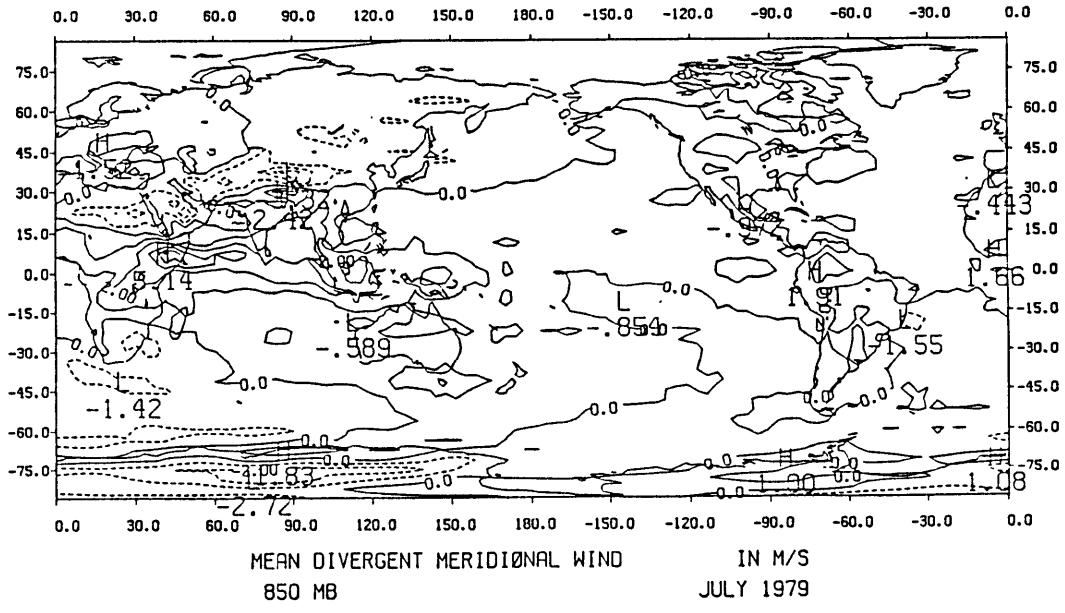

Fig. 4.14 As in Fig. 4.13, but for July 1979.

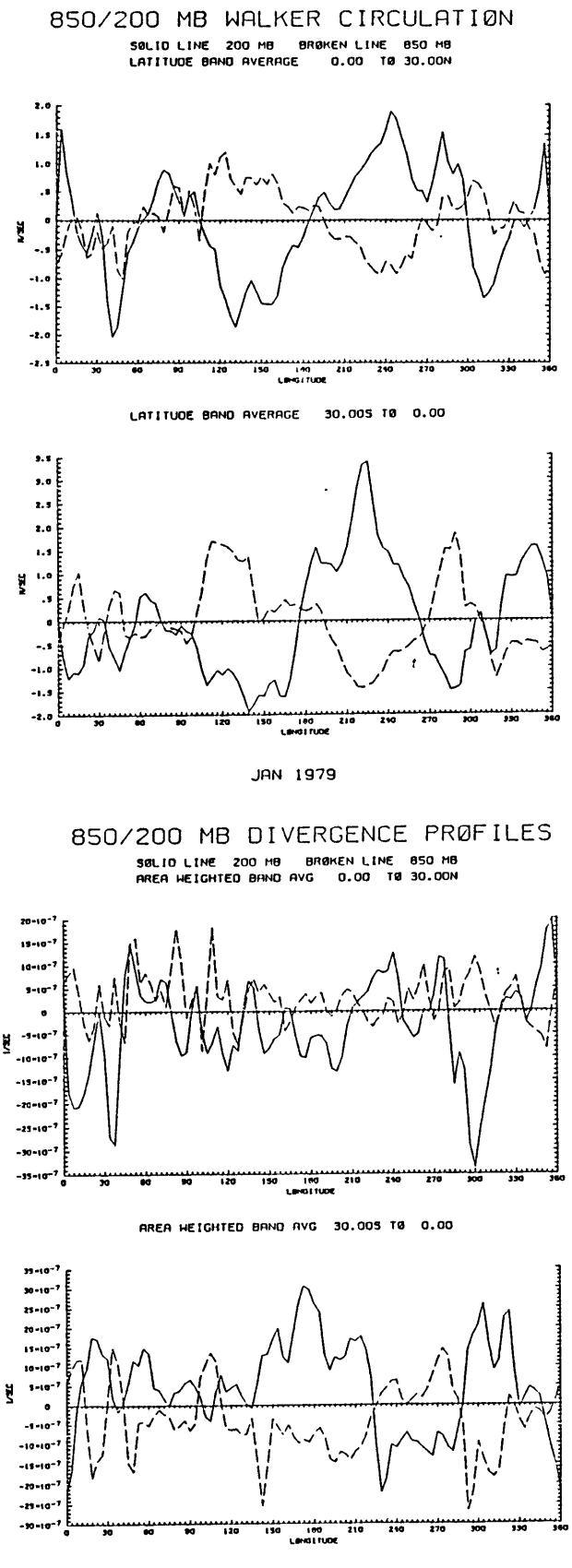

Fig. 4.15 January 1979 Walker circulation components at 200 mb (solid) and 850 mb (broken). Divergent zonal winds averaged across 0°-30°N (top) and 0°-30°S (upper middle); area-weighted divergence 0°-30°N (lower middle) and 0°-30°S.

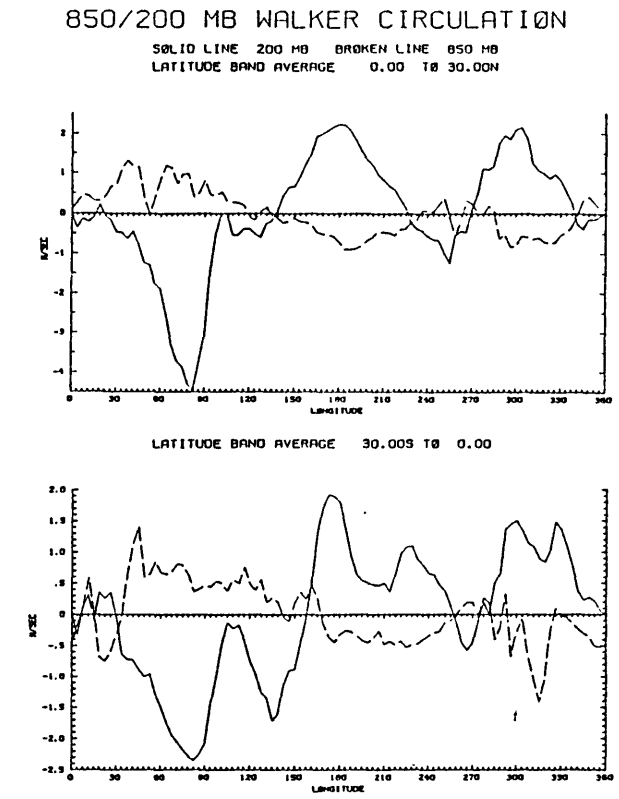

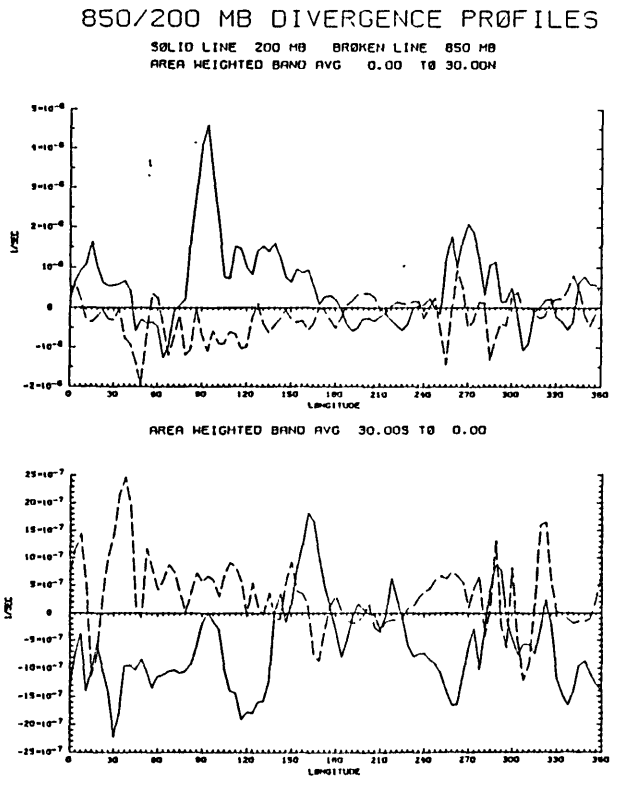

Fig. 4.16 As in 4.15 but for July 1979.

to the Southern Hemisphere center in January over the western and central Pacific is also consistent with the general shift of the position of the velocity potential.

The separate profiling of the two hemispheres in Figures 4.15 and 4.16 also highlights the dipole patterns of divergence and convergence associated with the local centers of meridional overturning. For example, January divergence between 60°W and 30°W in the Southern Hemisphere, primarily due to the rising motion over the southeastern Amazon basin, is closely paired, albeit slightly downstream in the total flow, with convergence over the southern Caribbean and northwestern South America. The July situation is somewhat similar although not as clearly defined. Here the rainy season over Central America seems to be associated with convergence slightly to its southwest in the Southern Hemisphere, over the southeastern Pacific. We are not suggesting that these are examples of quasi-independent, thermally direct, local circulations which would seem to be the definition of a "local Hadley cell"; in the face of strong transverse divergence it would be impossible to construct a streamfunction for example. It is more likely that the upper level convergence centers to a large extent are due to local cooling, just as the divergence centers are forced by local heating. In this perspective, "local Hadley cells" are more the result of local forcing conditions than the cause.

The Walker circulation is clearly in evidence in both figures, with the strong anti-symmetry between upper and lower levels which was characteristic of the year's averages shown in Figure 4.5. In the same sense as the north-south oriented dipoles of convergence and divergence discussed above, the Walker cells that appear quite prominently in

4.15 and 4.16 are not material circulations. Newell et al. (1974) defined a zonal mass flux for meridionally averaged Walker cells using the longitudinal height sections of Figure 2.5. The resulting fields clearly indicated an east-west overturning. Gutzler (1985) has defined a similar quantity for a limited set of longitudes spanning the heart of the Indian and Pacific cells with a similar resemblance. These "overturnings" are probably quite real, but these mass fluxes are not streamfunctions; as they are defined the patterns of the fluxes may be affected by longitudinal differences in meridional convergence. It may well be impossible to find, in the face of the significant interhemispheric mass readjustments that accompany the march of the seasons, a latitude band in which a true Walker streamfunction may be observed. On the other hand we will present in Chapter 6 evidence that the net meridional mass flux is effectively zero over reasonable period averages for the 30°S - 30°N tropical band. As such, the concept of a "local Walker cell" would perhaps be more useful.

January and July monthly average profiles over the separate hemispheres for the highly reflective cloud are presented in Fig. 4.17. The agreement once again is excellent between locations of maxima of divergence and HRC for the January case. In the July profile, it appears that the divergence between 120 $E^{\circ}$and 150°E is somewhat too weak in the ECMWF analysis: the sharp spike at 90°E (which corresponds to intense convection over the Bay of Bengal) is not matched with what appears to be nearly equally as strong divergence over the South China Sea region.

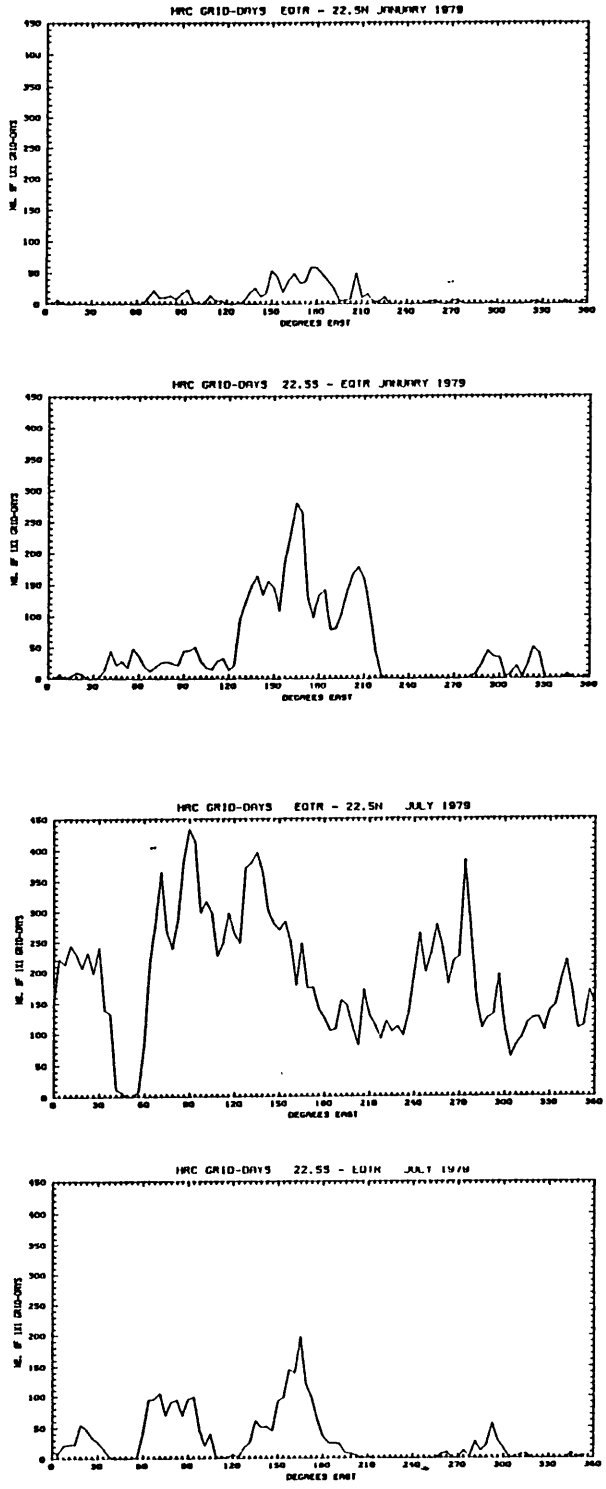

Fig. 4.17 HRC profiles for January 1979 (upper half) and July 1979 (lower half). Each month is represented by separate profiles for each of the latitude bands 22.5°N - 0° and 0° - 22.5°S.

4.3 Statistical Analysis of Fluctuations in the Divergent Wind Field at 200 mb

With twice-daily velocity potential and streamfunction fields at 200 and 850 mb, the variability of the large scale tropical circulation could be examined, from the scale of one day up to the annual cycle. In this section we will describe the results of a number of empirical orthogonal function analyses which for the divergent circulations in particular proved to be extremely successful in identifying coherent large-scale behavior.

4.3.1 Semi-Spectral EOF Analysis

Empirical orthogonal function analysis of a spatial field of NP time series of length NT consists of obtaining the NP eigenvalues and associated eigenvectors (empirical orthogonal functions) of the NPxNP variance-covariance matrix of the time series and constructing a corresponding set of NP principal components (time series). For this study we have obtained the eigenvalues, eigenvectors and principal components using the singular value decomposition (SVD) method which bypasses the calculation of the variance-covariance matrix. The numerical method used here is due to Businger and Golub (1969) and recently implemented by Hsiung and Newell (1983).

Empirical orthogonal function analysis decomposes the NTxNP time-space matrix **X** into NP principal components of length NT (here the NTxNP matrix **Z**) and NP eigenvectors length NP (NPxNP matrix Y):

$$\mathbf{X} = \mathbf{ZY}.$$

The singular value decomposition of **X** is

$$\mathbf{X} = \mathbf{U} * \mathbf{S} * \mathbf{V}'$$

where **U** is NTxNP, $\mathbf{S} = [s_i]_{diag}$ is an NPxNP diagonal matrix and **V** is NPxNP. (A prime denotes transpose). These are related to the eigenvalues, eigenvectors and principal components by

$$s_i^2 = d_i,$$

$$\mathbf{V}' = \mathbf{Y}$$

and

$$\mathbf{US} = \mathbf{Z}.$$

The vector **d** contains the M eigenvalues d_i of the variance-covariance matrix **X'X.**

Storage requirements of the EOF code employed and the restrictions of memory in the CRAY-1 computers at NCAR limited the number of spatial degrees of freedom in the EOF calculation to the vicinity of 500. One solution to this problem is to expand the data set into spherical harmonics and use a truncated set of coefficients in the EOF calcu-

lation. This would have been an efficient method had the velocity potential calculation been carried out directly from the spherical harmonic coefficients. (This incidentally is the method which was employed in the study by Lorenc, 1984.) However, as we were using the grid point data, the EOF analysis was done in a semi-spectral domain, i.e. spectrally decomposing the field in one direction only. For fields over a particular belt of latitudes, the logical choice is to expand in the zonal direction which yields a set of zonal wavenumbers at each of the grid latitudes. A subset of these zonal wavenumber coefficients can then be retained for inclusion in the spatial matrix input to the EOF analysis. For the ECMWF data this was done in the following way: as the grid spacing was 3.75°, the equatorial belt from 45°N to 45°S included 25 grid latitudes. Therefore for the limit of approximately 500 total degrees of spatial freedom dictated a truncation at zonal wavenumber 10. From the discussion in Chapter 3, this resolution is more than sufficient.

The SVD subroutine we used took as input the semi-spectral time series matrix **X** and output **U**, **S** and $\tilde{\mathbf{Y}}$, the tilde on the latter indicating that it consists of wavenumber coefficients. The variance in each mode is contained in the variance of the column vector principal component in matrix **Z**; each of these were of length 730. For a number of reasons, we felt it more useful to carry the variance of each mode entirely in the eigenvector alone rather than in the principal component as well. Thus we found the matrix $\hat{\mathbf{Z}}$ consisting of the NP column vector principal components $\hat{z}_k$, each normalized by its standard deviation σ_k. Each of the zonal Fourier components at each latitude in the corresponding eigenvector $\tilde{y}_k$ in maxtrix $\tilde{\mathbf{Y}}$ was multiplied by σ_k to yield the scaled eigenvectors $\hat{y}_k$.

All of the above operations are outlined in the three-part flow diagram in Fig. 4.18. In the results displayed in the figures below, the principal components (modal time series) are normalized; the mode's contribution to the variance of the input field is contained solely in the amplitudes of the corresponding eigenvectors of Fourier coefficients which are back transformed to obtain the grid point eigenvector maps shown here. An advantage of this presentation is that since the amplitudes of each of the principal components are equal, the relative importance of the separate modes in terms of anomalies is directly proportional to the amplitudes in the spatial fields. Furthermore, 'modal' winds can be derived from the velocity potential and stream-function eigenvectors of each mode without additional scaling operations. A third advantage is that a direct assessment can be made of the contribution by an individual EOF mode to the total variance at a single point simply by squaring the eigenvector at that location. Looked at in another way, the standard deviation is the average anomaly at a point, and the eigenvector values are the 'average' anomalies due to that mode, since we have normalized the principal components.

4.3.2 Results

Before embarking on a discussion of the results of the statistical analyses it is useful to have an idea of the regions where the highest variability is found. The standard deviation fields for the velocity potential at 850 mb and 200 mb for the 365-day period are displayed in Fig. 4.19. Looking at these two fields, one is immediately struck by the near perfect collocation of the major peaks and valleys in the 200

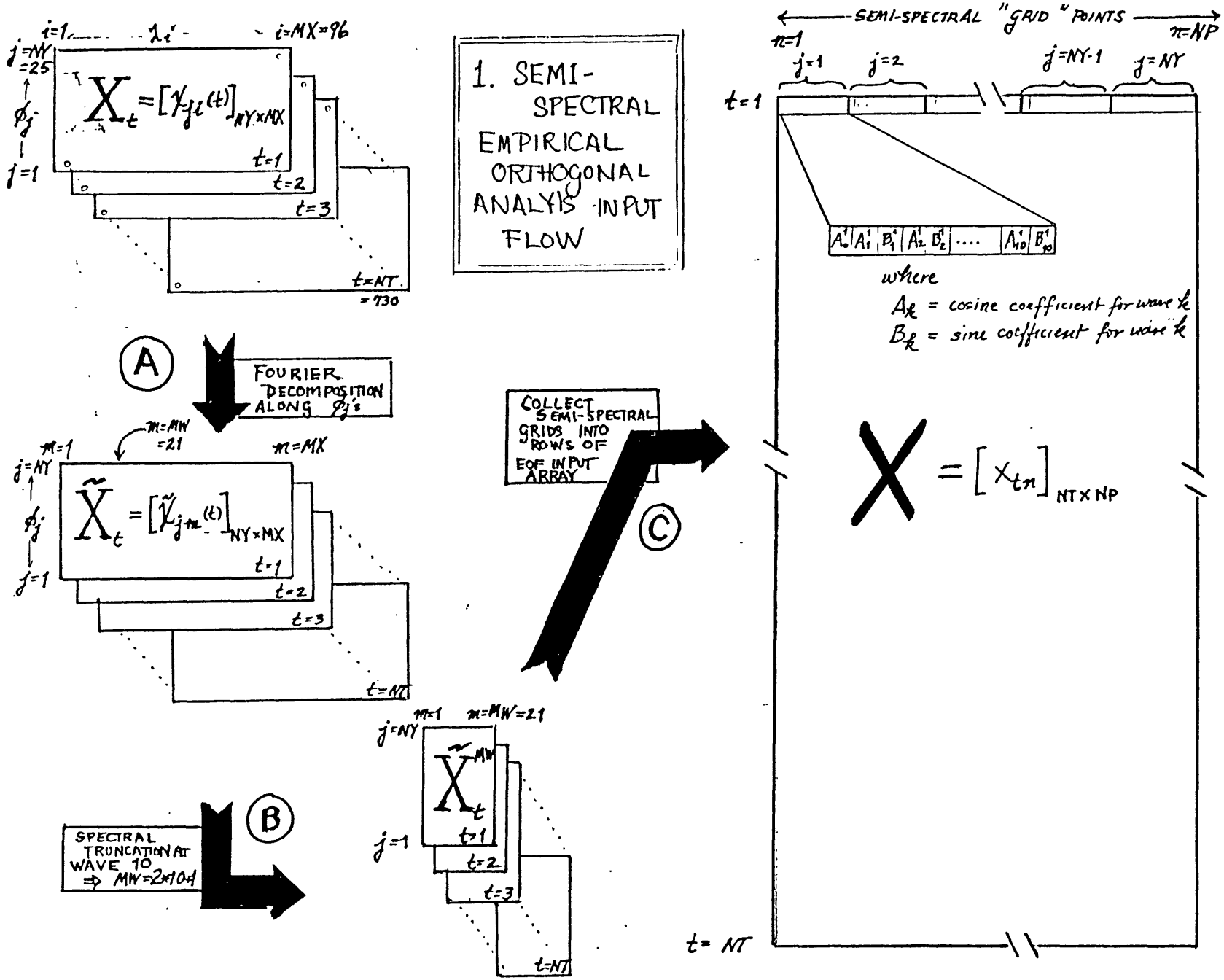

Fig. 4.18 Flow chart for semi-spectral empirical orthogonal analyses performed in Chapter 4. (1) Input flow.

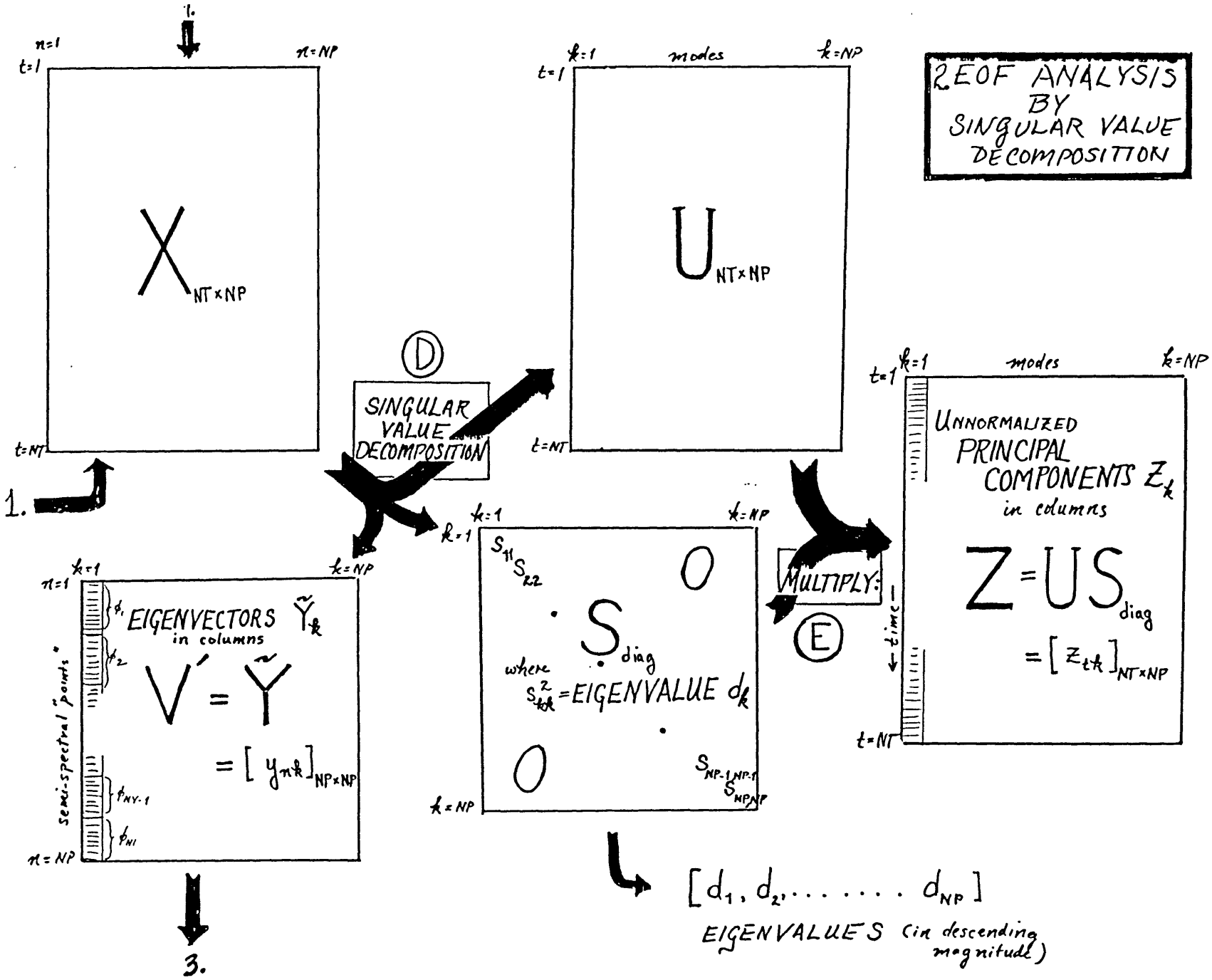

Fig. 4.18 Flow chart for semi-spectral empirical orthogonal analyses in Chapter 4. (2) Singular value decomposition.

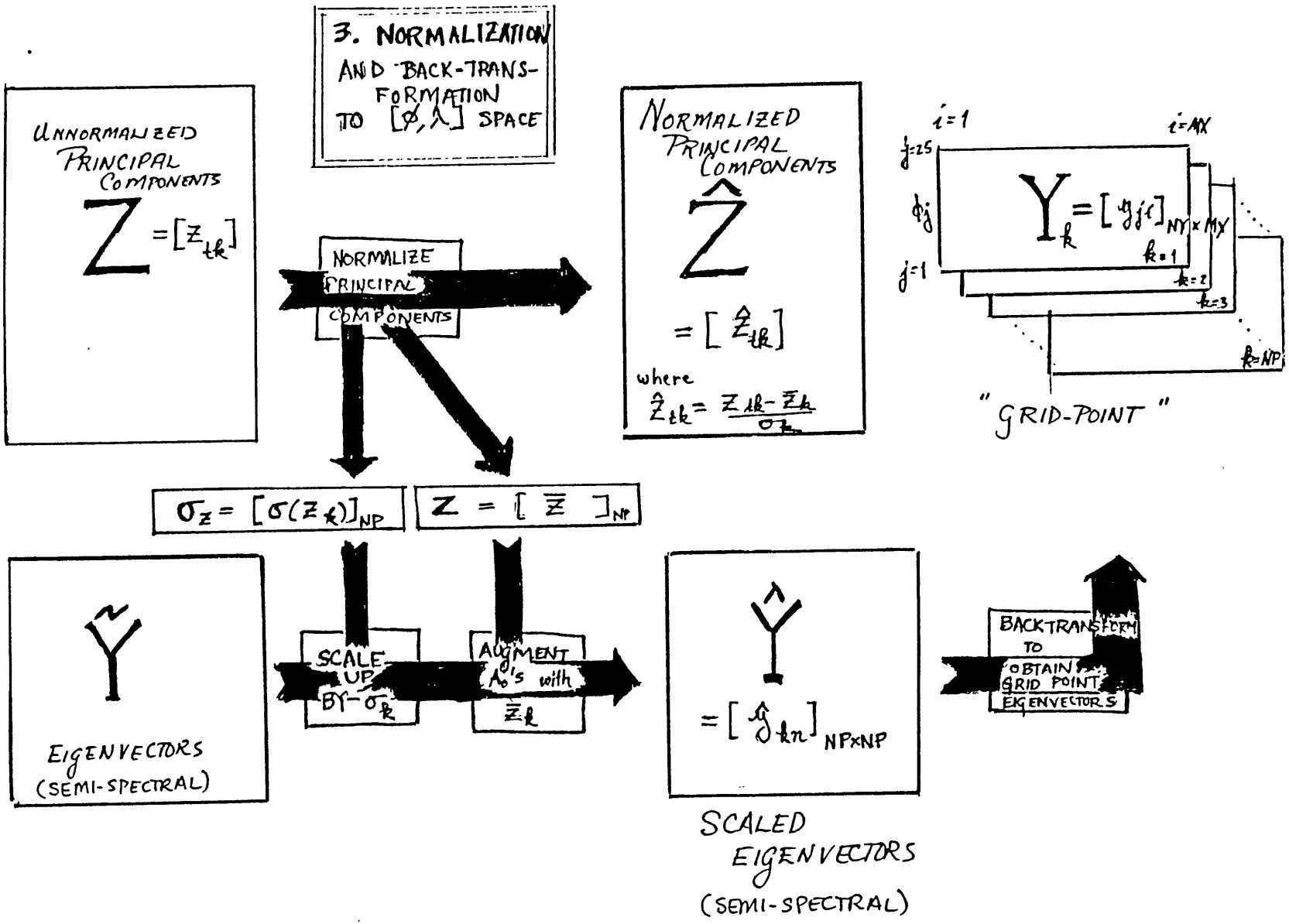

Fig. 4.18 Flow chart for semi-spectral empirical orthogonal analyses in Chapter 4. (3) Normalization and backtransformation to grid space.

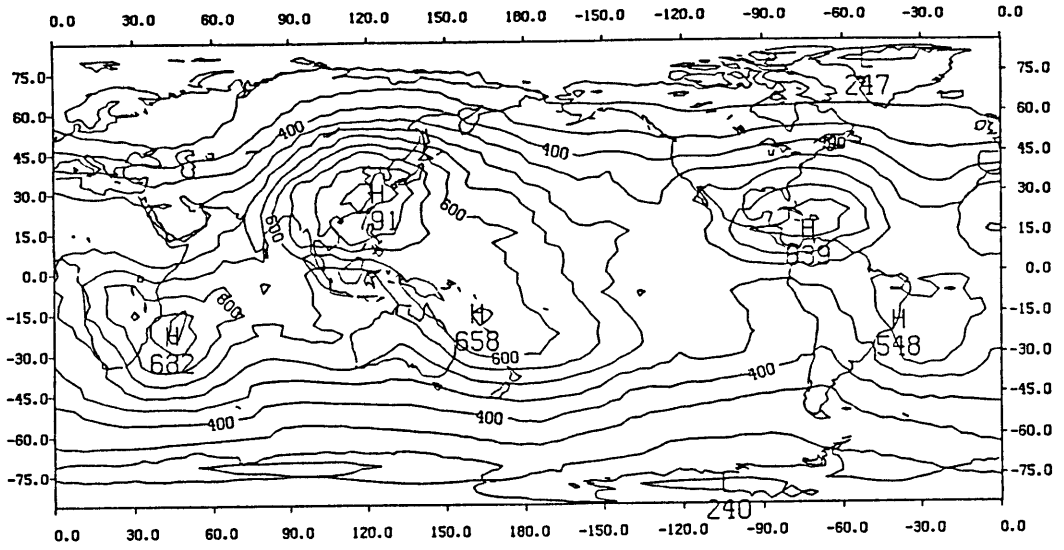

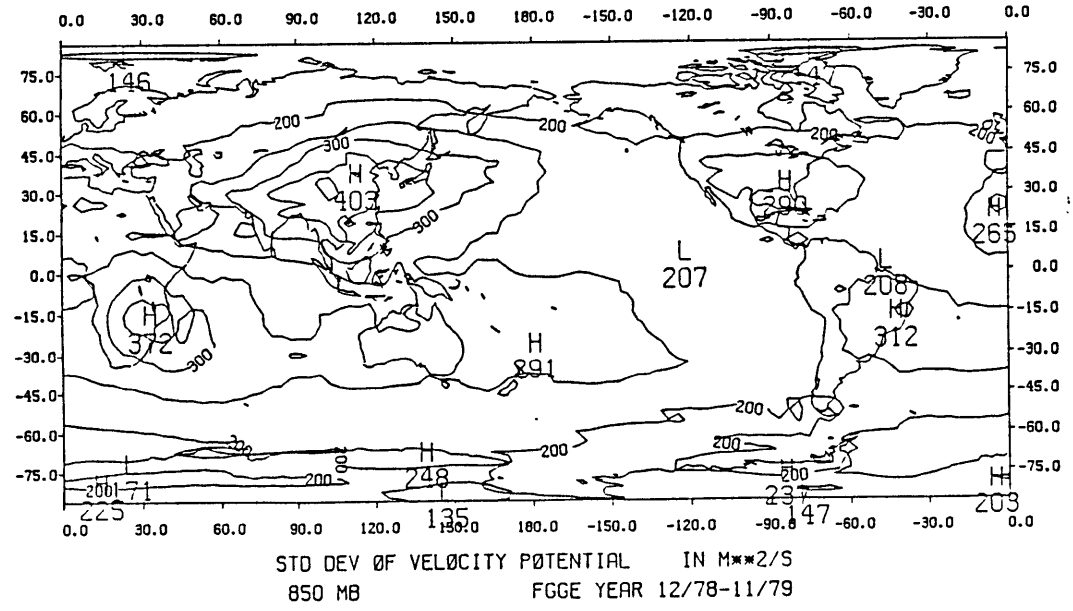

Fig. 4.19 FGGE period standard deviation of velocity potential at 200 mb, contour interval $50X10^4$ m/s (top); and 850 mb, same contour interval .

and 850 mb velocity potential variance fields. This is no accident as our results will later suggest.

The results of EOF analysis of the 200 mb velocity potential from 45°N to 45°S and for waves 0-10 are shown in Figure 4.20. [For convenience the characteristics of this analysis, i.e. the pressure level, maximum wave number and number of latitudes, are abbreviated 'C201025': 'C' standing for velocity potential (or chi), '20' for 200 mb, '10' for wave 10 and '25' the number of latitudes used (there are 25 latitudes from 45°S to 45°N on the 3.75° grid).] Figure 4.20 includes (a) the first five eigenvectors; (b) the first five principal components; (c) the divergent wind fields due to each of the first three modes and (d) the corresponding meridional wind fields. The first mode explains 32.6% of the variance and is dominated by the seasonal behavior of the Hadley circulation. The eigenvector has strong associated cross-equatorial winds over Africa, Indonesia and South America. In contrast, the Walker cell contributions from this mode are comparatively weak. The time series, as one might expect, is strongly seasonal in character, although there are indications of power at 40-50 days.

Modes 2 and 3, explaining 22.3% and 14.5% of the variance respectively, are quite similar in both spatial and temporal structure. Both of the principal components are dominated by power at 40-50 days and are in rough quadrature. The eigenvectors are both dominated by wave one and are centered near the equator. In addition, they too are roughly one-quarter wavelength out of phase. Consequently, the behavior of the two modes summed together describes a wave moving eastward along the equator with a frequency of approximately 45 days. This property will be discussed more fully in Chapter 5. Mode 2 also includes some

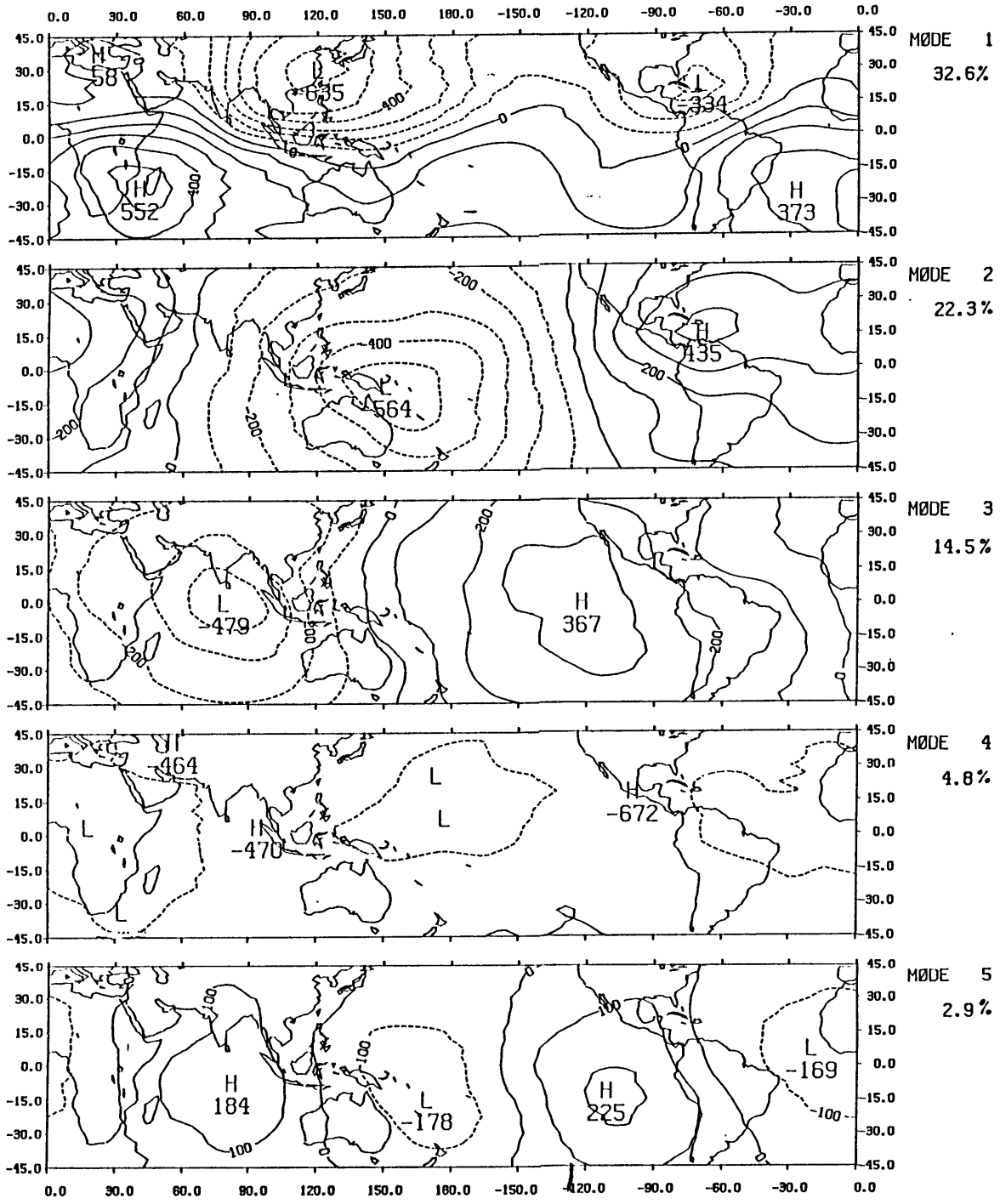

Fig. 4.20a Results of empirical orthogonal analysis C201025: 200 mb velocity potential 45°S-45°N, zonal wavenumbers 0-10. Grid-point eigenvectors for modes 1-5, contour intervals 100×10^4 m^2/s.

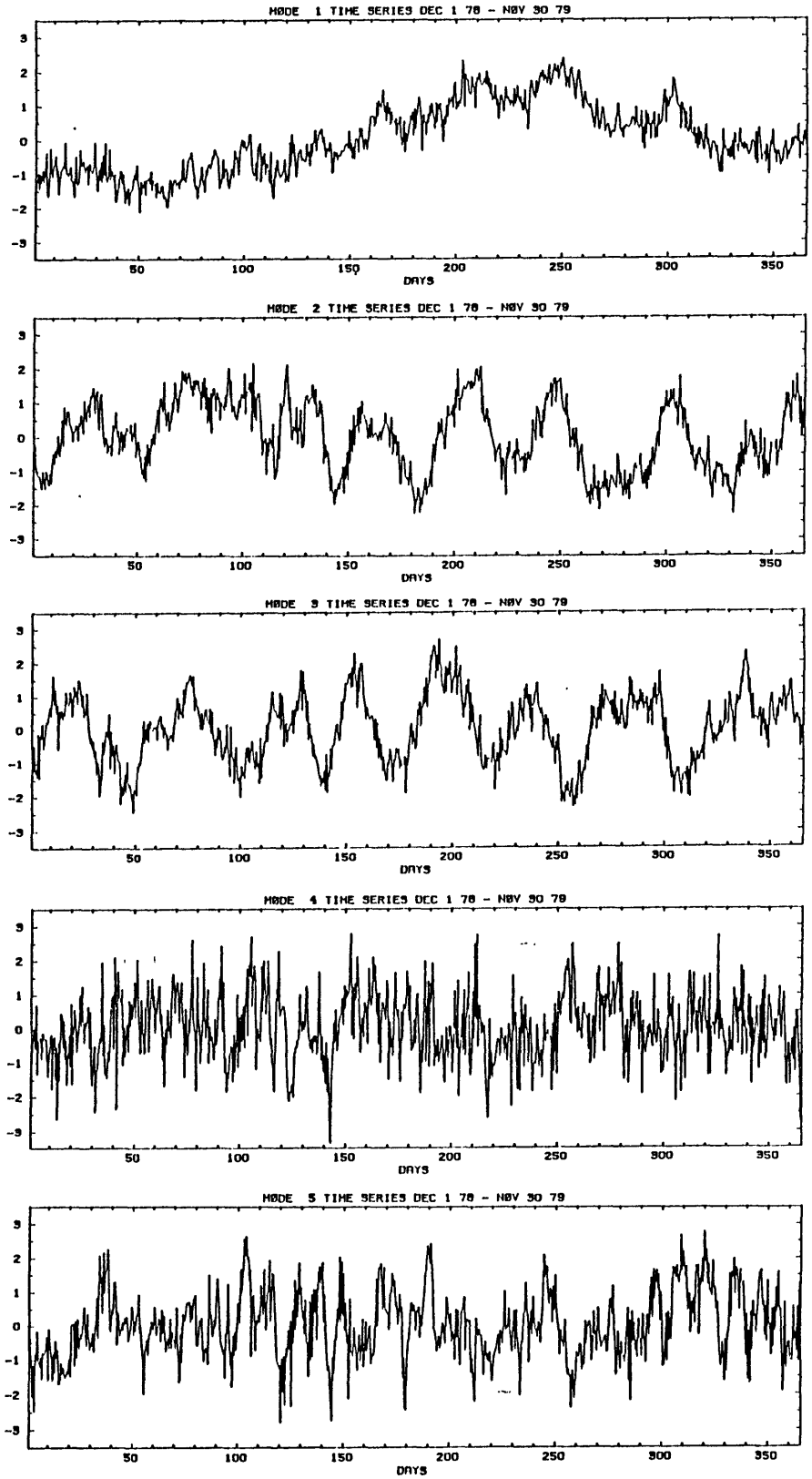

Fig. 4.20b Results of empirical orthogonal analysis C201025: 200 mb velocity potential 45°S-45°N, zonal wavenumbers 0-10. Normalized principal components, modes 1-5.

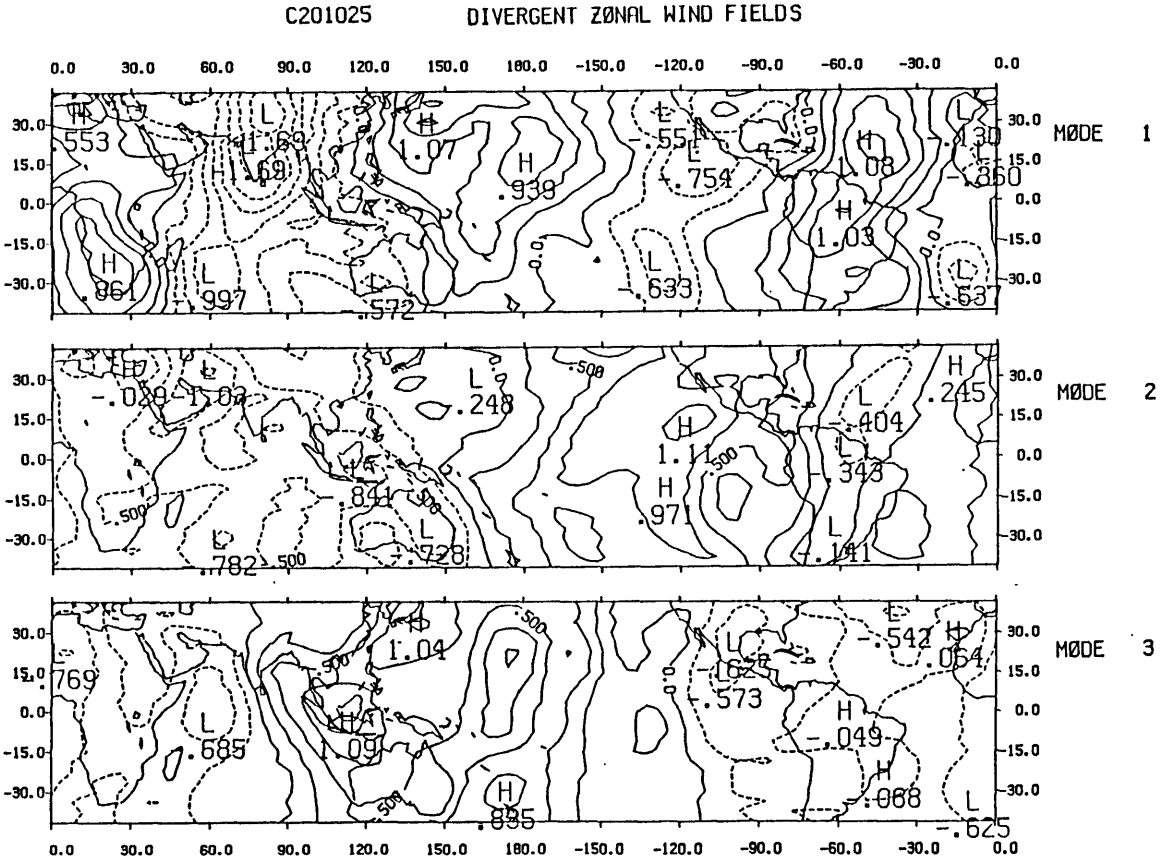

Fig. 4.20c Results of empirical orthogonal analysis C201025: 200 mb velocity potential 45°S-45°N, zonal wavenumbers 0-10. Divergent wind fields derived from eigenvectors 1-3, contour intervals 0.25 m/s.

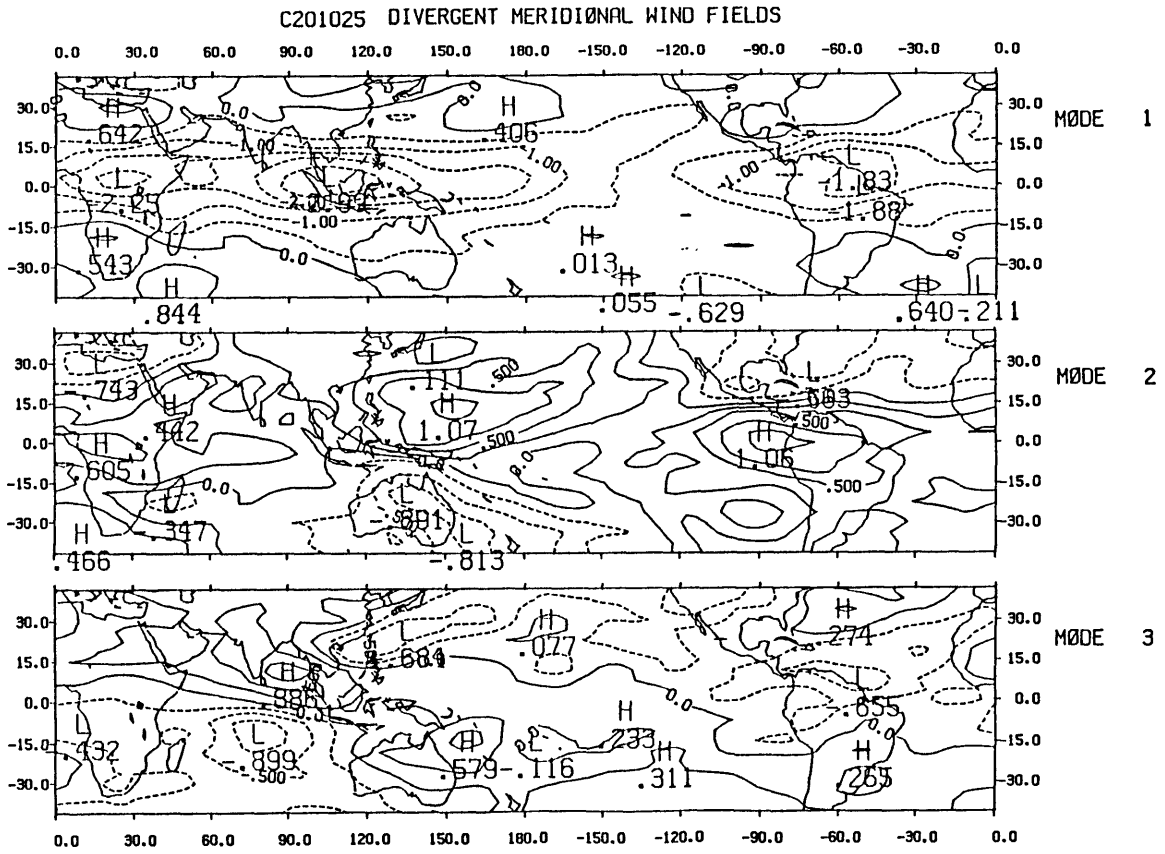

Fig. 4.20d Results of empirical orthogonal analysis C201025: 200 mb velocity potential 45°S-45°N, zonal wavenumbers 0-10. Meridional wind fields for eigenvectors 1-3, contour intervals 0.5, 0.25 and 0.25 m/s.

Hadley cell variability as there is a southward displacement from the equator of its negative center near 150°E and the northward displacement of the positive center near 75°W. The Hadley cell power appears in the time series as a slight seasonal cycle.

With the exception of the first mode the results of this EOF analysis are virtually identical to those in Lorenc (1984) who removed the annual cycle from the velocity potential data before proceeding with the EOF analysis. He also performed his EOF analysis upon the spherical harmonic coefficients, thus making no explicit restriction to the tropics as in this study. With the exception of the small amount of variability at 40-50 days in the first, "seasonal" mode, our results demonstrate the independence of the 40-50 day spatial structure from that of the seasonal cycle.

In Fig. 4.21 are displayed spectral estimates for each of the first three principal components. These estimates were made using a weighted covariance or Blackman-Tukey power spectral estimator [see Appendix A, also Koopmans (1974, Chapter 9)]. The spectra appearing in this figure provide quantitative measures of the long-period features readily apparent in the time series as well as the subtle features of more questionable statistical significance, such as the 40-50 day power apparent in the first principal component.

The seasonal cycle which is so strong in mode 1 cannot be resolved with the resolution practically achievable in a one-year time series; lying as it does at $0.00274f_N$, where f_N is the Nyquist frequency of 1.0 day^{-1}, it cannot be distinguished from zero frequency. 40-50 day power however is clearly distinguishable in each of the three time series. Error bars at the 95% confidence level are drawn at the 40-50 day peaks

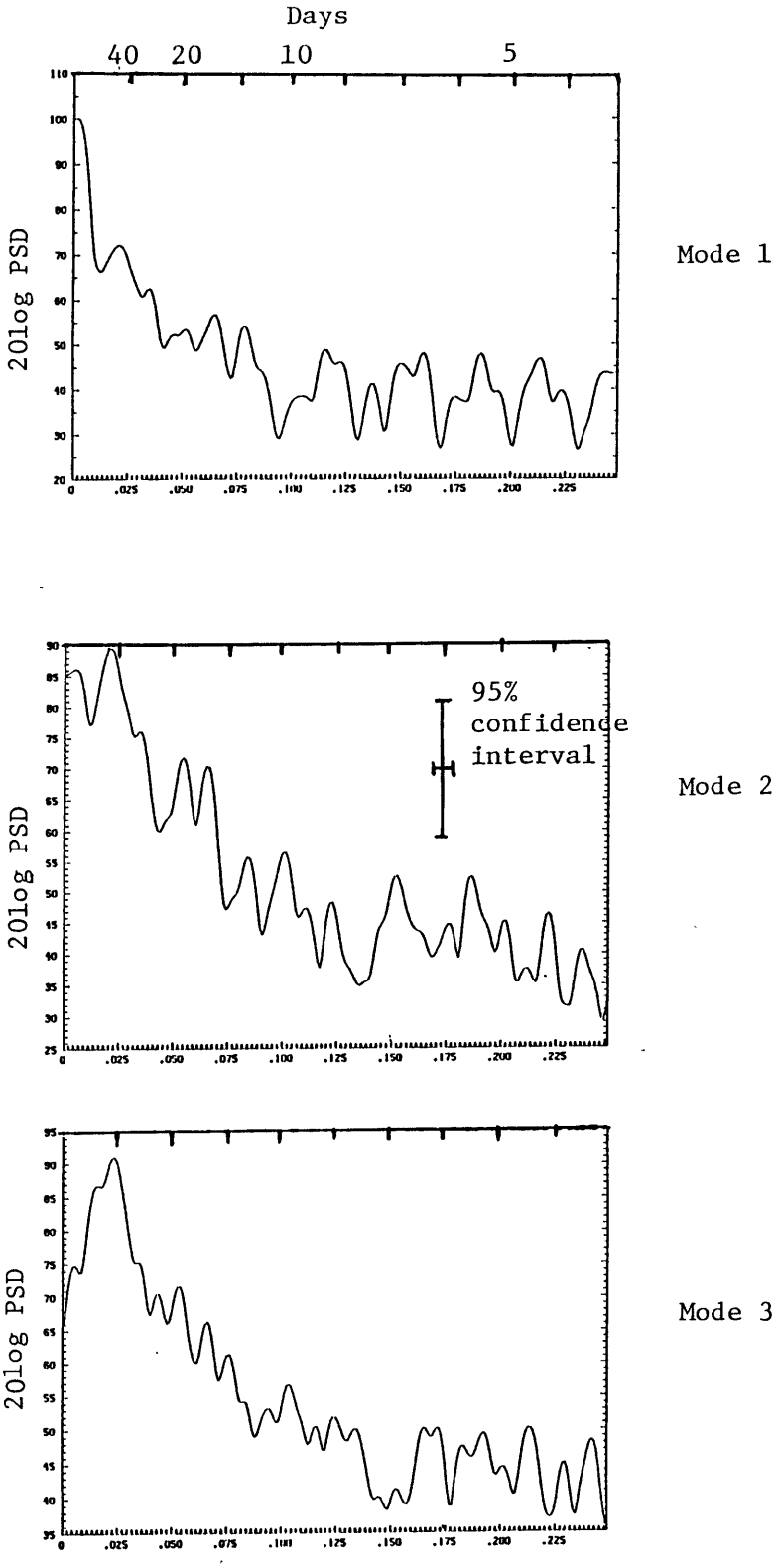

Fig. 4.21 Weighted covariance spectral estimates for C201025 mode 1 (top), mode 2 (middle) and mode 3 (bottom).

in each of the spectral estimates. The error bars indicate that these peaks are likely not due to chance. This is particularly true in the case with mode 3 where the peak appears near 45 days.

Before discussing the 40-50 day behavior in these time series, we will present in a more graphic form the seasonal cycle in the variance explained by the leading EOF modes. Fig. 4.22 is a reconstruction of the changes in the total field of velocity potential (mean plus anomalies) due to the annual and semiannual cycles in the first five modes of C201025 sampled at intervals of approximately 31 days, starting at day 61 and ending at day 304. The first and second annual harmonics here were derived by first cosine tapering the first and last 61 half-days in the mode one time series (to reduce the effect of side-lobe contamination) and then performing a simple Fourier expansion on the tapered series for these two components. The resultant fields at the sampled days were reconstructed by multiplying the resulting annual cycle "time series" by the eigenvector grids mode by mode, summing the mode contributions and then adding in the time mean value. From the top, the panels correspond to the following calendar days in the FGGE year: January 30, April 1, June 1, August 1 and September 30.

Although the seasonal cycle in the first principal component seems to be relatively close to a wave one sine function, the configuration of the total field during the northern summer is quite different from the southern summer. There is a significant westward movement of the Pacific velocity potential negative center as it moves northward with the advance of the year. Thus in the early parts of the FGGE year, there is a strong meridional overturning into the Northern Hemisphere over the western Pacific ocean from a center located in what is known as

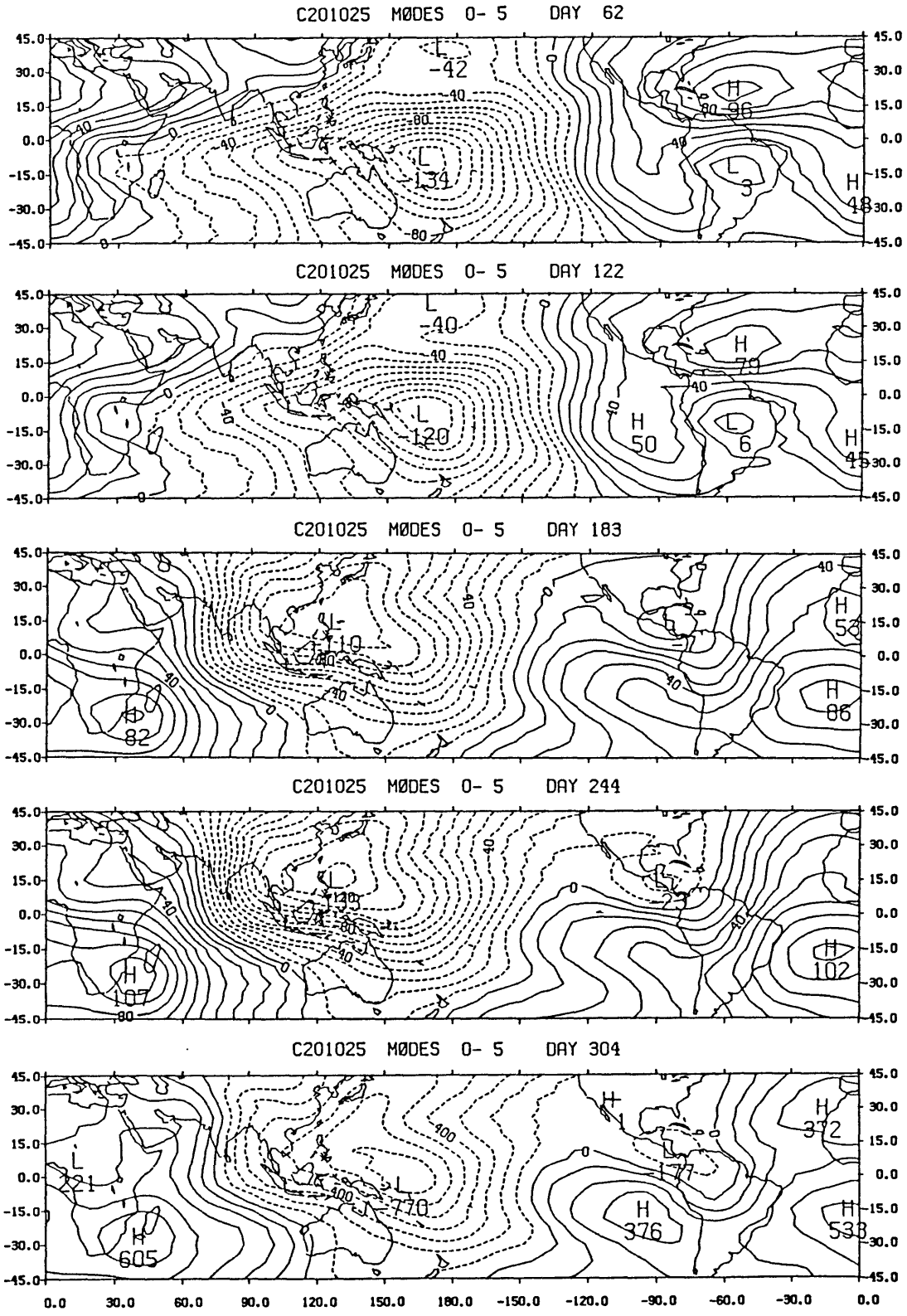

Fig. 4.22 Reconstruction of annual and semi-annual cycle of velocity potential using first and second harmonics of first five principal components from C201025. Panels (from top) correspond to January 31, April 1, June 1, August 1 and September 30 from the FGGE year. Contour intervals 100×10^4 m^2/s.

the South Pacific Convergence Zone. This pattern seems to peak in February. Also in this part of the year there is northward overturning near 60°W. During April and May, the northwestward movement of the anomaly changes the large-scale pattern rather abruptly. By June 1, a strong southward meridional overturning is now taking place over the central and eastern Indian Ocean and Indonesia as well as a westward divergent flow over South Asia. This abrupt movement roughly coincides with the onset of the summer monsoon over India (Krishnamurti et al., 1985) and represents the development of deep convection over the South Asian mainland and the Bay of Bengal region. The divergent easterlies in the Indonesian Walker cell are stronger than the westerly arm of the Pacific Walker cell which six months earlier was the dominant divergent zonal flow in the tropics. Over South America, there is an area of weak southward overturning associated with the rainy season in the eastern tropical Pacific and Central America.

Most of the changes in the seasonal cycle described here are associated with the Asian and Australian monsoons, although there is evidence of considerable movement in the South American region. Whether or not this reflects an actual preeminence of the Asian seasonal cycle is not clear, for the South American region was quite decidedly undersampled by rawinsondes and pilot balloons relative to South Asia. One would expect that this undersampling would be evident in a diminution of the variance in that region.

Figure 4.23 presents the first five eigenvectors and principal components from an EOF analysis of waves 1-10 only of the 200 mb velocity potential, i.e. with the zonally symmetric components at each

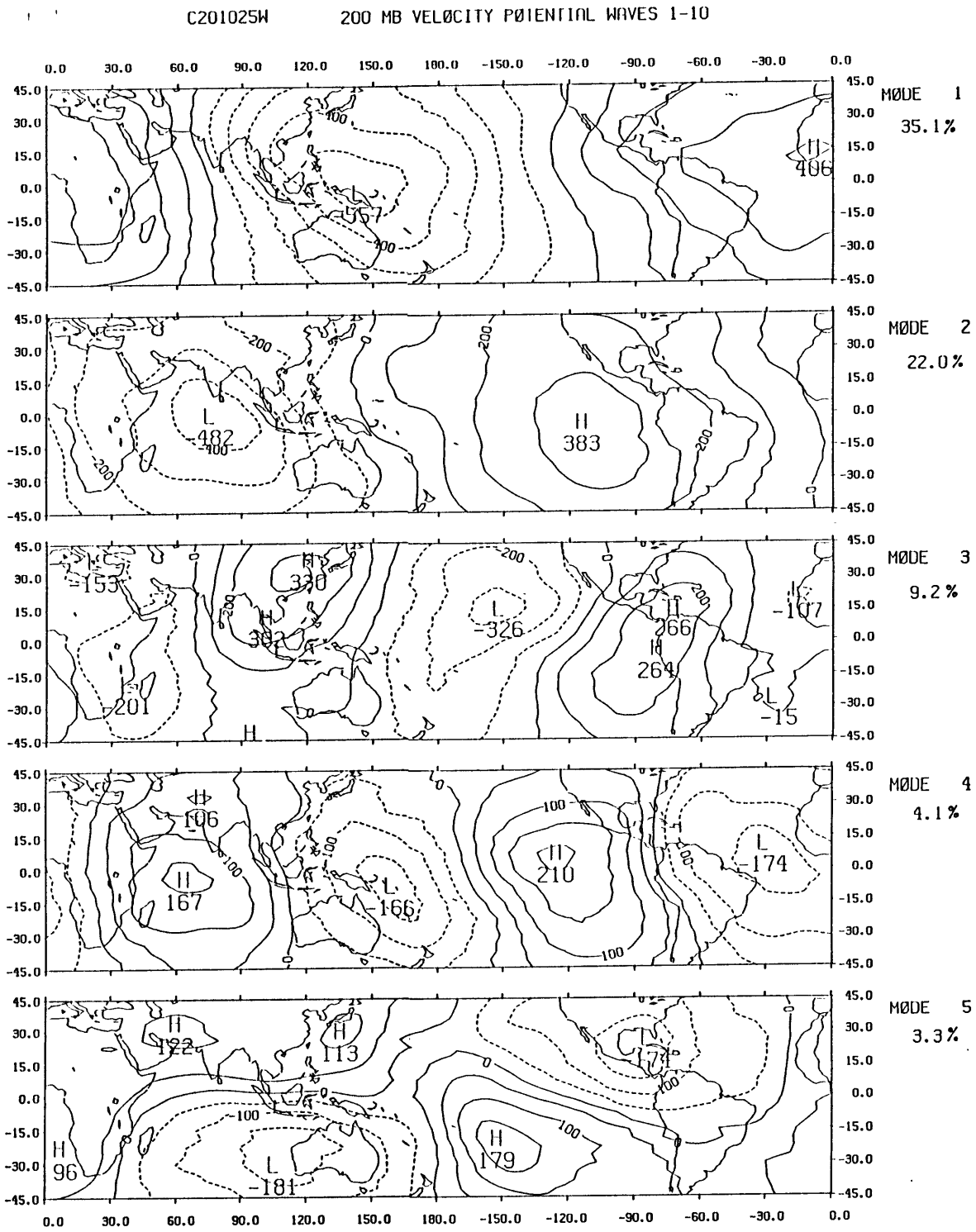

Fig. 4.23a Results of empirical orthogonal analysis C201025W: zonally asymmetric 200 mb velocity potential 45°S-45°N, zonal wavenumbers 1-10, Eigenvectors for modes 1-3, contour intervals 100×10^4 m^2/s; modes 4-5, contour interval 50×10^4 m^2/s.

C201025W

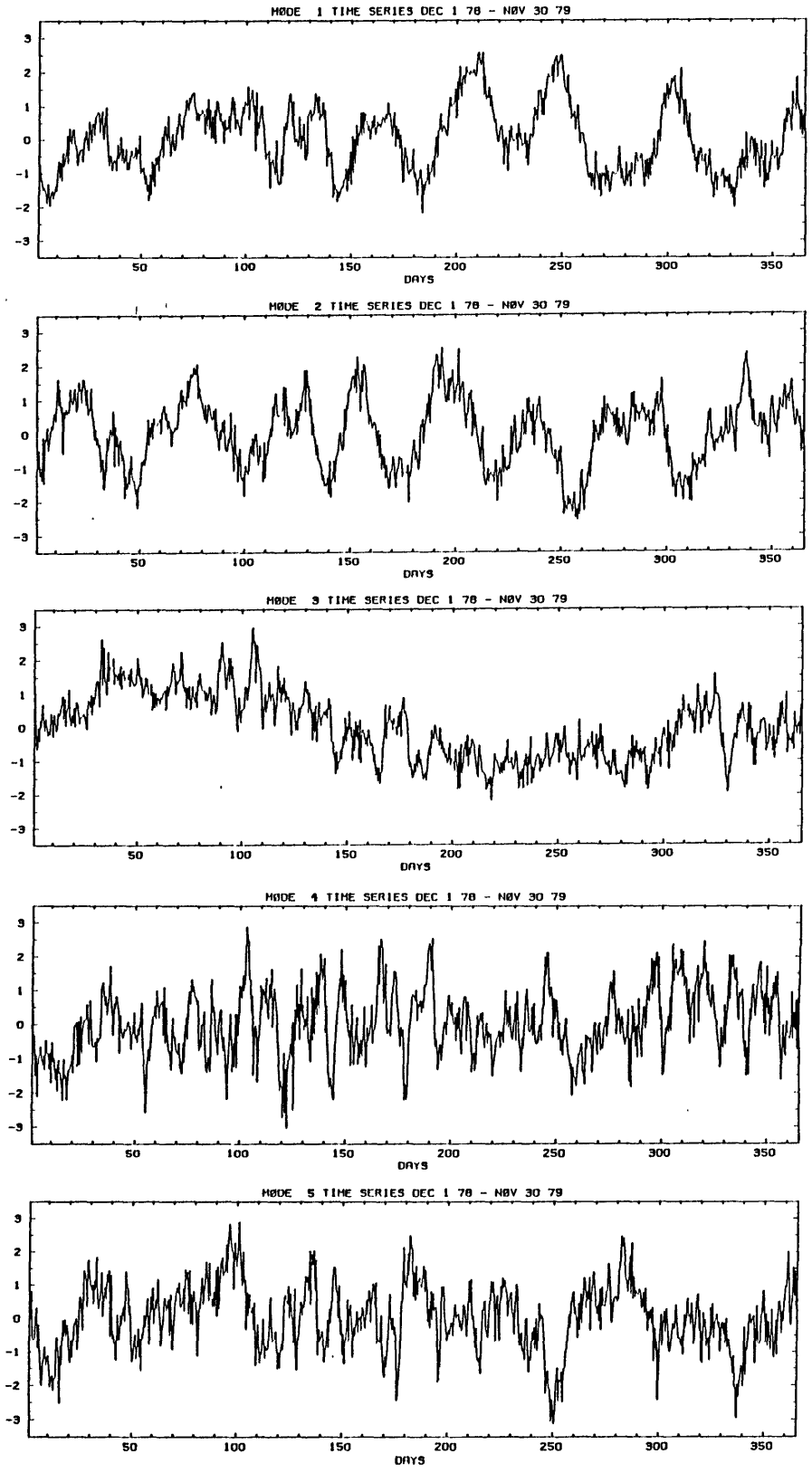

Fig. 4.23b Results of empirical orthogonal analysis C201025W: zonally asymmetric 200 mb velocity potential 45°S-45°N, zonal wavenumbers 1-10. Normalized principal components, modes 1-5.

latitude eliminated. [We will refer to this calculation as C201025W; the 'W' indicates the exclusion of wave 0 (after 'Walker').]

By eliminating the variability due to the Hadley circulation (i.e. wavenumber zero) we obtain the results reported by Lorenc (1984). This analysis clearly shows the Walker circulation. Although the peaks in the mean velocity potential map are shifted somewhat southward of the equator, the first two modes are nearly equatorially symmetric. In relative variance and conformation in both space and in time, these two modes parallel the second and third modes of C201025. In fact, the second mode of this analysis is almost indistinguishable from its C201025 counterpart. A seasonal cycle appears in the third mode which explains 9.2% of the variance. This has a wave two pattern which is partly confined to the Pacific sector of the Northern Hemisphere. The fourth mode (4.1%) in contrast is also wave two in character but is weighted toward the Southern Hemisphere. Both of these two modes have considerable power in the 10-15 day frequency range.

4.4 40-50 Day Variability of Divergent Winds in the Lower Atmosphere and Vertical Coherence of the Oscillation

The 850 mb velocity potential field tends to have finer structure than the 200 mb field, but the filtering effects of EOF analysis remove a great deal of the noise inherent in the variability. We have performed several EOF analyses of the 850 mb velocity potential in the 45°S-45°N region. The analysis of waves 0-10, C851025 (shown in Figure 4.24) tends to separate the zonal mean variability from the zonally asymmetric variability as in C201025, although the former dominated in

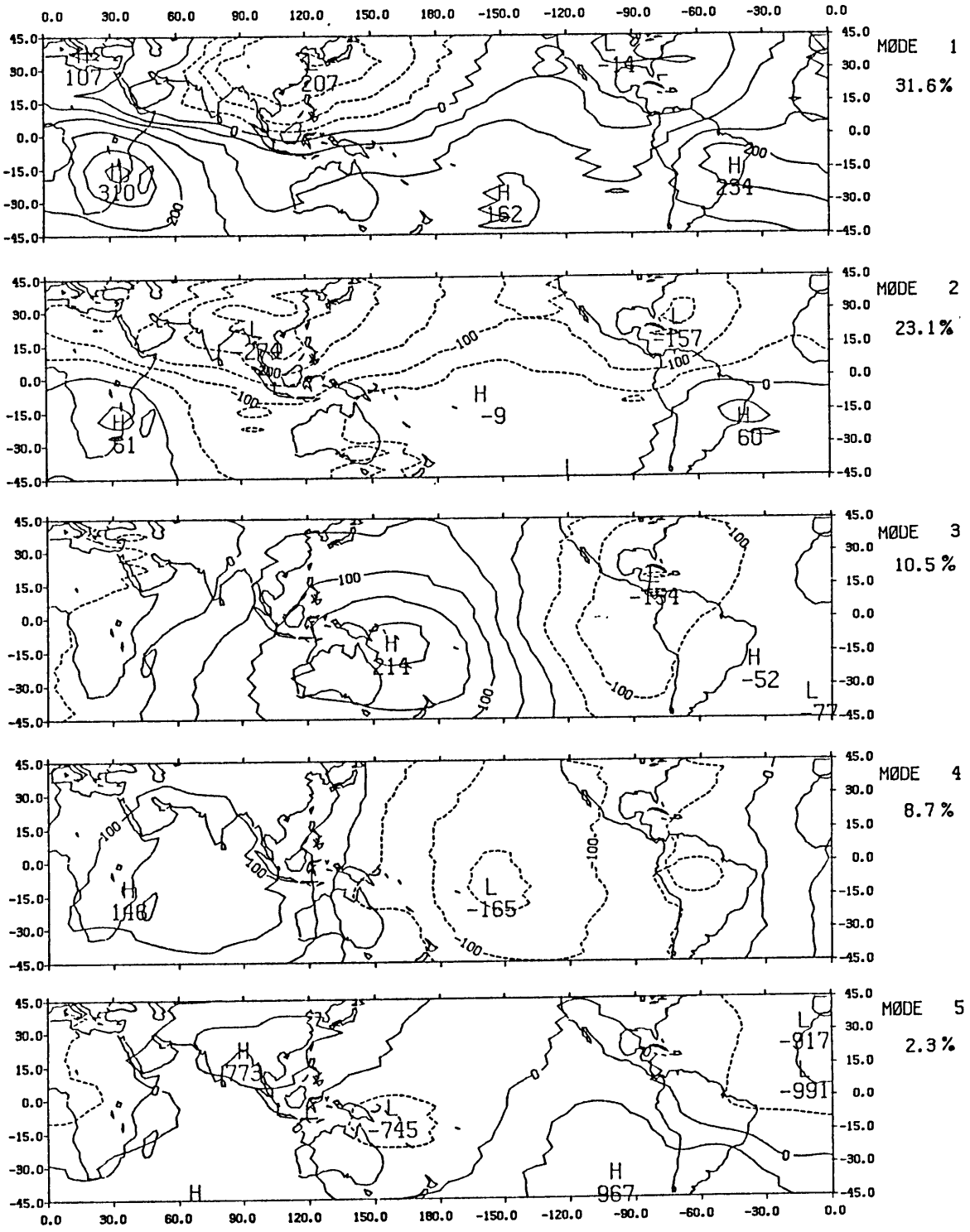

Fig. 4.24a As in 4.23a but for EOF C851025: 850 mb velocity potential, 45°S-45°N, zonal wavenumbers 0-10. Contour intervals 50×10^4 m^2/s.

C851025

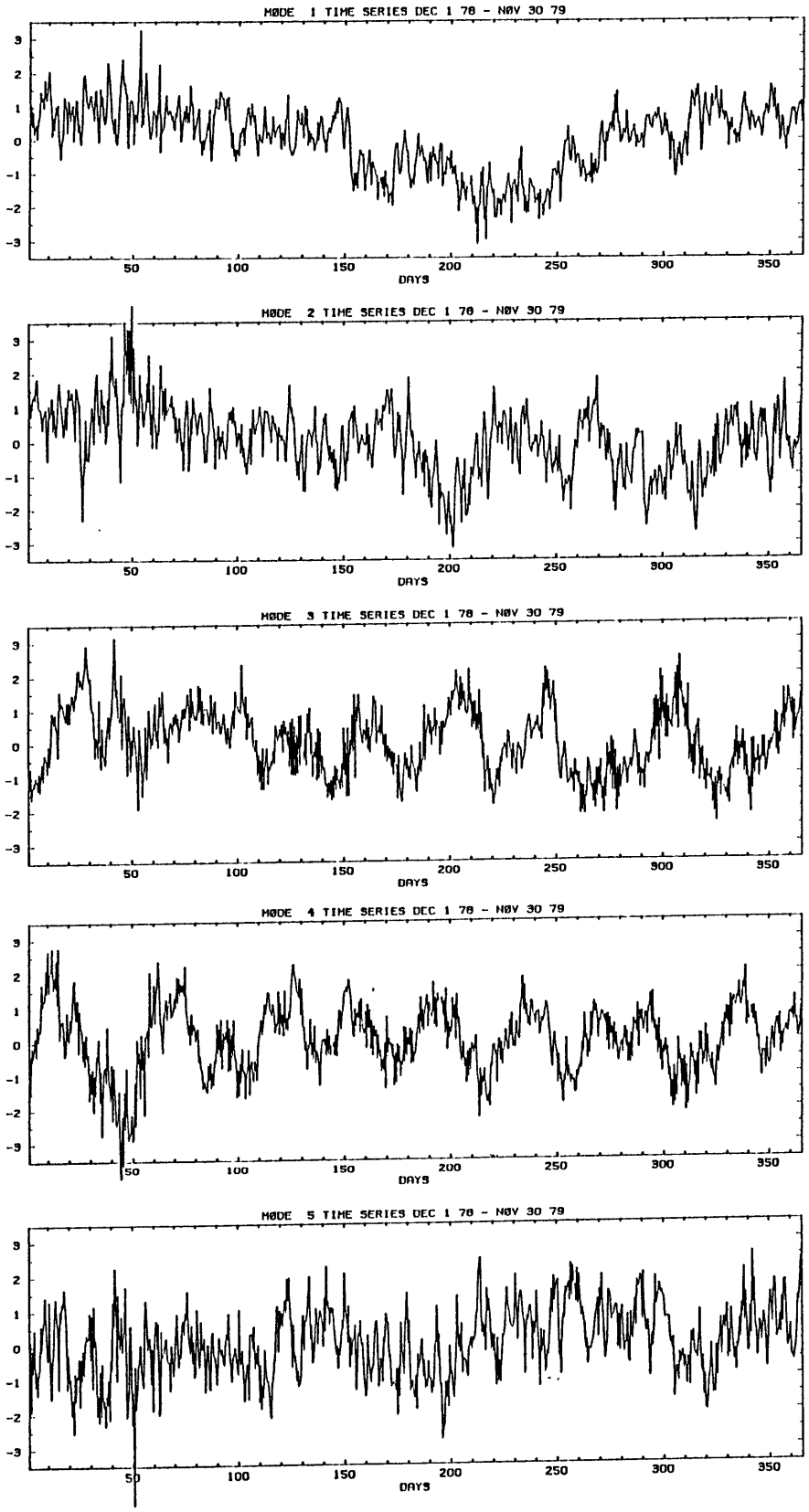

Fig. 4.24b As in 4.23b but for EOF C851025: 850 mb velocity potential, 45 S-45 N, zonal wavenumbers 0-10.

the first two modes rather than in the first alone. Note the mix of seasonal and intraseasonal variability in these modes containing relatively strong zonal symmetry with the intraseasonal variability seemingly beginning after day 150. (May 1 is day 152.) The two eigenvectors are quite similar; in this case the obvious orthogonality of the eigenvectors of previous EOF analyses is absent. The orthogonality in the modes is contained in the products of the principal components with the eigenvectors, but the closeness of the patterns in these two eigenvectors suggests that the two eigenmodes might reappear as a single eigenmode in an independent dataset.

Kendall (1980) and North et al. (1982) have advocated the use of the formula $\Delta d_i = d_i(2/N)^{1/2}$ for the calculation of the sampling error of the eigenvalues derived from EOF analysis. Here Δd_i is the sampling error of the eigenvalue d_i and N is the number of independent samples. Figure 4.25 graphs the first seven eigenvalues and their associated sampling errors for C201025 as well as C851025. The overlapping of the error bars of successive eigenvalues would be an indication that the corresponding EOF modes are not independent of each other and are not likely to reappear in a separate realization of the analyzed data fields. By straightforward application of the above criterion, using N=730, the length of the time series, the first five modes of C201025 and the first three of C851025 seem to be independent. On the other hand, the choice of N=730 independent points in time is clearly too large for a data set in which there are slow fluctuations on the order of 45 days. Empirically this seems likely for the 40-50 day power in the first principal component of C201025 seems to be in phase with the second, and the 'Hadley' peaks mentioned in the discussion of the mode 2

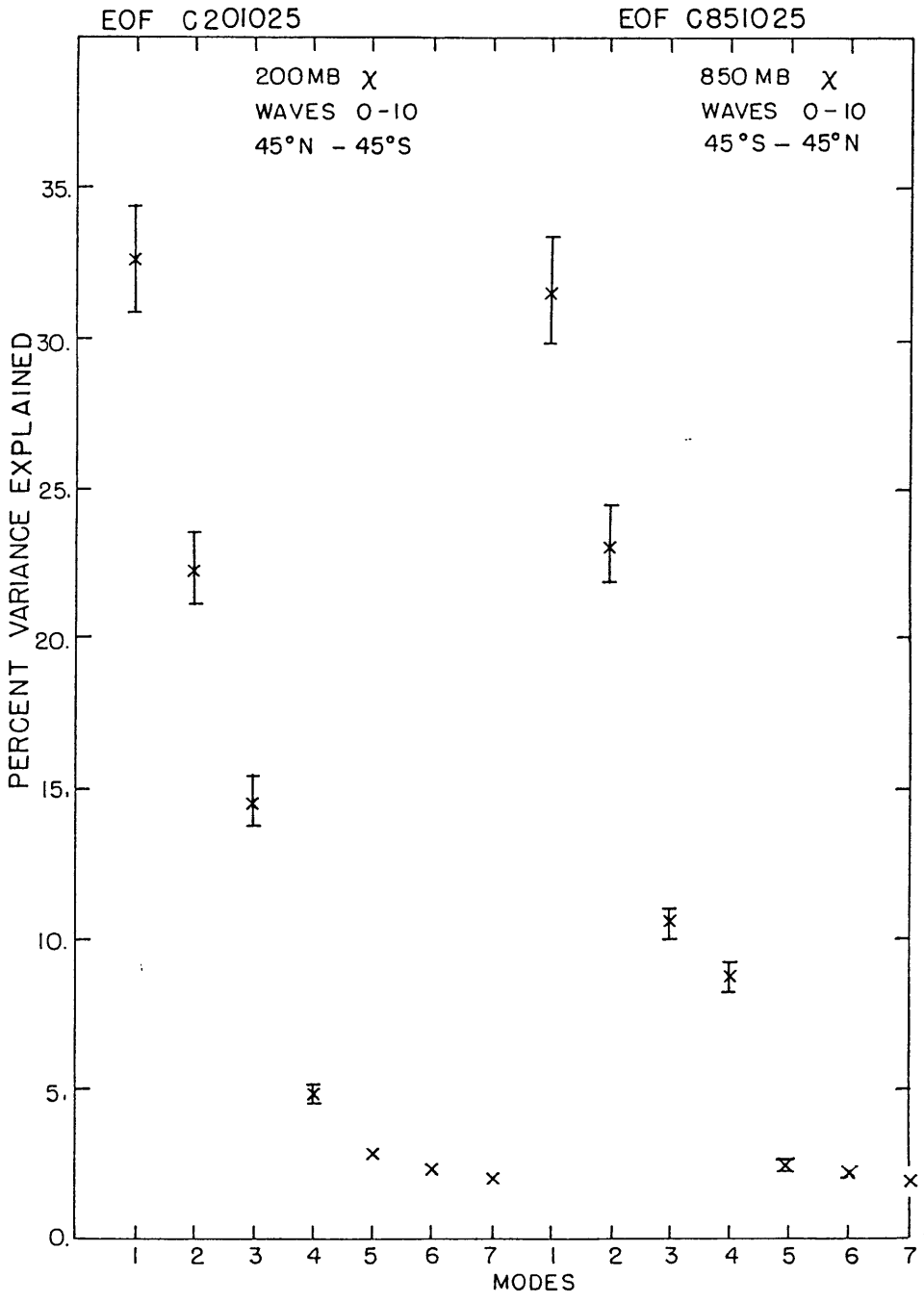

Fig. 4.25 Eigenvalues of C201025 and C851025. Error bars extend $\pm \Delta d_i$ (see text for explanation).

eigenvector could perhaps be incorporated (with opposite phase) into the mode 1 eigenvector; in short, modes 1 and 2 of C201025 do not seem completely independent of each other, as we have already suggested for C851025.

If we turn the sampling error criterion around and ask what is the critical value of N at which the error bars for the first two modes begin to overlap, viz.

$$d_1 - \Delta d_1 = d_2 + \Delta d_2$$

we obtain the following solution for this critical value:

$$N_c = 2\left\{\frac{d_1 + d_2}{d_1 - d_2}\right\}^2$$

For C201025, d_1=.326 and d_2=.223, and $N_c \approx 57$ or roughly 1 observation in 12 independent. Using the first two modes of C851025 (d_1=.316 and d_2=.231), $N_c \simeq 83$, or about 1 in 9 independent.

As at 200 mb, the dominant mode of variability in the zonally asymmetric 850 mb velocity potential is a 40-50 day fluctuation. The striking characteristics of the leading modes of C851025W (shown in Figure 4.26), the counterpart of C201025W, are the near perfect matches between the leading principal components of the former with the latter and the antisymmetry of the eigenvector patterns, with minima at 200 mb approximately collocated with maxima at 850 mb. Closer comparison of 4.23 and 4.26 of course reveals some minor, but clear, differences: a tendency for the 850 mb modes to be centered somewhat off the equator and a notable spatial phase shift of ~50° longitude between the opposite extrema of the second modes. The latter discrepancy may in part account for the subtle phase lead (roughly 2-3 days) of 850 mb over 200 mb in

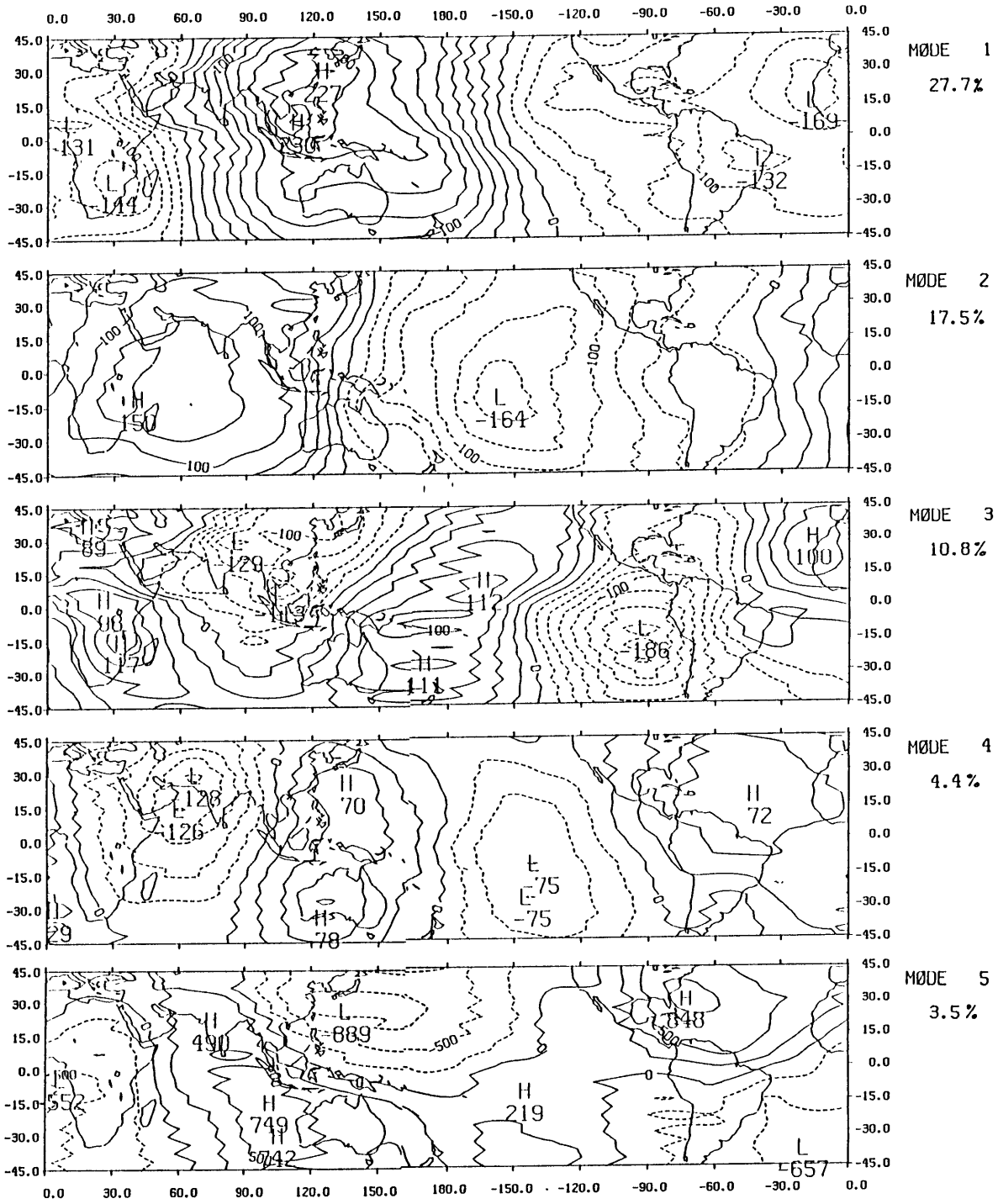

Fig. 4.26a As in 4.24a but for EOF C851025W: 850 mb velocity potential, 45°S-45°N, asymmetric zonal wavenumbers 1-10. Contour intervals 25×10^4 m^2/s.

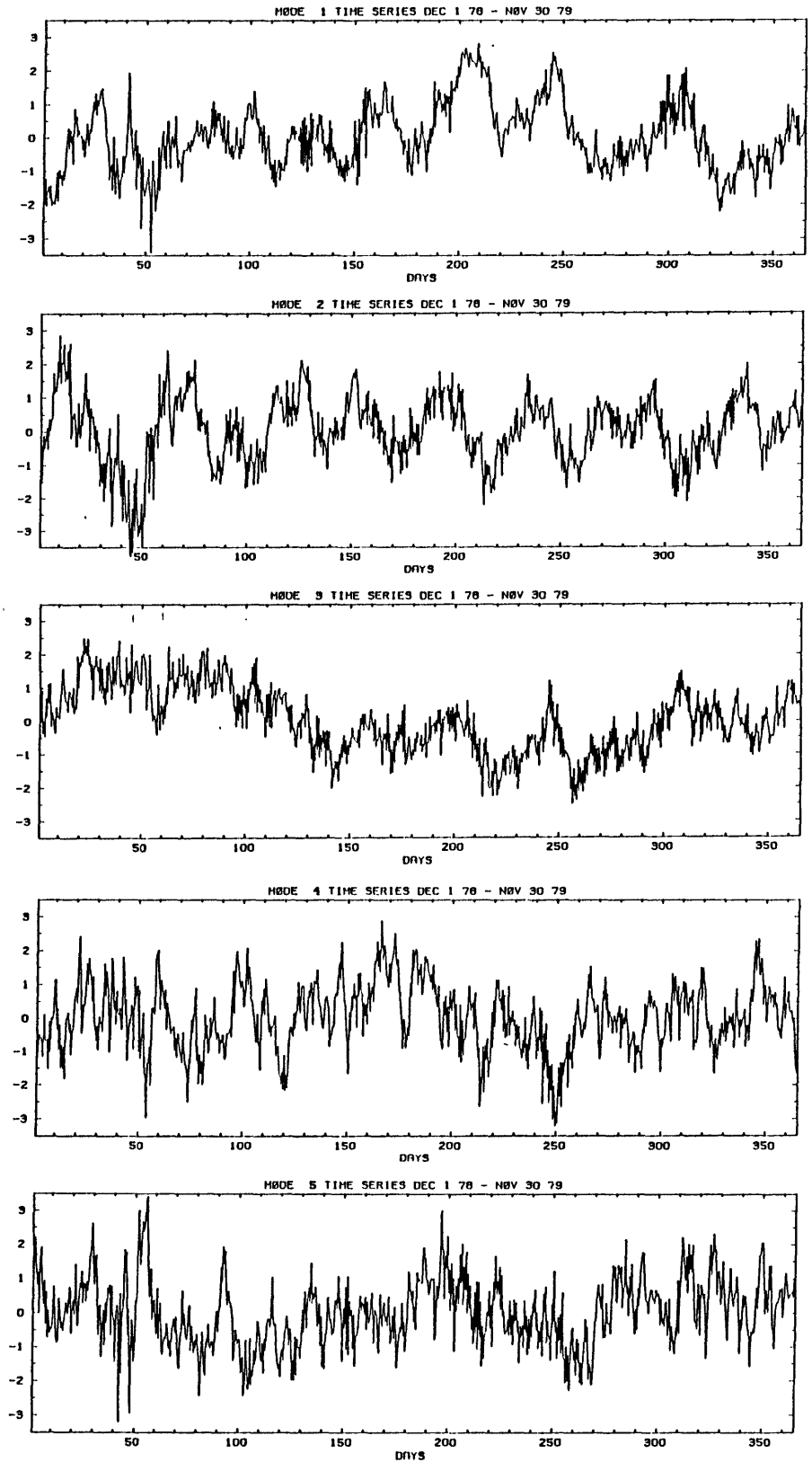

Fig. 4.26b As in 4.23b but for EOF C851025W: 850 mb velocity potential, 45 S-45 N, zonal wavenumbers 1-10.

the corresponding principal components. Despite these differences, it is strikingly clear that on the large spatial and time scales, the 200 and 850 mb velocity potential are closely tied, suggesting a strong coupling of divergence at 200 mb with convergence at 850 mb and vice versa.

To investigate this vertical coupling directly, we performed one final EOF analysis, this time on the combined variability of waves 1-5 at both 850 and 200 mb. The results are displayed in Figure 4.27 for the first three EOF's. The principal components for this EOF, C820525W, are remarkably similar to those for C201025W, and only slightly less similar to those of C851025W. Much the same can be said for the eigenvectors. The first three modes account for over 65% of the combined variance in the two levels combined

4.5 Discussion

The EOF results presented in this chapter complement and extend those of Lorenc (1984). We have shown that EOF analysis can separate out the essential elements of the 40-50 day variation in the seasonal cycle without initial filtering. It is also apparent that the dominant variance associated with the 40-50 day variation is in the very lowest wavenumbers of the velocity potential. This agrees with the results of Hollingsworth and Cats (1981) shown in Fig. 3.4 who found that most of the divergent energy in the time mean of the ECMWF analysis resided in the lowest five zonal wavenumbers.

Lorenc presented results for 850 mb and 200 mb separately whereas we have shown unambiguously in the results from C201025W, C851025W and

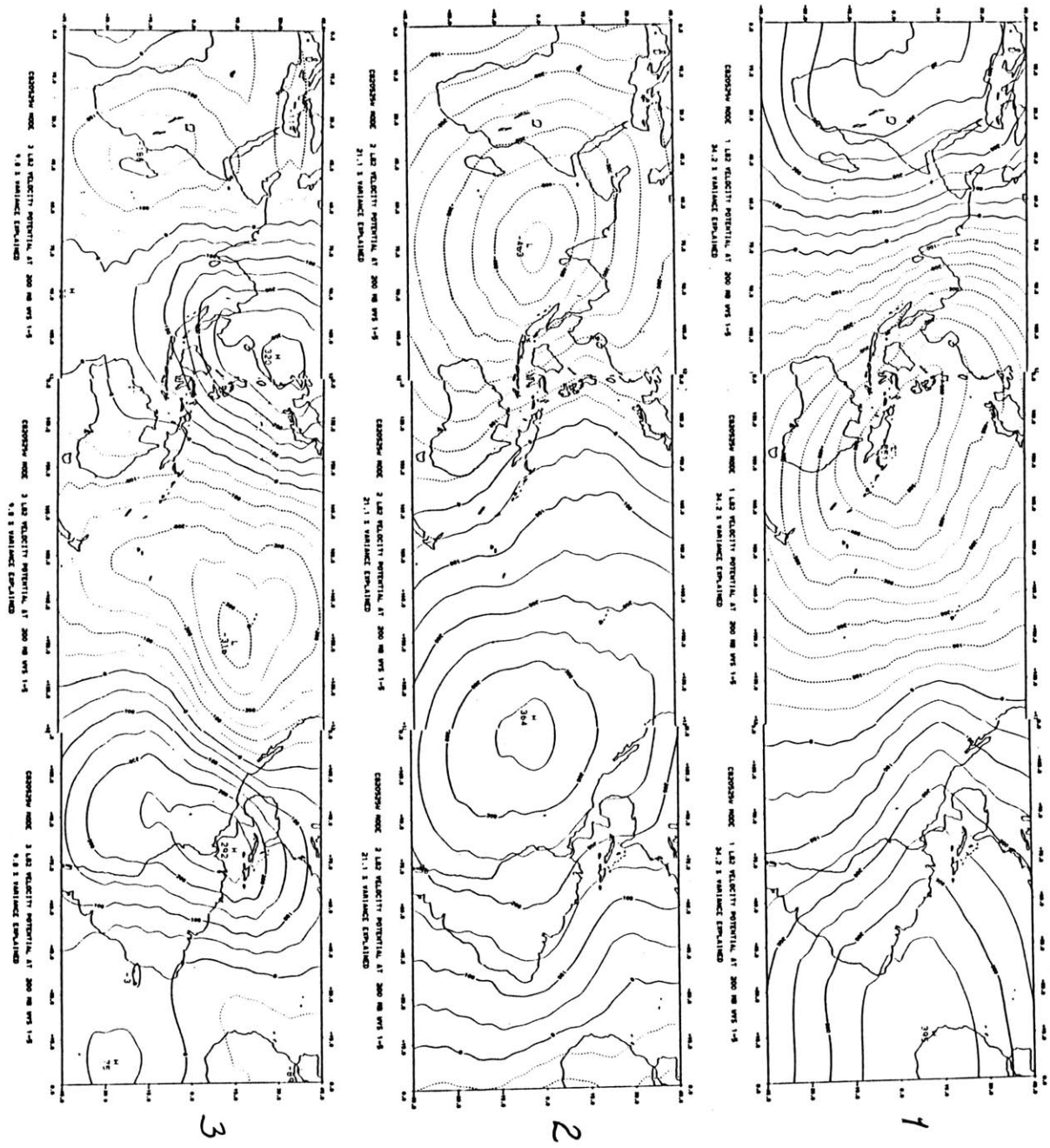

Fig. 4.27a Results of two-level empirical orthogonal analysis C820525W: combined 850 and 200 mb velocity potential 45°S-45°N, zonal wavenumbers 1-5. 200 mb components of eigenvectors for modes 1-5, contour intervals 100×10^4 m^2/s.

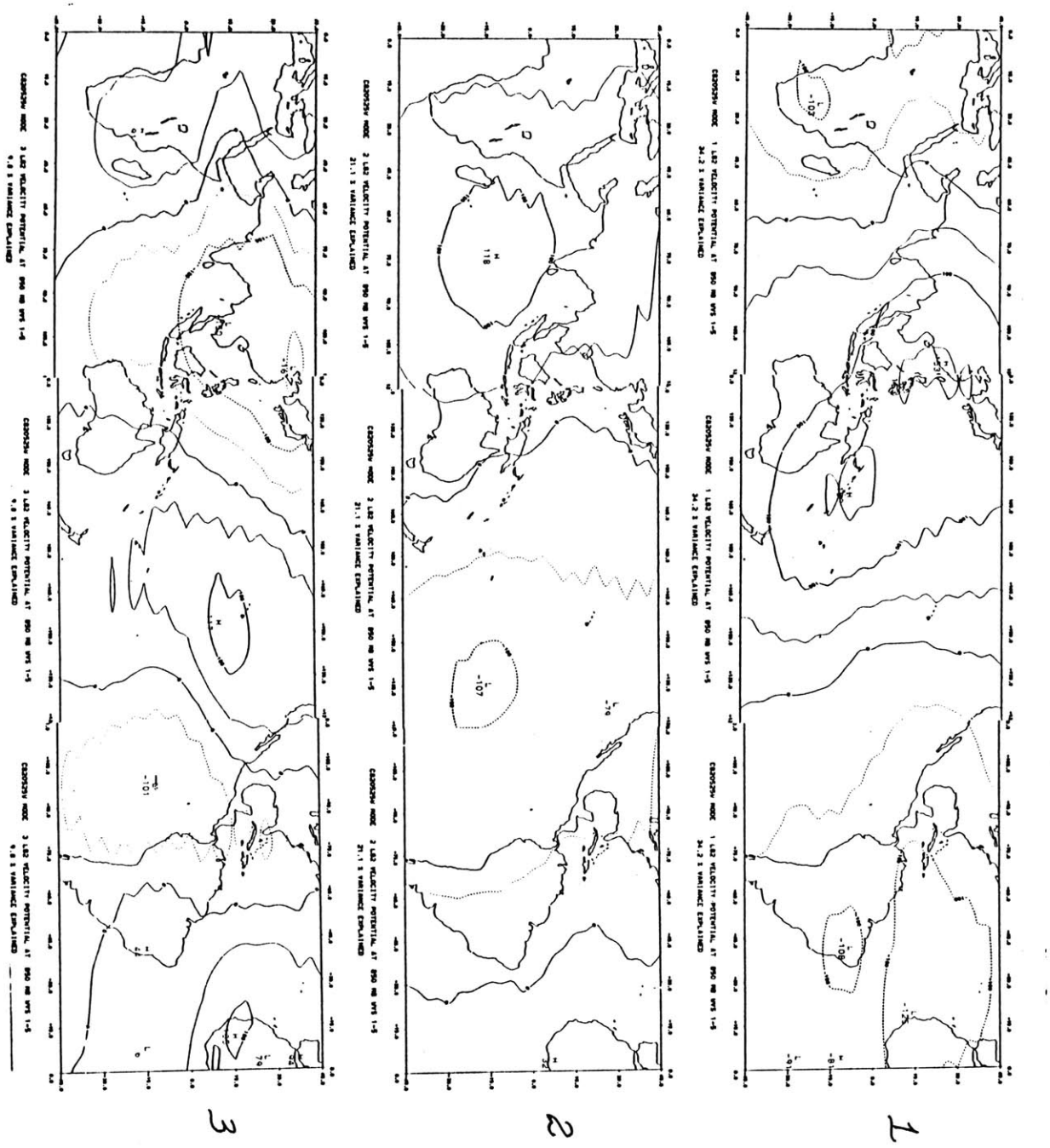

Fig. 4.27b Results of two-level empirical orthogonal analysis C820525W: combined 850 and 200 mb velocity potential 45°S-45°N, zonal wavenumbers 1-5. 850 mb components of eigenvectors for modes 1-5, contour interval 100×10^4 m^2/s.

C820525W

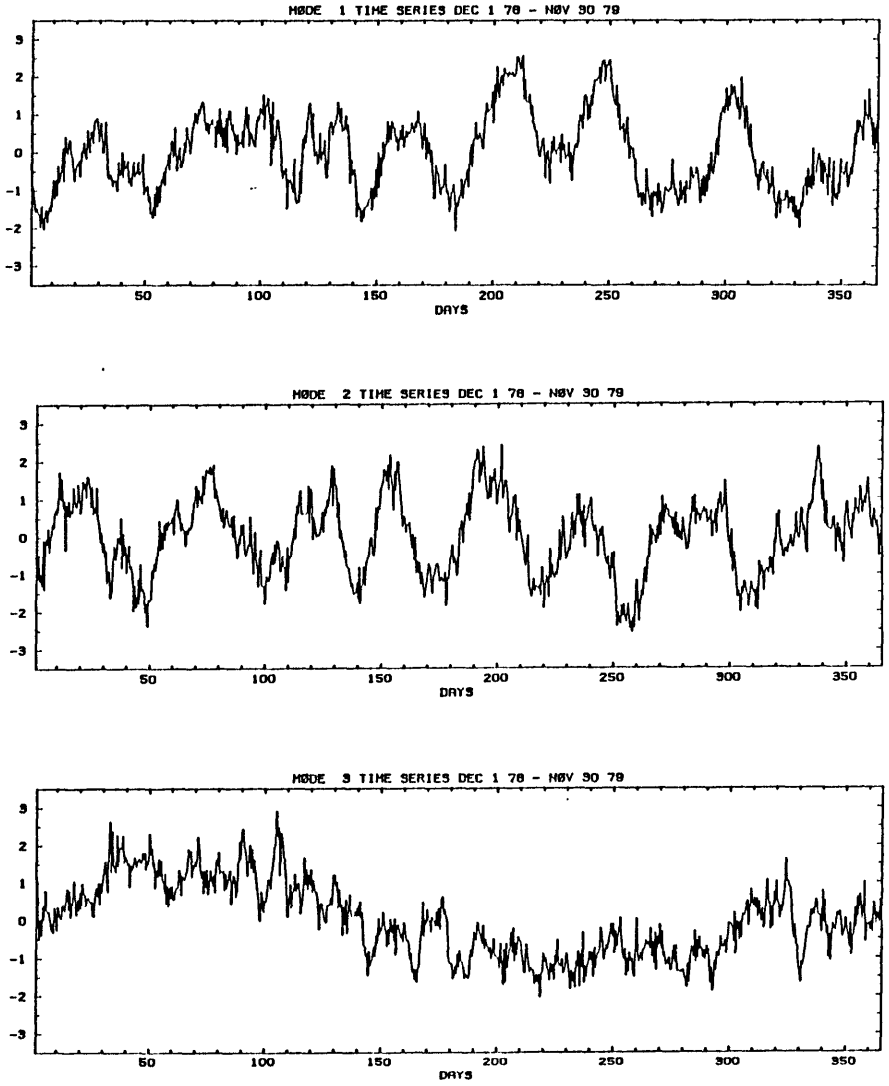

Fig. 4.27c Results of two-level empirical orthogonal analysis C820525W: combined 850 and 200 mb velocity potential 45°S-45°N, zonal wavenumbers 1-5. Normalized principal components, modes 1-5.

C820525W that the coupling between the upper and lower troposphere is in no way accidental. This evidence for a strong vertical coupling of the divergent circulation in the tropical atmosphere is entirely consistent with concepts of the structure of deep convection and its interaction with the synoptic scale. One might go further and suggest that the lack of vertical coupling in an analysis of this type would indicate that the variability in the divergent circulation is not due to latent heating. Clearly this is not the case.

5. Eastward Propagation of the 40-50 Day Anomalies and Relationship to Intraseasonal Variability of Highly Reflective Cloud

The changes in the divergent east-west circulation have characteristics of both standing and eastward propagating equatorially-symmetric waves. This chapter is a description of the morphology of the 40-50 day oscillation in terms of the eastward propagation of the velocity potential anomalies and the accompanying changes in divergence and divergent winds. We will also discuss parallel changes in tropical highly reflective clouds (HRC) which can indicate whether the disturbances in the divergent circulation are consistent with the increase or decrease of deep convection.

One method of characterizing the time dependence of a phenomenon is to form a time composite of the anomalies. As an averaged quantity, the utility of a composite depends upon the number and similarity of the separate events from which it is comprised. In this study, however, it seemed the number of 40-50 day "events" was small enough to consider each individually rather than present a "typical" behavior pattern. In this way we emphasize both the differences as well as the similarities from one cycle to another.

5.1 Changes of the Walker Circulation

As we have already seen, each of the EOF's in Chapter 4 contain pairs of modes that together describe an eastward moving anomaly pattern that recurs on a 40-50 day time scale. We will employ in this chapter reconstructions of anomalies from the modes containing the 40-50 day

variance. As the first few modes in each of the EOF's combine to account for major portions (>50%) of the variance in the total fields, the time dependent anomaly patterns associated with the 40-50 day phenomenon are also the dominant patterns overall. We will first focus on the time changes in the longitudinal profiles of velocity potential and the Walker circulation (by which we mean the divergent zonal wind fields at both 200 and 850 mb) that are associated with the 40-50 day velocity potential anomalies. This focus will emphasize the zonally asymmetric variance in the 850 and 200 mb velocity potential fields. Fig. 5.1 illustrates the separation of the first seven eigenvalues for each of the explicitly zonally asymmetric EOF analyses C201025W and C851025W.

We will present time sequences of longitudinal profiles which are similar to those of Figs. 4.5, 4.15 and 4.16, i.e. longitudinal profiles of meridionally averaged properties; here the profiles are latitude-band averages of the 9 grid latitudes from 15°S to 15°N. Two types of time dependent behavior are shown and can be distinguished by the details of the reconstruction process for the individual time dependent grid point values of velocity potential used as input to the meridional averages. In both cases, we have displayed reconstructed profiles sampled at a frequency of 11 days, approximately 1/4 of the 45-day period which is the center of the 40-50 day spectral band in the first and second principal components of C201025W and C851025W.

The first reconstruction method is based upon filtering of the principal components to explicitly highlight the 40-50 day anomalies. In this case the profiles are derived from fields reconstructed from the leading two eigenmodes from each of C201025W and C851025W; the time

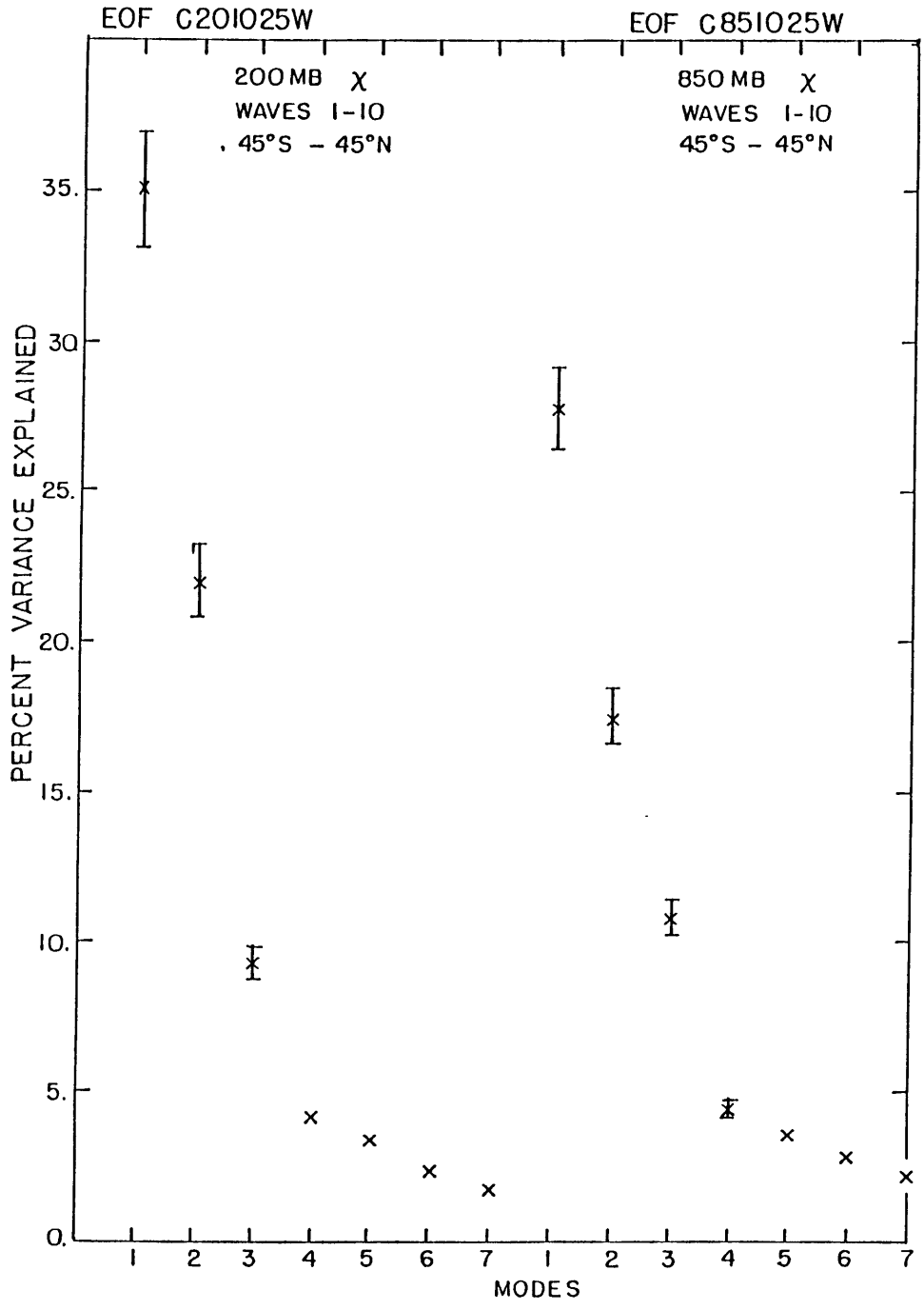

Fig. 5.1 As in Fig. 4.25 but for C201025W and C851025W and modes 1-7.

average profiles were not included. The principal components were previously time filtered with a finite impulse response (FIR) bandpass filter; the impulse and frequency responses of this filter are depicted in Figure 5.2. The impulse response length of the filter is 101 and for a Nyquist frequency f_N = 1/day, the frequency response is peaked at 40 days and falls off to 10% of original power at ~450 days and ~21 days. Variance in the sidelobes is attenuated over 97%.

Fig. 5.3 displays the first two principal components of the two EOF analyses C201025W and C851025W with their filtered versions superimposed upon the unfiltered series. The loss of 50 observations at each end of the time series limited this investigation to the time period from December 26 through November 5. From this time period we show profiles for the days December 28 through October 22.

Thus Figs. 5.4 and 5.6 present 40-50 day anomaly profiles which are reconstructed from the respective eigenvectors and filtered principal components for eigenmodes 1 and 2 of C201025W and C851025W respectively:

$$(5.1) \qquad \chi'^{R}_{i,j,k} = \sum_{m=1}^{2} \hat{Z}^{f}_{m,k} Y_{m,i,j}$$

where, using the bandpass filter H,

$$(5.2) \qquad \hat{Z}^{f}_{m,k} = \sum_{l=-50}^{50} H_l \hat{Z}_{m,k-l}$$

and $\chi^{R'}_{i,j,k}$ is a filtered anomaly of velocity potential at grid longitude and latitude (λ_i, ϕ_j) and time t_k, $\hat{Z}_{m,k}$ is the principal component of eigenmode m at time t_k and $Y_{m,i,j}$ is the grid point eigenvector at (λ_i, ϕ_j). The last is the transformation of the appropriate scaled semi-spectral eigenvector $\hat{Y}_m$ (see the EOF analysis

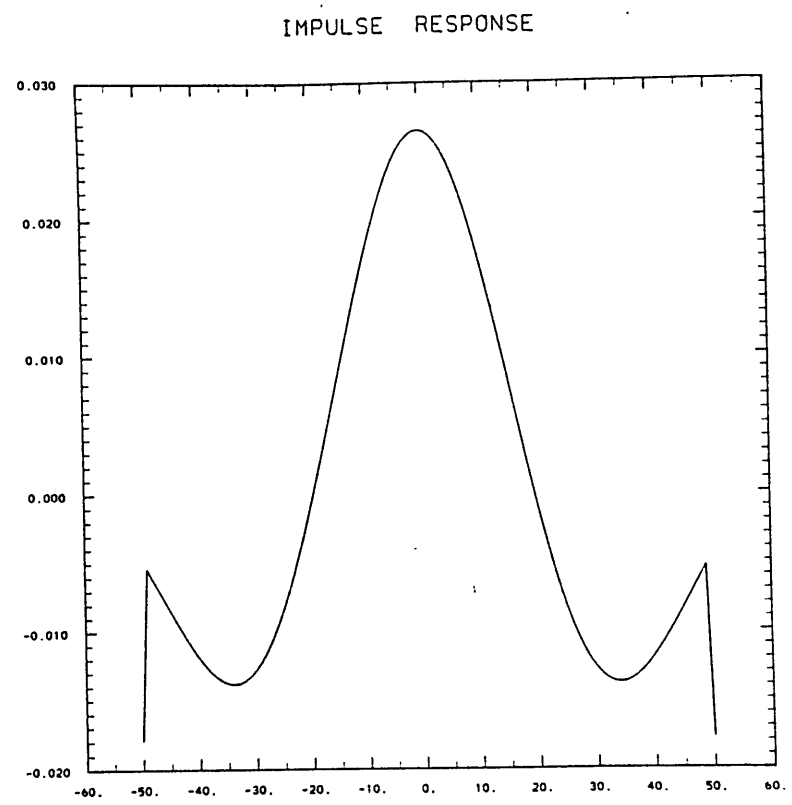

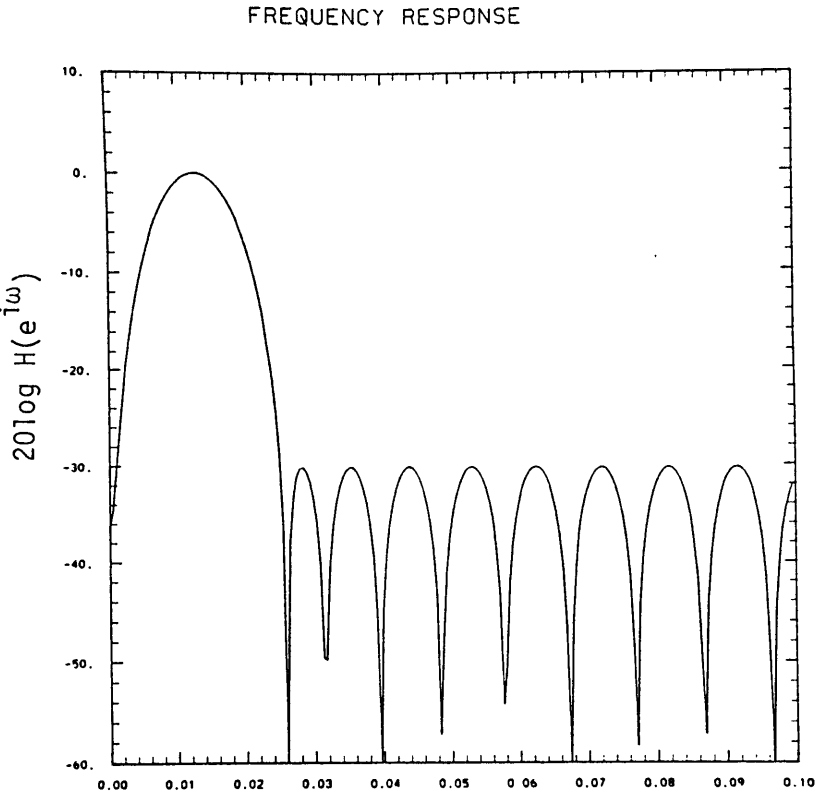

5.2 Impulse and frequency response for 40-50 day bandpass filter.

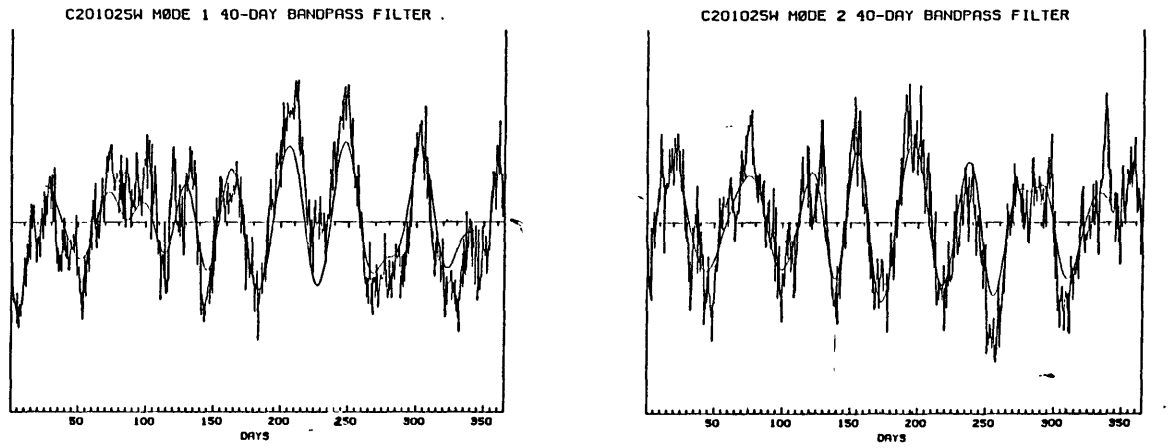

Fig. 5.3a Principal components of the first(left) and second eigenmodes from EOF analysis C201025W filtered with the bandpass filter of 5.2, superimposed upon their unfiltered versions. Filtered principal components are used in reconstruction of anomalies in Figures 5.4 and 5.6.

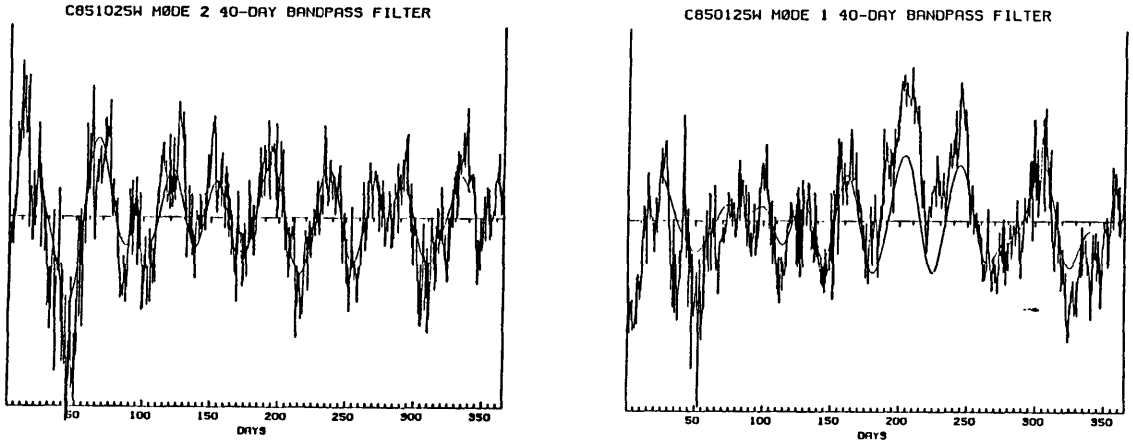

Fig. 5.3b As in 5.3a but for C851025W.

flow chart, Fig. 4.18) at i,j and time k. Modes 1 and 2 of C201025W most clearly show the 40-50 day power we are investigating.

It is worthwhile to discuss certain aspects of our filter choice. Several recent studies of the 40-50 day phenomenon during the FGGE year (e.g. Krishnamurti et al., 1985; Murakami and Nakazawa, 1985) have used recursive bandpass filters in an effort to reduce the data loss at the ends of the data. One problem with this approach is that these recursive filters introduce non-constant phase shifts into the filtered data (cf. Oppenheim and Schafer, 1975, Chapter 5) which may be a significant handicap on analysis. In contrast, FIR bandpass filters produce no phase shift in the passband. With the choice of an FIR filter then the basic impediment to reducing filter length is frequency resolution, which is set by the impulse response length. For a half-day sampling period, effectively the first resolved non-zero frequency is 0.5/N where N is the impulse response length. Thus to distinguish 50-day variance from zero frequency, it is necessary to have a filter of length 100 or more. As we did not want to sacrifice more than 100 observations, we sought the best possible filter with a length of 101 samples. This limitation on impulse response seriously constrained the stopband attenuation and transition bandwidth of filters produced by some of the more straightforward filter design techniques discussed in Oppenheim and Schafer (loc. cit.). We eventually derived a satisfactory digital filter using a Chebyshev filter design program (McClellan et al., 1979), though we found that the 40-day peak was the closest approach to 45 days for the set of filters we tried with impulse responses of 101 or less.

In the second method (Figs. 5.5 and 5.7), the seven leading modes and the time mean are used in the reconstruction of 'total' velocity potential fields from both C201025W and C851025W:

$$\chi^{R}_{i,j,k} = \bar{\chi}_{i,j} + \sum_{m=1}^{7} \hat{Z}_{m,k} Y_{m,i,j} \qquad (5.3)$$

where $\chi^{R}_{i,j,k}$ is the reconstruction of the total field of the 850 or 200 mb velocity potential. It will be seen that in this second reconstruction process the addition of the moderate amount of variance in the higher modes in no way obscures the phenomenon and underlines the dominant character of the 40-50 day phenomenon.

The smoothness of the profiles reconstructed from the unfiltered EOF's in Figs. 5.5 and 5.7 results from (1) the truncation of the variance to zonal wavenumbers 10 and lower in the EOF analyses and (2) the restriction to the lowest eigenmodes within this zonally smoothed variance space which tend to emphasize the largest scale features. These considerations might argue against the EOF reconstruction approach if there were evidence of coherent 40-50 day oscillations on much more restricted space scales. In that case, use of rotated eigenvectors (Horel, 1981) or some more sophisticated technique might be indicated. Here however it is clear that there is a very large-scale coherent pattern that completely dominates the variance both in space and in time, and we feel it is unlikely that more sophisticated techniques would reveal different characteristics.

We turn now to Figure 5.4 which contains an 11-day sampled set of filtered anomaly profiles of velocity potential. These anomalies have characteristics both of eastward propagation and of a standing oscillation: there is a tendency, particularly at 200 mb, for the

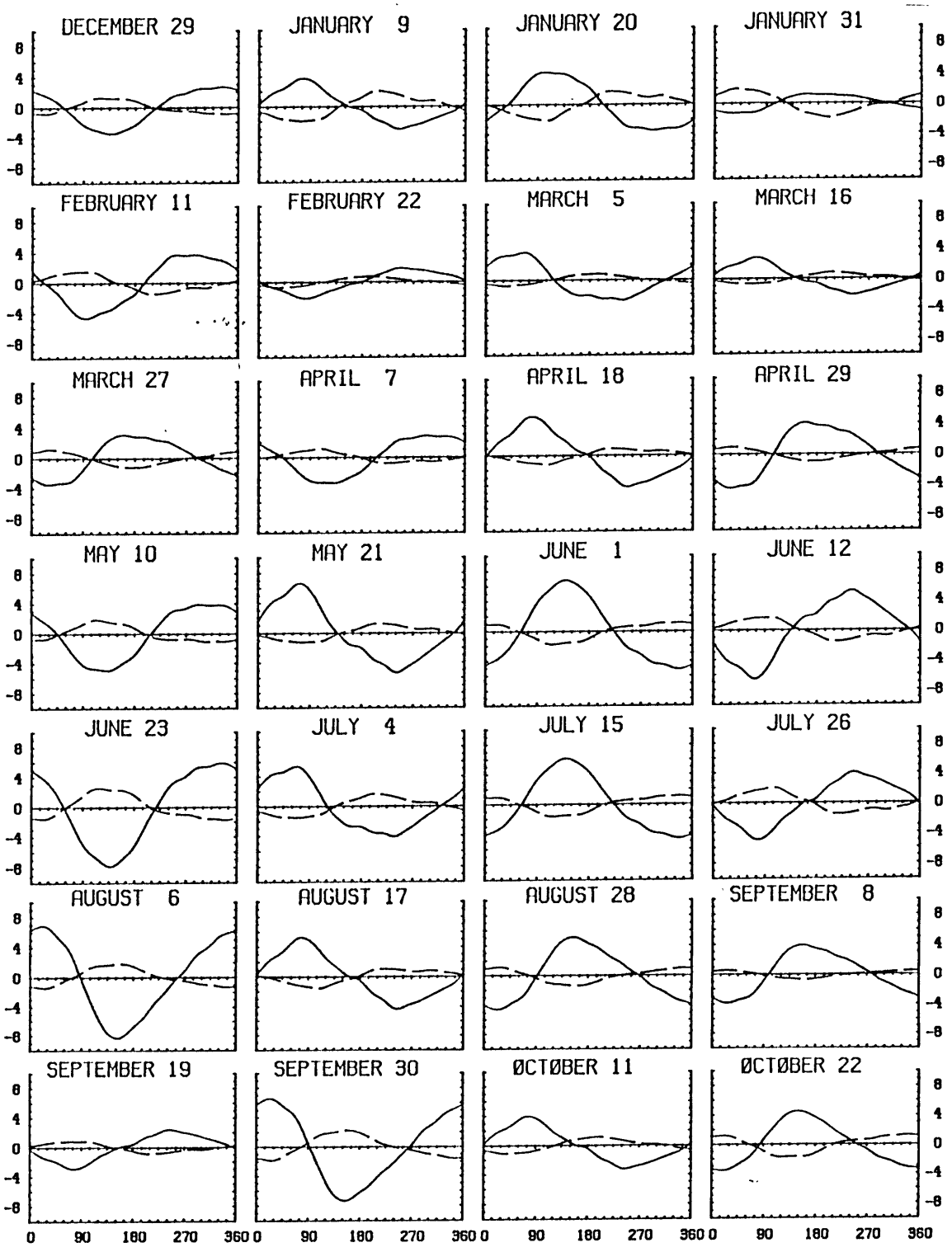

Fig. 5.4 Time lapse sequence of longitudinal profiles of velocity potential anomalies, reconstructed from modes 1 and 2 of C201025W and C851025W, filtered at 40 days and averaged across the latitudes 15°S-15°N. Sampling every 11 days. 200 mb profiles solid lines; 850 mb broken.

anomalies to be enhanced in the second quadrant (90°E-180°). This is in part due to the less-than-perfect quadrature in the eigenvector pairs used in the reconstructions. At each level, the first mode has wave one amplitude somewhat larger than the second; in C201025W the equatorial wave one amplitude of eigenvector 1 exceeds that of eigenvector 2 by more than 10%. This enhancement of the anomalies in the eastern Indian Ocean and maritime continent/western Pacific region is consistent with the results of Weickmann (1983), Murakami and Nakazawa (1985) and Lau and Chan (1985). When we consider the HRC data later on in this chapter this will be considered again.

The eastward propagation however is the most striking characteristic of these filtered anomaly profiles. It might be argued that this is an artifact of the regularity of the anomalies imposed by the relatively narrow bandwidth($\Delta\omega$=.1527 or Δf=1/20.5 $days^{-1}$) of the filter used here. However if one considers the obvious strength of the 40-50 day oscillation in the separate modes, it is apparent that we are not eliminating any important signal; rather the filter is cleaning the short time scale noise off of the much slower undulations in the time series.

Five very similar 45 day oscillations appear in Figure 5.4. In the context of the frames we present here, the first spans the period December 29 - February 11. Beginning at the end of April and continuing through most of August there are three successive oscillations and finally one beginning in mid-September and ending late in October. During the remainder of the year the cycles tend to be delayed; for example, it appears that during the period between February 11 and March 16, the anomalies are oscillating in place rather than undergoing an

eastward propagation. It may be significant that the clear and regular propagation is interrupted during the time at which the global minimum of the velocity potential is either straddling the equator or lingering closely nearby (see Figure 4.22); the orientation of the primary Hadley overturning also changes at this time. Clearly the Northern Hemisphere monsoon season which follows upon this stretch of time exhibits three very regular cycles which are also nearly equal in amplitude. The same might be said for the slowing down of the propagation in the last week of August and early September, the period of time when the velocity potential minimum was passing southward back across the equator, rather more quickly this season than in the spring.

To understand their effect on the total field velocity potential, we need to mix the 40-50 day anomalies with a remainder of the important variance in an unfiltered manner and add them to the mean field. This was carried out in the reconstruction for the profiles of velocity potential in Figure 5.5. The choice of using 7 modes in the reconstruction was somewhat arbitrary, but the reconstructed anomalies are not greatly sensitive to choice of cutoff mode provided the first three are included. In the case of C201025W, the first seven modes explain 77.8% of the variance; for C851025W they explain 69.8%.

In Figure 5.4 the degrees of freedom are restricted by the summation over only two modes and the filtering operations performed on the principal components. Thus the profiles in the 11-day span between frames are more or less smooth transitions between the profiles that are shown. The same is not true in Figure 5.5. Here we have placed no constraints on the profiles other than an exclusion of a certain amount of 'noise' variance at short time and space scales. We feel that this

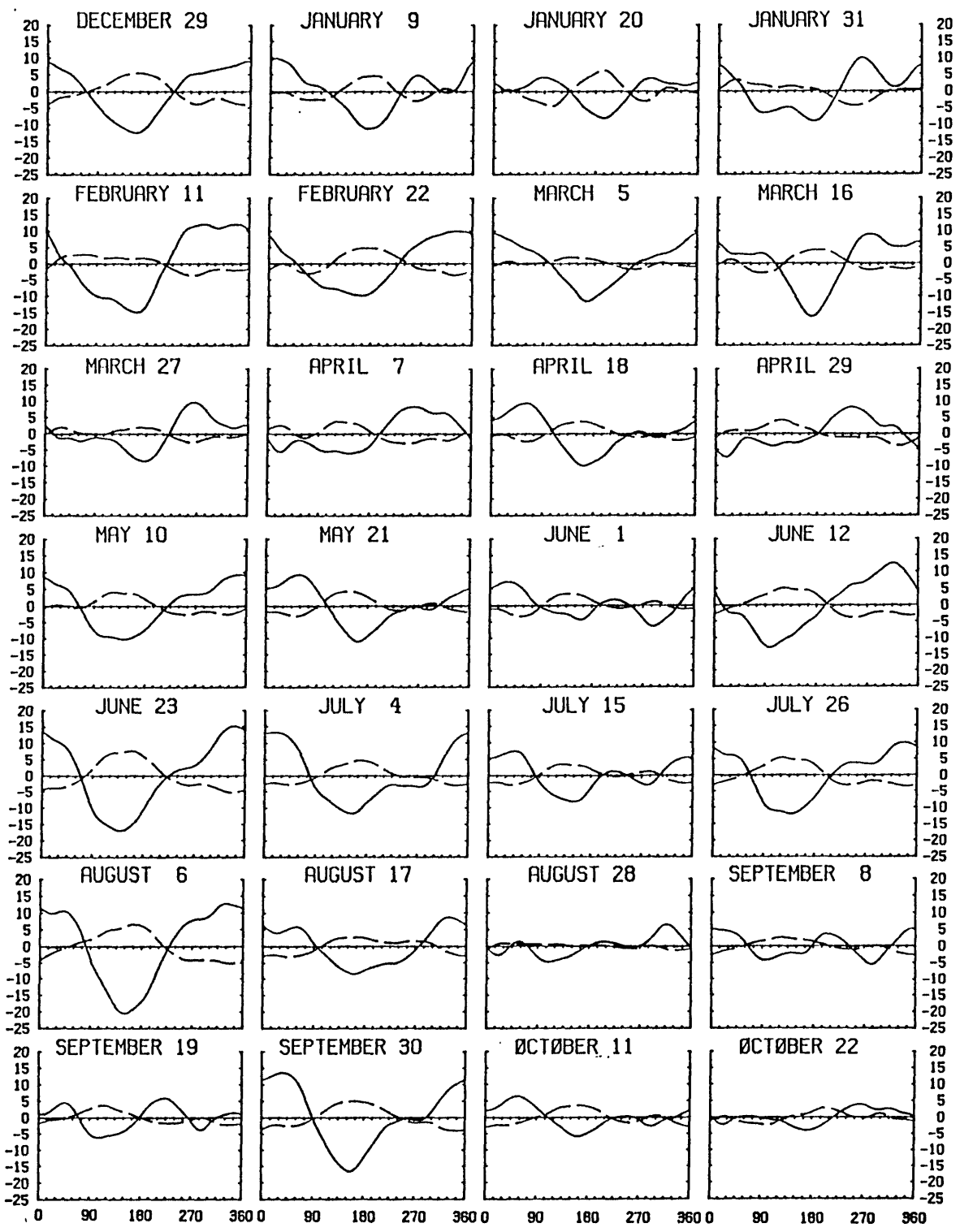

Fig. 5.5 Time lapse sequence of longitudinal profiles of total velocity potential (anomalies plus mean), reconstructed from modes 1-7 of C201025W and C851025W and averaged as in Figure 5.4. These profiles are not time filtered.

allows a less biased objective assessment of the 40-50 day signal's effect upon the total circulation than would be the case if the entire set of data were time filtered. Thus the profiles depicted Figure 5.5 should be considered as fairly independent 'snapshots' of the actual sequence of day-to-day variability.

If we compare Figs. 5.4 and 5.5 frame by frame, we can see that as the eastward propagating anomalies come into phase with the mean field near the longitudes of Australia. The effect is first the development of a westward 'shoulder' on the velocity potential minimum, followed by a deepening of the minimum itself and then a stretching of the negative region across the Pacific and at times all the way to South America.

We can assess the amplitude of the 40-50 day changes in the Walker circulation in Fig. 5.6 which displays profiles of filtered anomalies of the Walker circulation derived from the fields used to create Fig. 5.4. The divergent zonal winds at each grid point were derived from the field of reconstructed velocity potential using Eq. 4.1. The enhancement of the higher wave numbers in the EOF reconstruction is immediately apparent in the generally higher degree of waviness in the profiles. Nonetheless large-scale changes of the divergent zonal wind field at both levels are clearly visible. At 200 mb during the winter season these are on the order of 1.0 m/s. During the summer the magnitudes of the anomalies average somewhat greater, and in several frames they approach 2.0 m/s. It also appears that the largest magnitude anomalies appear in the Indian Ocean region in the quadrant west of 150°E.

Fig. 5.7 displays 'snapshots' of the Walker circulation throughout the sampled period. The reconstructed velocity potential fields used to

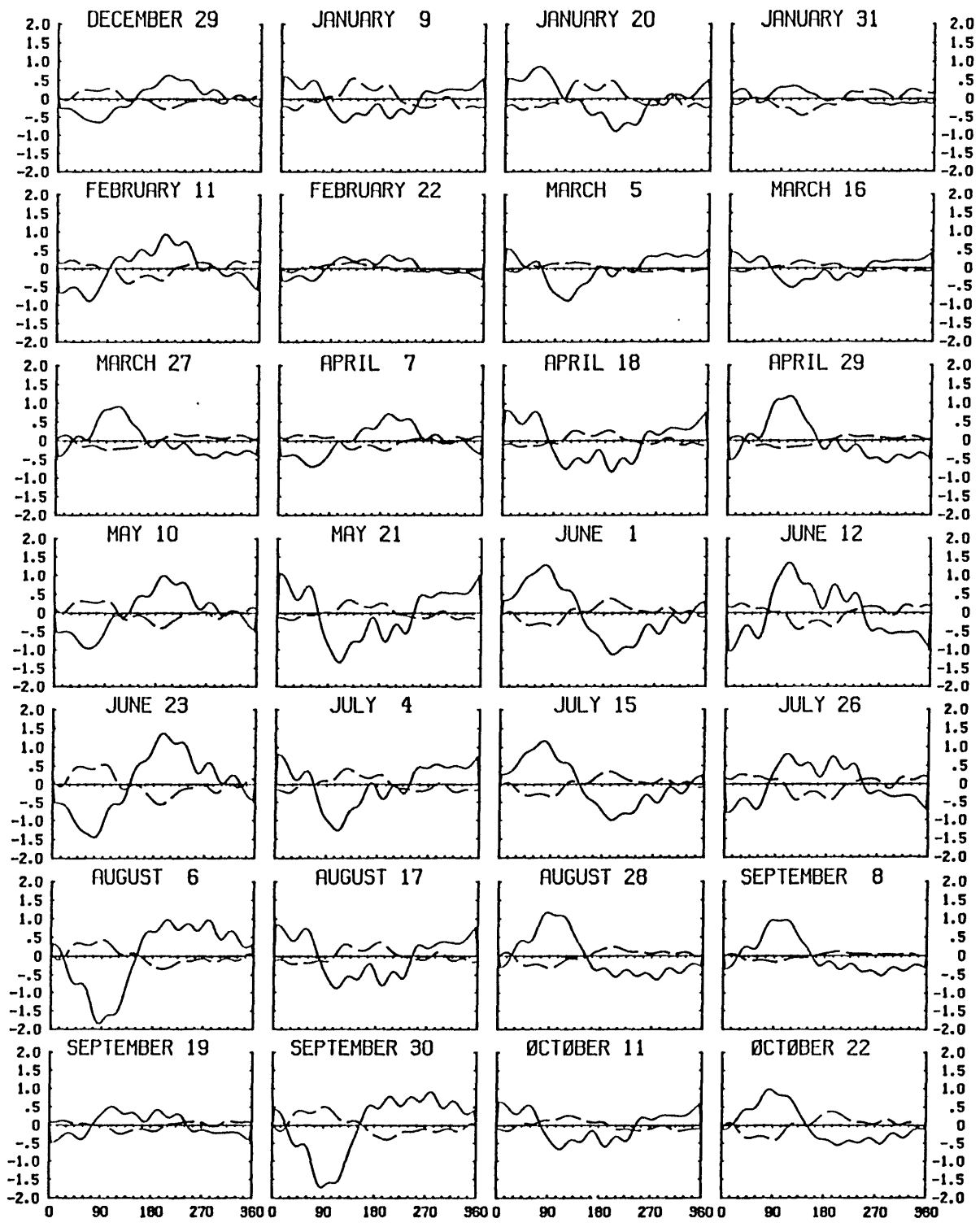

Fig. 5.6 As in 5.4 but for Walker circulation (divergent zonal winds) anomalies. Winds are derived from reconstructed velocity potential anomalies in 5.4.

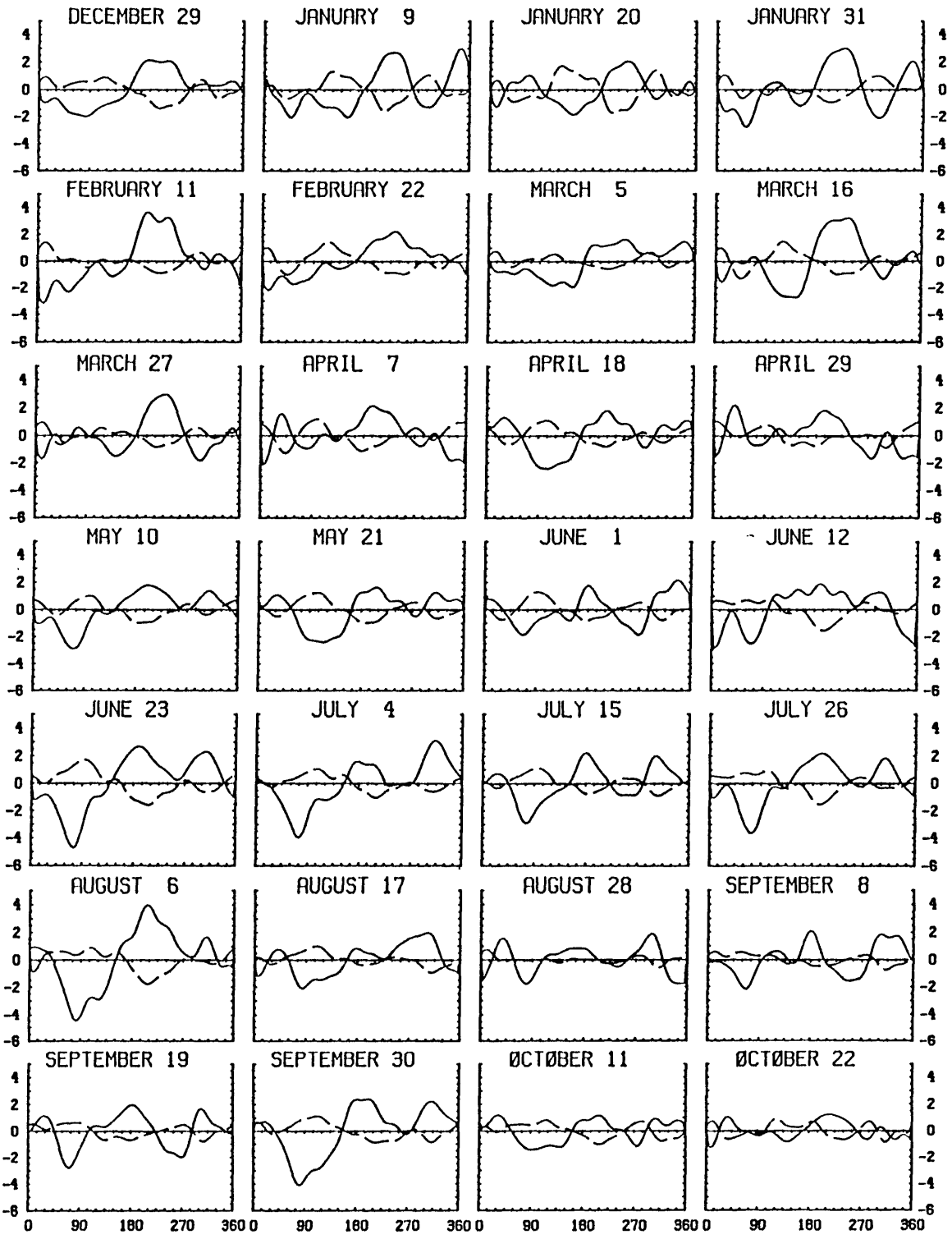

Fig. 5.7 As in 5.5 but for total Walker circulation. Winds derived from total velocity potential in 5.5.

generate the divergent zonal winds here are the same used for its counterpart, Fig. 5.5. As in the latter figure, we do not necessarily see an eastward propagation of the mean Walker cells. Since the amplitude of the divergent zonal wind at any one point is sensitive to the steepness of the velocity potential zonal gradient, it is not surprising to see a degree of independence in the intensity of the zonal overturning from cell to cell across the band. It is clear however, if we compare this figure with Fig. 5.4, that if the velocity potential anomaly is out of phase with respect to its mean field, as it is in the June 1, July 15 and August 28 frames, the Indian and Pacific Ocean pair of Walker cells is depressed. The reverse is also true. It is harder to account for the behavior of the South American Walker cell, as it appears to change its amplitude more on a seasonal basis, with the strongest divergent winds at 200 mb in the months of January and May through September. If we consult once again Fig. 4.22, we see that during the weak period for the South American cell from February through April, the cross-equatorial Hadley component over the region is the strongest of the year. We also observe drifts in the longitudinal locations of the maximum divergent westerlies in each of the South American, Indian Ocean and Pacific Ocean cells.

An alternative way to observe the eastward propagation seen in Figs. 5.4-5.7 is contained in Fig. 5.8. Here we have reconstructed one-year time series of the 200 mb divergent zonal wind field at intervals of 60° longitude along the equator. As indicated in the figure caption, the divergent winds were derived from instantaneous equatorial velocity potential profiles reconstructed from the first five EOF's and the mean of C201025 in the same manner as the figures earlier in this chapter;

the exception is that these are single grid point time series and are not averaged in the north-south direction at all. To aid in the tracing of the anomalies we have drawn dotted lines on the figure connecting the modes of the 40-50 day anomalies. The lower case letters will be used to identify the particular 40-50 day cycles evident in Fig. 5.8. The phase speeds and longitudes spanned by the propagating Walker anomalies are listed in Table 5.1.

Although there is a certain amount of noise in these unfiltered time series, the 40-50 day divergent wind anomalies can be clearly traced eastward. The propagation is not steady however. The anomalies traverse fairly quickly the longitudes 0° - 60°E and 180° - 120°W. For example between roughly day 240 and 248 a positive anomaly crosses the central Pacific, which is approximately a speed of 10 m/s. In the longitude sector from eastern Indian Ocean to the dateline, however, the propagation speed is closer to 5 m/s. Murakami et al. (1984) obtained phase speeds for total wind anomalies at 200 mb during the northern summer of the FGGE year closer to 6 m/s. In the final section of this chapter we will make further comparisons between our results and other studies.

Along with this variation in longitude of the phase propagation speed, we note that the propagation appears more regular in the middle months of the year. Anomalies at this time seem to progress farther eastward, including one example (cycle e) in which a positive divergent wind anomaly passes through 60°W and links up with the next cycle.

The properties of individual cycles are summarized in Table 5.1. Average phase speeds in Table 5.1 for the divergent zonal wind anomalies range from 6 m/s to 17 m/s and have peak amplitudes of about 3 m/s at

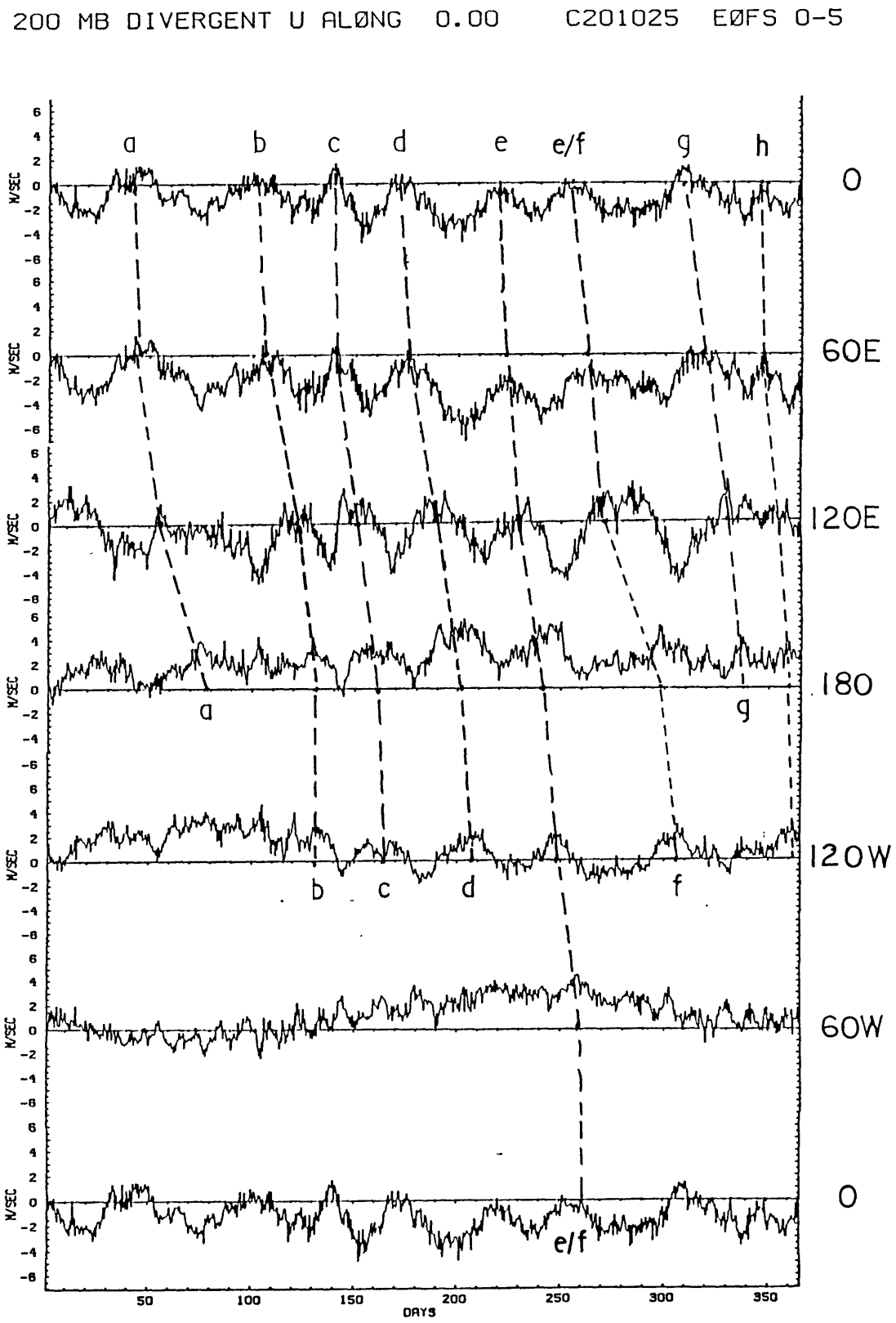

Fig. 5.8 FGGE year (12/1/78 - 11/30/79) time series of 200 mb divergent zonal winds at the equator reconstructed from modes 1-5 of C201025 added to the mean at 6 longitudes: (from top) 0°, 60°E, 120°E, 180°, 120°, 60°W and 0° (repeated). In m/s.

Table 5.1 Duration, Longitudinal Span Traversed and Phase Speeds for Divergent Wind Anomalies at 200 mb

-- Underlines indicate continuation of previous cycle --

a) Divergent U at Equator (Fig. 5.8)

	Longitudes Traversed	FGGE Dates	No.	Days	Speed (m/s)
a	0° - 180°	1/9 - 2/18		40	6
b	0° - 120°W	3/10 - 4/9		30	10
c	0° - 120°W	4/19 - 5/13		24	13
d	0° - 120°W	5/19 - 6/26		38	8
e	0° - 0°	7/8 - 8/12		35	17
f	0° - 120°W	8/17 - 10/2		46	7
g	0° - 180°	10/4 - 11/3		30	8
h	0° - 120°W	11/13 - 11/27		15	20

b) Divergent V at 15°N (Fig. 5.9)

A	0° - 180°	5/3 - 5/21		18	12
B	0° - 0°	6/11 - 7/24		43	15
C	0° - 120°W	7/24 - 8/17		24	12
D	0° - 180°	9/6 - 10/6		30	8

c) Divergent V at 15°S (Fig. 5.10)

1	120°W - 120°E	12/3 - 12/13		10	31
2	120°W - 120°E	1/19 - 2/10		22	14
3	60°W - 60°W	3/20 - 4/23		34	13
4	60°W - 180°	4/23 - 5/15		22	14
5	180° - 180°	5/31 - 7/14		44	10
6	180° - 180°	7/14 - 8/17		34	13
7	180° - 60°E	8/17 - 9/30		44	7
8	60°W - 120°E	10/12 - 11/4		23	10

120°E. There is little if any evidence of 40-50 day variability in the divergent wind field at 60°W.

5.2 Eastward Propagation of Meridional Overturning Anomalies

So far we have paid closest attention to the effects of the eastward moving velocity potential 40-50 day anomaly on the zonal divergent winds in the equatorial latitudes. We have referred to this phenomenon as a modulation of the Walker circulation. It is quite clear from Fig. 4.20d however that the changes in the divergent circulation associated with the leading modes in the EOF analysis of the velocity potential are not confined to the Walker circulation; significant local modifications of the divergent meridional wind take place as well. The simple, equatorially symmetric structure of the 40-50 day "propagating" mode pairs (modes 2 and 3 of C201025 and 1 and 2 of C201025W) puts the modes' strongest contributions to the divergent meridional wind anomaly not only poleward of, but also midway between the easterly and westerly enhancements of the Walker circulation as well. In other words, the eastward-moving modulation of the Walker circulation is accompanied by local modification of the meridional overturning. In the regions of significant divergent meridional flow, i.e. over the longitudes spanned by the maritime continent, South America and Africa, the 40-50 day oscillation alternately enhances and suppresses the local contributions to the Hadley circulation. In this section we examine the variability in these local divergent meridional winds.

We examine the changes in the local fields of divergent meridional wind by the same anomaly reconstruction procedure used to produce Fig.

5.8. In other words, at selected longitudes along a latitude circle at 200 mb, time series of total velocity potential (i.e. mean plus anomaly) were reconstructed from the first five modes of the C201025 EOF analysis using Eq. 5.4. The divergent meridional winds were then calculated using Eq. 4.2.

The results of this calculation for the "local" v^d at 15°S and 15°N are contained in Figs. 5.9 and 5.10 respectively. As in Fig. 5.8 we display time series at 0°, 60°E, 120°E, 180°, 120°W and 60°W which permits an assessment of the eastward propagation, if any, of divergent meridional flows. In some respects, the time series of subtropical divergent meridional winds in Fig. 5.9 viewed together produce an effect quite similar to Fig. 5.8 which depicts eastward progression of divergent zonal wind anomalies at the equator. Closer inspection reveals important differences, however, both between these two figures as well as between the two hemispheres themselves. As in Figure 5.8 we have drawn dotted lines to connect the prominent peaks in the neighboring time series. In Fig. 5.9 the capital letters refer to the cycles in Table 5.1 while numbers are used in Fig. 5.10.

In the Northern Hemisphere 40-50 day oscillations on the order of 1-2 m/s are visible at all the displayed longitudes west of 120°W; phase speeds range from 8 to 15 m/s. There is a hint of 40-50 variability at 60°W during the northern summer season. In fact, in all the time series at this latitude, the oscillation is more clearly defined after ~day 140, which is in sharp contrast to the Walker cell anomalies (at the equator) which showed the oscillation throughout the year. The phase propagation in the meridional winds is also not so regular as in the Walker anomalies. The time series at 0° and 60°E are nearly in phase,

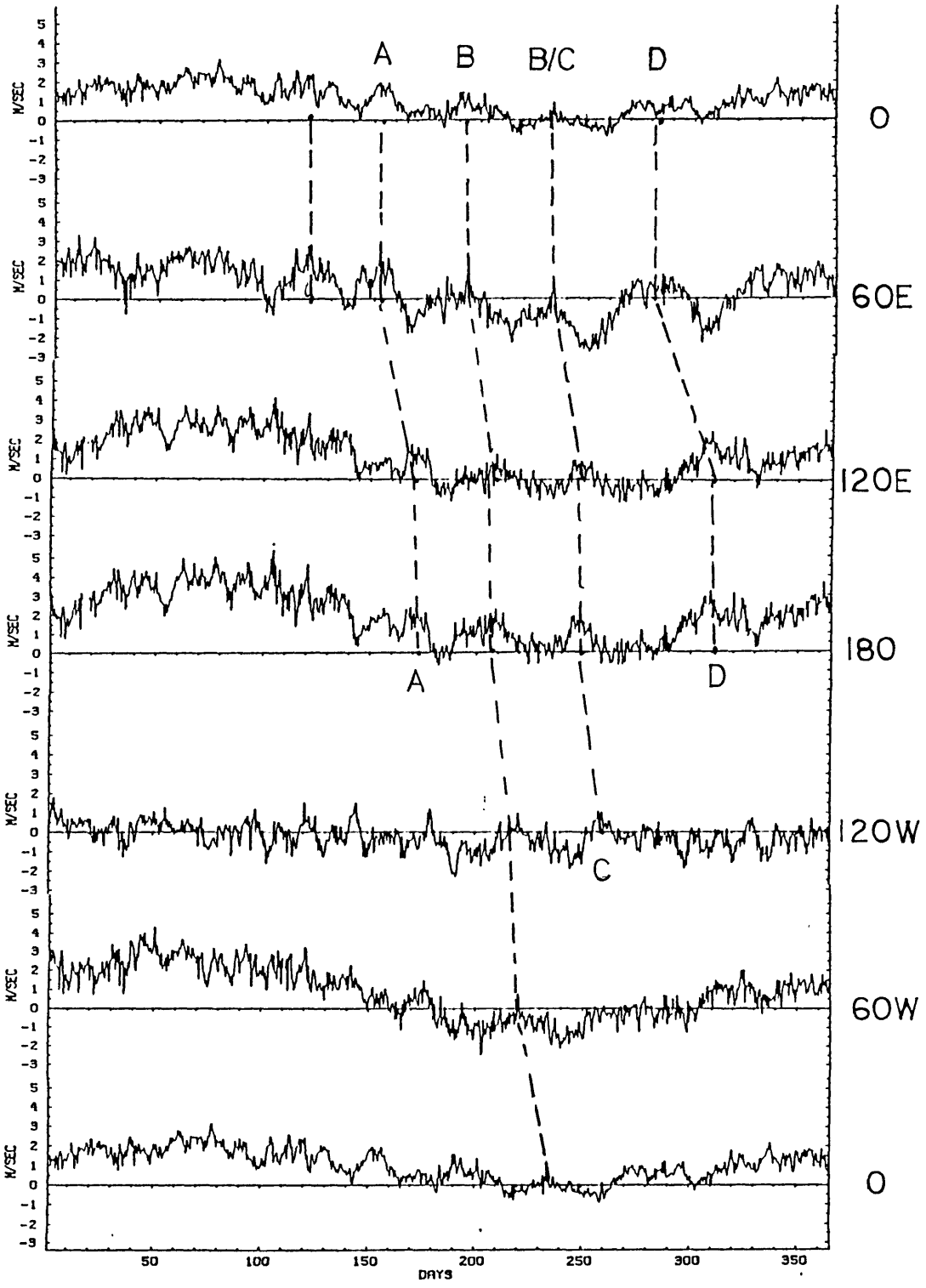

Fig. 5.9 As in Fig. 5.8 but for divergent meridional winds along 15° N.

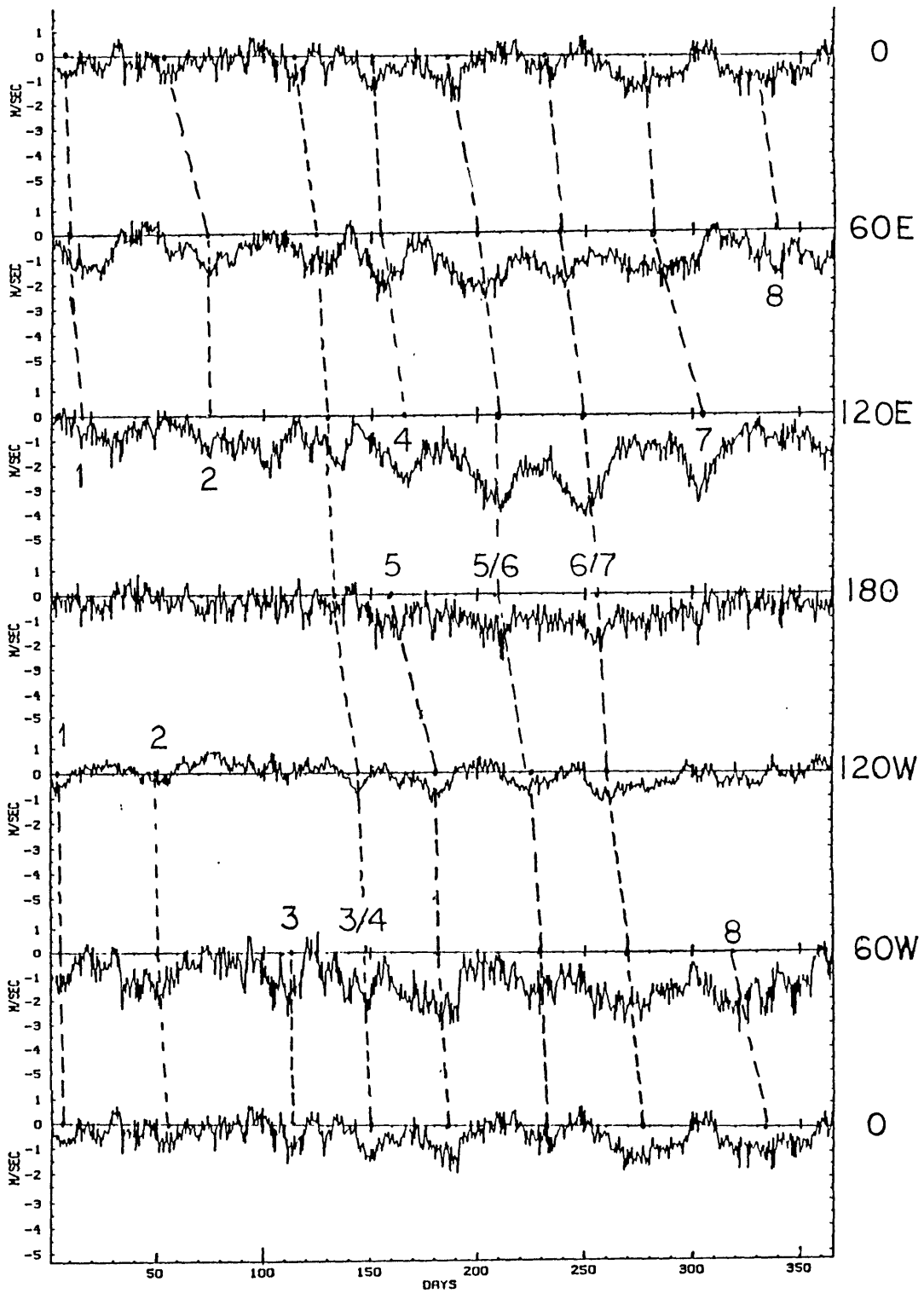

Fig. 5.10 As in Fig. 5.9 but for 15°S.

as are those at 120°E and 180°. However there is a phase jump of nearly 1/4 of a cycle between 60°E and 120°E.

South of the equator, phase speeds range from 7 to 14 m/s. (Anomalies in cycle (1) which has a speed of 31 m/s cycle were fairly weak.) Amplitudes of the divergent wind anomalies are comparatively large at certain longitudes. For example, in August at 120°E the flow changes from ~-3.5 m/s to ~1.5 m/s in the space of 15 days. On the other hand, the oscillation is noticeably weaker at the dateline in the Southern Hemisphere than in the Northern Hemisphere, although in sum it appears that the oscillation is present nearly throughout the year at all other longitudes. In particular, it is quite prominent at 60°W, i.e. over South America and seems to begin near 120°W in many instances. Since the oscillation is so weak at the dateline, it is difficult to trace a continuity of phase eastward across the Pacific and into the South American region. In the northern summer the propagation seems to be continuous around the world, whereas in southern winter the oscillation may well be originating over South America and the eastern Pacific, in striking contrast to the anomalies shown in Figs. 5.8 and 5.9. It should be stressed that this characteristic may be the result of the filtering operation implicit in the use of the EOF reconstruction, so such a conclusion must be considered rather tentative.

If one compares 5.9 with 5.10 it is evident that the 40-50 day anomalies at 15°N and 15°S are out of phase, i.e. poleward anomalies in their respective hemispheres are <u>in phase</u> with each other. The symmetry is by no means perfect, but there is no strong indication that one hemisphere leads the other. In addition, as the amplitudes are roughly the same, this is evidence for the equatorial symmetry of not only the

velocity potential anomalies but also the large-scale divergence anomalies. Where the relationship seems to break down somewhat is over the South American band of longitudes where as we have noted, 40-50 day anomalies are present in the Southern Hemisphere but mostly absent in the Northern Hemisphere. The converse is true at 180° where 40-50 day anomalies are absent in the Southern Hemisphere.

Interesting comparisons can be made between Figs. 5.9 and 5.10 and the divergent zonal wind anomalies along the equator from Fig. 5.8. Westerly Walker anomalies in the Eastern Hemisphere seem to lead the poleward meridional wind anomalies by ~60° of longitude. For example, the time series of u^d at 120°E can be superposed rather well on the time series of v^d at 15°N and 60°E. This counter-clockwise rotation in the divergent wind over a span of 60° is consistent with the spatial patterns defined by the two leading velocity potential in which the maxima and minima are separated by roughly 120° of longitude. As remarked upon just above, this quadrature relationship does not hold up over the entire tropical belt however. Over South America, the 40-50 day Walker anomalies are weak, whereas there is a distinctive modulation of the Southern Hemisphere meridional divergent flow. This pattern would require there to be rather more zonally-elongated anomalies in the velocity potential field over this region.

5.3 Eastward Propagation of Intraseasonal Highly Reflective Cloud Anomalies

We obtained in Chapter 4 (Fig. 4.5) an excellent correspondence between the equatorial zonal profiles of the FGGE time mean HRC and the mean upper level divergence; we argued there that this agreement connects the upper level divergence in the ECMWF analysis unequivocally with deep convection. Here we ask whether this relationship is present on the intraseasonal time scale which we have seen dominates the divergent circulation. We examine intraseasonal behavior of the highly reflective cloud, in both unfiltered as well as bandpassed form, in sets of time series across the tropical band. The presentation is similar to that of Figs. 5.8-5.10, and many of the features observed in the divergent zonal and meridional wind time series are apparent also in the highly reflective cloud index.

The time series of HRC we have used here are spatial averages over a region 30° wide in longitude and with varying widths in the meridional direction. This reduces the considerable noise inherent in the HRC data to an acceptable level; at the same time this longitudinal interval for averaging does not obscure the eastward propagation of the long waves in which we are primarily interested. Thus we have formed time series of HRC at intervals of 30° longitude at the 12 longitudes starting from the prime meridian.

To examine the longitudinal asymmetry of the HRC across the tropics we created time series centered at each of the 12 longitudes and summed over the entire set of thirteen latitudes in our interpolated HRC data grid. Unfiltered versions of these time series are shown in Fig. 5.11

which consists of two parts: (a) the eastern longitudes 0° - 180° and (b) the western, from 180° back to the prime meridian inclusive. In the interests of space we have skipped every other time series in the band; nonetheless, the essential character of the longitudinal asymmetry is quite clear. The width of this latitude band is 48.65° so if every $1^{\circ} \times 1^{\circ}$ square contained highly reflective cloud the HRC value would be 1459.5. This is a rather wide band of latitudes with respect to the time average vertical motion since it encompasses a considerable amount of sinking as well as upward motion. We employ it here to avoid any arbitrary omission of variance, although the results would not be dissimilar if only the central 9 latitudes were used (15°S - 15°N). Typical HRC values for the $30^{\circ} \times 48.65^{\circ}$ regions are 25-75 with maxima reaching to nearly 300. This latter value represents almost 20% coverage of a region by deep convective cloudiness.

Even considering the spatial averaging we have performed in obtaining the 30° longitudinal band averages, there is a high degree of variability in the time series. Much of this is probably quite real as the basic $1^{\circ} \times 1^{\circ}$ grid of the highly reflective cloud allows individual convective events to show up in the data. In this respect, we can identify the spatial average quantities here as an integration of the convective scale heating within the respective regions.

At first glance, the HRC time series in Fig. 5.11 appear to have little consistent pattern beyond somewhat irregular bloomings of convection. At 60°W there is in fact a strong semi-annual oscillation in the time series. Closer inspection however indicates that it might be worthwhile filtering the time series to remove the higher frequency power and highlight the 40-50 day variance.

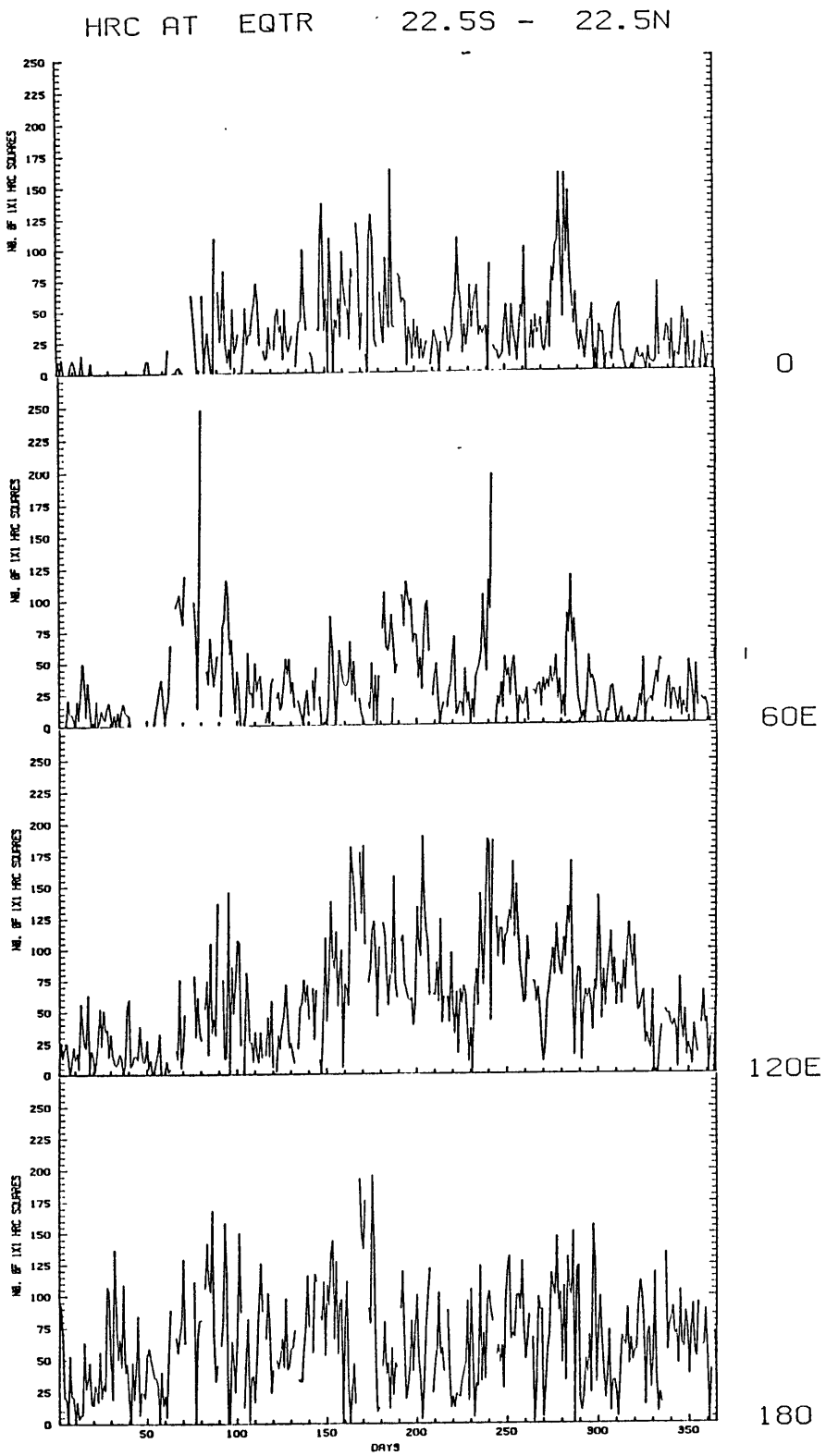

Fig. 5.11a Time series of total HRC in equatorially-centered regions 30 degrees wide in longitude and covering the latitudes 22.5°S - 22.5°N; 4 longitudes at intervals of 60° from 0° eastward to 180°. Units: number of 1° x 1° grid squares covered by highly reflective cloud.

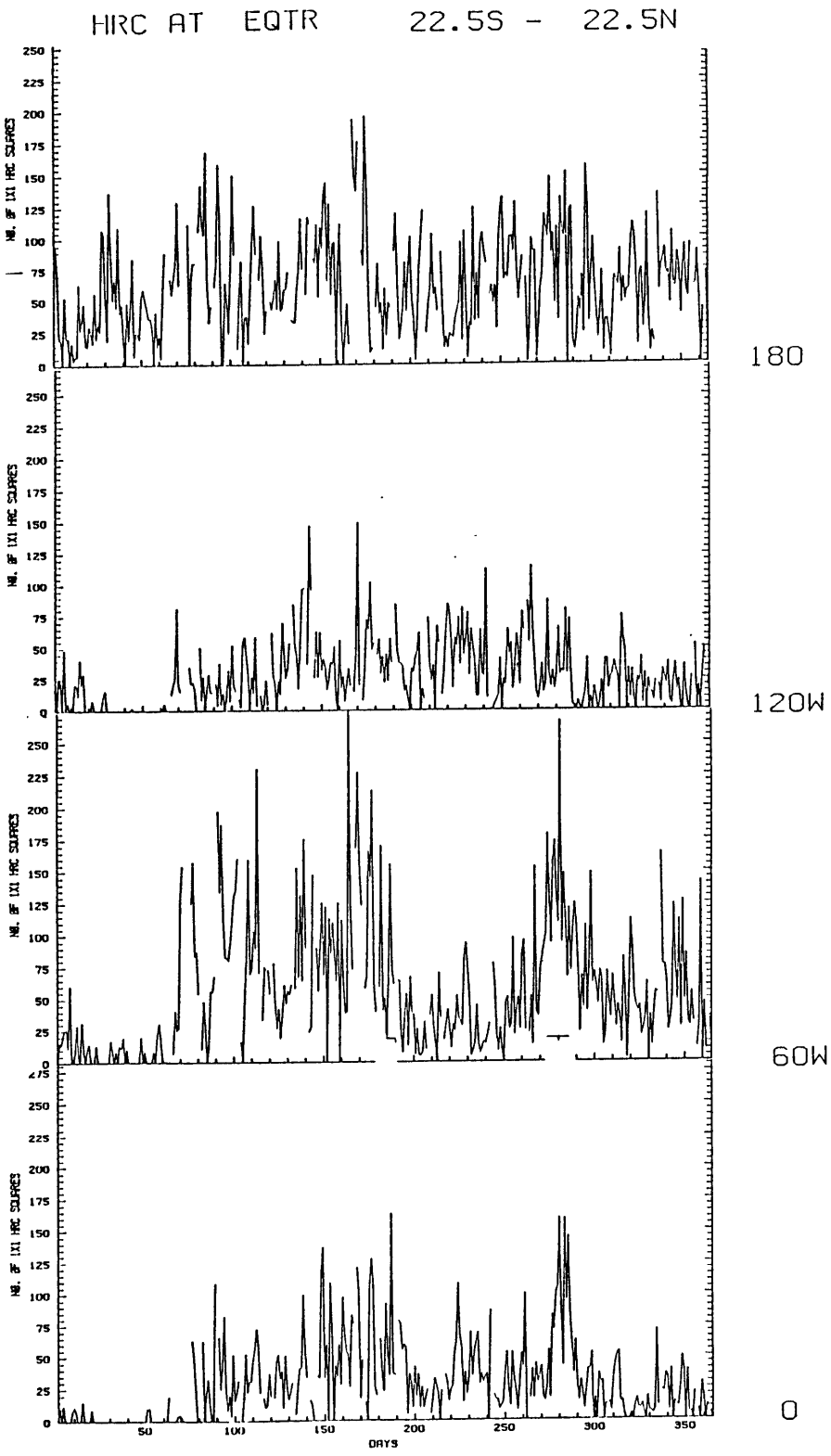

Fig. 5.11b As in (a) but for the western hemisphere 180° - 0°.

Since the HRC data are only available at one-day intervals, the filter used for the twice-daily velocity potential data would not be appropriate. Thus for the HRC data we instead obtained a bandpass filter with an impulse response length of 75 centered at approximately 44 days. The impulse and frequency responses for this filter are displayed in Fig. 5.12.

The results of the filtering appear in two parts in Fig. 5.13. This has the same format as Fig. 5.11 with the exception that the intervening longitudes 30°E, 90°E, etc. have been included. The filtering operation was not totally satisfactory as some high frequency noise appears. However this does not obscure the 40-50 day power and will not affect the conclusions we draw here.

Before discussing the relationship between propagating anomalies in the divergent wind field, we consider the gross relationship between the variability in the divergent circulation and highly reflective cloud. We saw in Chapter 4 that the local minima over the West Pacific and South America in the time mean 200 mb velocity potential (Fig. 4.3) are also local maxima of HRC (Fig. 4.6). The longitudinal profiles of velocity potential and divergence (Fig. 4.5) and HRC (Fig. 4.6) also support the conclusion that negative extrema of velocity potential indicate large-scale upper level divergence due to cumulus convection. Following this pattern, maxima in the principal components of the 40-50 day dominated 200 mb eigenmodes should be closely associated with peaks in the time series of HRC for the regions centered around the respective minima in the velocity potential eigenvectors.

To address this question we have assembled Table 5.2. It compares the times of occurrence (in days since December 1, 1978) of successive

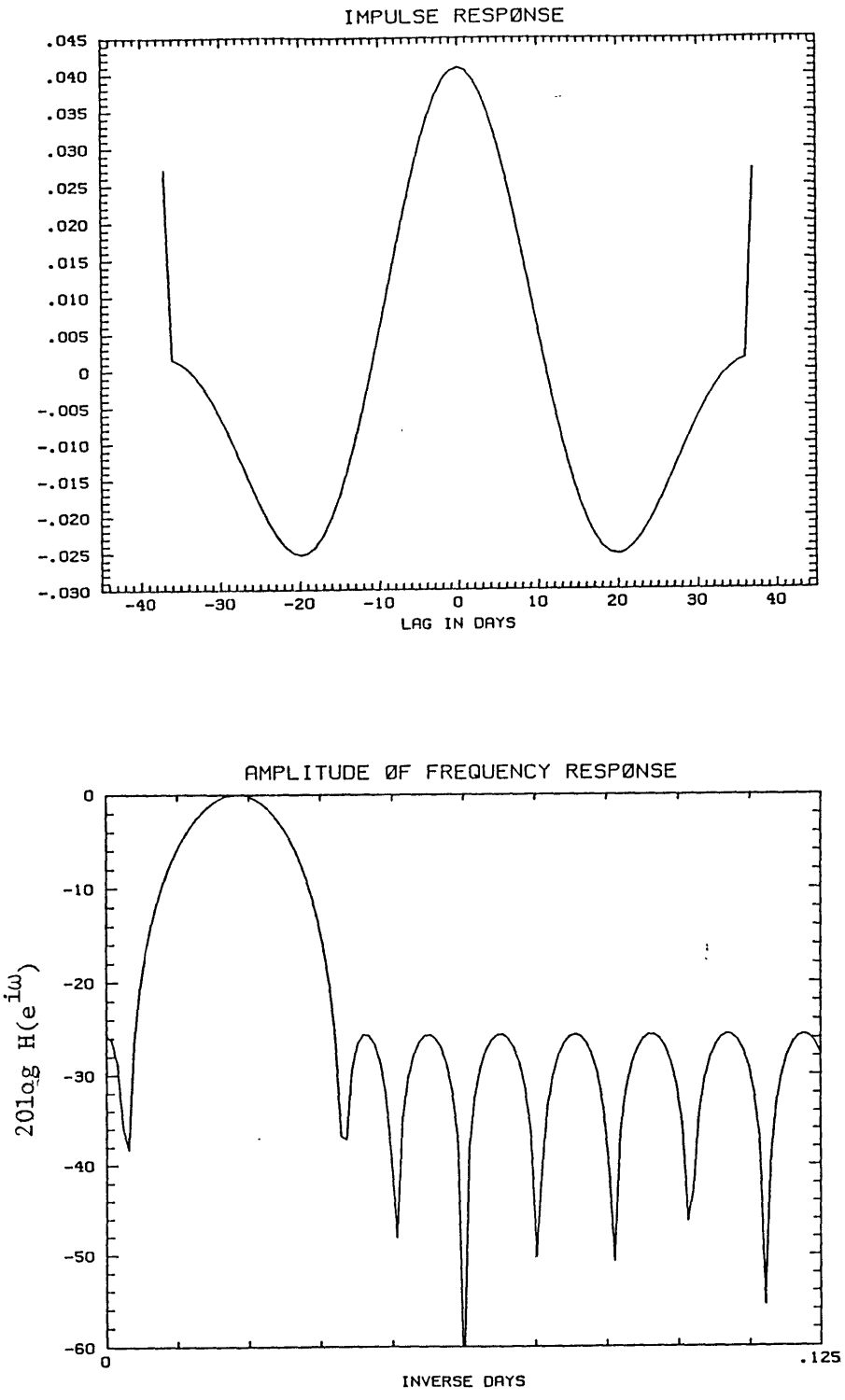

Fig. 5.12 As in Fig. 5.2 but for a 44-day bandpass filter used for filtering daily data.

peaks and troughs in the 40-day filtered principal components of eigenmodes 1 and 2 of EOF analysis C201025W (shown in Fig. 5.3a) with those in the 44-day filtered HRC time series approximately collocated with the minima in the first and second eigenvectors. For the first mode this is the HRC series at 150°E. For the second we estimated the phase at 75°E by interpolating subjectively between the series at 60°E and 90°E. In the table, peaks and troughs are considered separately. After each HRC date, the lag of the HRC behind the corresponding feature in the principal component is listed, positive values for HRC lagging. The results are mixed. The general pattern is a lag of approximately 3-4 days or more of the HRC peaks behind the velocity potential, although there are extreme cases of 10 and 12 day lags, and two cases where the HRC led the velocity potential by more than 5 days. The closest and most consistent correspondence is between the HRC in the Indian Ocean and the principal component peaks of the second mode. HRC peaks in the western Pacific sometimes are coincident with the principal component peaks of the second mode, but here the lags can be considerable, up to 1/4 of a cycle. Comparisons with HRC series at other longitudes suggests that the results in Table 5.2 are not greatly sensitive to the choice of longitude for the HRC time series. Thus the time dependent patterns of upper level divergence are somewhat more weakly connected to the velocity potential than in the time mean patterns. Nonetheless there is certainly ample support for the view that negative (positive) 40-50 day anomalies of velocity potential are associated with enhanced (suppressed) convection.

Table 5.2 Comparison of Eigenmode and HRC Extrema
(Lags of HRC behind EOF modes in days)

Mode 1	HRC at 150°E		Mode 2	HRC at 75°E	
Peaks					
26	38	+12			
73	85	+12	75	78	+3
98	91	-7	100	104	+4
129	135	+6	122	125	+3
163	173	+10	155	156	+1
206	206	0	196	195	-1
247	250	+3	238	242	+4
280(weak)	280	0	275P-281T-290P	283	+2
305	310	+5			
Troughs					
51	58	+7	44	53	+9
86					
113	113	0			
145	151	+6	149	140	-9
184	190	+6	173	173	0
227	222	-5	213	218	+5
268	268	+1	256	260	+4
284?	294	+10			

If we had found consistently positive lags of the convection behind the velocity potential, it may have indicated a tendency for the large scale divergence pattern represented by the velocity potential to enhance or suppress convection in advance of its progress. However our results are not definitive enough to make this conclusion. This question would be better studied with actual divergence fields rather than the velocity potential.

More conclusive inferences can be made from Fig. 5.13. Here we consider not only the relationship between 40-50 day anomalies in HRC along the equator but also their relationship to the divergent equatorial zonal winds examined earlier. The general format of the figure is the same as Fig. 5.11 with the addition of time series at 30°E, 90°E etc. The lower case letters and dotted lines are taken from Fig. 5.8 to indicate the phase relationships between the eastward propagating anomalies of westerly divergent winds at the equator and the increased convection we presume follows. And indeed the figure does demonstrate, with just a few exceptions, that eastward propagating westerly divergent wind anomalies at 40-50 days do in fact lead increased convection at each longitude. Furthermore the mean HRC values are small (~25) over the region in which eastward propagation ceases (in cases b, c, d and f between 120°W and 60°W), suggesting that further propagation was inhibited by insufficiency of available latent heat. This is the argument originally made by Madden and Julian (1972).

There are some puzzling aspects to Fig. 5.13 however. The phases of the HRC time series in the region from 60°E westward to 120°W at times suggest westward, rather than eastward, propagation of convection or even a simultaneous blooming of convection across a wide longitudinal

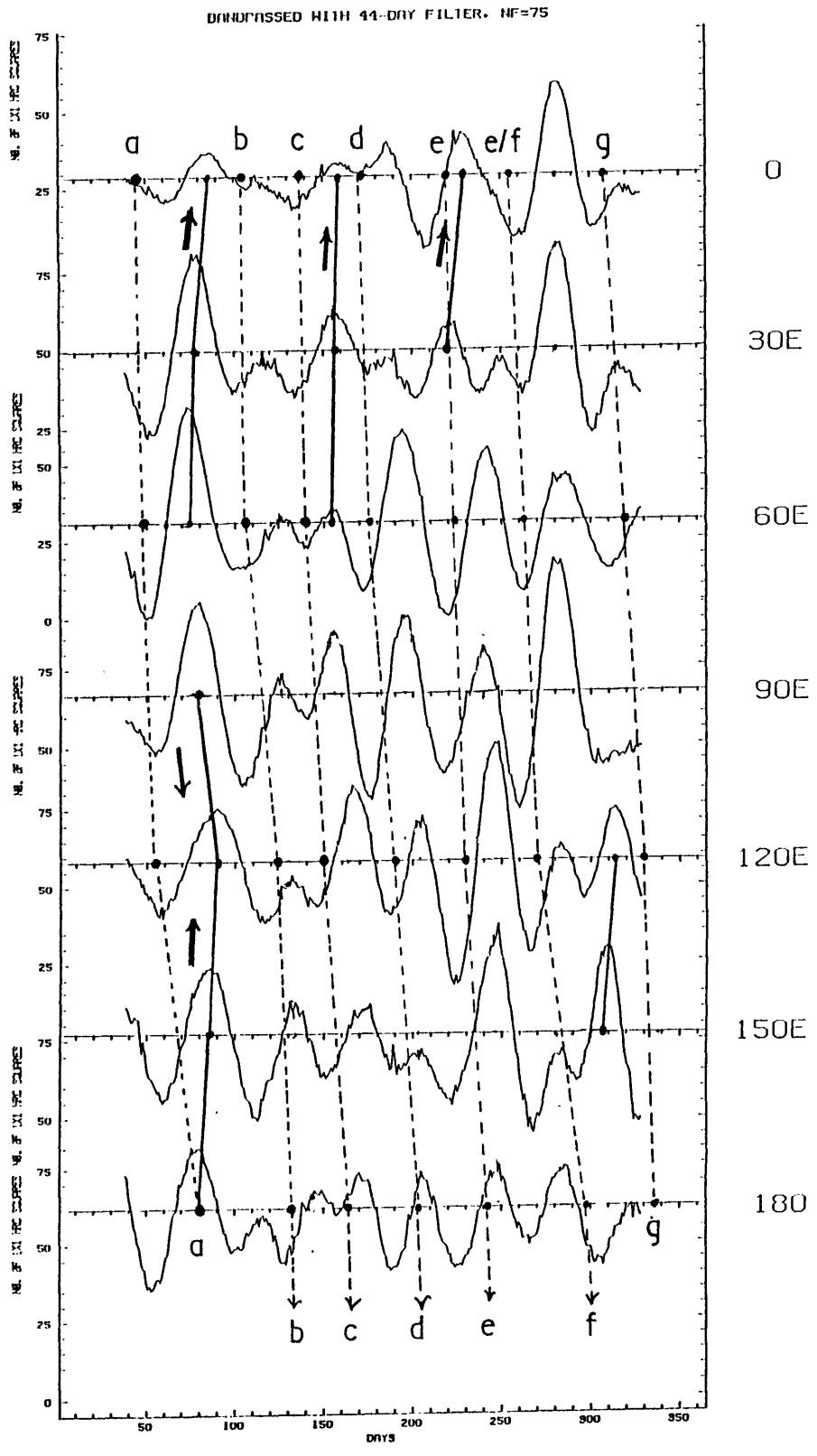

Fig. 5.13a As in Fig. 5.11a but for 44-day filtered HRC time series at 7 longitudes at 30 intervals.

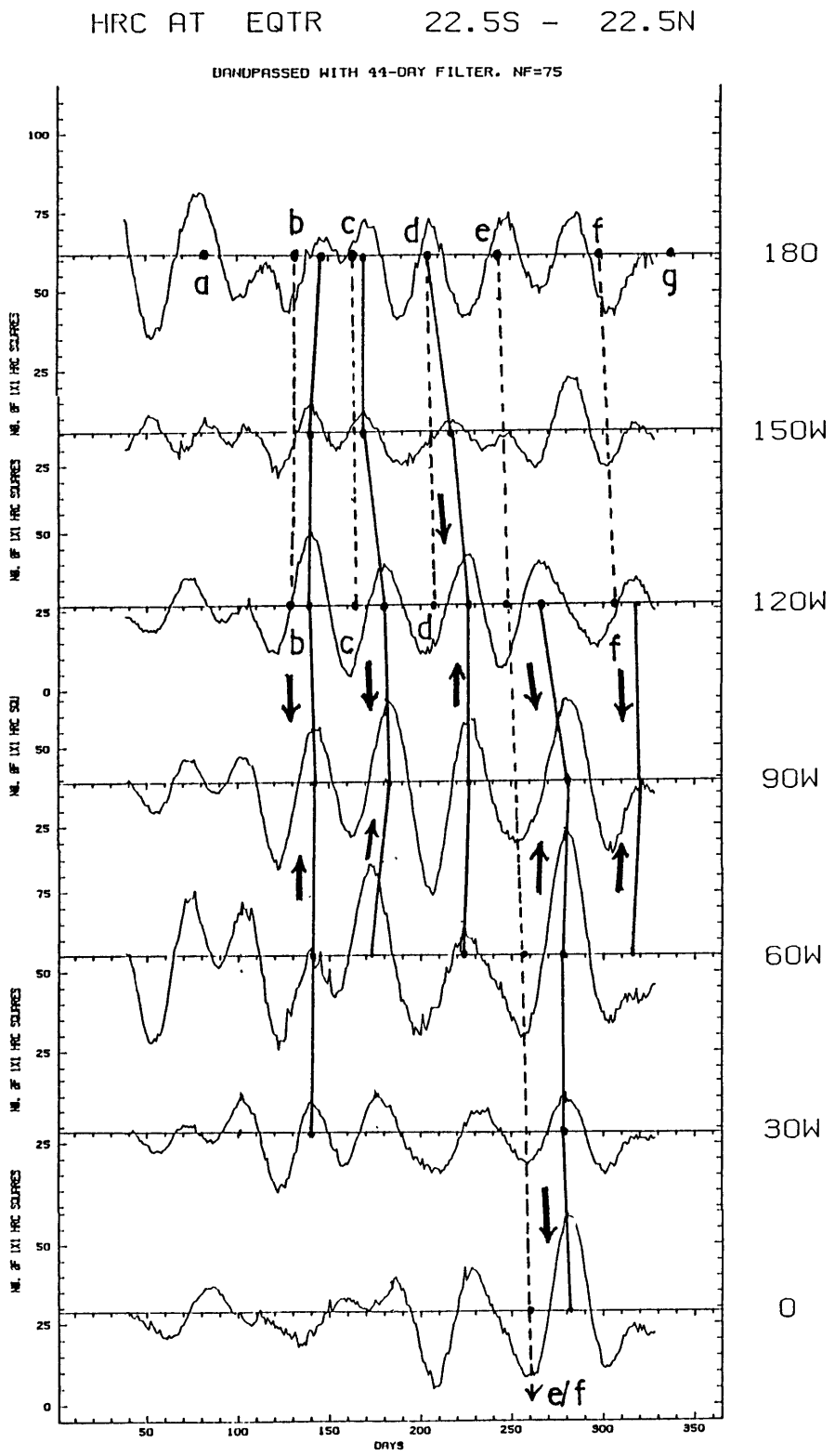

Fig. 5.13b As in (a) but for the western hemisphere.

span. An example of the latter is the nearly zonally symmetric anomaly in HRC which peaks at day 282-3 in a wide band of longitudes from 90°W eastward to 180°, three-quarters of the way around the globe. In Chapter 6 we will show that this time corresponded with an increase of HRC at all latitudes between the 25th parallels. We have drawn solid lines connecting the peaks in HRC and arrows to indicate the apparent changes in propagation from eastward to westward and vice versa.

We present in the final two figures the separate contributions of the Northern and Southern Hemispheres to the bandpassed tropical band totals depicted in Fig. 5.13. Fig. 5.14 presents the Northern Hemisphere components and Fig. 5.15 the Southern Hemisphere. These can be interpreted as displaying the average HRC in a band centered at 11.25° from the equator. We omit every other time series and simply present HRC series at 60° intervals. A striking difference is apparent between the variability in the two hemispheres. North of the equator there are clear eastward moving anomalies of convective cloudiness. Phase speeds in this hemisphere range from 7 to 13 m/s, in agreement with the divergent meridional winds at 15°N and 15°S. To the south, the anomalies are considerably weaker and irregular in phase, with the strongest 40-50 day variability appearing to occur in the southern summer. We note that positive Northern Hemisphere HRC anomalies are even more strongly tied to anomalies of poleward divergent flow in the Southern Hemisphere than to those north of the equator. We have identified by numbers in Fig. 5.14 the times of southward peaks of meridional divergent winds from Fig. 5.10 for cycles 3 - 7. We can see that positive HRC anomalies north of the equator accompany increases in poleward flow south of the equator. Since this cross-equatorial

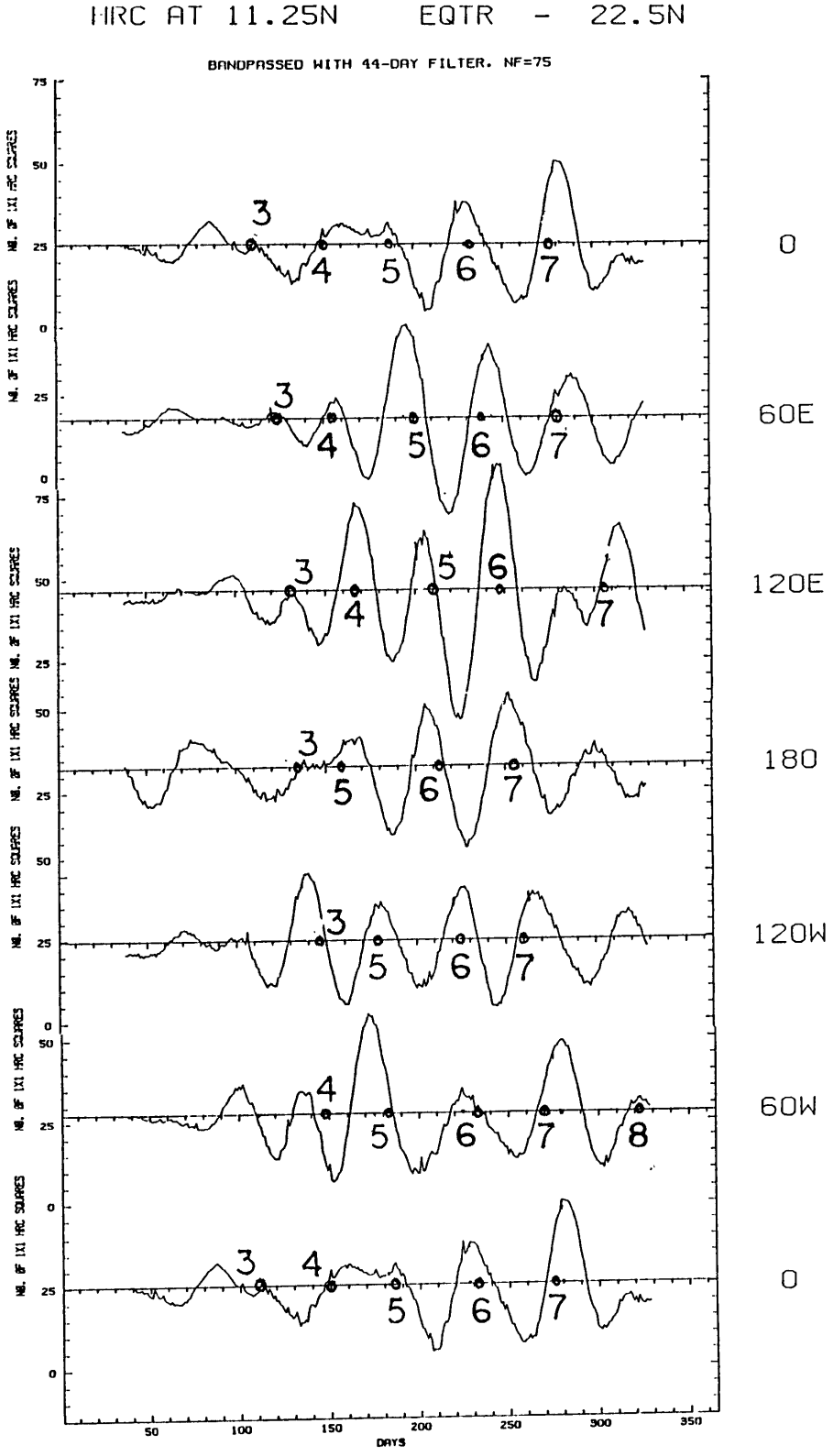

Fig. 5.14 As in Fig. 5.13 but for regions between the equator and 22.5°N at intervals of 60° eastward from 0° through 180° and back to 0°.

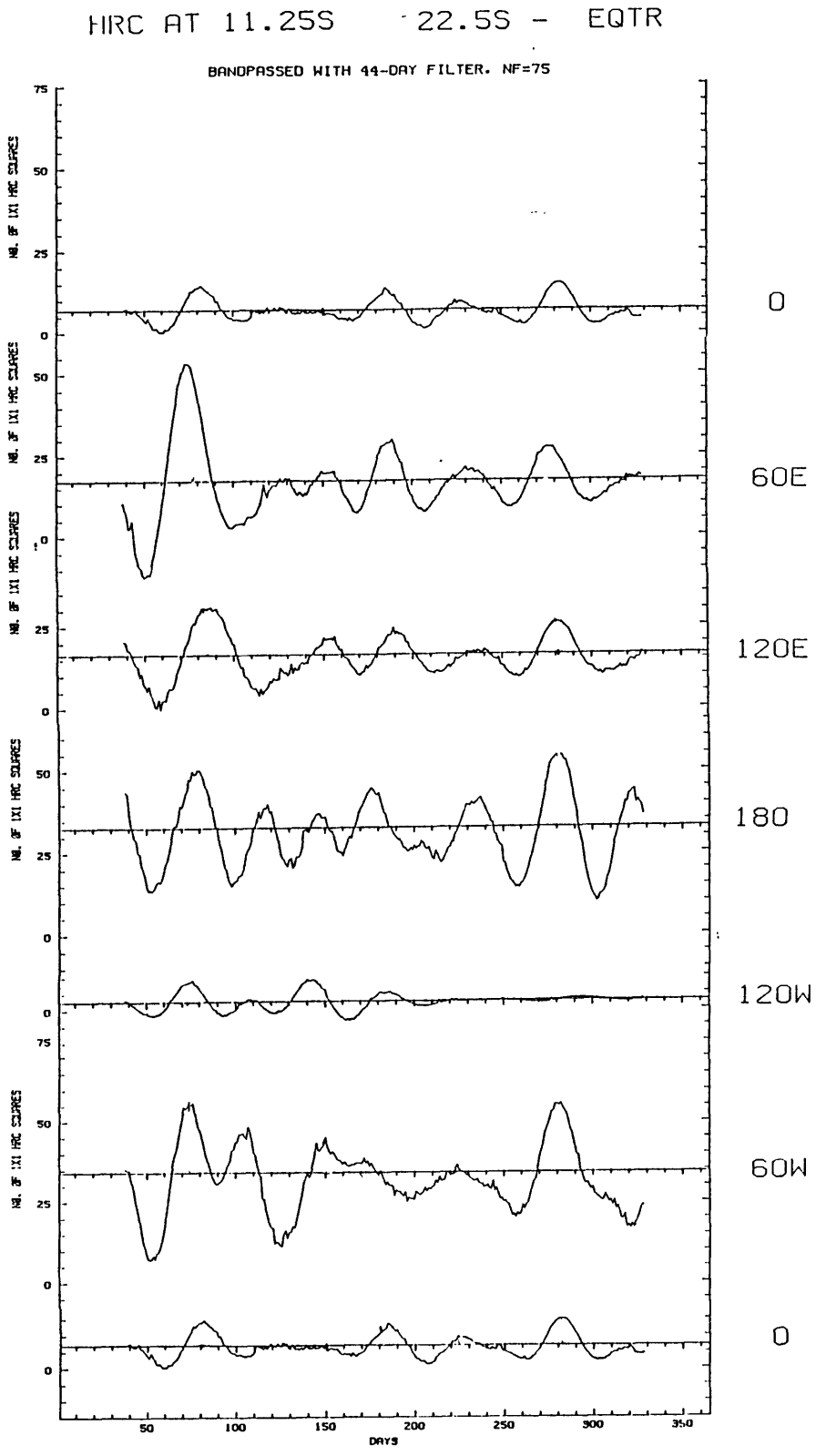

Fig. 5.15 As in Fig. 5.14 but for regions between 22.5°S and the equator.

association appears strongest in northern summer, it may simply be a reflection of the dominance of the Southern Hemisphere meridional flow during this time of the year. The converse is not true as Fig. 5.9 shows that there is little 40-50 day variability of the meridional flow during Northern Hemisphere winter.

5.4 Discussion

Our detailed examination of the eastward propagation of both meridional and zonal divergent wind anomalies has extended Lorenc's (1984) description of the 40-50 day oscillation in velocity potential. We have found that in terms of divergent zonal wind anomalies, i.e. modulations of the Walker circulation, uninterrupted transit of the equatorial belt was limited to one 40-50 day cycle in mid-summer. In particular, the eastward progression of divergent zonal wind anomalies generally appears to stop in the South American region. This behavior contrasts sharply with the divergent meridional winds of the Southern Hemisphere where several transits during the year were completed, one in March and April and two more during the southern winter. The physical significance of the meridional wind anomalies is well supported from their close correspondence with HRC data at the same longitudes in the Northern Hemisphere during the southern winter months. Further more detailed study of the evolution of the 40-50 day velocity potential fields may uncover the source of this discrepancy. At present, though, our results are somewhat ambiguous as to the source region for the oscillation.

The studies of Weickmann (1983) and Lau and Chan (1985) were limited to the northern winter period so conclusions drawn from comparisons to their work must be considered tentative. They found phase speeds for the eastward passage of 40-50 day anomalies of outgoing longwave radiation through the Indian Ocean region in the neighborhood of 5 m/s with an unmistakable slowing in the 120°E - 180° region. They do not in fact find much evidence of 40-50 day activity propagation past the central Pacific. Taking the tropics as a whole, our results tend to agree, but if the Northern Hemisphere alone is considered, there does seem to be eastward propagation in this region. Phase speeds derived here from both the HRC time series as well as the divergent wind anomalies themselves are somewhat greater, ranging up to 15 m/s. Much of this may be accounted for by the accentuation of 40-50 day variability in the FGGE year noted by Weickmann (1983) and others. The trans-Pacific HRC propagation in what appears to be the northern ITCZ may also reflect more favorable conditions for eastward propagation of wavelike disturbances during the northern summer than in the winter. If that were the case, then one might expect the higher phase speeds that we observe. Weickmann and Kutzbach (1985) suggested that the deep easterly background flow results in the more consistent eastward propagation of u anomalies during the FGGE northern summer than winter.

There are some details from the Weickmann and Lau and Chan studies that we either do not observe or are unable to verify which deserve mention. Foremost among these, we do not obtain the same dipole signature in the HRC anomalies as Lau and Chan do in the OLR. During most stages of their composite 40-50 day oscillation, the equatorial centers of positive and negative anomalies are separated by approximate-

ly 90° of longitude. We have not performed EOF analysis on the HRC data for this study, but the phases of the time series in Fig. 5.14 for example suggest a separation scale roughly twice that of Lau and Chan. Again, this may be an example of the interannual variability of the 40-50 day oscillation. A second difference was that we do not see evidence of a significant attenuation of 40-50 day variance in the central Indonesian region near 120°E in any of the circulation indices discussed here. This feature is apparent in the work of both Weickmann and Lau and Chan. Finally, some of the detailed aspects of the change in phase speeds noted by Lau and Chan were not amenable to verification with the methodology we adopted.

Chapter 6. Slow Changes in the Hadley and Zonal Circulations

In the last chapter we saw how eastward propagating 40-50 day anomalies in the velocity potential are associated with alternating intensification and relaxation of the local divergent meridional wind fields over broad longitudinal spans of the tropics. In this chapter we will examine the intraseasonal variability in the zonal average of the divergent meridional winds. (Intraseasonal will be taken to mean fluctuations on all time scales between 25-30 days and the semiannual and not necessarily strictly 40-50 days.) We will examine the variability of the meridional circulation both in the form of the zonally-averaged meridional wind field and of the streamfunction that can be derived from it. In addition, time series of zonal average totals of highly reflective cloud will be studied as an index of convective forcing for the Hadley circulation. Finally, as a first attempt to assess the role of the Hadley circulation in the maintenance of the 40-50 day oscillation in the zonal circulation in the tropics, we present the results of zonal mean zonal momentum budgets calculated on a twice-daily basis throughout the FGGE year.

6.1 The Variability of the Zonal Circulation during the FGGE Year

To provide a setting in which to consider the possible interactions between the Hadley circulation and the zonal circulation we first examine the fluctuations of the global relative angular momentum during the FGGE year and then the individual time series of [u] that together contribute to the observed 40-50 day fluctuations in the angular

momentum. Anderson and Rosen (1983) have presented the structure of the 40-50 day variability of the zonal circulation for a four-year period; we will not duplicate their work here. However we will show FGGE year time series of the zonal circulation at individual latitude-height locations.

The FGGE year relative angular momentum for the globe has been plotted in Fig. 1.2. This quantity was calculated for each twelve-hour observation time in the FGGE year from zonal averages of the u component of the wind at each of the fifteen levels and 47 non-polar grid latitudes (86.25°S-86.25°N) in the ECMWF III-b analysis.

The relative angular momentum M of the atmosphere is the integral

$$(6.1) \qquad M = \frac{2\pi a^3}{g} \int_0^{P_s} \int_{-\pi/2}^{\pi/2} [u] \cos^2\phi \, d\phi \, dp.$$

We approximate this integral with the summation

$$(6.2) \qquad M = \frac{2\pi a^3}{g} \sum_{i=1}^{15} \sum_{j=2}^{47} [u]_{i,j} \cos^2\phi_j \Delta\phi \Delta p_i$$

where $\Delta\phi$ is equivalent to the grid spacing of 3.75°. The 15 pressure levels and corresponding values of Δp_i are listed in Table 6.1. The approximation used here assumes that the zonal average surface pressure P_s is 1000 mb and that the III-b analysis [u]'s at 10 mb are the mass-weighted average for the entire atmosphere above 15 mb. This summation diverges from those by Rosen and Salstein (1983), for example, in that the stratospheric winds are included. We felt that inclusion of the levels above 100 mb, where the winds are weaker than at the jet levels near 200 mb, was unlikely to change instantaneous values of the index by more than 5-10%. We compared our index with that of Rosen and Salstein (1983) and found no significant differences.

Table 6.1 Vertical Discretization for the Calculation of Atmospheric Angular Momentum and the Meridional Stream Function ψ_{MC}

	P_i	layer	P_j	P_i
1:	10			
		0-15	15	15
2:	20			
		15-25	25	10
3:	30			
		25-40	40	15
4:	50			
		40-60	60	20
5:	70			
		60-85	85	25
6:	100			
		85-125	125	40
7:	150			
		125-175	175	50
8:	200			
		175-225	225	50
9:	250			
		225-275	275	50
10:	300			
		275-350	350	75
11:	400			
		350-450	450	100
12:	500			
		450-600	600	150
13:	700			
		600-775	775	175
14:	850			
		775-925	925	150
15:	1000			
		925-P_s		P_s-925

Here we have filtered the angular momentum time series with the 40-day bandpass filter used in Chapter 5. From the filtered time series one can estimate the amplitude of the oscillation as well as its phase with respect to other time series. With respect to the relative angular momentum the 40-50 day oscillation during the FGGE year peaked near days 50, 140, 210, 260 and 320.

Fig. 6.1 is taken from Anderson and Rosen (1983) and shows the latitude-height structure of 40-50 day anomalies in the zonal circulation as revealed in the first mode of their complex EOF analysis of zonal circulation band-pass variance in the 40-50 day frequency band. The amplitude of the oscillation at each latitude and height is depicted in the upper panel while the phase appears in the lower panel. (In contrast to the EOF analyses used in this work in which the structure and time behavior of each mode in the analysis is described by a real eigenvector and principal component, the eigenvectors and principal components of complex EOF analysis have both real and imaginary parts. A practical method of presentation of both eigenvectors and principal components is in terms of amplitude and phase diagrams.)

Anderson and Rosen found that 40-50 day anomalies in the tropical zonal circulation originate in the high equatorial troposphere near the 150 and 200 mb levels. From there the anomalies propagate poleward. In the Southern Hemisphere the oscillation is largest at 10°S at 150 mb which lags the equatorial zone by $\sim 1/20$ of a full cycle, which for a 45-day oscillation is a little more than 2 days. Further propagation into that hemisphere is not indicated. In the Northern Hemisphere, there is also propagation into the subtropics where it lags the equator by 4-5 days at 20°N. Northward of that point the phenomenon more

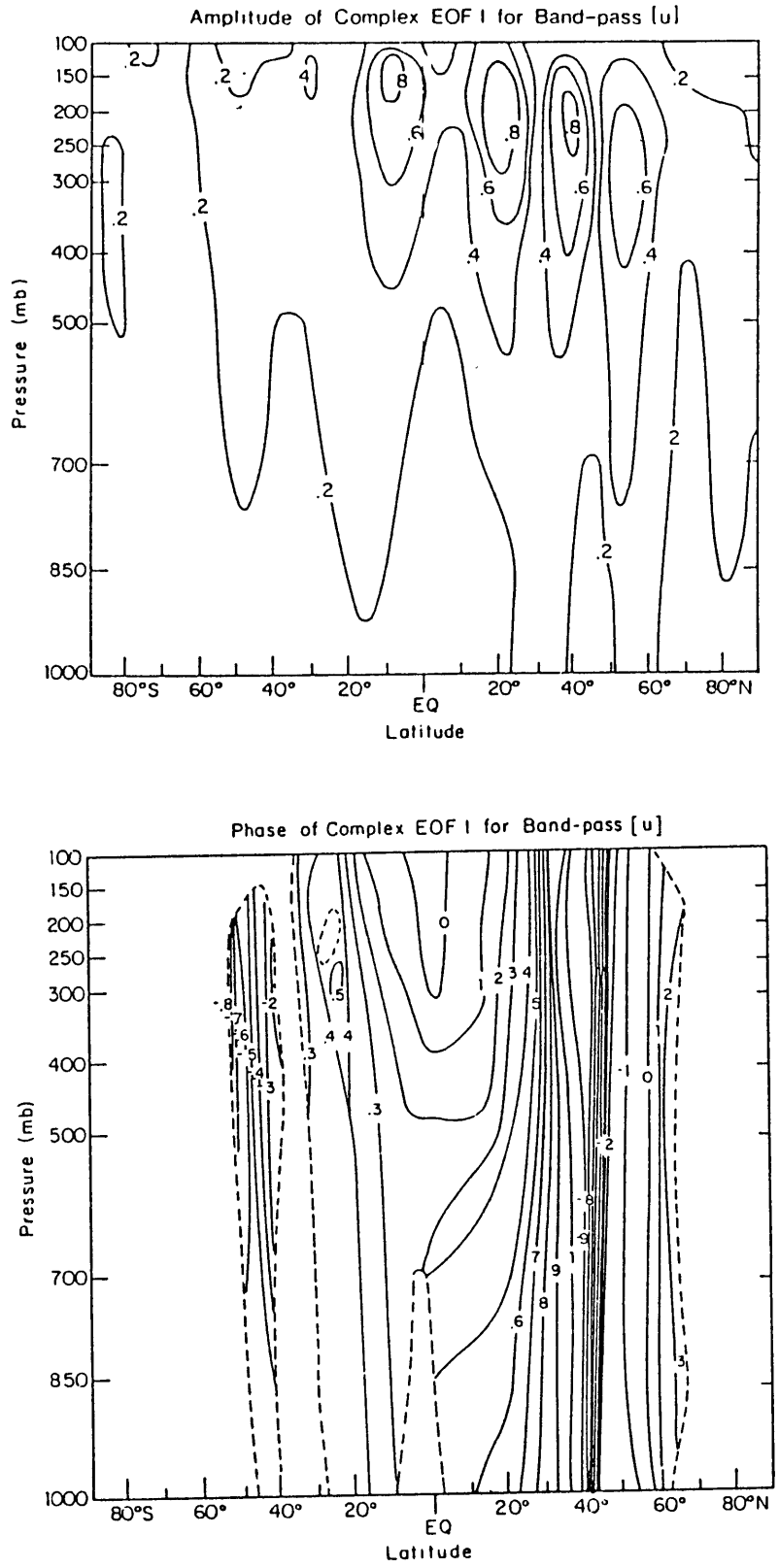

Fig. 6.1 Latitude-height fields of the amplitude (upper panel) and phase of the first eigenmode in complex EOF analysis of 5 years of daily values of [u]. Taken from Anderson and Rosen (1983).

closely resembles a standing oscillation with an opposing peak at 40°N. With respect to their time series of angular momentum, Anderson and Rosen's results suggest that the strongest in-phase complex correlations are to [u]'s near 10°S in the upper troposphere and at 20°N and 200 mb.

Fig. 6.2 presents 200 mb time series of [u] at every other grid latitude in the tropical portions of the Southern and Northern Hemispheres. Superposed upon each is the 40-day bandpass filtered version. This presentation allows easier estimation of the phase lags betweeen the time series. We have drawn dashed lines across the figure to connect the modes in the filtered time series. The tilts of the dashed lines for the most part indicate the anticipated poleward propagation of the wave. One interesting feature is the rapid phase change between 15°S and 22.5°S. Another is the attenuation of the oscillation at 7.5°N in the period from days 220 to ~280 (early July to early September). This weakness is also apparent at 3.75°N (not shown) during this period and during the period from ~day 65 thru ~day 140.

We consider briefly here the vertical structure of the oscillation as it is manifested in the equatorial time series of [u]. Fig. 6.3 displays the time series of [u] at 850, 700, 500, 300, 200, 100, 50, 20 and 10 mb. To facilitate phase identification the bandpass filtered time series are displayed as well; note that the amplitudes of the latter time series have been doubled to highlight the phases. Thus what would appear at 10 mb as an average bandpassed amplitude of ~5 m/s is actually half that magnitude. Inspection of the diagram by drawing a vertical straight line upward from the 850 mb time series reveals a fairly steady decrease of phase with height. We also emphasize the

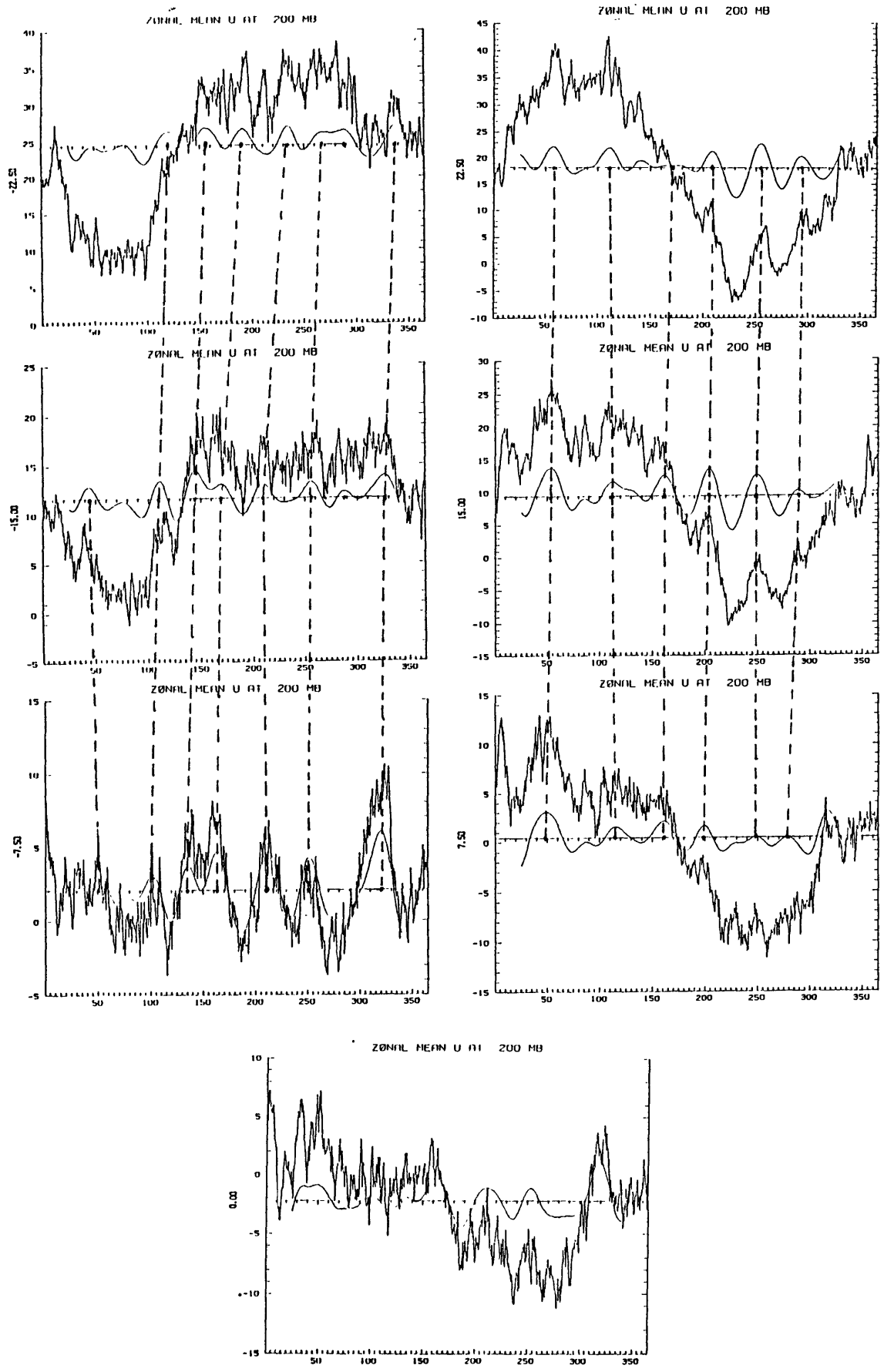

Fig. 6.2 40-day filtered and unfiltered time series of [u] derived from the ECMWF III-b analysis at 200 mb for the latitude bands 22.5°S - 7.5°S (downward on left), 22.5°N - 7.5°N (downward on right) and the equator (bottom). Values in m/s.

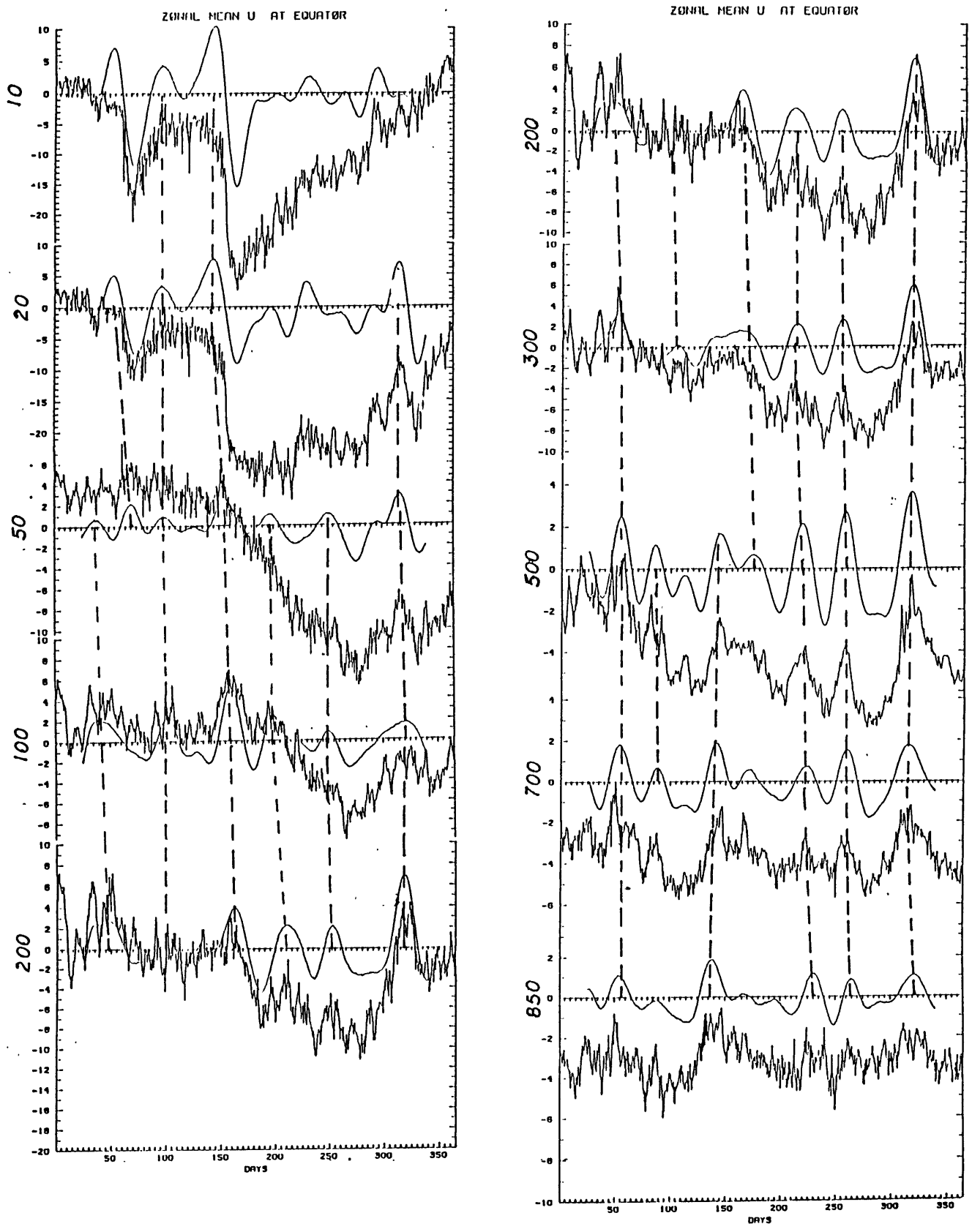

Fig. 6.3 40-day filtered and unfiltered time series of [u] at the equator at 10, 20, 50, 100 and 200 mb (downward on left) and 200, 300, 500, 700 and 850 mb (downward on right) in m/s. Filtered time series are scaled up by a factor of 2.

phase propagation with dotted lines which connect the modes of the bandpass filtered series.

Anomalies in the high troposphere are of the opposite sign as the original work by Madden and Julian (1971, 1972) would suggest. What is interesting is that the phase continues to decrease with height, although not in a completely systematic manner. Nonetheless if the 850 mb time series is superimposed on the 10 or 20 mb time series, it would appear that the anomalies above 25 km are in phase with the lowest kilometer. The sudden drops in the latter two time series are a matter of some concern, representing as they do easterly accelerations of up to 15 m/s in the zonal circulations in a matter of several days at the most. These levels are doubly suspicious as they are above the range of most of the soundings.

This upward decrease of phase is consistent with upward energy propagation from the lower troposphere. We note from the figure however that the environment through which the wave is propagating changes through the year. In the first half of the FGGE period, the flow is easterly in the lower troposphere and weak westerly in the upper troposphere and lower stratosphere. This pattern peaks at 70 mb (not shown). The descending easterlies of the biennial oscillation reach this level by day 210 (June 28). From this time onward the slowly varying flow is everywhere easterly. It appears that the upward phase propagation is not affected in any systematic way by the "mean" flow structure. (By "mean" flow we refer to that which is changing on a seasonal or longer time scales.)

6.2 Intraseasonal Varibility of the Meridional Circulation

The local modulations of meridional overturning shown in Chapter 5 are for the most part zonally asymmetric. That is, the meridional wind anomalies along a given latitude circle tend to cancel each other out. It may have been expected, given the tendency of the ECMWF initialization to suppress the Hadley cell, that there would be little if any coherent signal in the zonal mean of the divergent meridional winds. However as we shall see in this section, there is variability in the meridional circulation at the time scales we are interested in, and this variability is somewhat coherent.

We will examine two types of indices of the meridional circulation. First, there are the individual time series of [v] which we have calculated on a daily basis by direct averaging of the 96 points along each latitude and pressure level. Secondly, we have calculated daily fields of streamfunction of the meridional circulation Ψ_{MC} from the fields of [v] using an approximation to Eq. 2.2. (To our knowledge, this is the first time that the meridional streamfunction has been computed on a day-to-day basis.)

6.2.1 Variations of the Zonally Averaged Meridional Winds

Fig. 6.4 displays the latitude-height fields of the time average and standard deviation of [v] for the FGGE year. The mean field possesses four significant extrema within 15° of the equator: at 200 mb there is a local maxima of poleward flow at 15°N (0.81 m/s) and near 12°S (-0.86). At the lowest analysis level, 1000 mb, there are

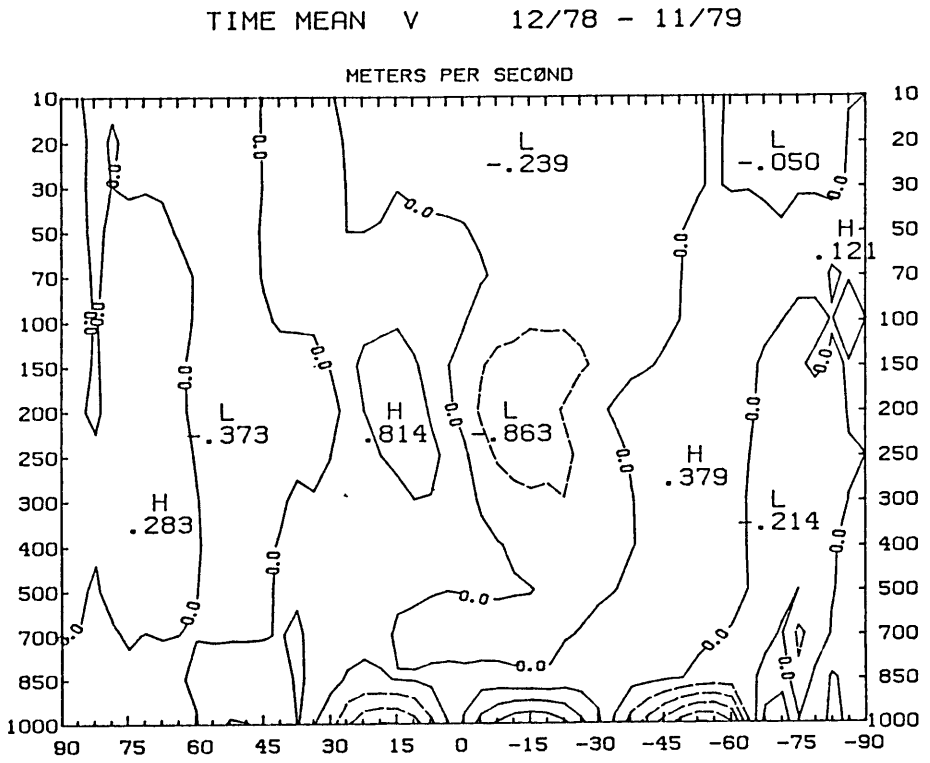

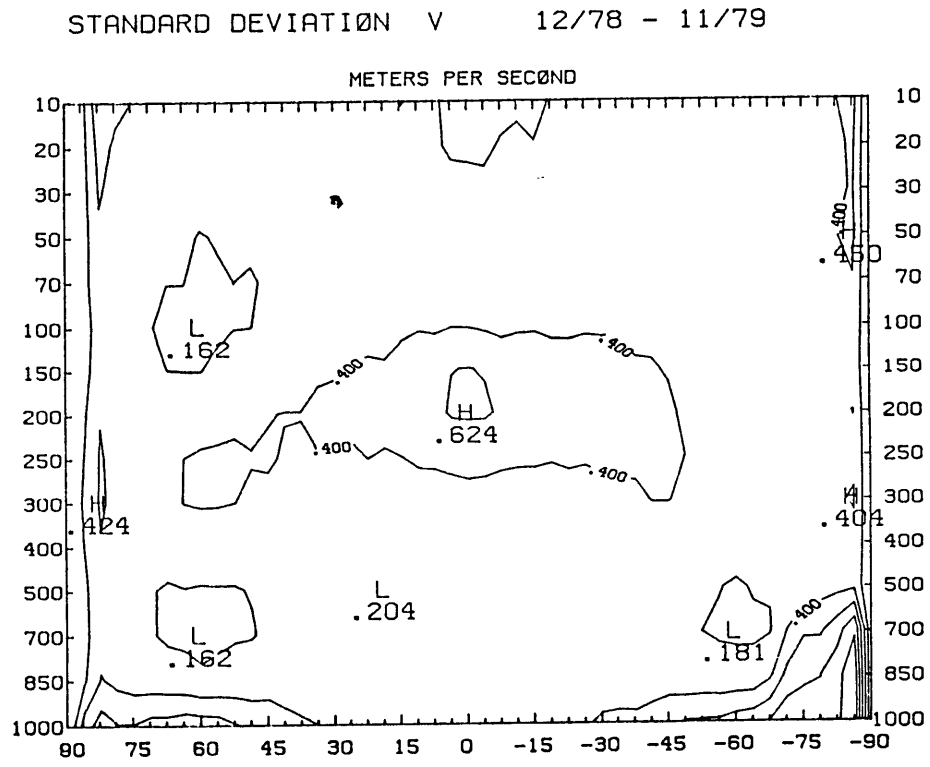

Fig. 6.4 Latitude-height fields of FGGE-year time averages (top) and standard deviations of [v] derived from the ECMWF III-b analysis. Values in m/s.

equatorward maxima of over 1.2 m/s at approximately the same latitudes. These features of the meridional circulation are to be expected: low-level inflow concentrated at the lowest layer of the analysis and outflow distributed over a rather deep layer of the upper troposphere.

In the Southern Hemisphere between latitudes 30° and 60° there is strong northerly flow at 1000 mb, with a maximum of 2.5 m/s near 50°S. Lau (1985b) has shown that GFDL analyzed FGGE values of [v] in these regions are similar to those in the ECMWF meridional circulation; they are apparently not a product of ECMWF analysis system peculiarities. However, Oort and Peixoto (1983) using rawinsonde data from 1958-1973 obtained values for [v] of less than 0.5 m/s for the extratropical wind field in the surface boundary layer. The differences here are due to the constraints that their indirect calculation of [v] puts on the analysis of the surface boundary layer flow [cf. Oort (1983, Appendix B)] which are not applied in our time mean profile. The important issue probably has been raised by van Loon (1980) who had serious questions as to the accuracy of FGGE eddy flux statistics in the middle and high latitude Southern Hemisphere during due to the sparsity of stations. This same caution should also be applied as well to the large [v] values in the high southern latitudes.

Another feature of interest is a definite alternation of the direction of the lower and mid-tropospheric meridional flow in the vertical near the equator: weak southerly flow at the surface turns to weak northerly above 850 mb and then back to weak southerly above ~600 mb. This may be an indication of a surface boundary layer circulation of the type found in the models by Schneider and Lindzen (1977) and

Schneider (1977). However the 400 mb depth of the lower "cell" seems somewhat greater than in their results.

Aside from the discrepancies in high southern latitudes at the surface, the time mean values of [v] derived from the European Centre's analysis are in good agreement with the 10-year means from Oort and Peixoto (1983). As noted in Fig. 3.10, for the individual months of January and June, values of [v] in the GFDL analysis fields of are generally ~50% larger than the European Centre's. In the time mean, for the FGGE year (cf. Lau, 1985b, p. 417) the same relationship holds, although the 200 mb poleward maxima of 1.6 m/s in the GFDL time mean are located 5-10° farther away from the equator in the respective hemispheres.

The largest variance of [v] outside of the polar regions is located over the equator near the null line at 200 mb. The upper tropospheric [v] over the tropics is in general more variable than elsewhere. This will be apparent in figures we will present later.

In Fig. 6.5 we show the monthly averages of [v] for the months of January and July. The January field has already appeared in Fig. 3.10 (taken from Lau, 1985a). We present it here for the sharp contrast it presents to the July mean. In July the ECMWF analysis provides even stronger evidence of a two part Hadley circulation than appears in the year's mean. The deep Hadley cell circulation is characterized by relatively strong (-2.3 m/s) southward flow at 200 mb near the equator and northward flow of a similar magnitude below 850 mb. Between these two levels there appears a southward local maximum near 1 m/s at 700 mb and a northward flow of 0.45 m/s at 400 mb. The June average displayed in

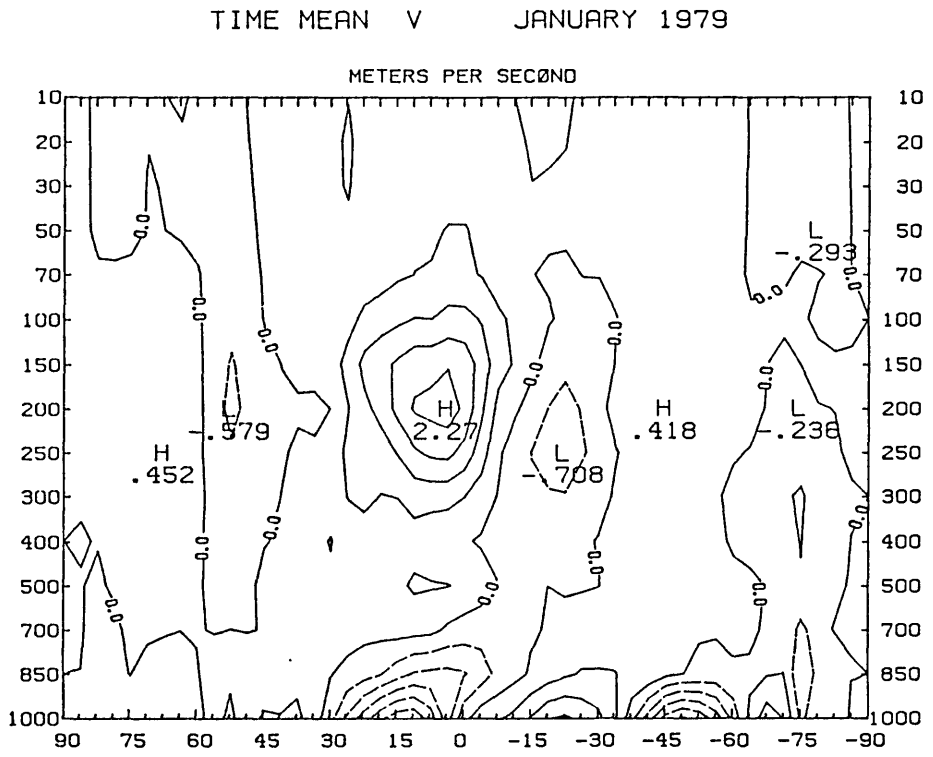

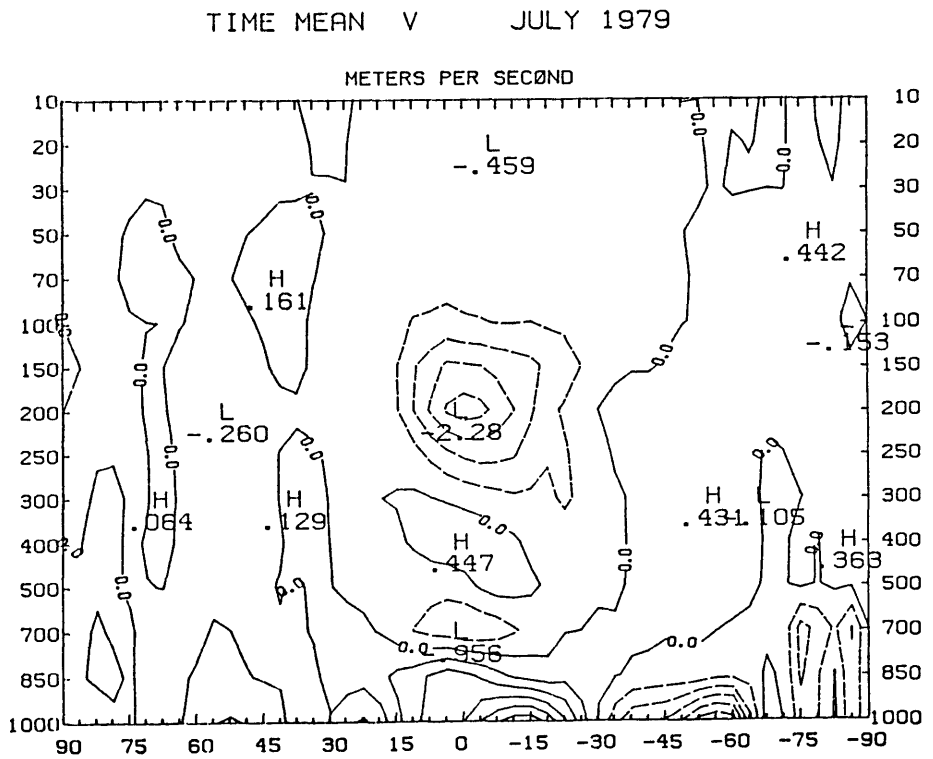

Fig. 6.5 January (top) and July averages of [v] derived from the ECMWF III-b analysis. Values in m/s.

Fig. 3.9 also showed a hint of this structure whereas the GFDL analysis showed only a deep layer of northward flow in that month.

If the lower level cell of July is a real feature, then we might speculate that its presence in the northern summer season and absence in winter might be due to the peculiarities of the two different monsoon regimes. In the models of Schneider and Lindzen (1977) and Schneider (1977), the lower cell is a product of the meridional temperature gradients at the land and ocean surface in the tropics. We would expect then that the most significant meridional temperature gradients would be associated with monsoon flows across land-ocean boundaries, such as occurs during the monsoon over South Asia in northern summer. In northern winter, the land areas over which sensible heating is likely to be strong are more limited in scale.

Rosen and Salstein (1985) also have found an unmistakable double cell structure in the meridional circulation fields derived from the initialized European Centre analyses for both January and July in 1983. At this time the European Centre was using a diabatic nonlinear normal mode initialization and it may be that the double cells are artifacts of that procedure. However the presence of two cells in the uninitialized analyses from the period before the inception of diabatic initialization suggests that this unusual vertical structure owes its existence to more general properties of the optimum interpolation used at ECMWF.

As a first estimate of the importance of the strength of intraseasonal oscillations in the meridional circulation we present in Fig. 6.6 the 40-day bandpass standard deviation and percentage of the total variance in the filter passband for each [v] time series. (The filter is the 40-day bandpass filter of Chapter 5.)

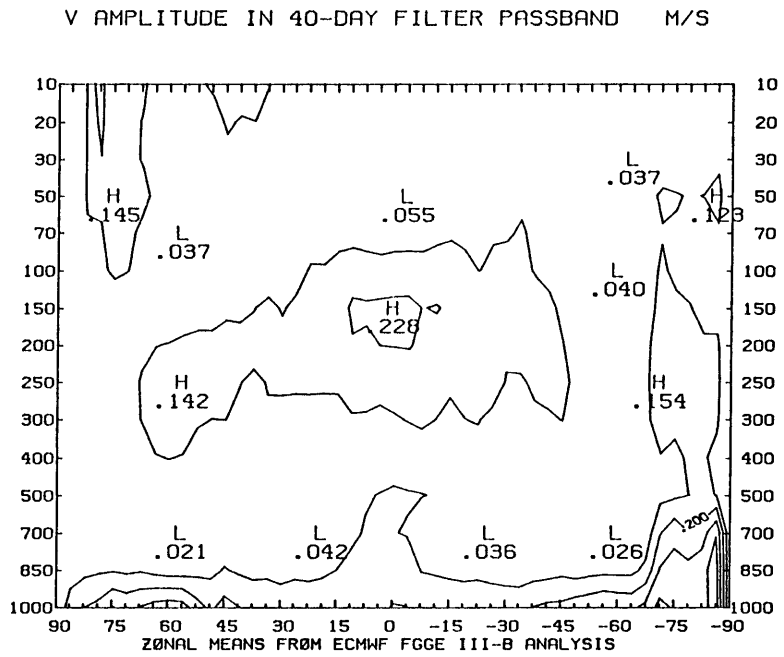

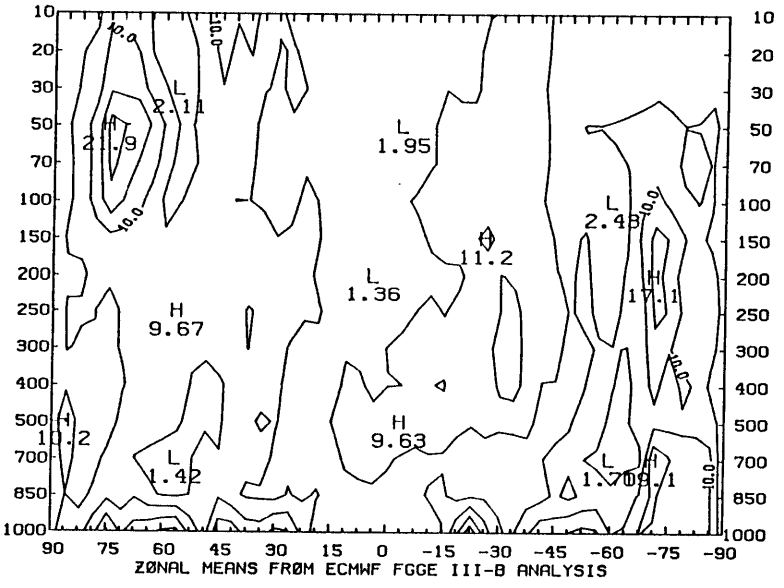

Fig. 6.6 Amplitude (in m/s) of 40-day bandpass filtered [v] anomalies (top) and percentage of total variance in 40-day passband.

Fig. 6.6 indicates that, at least in the tropical region, the strongest 40-50 day variance in the meridional circulation appears in the upper troposphere at 150 mb, slightly higher than the 200 mb level where the mean flow is strongest and where there is also slightly more overall [v] variance. In the lower troposphere there is also a concentration at 1000 mb. The percentage variance is actually largest near the surface in a number of latitude bands and in the lower polar stratospheres. We examined the time series at 1000 mb and 60°N. The 40-50 day variance was contributed largely by a single strong cycle during the winter months.

To illustrate this variability in the tropics more clearly we present in Fig. 6.7 and 6.8 time series of [v] for the 150 mb and 850 mb level respectively which are plotted for the 5 lowest latitudes in each of the Southern and Northern Hemispheres including the equator. As in previous figures, we have superposed the bandpassed filtered time series to emphasize the 40-50 day variability. The latter are amplified a factor of 2 for readability as they were in the vertical structure figure. Because the [v] time series are considerably noisier than other series we have so far considered, some of the highest frequency noise finds its way through the filter into the filtered time series. This relatively unsatisfactory performance of the filter would be remedied by a longer impulse response. However, we feel that the lack of smoothness in no way distorts the picture presented here.

The most noticeable feature of the variability of the meridional circulation in the upper troposphere is the difference in the amplitudes of the intraseasonal variability between the time series at 15°N and those from 7.5°N and southward. That is, the intraseasonal amplitude of

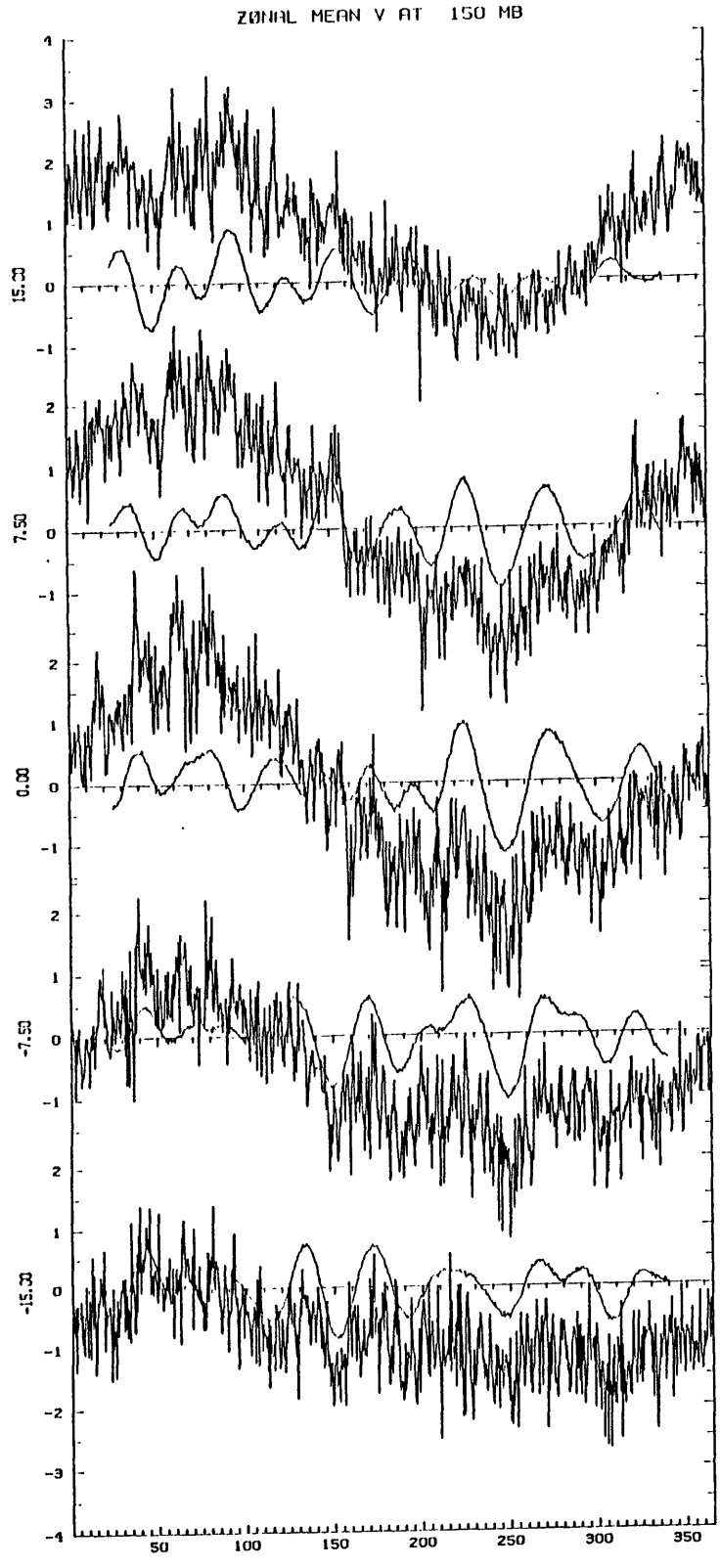

Fig. 6.7 40-day filtered and unfiltered time series of [v] (in m/s) at 150 mb between 15°S and 15°N. As in Fig. 6.3, filtered anomalies are scaled up by a factor of 2.

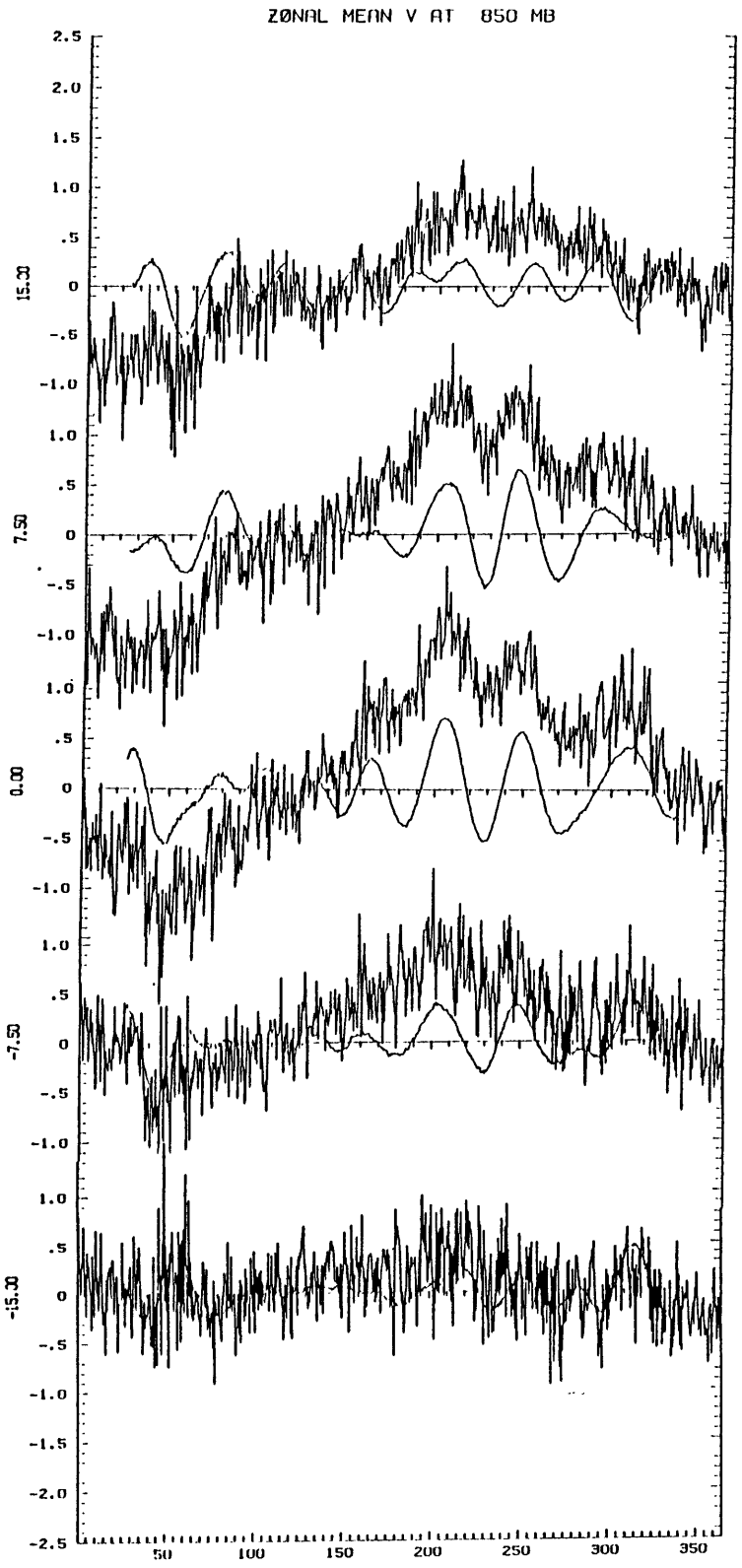

Fig. 6.8 As in Fig. 6.7 but for 850 mb.

the former is larger in the first half of the year, while that of the latter is larger in the second part of the year. Peak amplitudes at this level are approximately 0.5 m/s. It would appear then that the 40-50 day oscillation is stronger in the winter Hadley cell than the summer cell. At 850 the intraseasonal variability is primarily restricted to the winter Hadley cell of the Southern Hemisphere; the amplitudes in this season are roughly half of the 150 mb amplitudes.

By superposing the 850 mb and 150 mb figures, it can be seen that there is an excellent out-of-phase relationship between the 850 and 150 mb [v] time series at each latitude. Thus, despite the considerable amount of noise in these time series, the intraseasonal variability seems to be coherent, with increases of inflow at 850 mb coinciding with increases in 150 mb outflow and vice versa. There is also some evidence of phase lags in the time series' relationships, but the patterns are not consistent.

6.2.2 Time Average and Intraseasonal Behavior of the Streamfunction of the Meridional Circulation

The vertical structure in the variations of the meridional circulation is implicit in the second index of the meridional circulation, the meridional streamfunction ψ_{MC} which we have computed at each latitude and height for each of the 730 observation periods. The streamfunction was calculated using each of the fifteen levels of our derived fields of [v]. Before the actual summation was performed, we imposed the criterion of no net meridional mass flux by removing the instantaneous

vertical mean value of [v] from the values of [v] at every level of a particular latitude (see the discussion in Section 2.1.)

In an attempt to improve the determination of the height of the lower boundary and also the net mass flux, we made the following small adjustment at each observation time: we estimated the zonal mean surface pressure by first finding the difference at each grid latitude between the instantaneous value of the zonal mean sea level pressure from the analysis and the corresponding long term mean value of sea level pressure interpolated from the data in Trenberth (1981). The estimate of the instantaneous zonal mean surface pressure was then obtained by adding this difference to the long term mean values of surface pressure at the same latitudes, also interpolated from Trenberth (1981). The estimated surface pressure values were then used as the lower boundaries for the finite difference calculations of the vertical mass-averaged [v] at each latitude. In hindsight, the increase in accuracy gained through this estimation of the lower boundary was insignificant compared to the spurious mass fluxes due to analysis errors in the free atmosphere.

Having derived for each latitude ϕ_j a set of [v]'s with no net meridional mass flux, the instantaneous values of ψ_{MC} were derived by summing the meridional winds downward from the boundary value $\psi_{MC}=0$ at the top of the analysis, treating the values of the [v] at each ECMWF analysis level as representative of a layer extending from half the pressure increment to the level above and to half the increment to the level below. (The 15 ECMWF analysis levels and intervening layers are listed in Table 6.1.) Thus the value of ψ_{MC} midway between successive analysis levels p_l and p_{l+1} was obtained from the following summation:

$$(6.3) \qquad \psi_{MC\ j,1} = 2\pi\cos\phi_j \sum_{k=1}^{1} [v]'_{j,k}\Delta p_k$$

where $[v]'_{j,k} = [v]_{j,k} - [\hat{v}]$ and $[\hat{v}]$ is the mass-weighted vertical average of [v].

Fig. 6.9 shows the FGGE time average and standard deviation of ψ_{MC} in latitude-height section. The time average, like that for [v] above, can be compared with the 10-year mean field (from station data) presented in Oort and Peixoto (1983, Fig. 7f). The comparison is relatively good: although the maxima and minima in our field are located somewhat farther poleward than in the 10-year average, the heights and magnitudes of the extrema are comparable to the station data. Thus, at least in this time mean sense, the Hadley cell in the European Centre's analysis is consistent with analyses generated from station data.

January and July time means of the meridional streamfunction are shown in Fig. 6.10. These can be compared to the seasonal averages in Newell et al. (1972, Fig. 3.19). There is good correspondence in the cross-equatorial Hadley cell during January. In July the two-part Hadley pattern in the meridional wind discussed above leads to a considerably weaker streamfunction in our analysis than in Newell et al.

We have analyzed the ψ_{MC} data for coherent variability on intra-seasonal time scales. As we were interested in variations of the Hadley circulation we decided to limit the investigation to the pressure layers below 100 mb. (Thus the top layer in the eigenfunctions that are plotted in the succeeding figures will be labeled as 125 mb. Note also that the value of ψ_{MC} is always identically zero at the surface, so the bottom layer will always be labeled 925 mb.) Various choices were made as to the poleward limits of the EOF analysis domain. Generally these

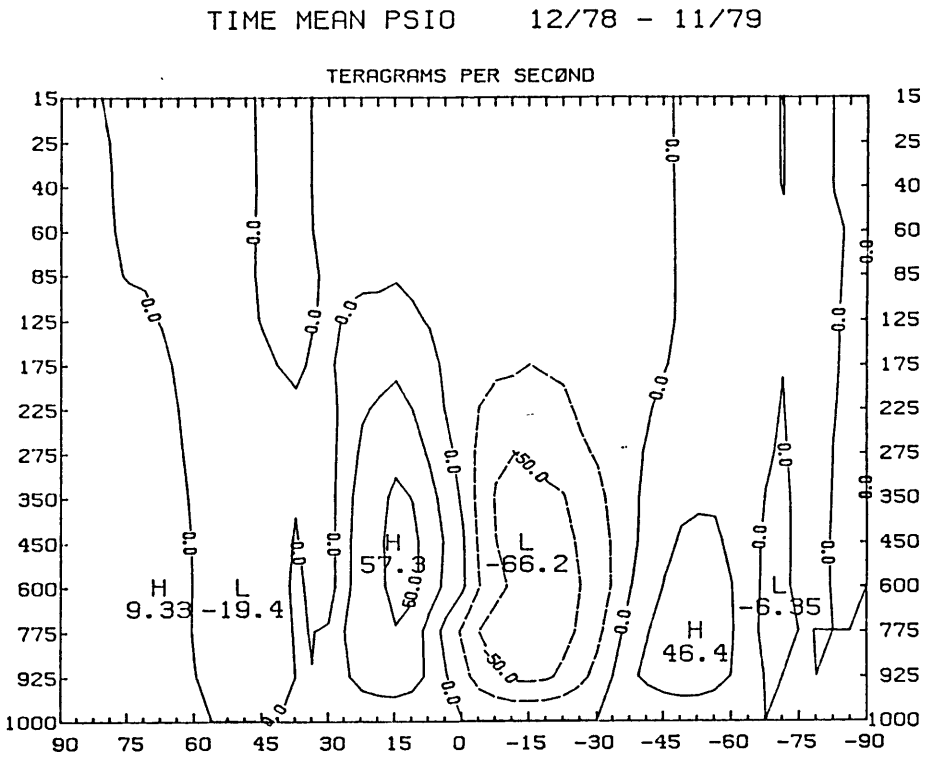

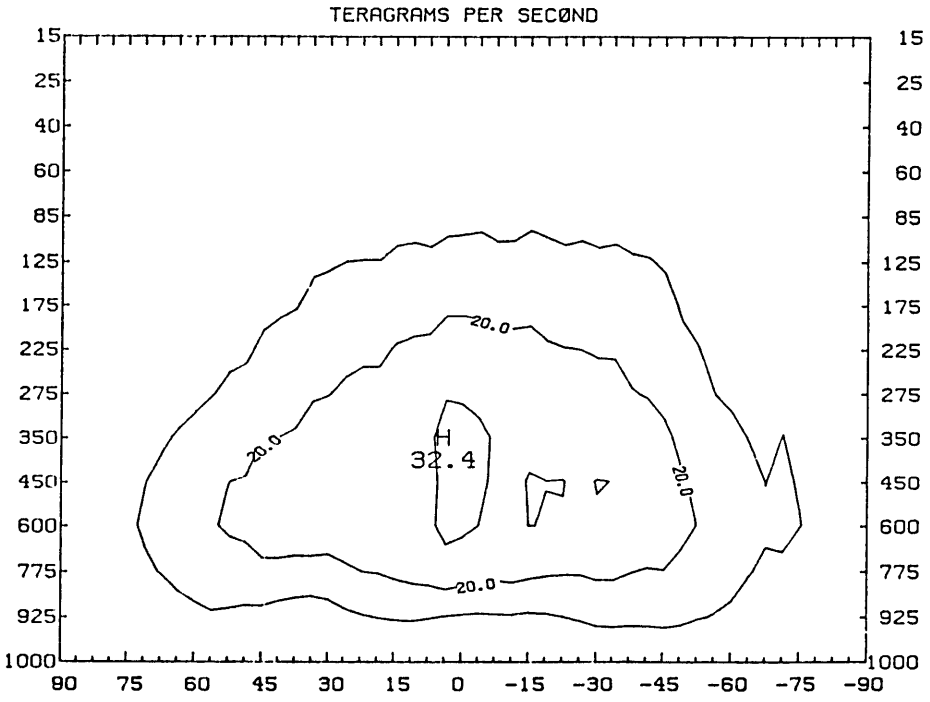

Fig. 6.9 As in Fig. 6.4 but for the streamfunction of the meridional circulation ψ_{MC}. Values in 10^{12} g/s.

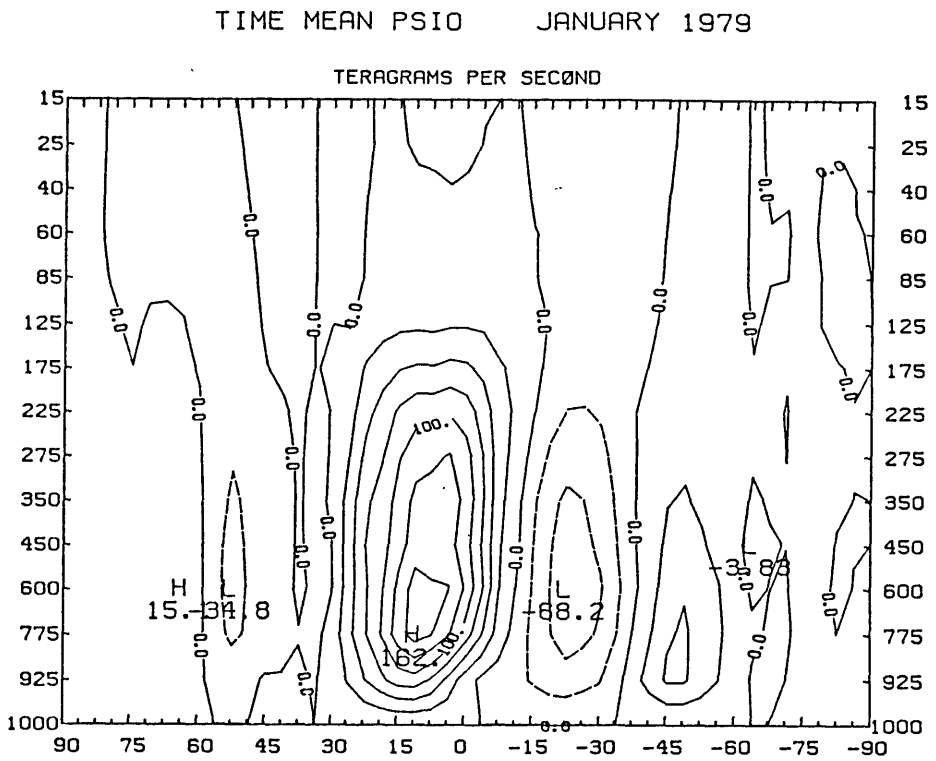

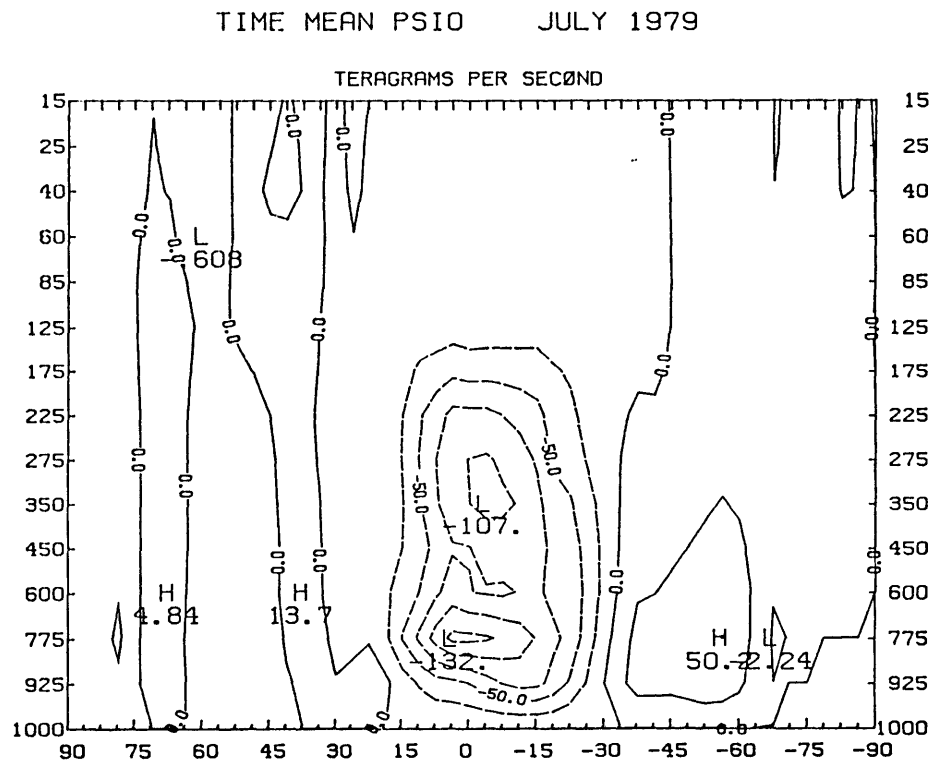

Fig. 6.10 As in Fig. 6.5 but for the streamfunction of the meridional circulation ψ_{MC}. Values in 10^{12} g/s.

made no great impact on the eigenstructure of the leading modes in the analyses as the most prominent variability in ψ_{MC} is centered in the tropics. The EOF procedure used here with regard to normalization of the principal components and the transformation of the eigenvectors is the same as the analyses discussed in Chapter 4. Thus with the standard deviations of the principal components normalized to unity, the eigenvectors can be interpreted as the average amplitude of an anomaly due to that particular mode.

Fig. 6.11 presents the first three eigenvectors and principal components for an analysis of the ψ_{MC} data between 45°S and 45°N and the 9 layers between 100 mb and the surface. The first mode in this analysis contains 71.63% of the variance, and not unexpectedly, its principal component is dominated by an annual cycle. The structure of the eigenvector is nearly equatorially symmetric, being centered at the first northern grid latitude 3.75°N. The meridional wind anomalies derived from this mode, which we have not displayed here, are concentrated in the bottom layers and above 250 mb. Average magnitudes for the 200 mb [v] anomalies near the equator would be in the neighborhood of 0.7-1.0 m/s and at 850 mb closer to 1 m/s. For this mode, positive values of the principal component would yield southward winds in the upper troposphere and northward in the lower troposphere. [ω] anomalies from the first mode near 15°N would have an amplitude on the order of 10 mb/day, upward during positive phases of the principal component.

The second and third modes from this analysis are nearly equal in variance explained, so the question might arise as to their true independence. Although there are hints of 40-50 day variability in the second mode and of a semiannual signal in the third mode which are

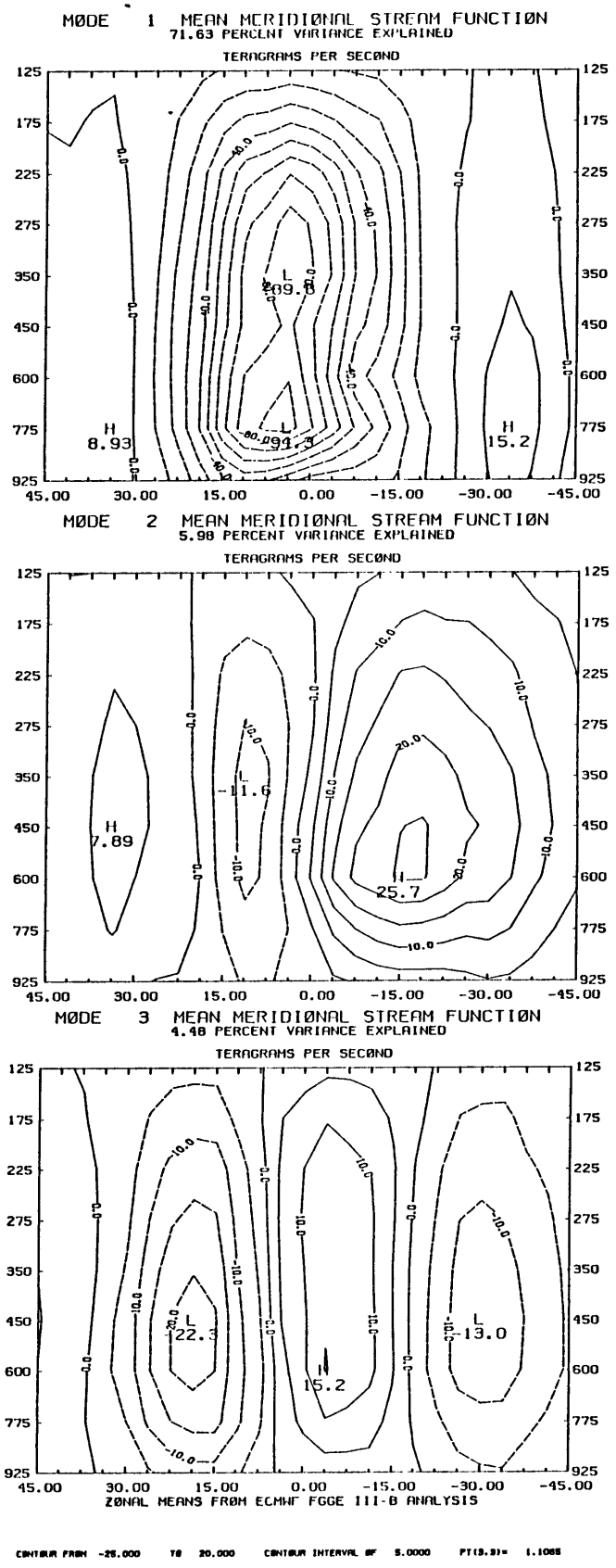

Fig. 6.11a Eigenvectors of the first 3 modes from EOF analysis of the meridional streamfunction for the 25 latitudes 45°N - 45°S and the 9 pressure layers between 100 mb and the surface. Values in 10^{12} g/s.

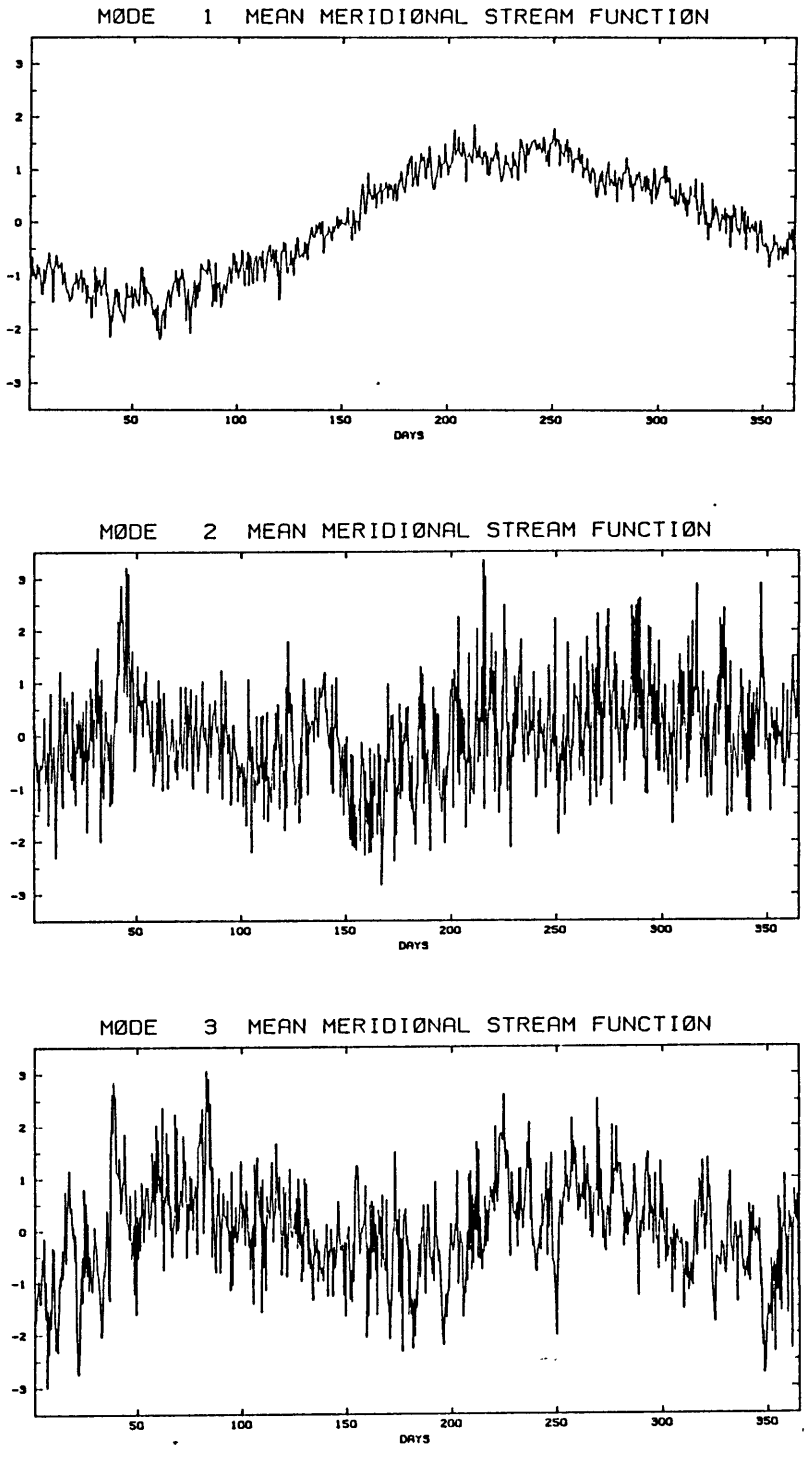

Fig. 6.11b Principal components for the eigenvectors in (a).

probably not accidental, modes 2 and 3 together account for only another 10% of the variance. There is also a suggestion of intraseasonal variability in the first mode. This appears as slight undulations in the principal component of the first mode during the latter half of the FGGE period.

The overwhelming dominance of the seasonal cycle in our analysis of the streamfunction of the meridional circulation, while expected, tends to obscure the intraseasonal phenomenon we are investigating. We have carried out a second analysis, this time for the latitude band between the 30th parallels, on a data set in which we have attempted to remove the annual and semiannual variance. This was effected by frequency domain filtering in a manner similar to the filtering used in the construction of the seasonal cycle in Figure 4.22. Specifically, the first and last 73 of the 730 total values in each latitude-height time series of ψ_{MC} were tapered with a cosine bell and then the entire time series was transformed to wavenumber space. The wave coefficients corresponding to the time average and the first two harmonics were then set to zero. The filtering process was then completed by backtransforming to the time domain the altered set of Fourier coefficients.

The pitfalls in this approach have been discussed by Koopmans (1974, Chapter 6). The perfect "rectangular" highpass frequency response implied by setting a group of the lowest frequency wave coefficients to zero and leaving the remainder unaffected is not possible with any time domain filter of finite length or its equivalent in the wave number domain. Errors are introduced into the filtered time series reconstructed from the wave coefficients due to the uncompensated wings of the perfect filter which has infinite length. These effects

are spread over the entire time series but are greatest at the ends. In practice, after comparing the raw and filtered time series, we found that distortion of the signals was not noticeable.

A second consideration is the attenuation of the unwanted stopband, in this case the frequencies higher than 3 cycles/year. Since the frequency domain implementation of the filter we have been discussing samples at frequencies in multiples of 1/year, the filter design process can be considered a problem in frequency sampling. This is discussed at some length in Oppenheim and Schafer (1975, Chapter 5). They recommend weighting at least one harmonic between the pass band and the stopband to ensure a minimum attenuation in the stopband. For a single harmonic transtion band the optimum weighting is 0.3904. Thus in the frequency domain filtering above we have additionally weighted the wavenumber 3 coefficients before the back transform to the time domain.

Having thus filtered our data set of ψ_{MC} time series, we performed a new EOF analysis. The results (modes 1-3) are displayed in Fig. 6.12 and show definite 40-50 day variability. The first mode explains 26.6% of the variance and, like the first mode of the initial EOF analysis, is equatorially-centered; in this case the center is shifted south of the equator rather than northward. Anomalies of [v] in the upper troposphere associated with the first mode are on the order of 0.2 m/s. The principal component of the first mode considerably noisy but undeniably possesses intraseasonal variance. The eigenvector of the second mode (19.89%) has amplitudes similar to the first, and is primarily a Southern Hemisphere phenomenon. The third mode is out of phase with the second mode and is stronger in the Northern Hemisphere. Both of these modes contain some variance at 40-50 days.

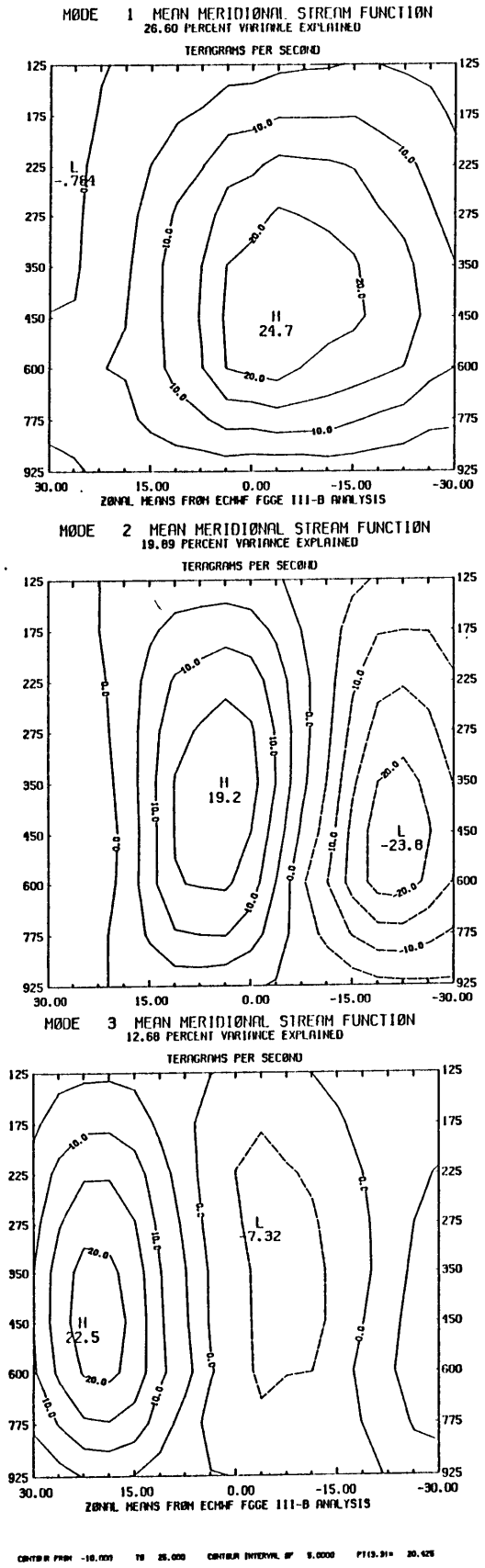

Fig. 6.12a Eigenvectors of the first 3 modes form EOF analysis of the nonseasonal variance of the meridional streamfunction for the 17 latitudes 30°N - 30°S and the 9 pressure layers between 100 mb and the surface. Values in 10^{12} g/s.

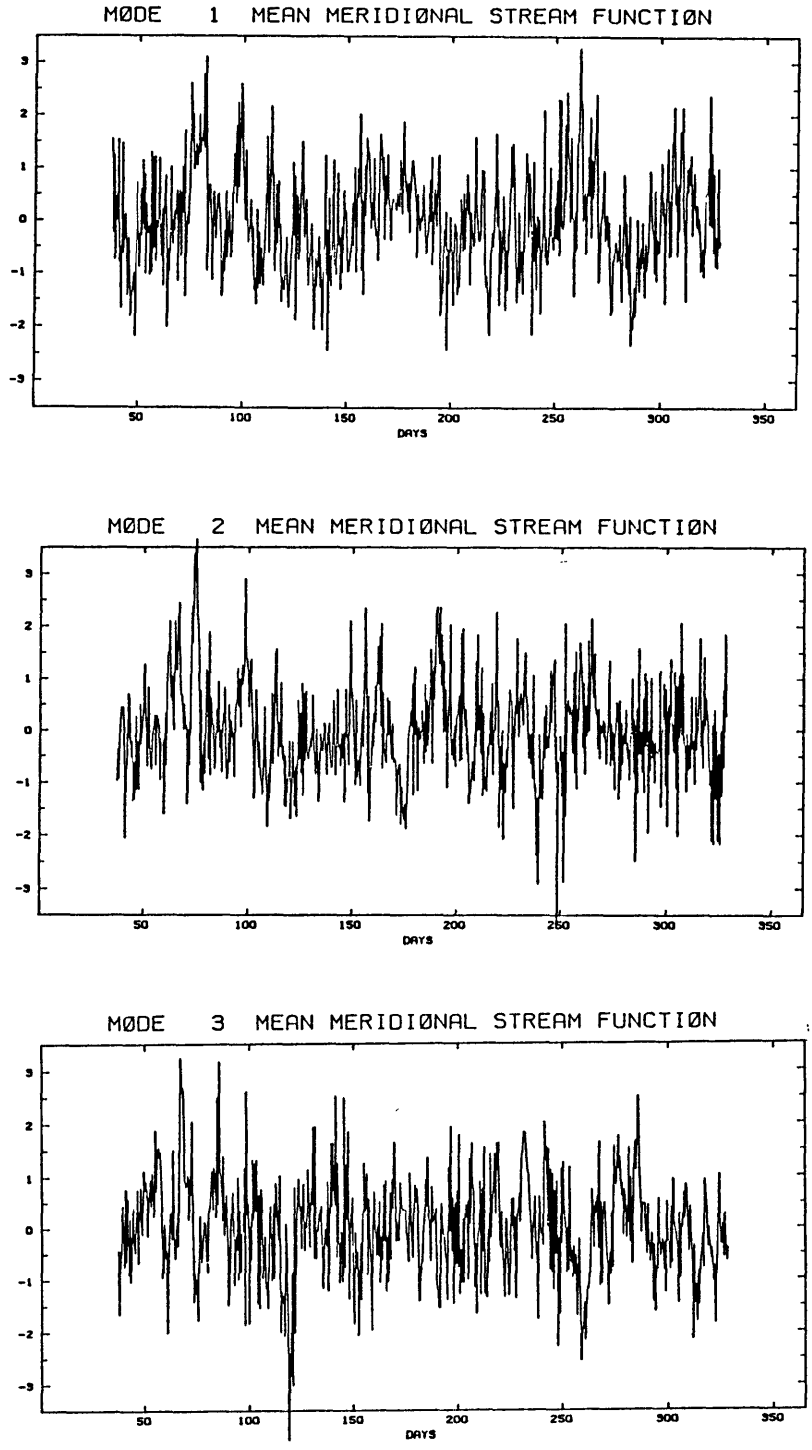

Fig. 6.12b Principal components for the eigenvectors in (a).

6.3 Variations in Zonal Totals of Highly Reflective Cloud

We have seen evidence in the EOF analyses above of intraseasonal variability in the Hadley circulation. It is logical then to ask whether our index of deep convection shows evidence of similar variability. We saw earlier in Fig. 5.13 that there was some tendency for significant portions of the tropics to show nearly simultaneous increases of convection. In this section we examine time series of the total HRC along each of the 13 ECMWF reduced grid latitudes between 22.5°S and 22.5°N.

We present both raw (Fig. 6.13) and filtered (6.14) versions of the HRC time series. The seasonal variability of highly reflective clouds in the fringe latitudes of the Hadley circulation can be seen in Fig. 6.13. South of the equator the peak times for convective activity southward of 15°S are the southern summer months. (We mention again the artificially weak fields for the month of December 1978.) In the north, a similar summer enhancement of convection is particularly noticeable north of 15°N. In lower latitudes there is some indication of a semi-annual cycle which would correspond to the twice yearly passage of the Intertropical Convergence Zone through those latitudes.

The time series shown in Fig. 6.13 show no obvious coherent intraseasonal variability. Not only are the noise levels high, but there appear a whole assortment of long time scales in the data. The time-filtered series in Fig. 6.14 were created using the 44-day bandpass filter (length 75 days) used on the HRC anomalies in Chapter 5. The signal-to-noise ratio of the time series in this figure is marginal as the "hairiness" of the time series attests, so not a great deal of

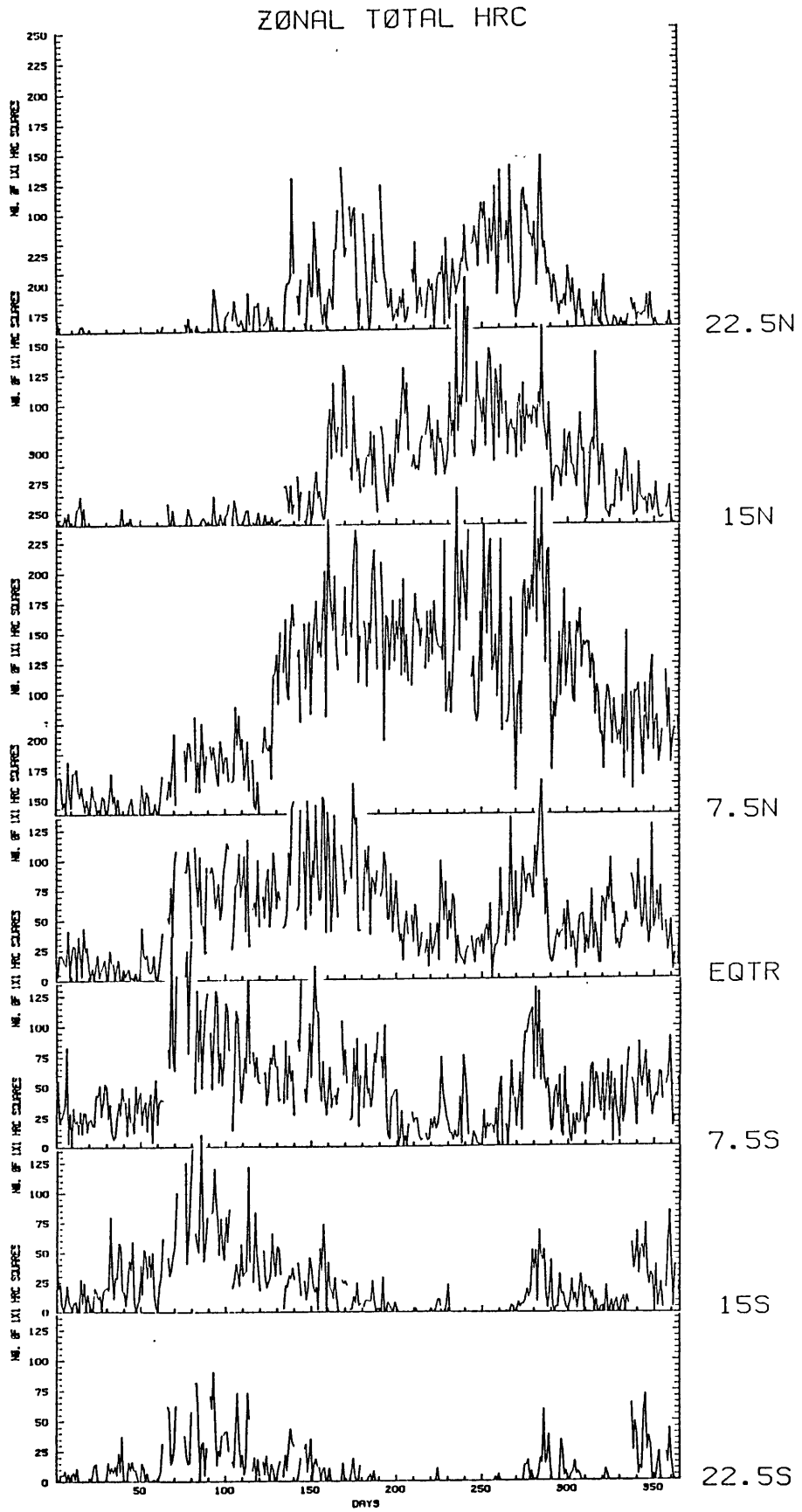

Fig. 6.13 Time series of zonal totals of highly reflective cloud (HRC) in the band from 22.5°N (top) to 22.5°S (bottom). Ordinate is the number of 1°x1° grid squares each day covered by HRC in strips 3.75° wide centered on the respective latitudes.

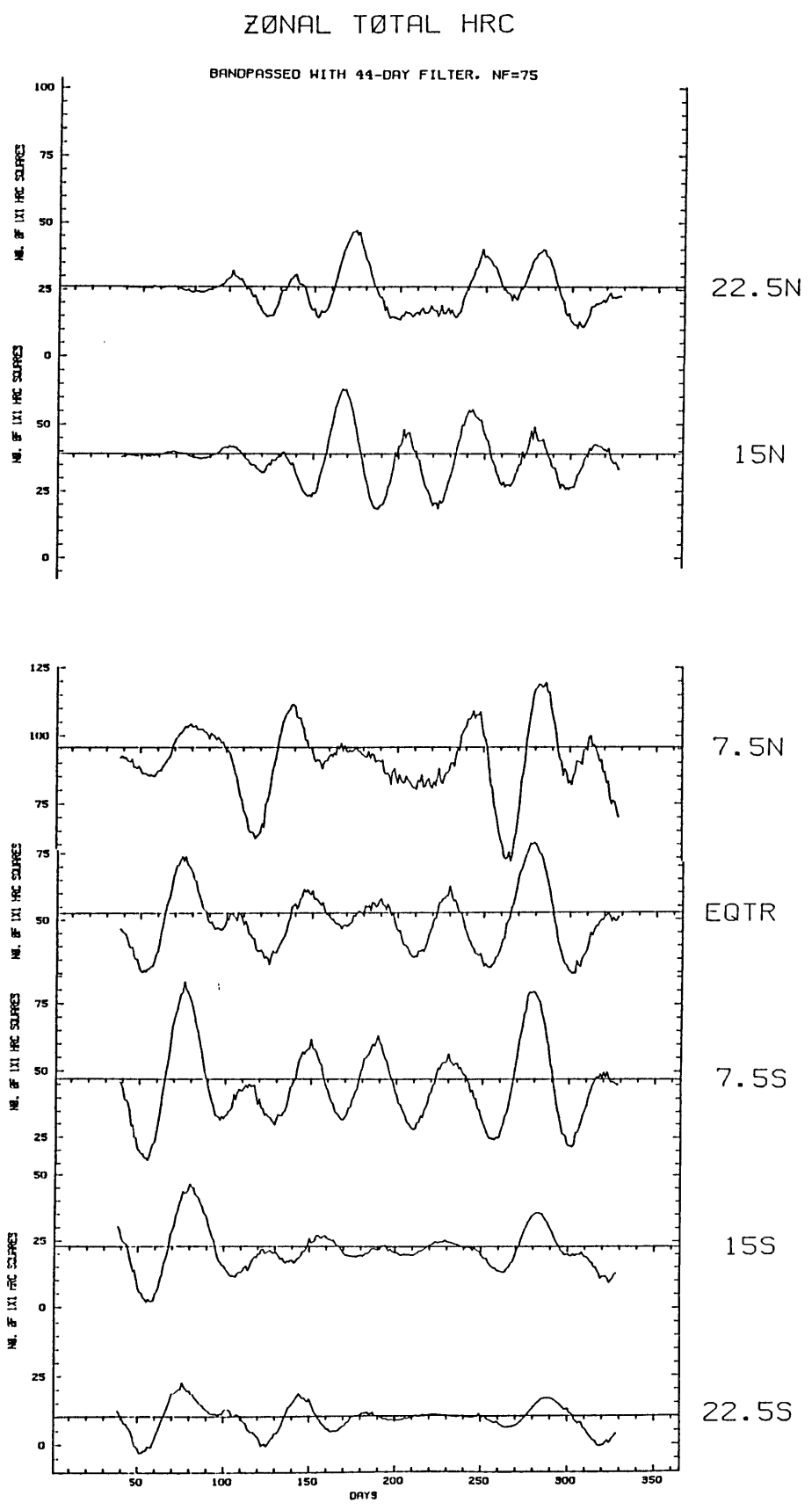

Fig. 6.14 As in Fig. 6.13 but for 44-day filtered values of HRC.

faith can be placed in the resultant series. However several features clearly visible in the original time series are given better definition in Fig. 6.14. The most prominent of these is the peak near days 280-290 which was mentioned in the discussion of the HRC in Chapter 5. A second is an approximately two month stretch of fairly steady zonal total HRC values which spans February and March. Thus although the 40-50 day oscillation does not appear in the zonal average convection, there is evidence of intraseasonal variability to support our finding of intraseasonal behavior in the streamfunction of the meridional circulation. However, this variability is by no means as organized as either the Walker circulation modulation or the 40-50 day changes in the zonal circulation. There is also the possibility that the corrected HRC data set will contain 40-50 variability obscured by the satellite problems (see Section 4.1.2).

6.4 Daily Variations in the Budget of Zonally-Averaged Zonal Momentum

We have demonstrated that there are indeed variations in both the local meridional winds associated with the eastward propagating velocity potential anomalies as well as in the meridional circulation taken as a whole; the question remains as to how 40-50 variability in the meridional circulation is linked to the very prominent 40-50 day variations in the zonal circulation. In this section we demonstrate that insight into the dynamics of the 40-50 day variation in the 200 mb zonal circulation can be gained from the computation of the zonal momentum budget on a time-depedent basis. Although the results are not entirely unambiguous, we will show that the Coriolis torque due to the

Hadley circulation is not directly related to the acceleration of the upper tropospheric zonal mean zonal wind.

It is often difficult to obtain meaningful results from momentum budgets, as the net acceleration is commonly the very small difference between nearly equal but opposing terms. In this respect the uncertainties in geopotential height measurements can prove to be a handicap, especially in mid-latitudes where the winds are in near geostrophic balance. In zonally-averaged budgets, these uncertainties are not a factor, except where they may enter into the estimation of the mountain torque. We can safely ignore the latter component of the momentum balance at the 200 mb level.

Stevens (1979) examined the perturbation zonal momentum balance in composited easterly waves from GATE. He found that the three dimensional advective terms together did not contribute significantly to the net acceleration. In particular, the advection of perturbation zonal momentum by the time average wind field and the advection of time average zonal momentum by the perturbation meridional wind strongly offset the advection of the wave zonal momentum by the time average flow. He considered the evidence for cumulus friction in the field of budget residuals which in his calculations were roughly one-third to one-half the magnitude of the largest of the explicitly calculated terms. No simple pattern seemed to emerge. We note that Sardeshmukh and Hoskins (1985) were able to obtain excellent results in their 150 mb vorticity budgets without resorting to convective scale frictional terms.

Following the notation and the results of Newell et al. (1972) and leaving out terms for the mountain torque and both the vertical eddy and

turbulent fluxes of momentum, we can write the instantaneous momomentum budget for the upper tropospheric zonal circulation as

$$(6.3)\qquad \frac{\partial [u]}{\partial t} = \underbrace{-\frac{[v]}{a\cos\phi}\frac{\partial}{\partial\phi}[u]\cos\phi}_{(1)} \underbrace{- [\omega]\frac{\partial [u]}{\partial p}}_{(2)} \underbrace{+ f[v]}_{(3)} \underbrace{- \frac{1}{a\cos^2\phi}\frac{\partial}{\partial\phi}[u^*v^*]\cos^2\phi}_{(4)}$$

where $[u^*v^*]$ is the horizontal eddy flux due to correlations between deviations in both grid point u's and v's from their respective zonal averages, which at grid latitude j is

$$(6.4)\qquad [u^*v^*]_j = \sum_{i=1}^{N} (u_{i,j} - [u]_j)(v_{i,j} - [v]_j)$$

where N=96 for the reduced ECMWF grid. (In a time average budget, this term would become the standing eddy term.) The remaining notation is as before. In their study of seasonal mean momentum budgets, Newell et al. (1972) found that each of these terms can be of some importance in the upper tropospheric subtropics. The fact that we have not calculated grid point vertical velocities in this study necessitated the omission of the vertical eddy flux term and does not imply that we consider it unimportant. We were able to obtain the zonal mean vertical velocities from our twice-daily data set of ψ_{MC} using Eq. 2.1.

We calculated each of the terms in Eq. 6.3 from the twice-daily data in our zonal average data set for each of our grid latitudes from 15°S through 22.5°N. The eddy term [u*v*] was calculated at the time of the zonal averaging. The procedure for each budget was as follows: first, we computed the tendency term $\partial u/\partial t$ and the righthand side terms (1)-(4); second, (1)-(4) were summed to obtain the net acceleration which we will abbreviate as "RHS"; and third, RHS was subtracted from $\partial [u]/\partial t$ to obtain the residual acceleration which we will call "RES".

Since all the accelerations are here presented in units of m/s/day the time tendency term at observation k was calculated using the simple difference $[u]_{k+1}-[u]_{k-1}$, the time between these k+1 and k-1 being 24 hours. The righthand side terms were scaled upwards the number of seconds in a day, Δt and horizontal derivatives were all approximated by second-order centered differences. Thus we used the following approximations to obtain RHS at latitude j and level l:

$$
\begin{aligned}
(6.5)\quad RHS_{j,l} = & -\Delta t[v]_{j,l}\left(\cos\phi_{j+1}[u]_{j+1,l} - \cos\phi_{j-1}[u]_{j-1,l}\right)/\, 2\Delta a\cos\phi_j \\
& -\frac{\Delta t}{2}\Big([\omega]_{j,l} \quad ([u]_{l,j} - [u]_{l-1,j})\ /\Delta p_l \\
& \quad + [\omega]_{j,l-1} \quad ([u]_{l-1,j} - [u]_{l,j})/\Delta p_{l-1}\Big) \\
& + \Delta t f_j [v]_{j,l} \\
& - \frac{\Delta t}{2\Delta a\cos^2\phi_j}\left(\cos^2\phi_{j+1}[u^*v^*]_{j+1,l} - \cos^2\phi_{j-1}[u^*v^*]_{j-1,l}\right)
\end{aligned}
$$

where the subscripts l and l-1 on $[\omega]$ and Δp refer to the layers above and below 200 mb respectively in which the vertical velocity is defined. The Δp are layer thicknesses in mb. As this equation stands, the residual term RES=$\partial[u]/\partial t$-RHS contains all the observational errors as well as imbalances in the analysis. In addition this term contains physical processes which may be of importance; among these might be cumulus friction and convergence of the vertical eddy momentum flux $[u^*\omega^*]$.

Once the acceleration and residual terms were calculated, we computed period means and standard deviations for each of the terms as well as correlations to the time tendency $\partial[u]/\partial t$ for each of (1)-(4),

RHS, and RES. The above time series, particularly the time tendency, net and residual acceleration terms, are dominated by high frequency signals. In order to display the dynamics of the 40-50 day time scale we filtered each of the time series and computed a set of standard deviations and correlation coefficients based on these as well. The long term means for each of the elements of Eq. 6.5 as well as [u] and the time tendency are tabulated in Table 6.2. The standard deviations for both the unfiltered and filtered time series at 6 latitudes between 22.5°N and 15°S are shown in Table 6.3; correlations are in Table 6.4. The 18 degrees of freedom for the correlation coefficients of the filtered series was estimated from the approximate fraction (~2.4%) of the full spectrum (0.0 - 1/day) which is passed by the bandpass filter.

In addition we present in Figs. 6.15-20 the results from the budget calculations for the 6 latitudes 22.5°N - 15°S respectively in the form of time series for each of the terms involved. In the left upper half of each figure are displayed the unfiltered time series of [u], $\partial[u]/\partial t$, RHS, RES and in the left upper half the four righthand side terms from Eq. 6.5 in order, i.e. the meridional advection of zonal momentum, the vertical advection, the Coriolis torque and the convergence of the horizontal eddy momentum flux. The format for the 40-day filtered time series appearing in the lower half is slightly different. In order to compare phases and magnitudes in the 40-50 day band, the time series of $\partial[u]/\partial t$ is not presented separately but is instead superposed (in solid) upon each of the other terms which are drawn with dashed lines. Otherwise the format is the same as the upper half.

It is apparent from Table 6.2 that the year's mean momentum budget is not balanced, generally to the extent of several tens of cm/s per

Table 6.2 FGGE Means of [u] and Components of Momentum Equation at 200 mb 12/1/78 - 11/30/79

(Individual terms are numbered as in Eq. 6.3)

Term:	22.5°N	15°N	7.5°N	EQTR	7.5°S	15°S	Units
[u]	18.19	9.42	0.43	-2.25	2.06	11.65	m/s
(1)	-0.40	-1.03	-0.68	-0.45	-0.90	-1.20	m/s/day
(2)	-0.11	-0.08	0.01	0.04	0.00	-0.02	"
(3)	2.39	2.63	0.72	----	1.36	2.69	"
(4)	-2.16	-2.00	-0.18	0.03	-0.58	-1.03	"
RHS	-0.29	-0.49	-0.14	-0.39	-0.12	0.44	"
$\partial [u]/\partial t$	0.02	0.01	-0.02	-0.02	-0.01	0.01	"

day. From the size of the terms in the table we could guess that the imbalance lies in analysis bias underestimating the zonal average wind; the Coriolis torque is the largest single portion in the mean imbalance and likely to be less accurately measured than the eddy flux term although additional imbalances arising from the uncalculated terms as well as the eddy flux could certainly important.

Tables 6.3 and 6.4 as well as the figures provide information on the degree to which the time tendency of the zonal circulation on any given day is accounted for in the terms computed here. However, the results clearly suggest that the vertical advection term is not of major importance in either the filtered or unfiltered momentum balance. The remaining three terms each contribute significantly to RHS, the Coriolis torque being the largest term off the equator, followed by the eddy flux convergence and the horizontal advection. However, at all of the latitudes shown here the residual term RES is of the same magnitude as the other terms on a day-to-day basis. In particular, in four out of the five latitudes it exceeds the size of RHS. Apparently this term must contain either large analysis errors, large vertical eddy flux convergences or a combination of both. On the face of it further inferences from the results might appear quite speculative.

We can make an estimate of the importance of the vertical eddy flux divergence by considering both the mean and time varying behavior of the velocity potential and divergence. In Fig. 4.5 it is apparent that the 200 mb divergence values in the primary centers of the equatorial profile have positive peak values of over 1.5×10^{-6} s^{-1}. 40-50 day anomalies of divergence are of this magnitude. If we make the reasonable assumption that upward velocities in the 40-50 day convective

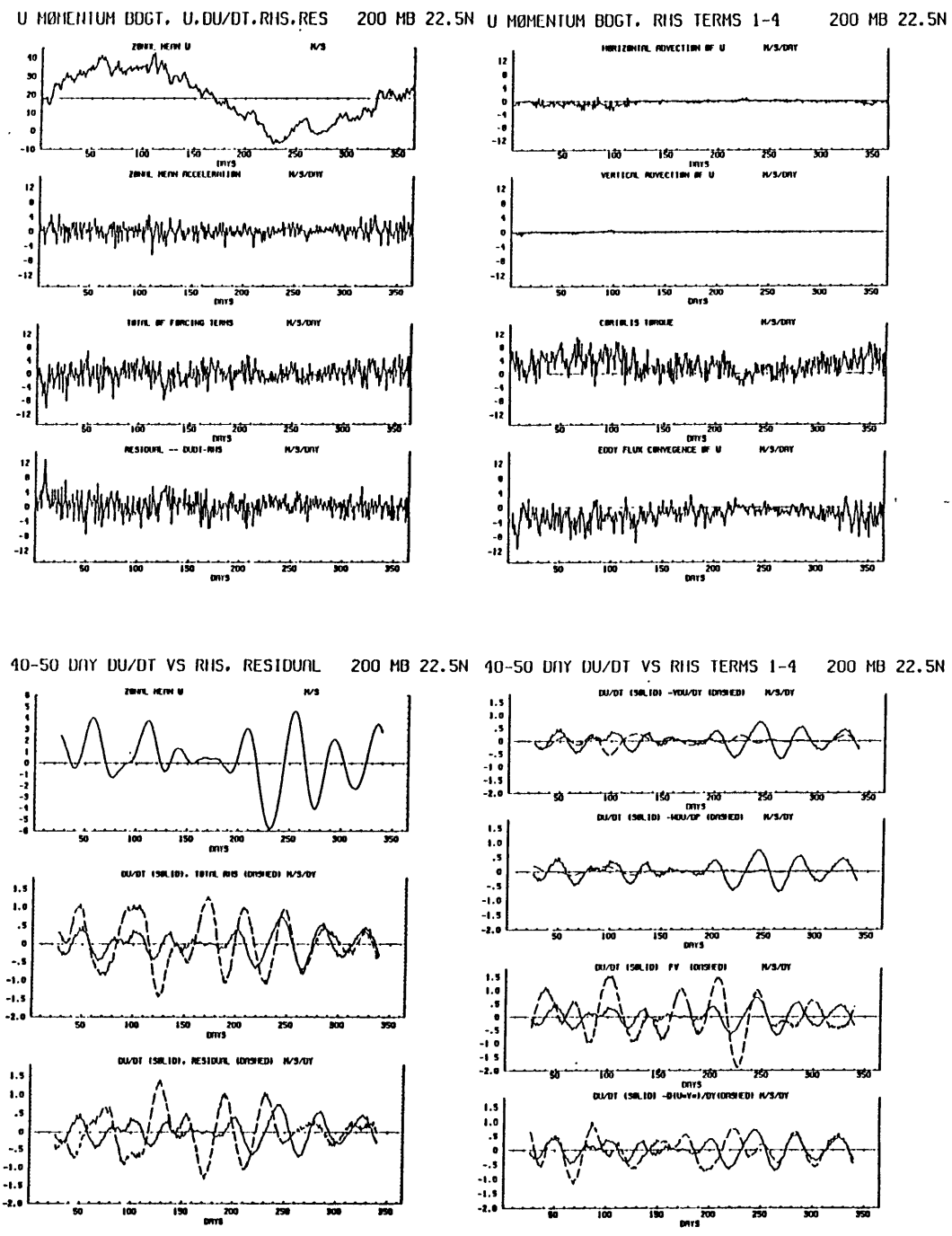

Fig. 6.15 Results from instantaneous zonal momentum budget calculations at 22.5 N. Upper left: unfiltered time series of [u], $\partial[u]/\partial t$, RHS, RES. Upper right: the four righthand side terms from (6.5) in order, i.e. the meridional advection of zonal momentum, the vertical advection, the Coriolis torque and the convergence of the horizontal eddy momentum flux. Lower left: 40-day filtered time series of [u], RHS and RES, the latter two (dashed) are superposed by the 40-day filtered time tendency (solid.) Lower right: 40-day filtered series for the four righthand side terms (dashed) also superposed by the time tendency.

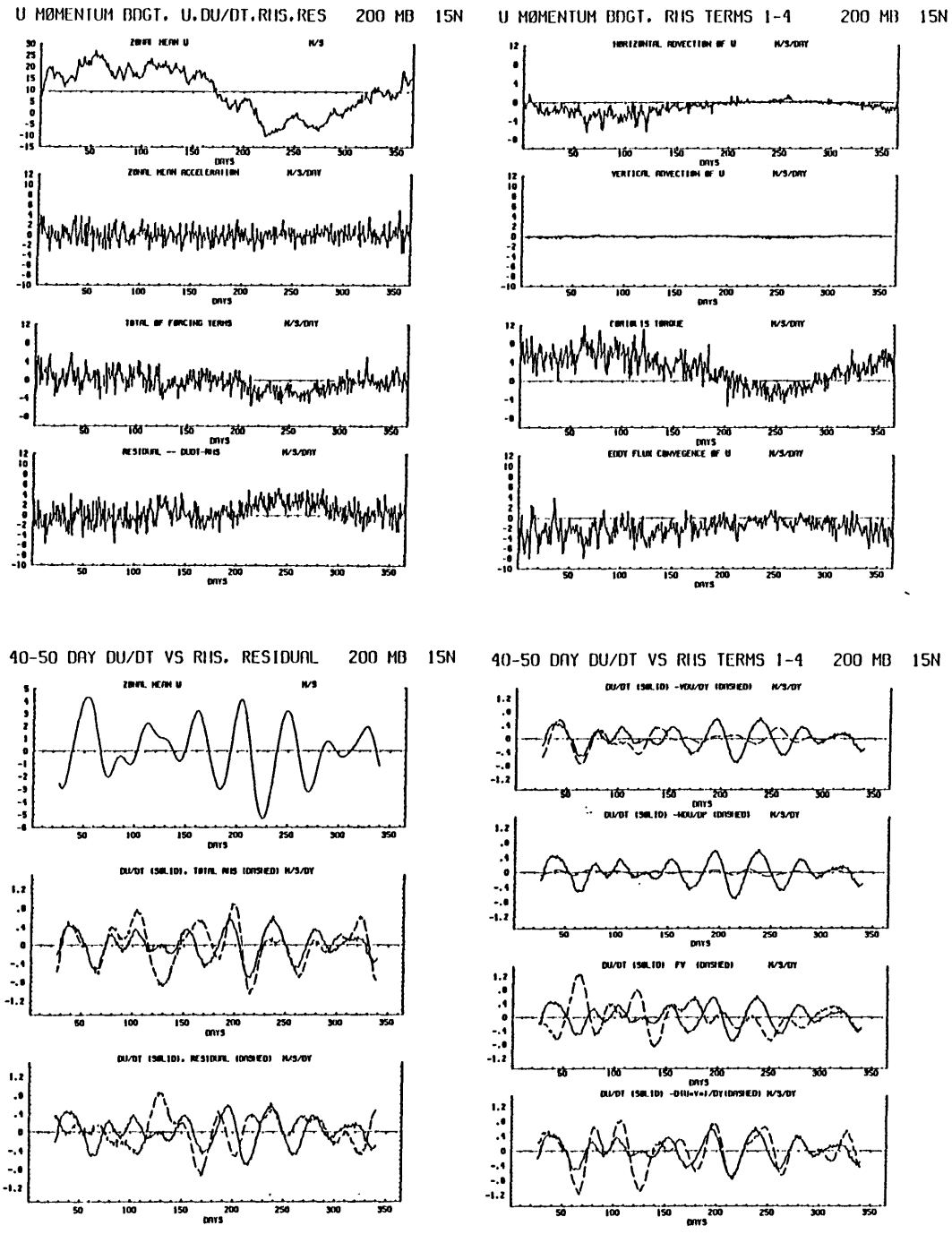

Fig. 6.16 As in Fig. 6.15 but for 15°N.

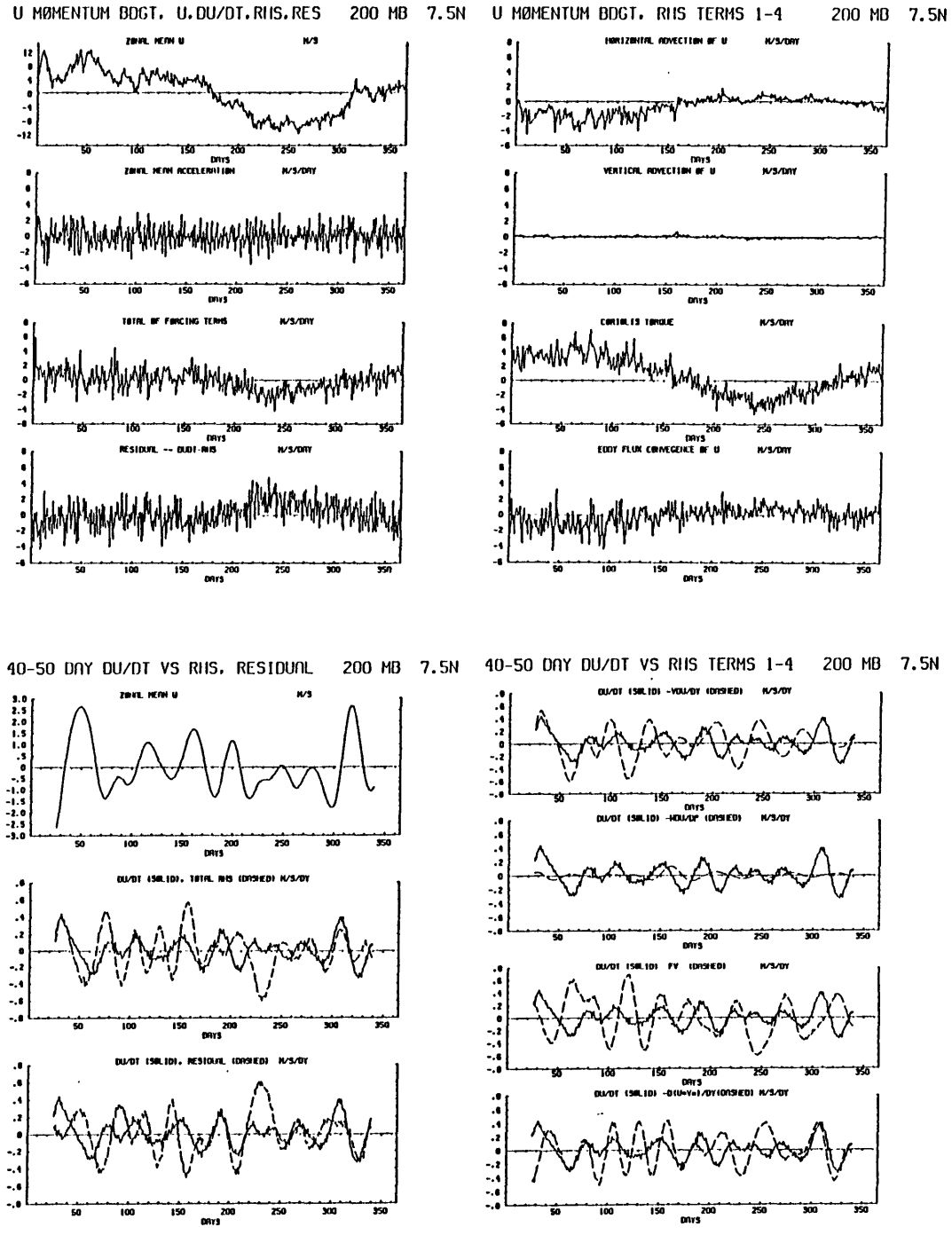

Fig. 6.17 As in Fig. 6.15 but for 7.5°N.

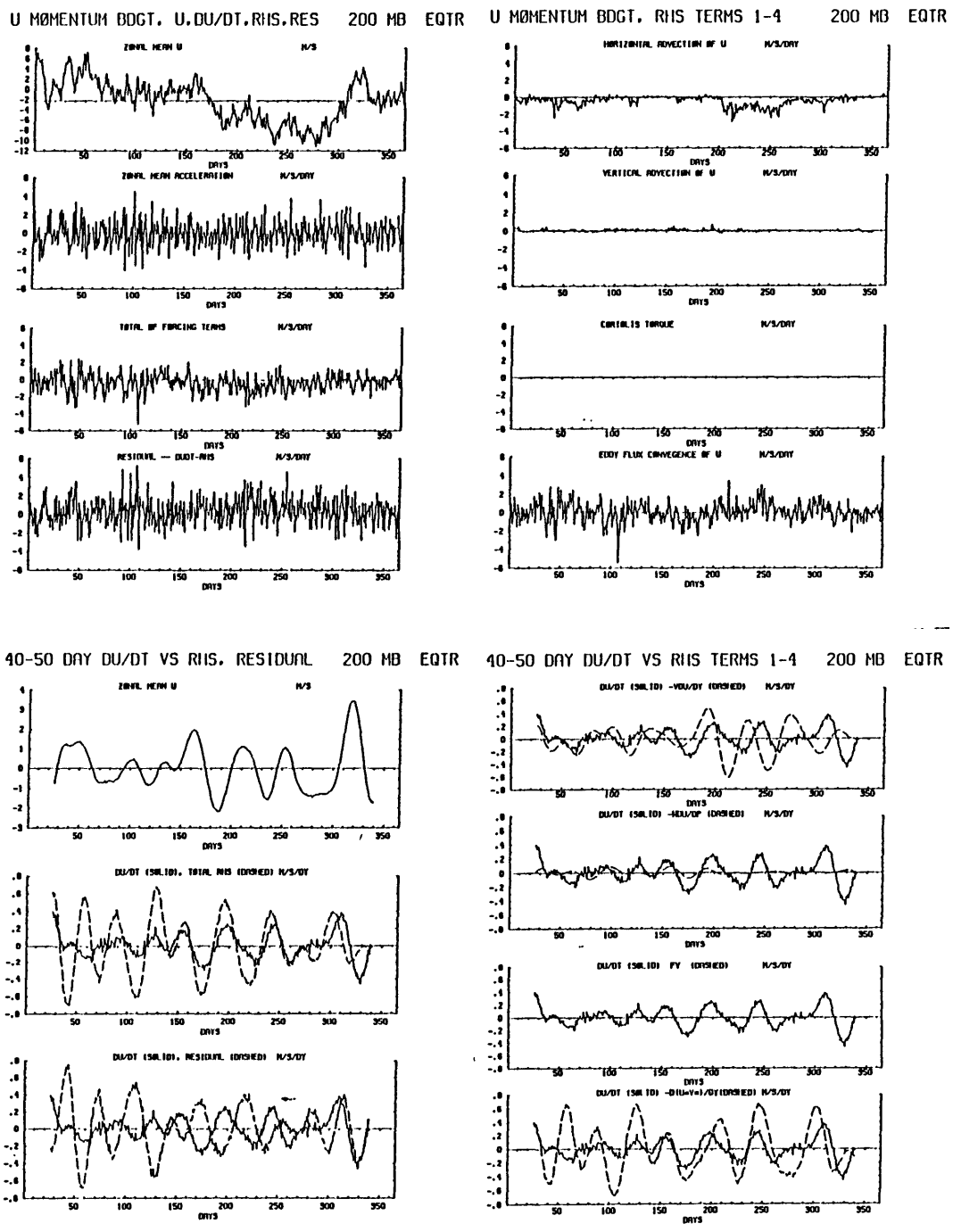

Fig. 6.18 As in Fig. 6.15 but for the equator.

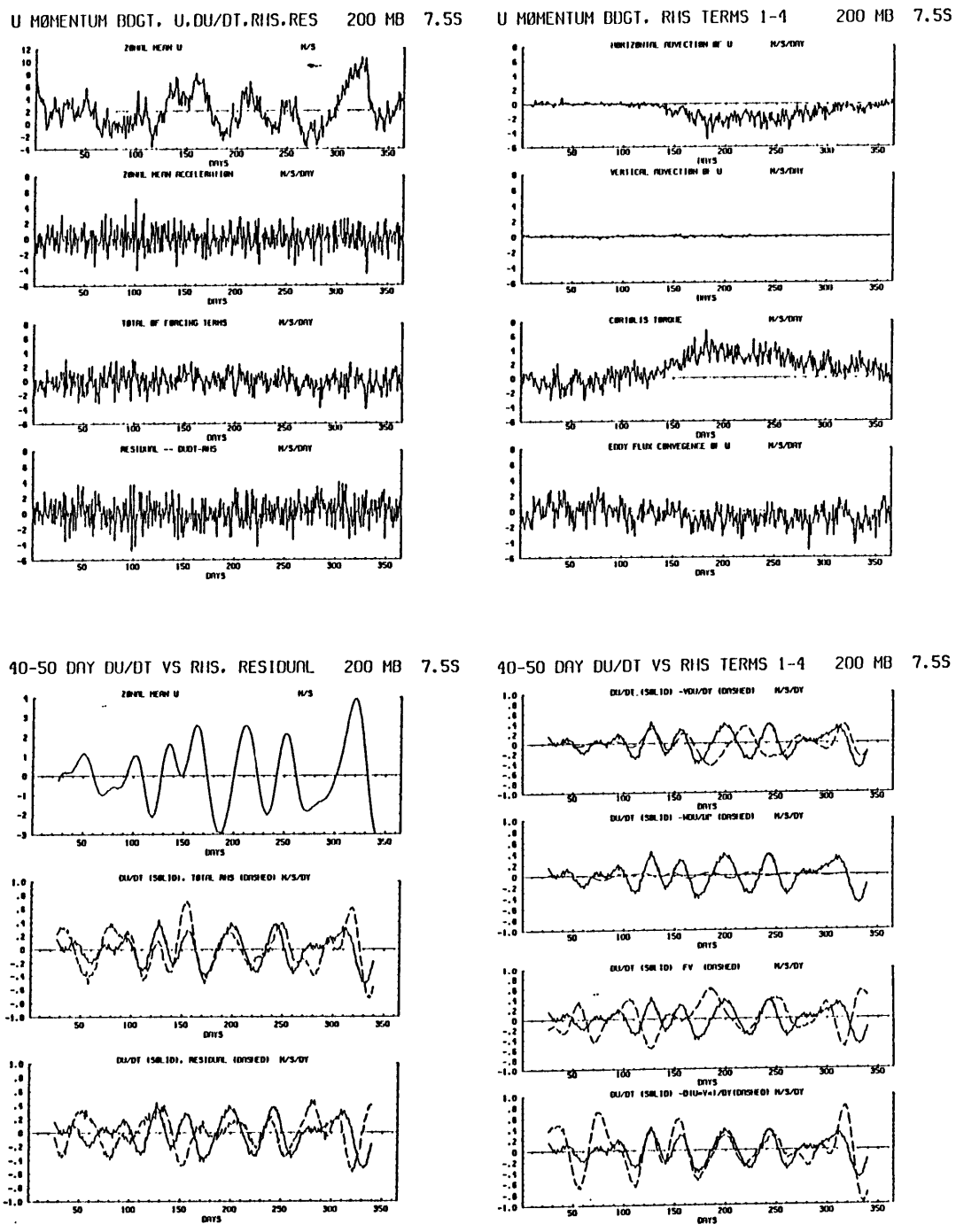

Fig. 6.19 As in Fig. 6.15 but for 7.5°S.

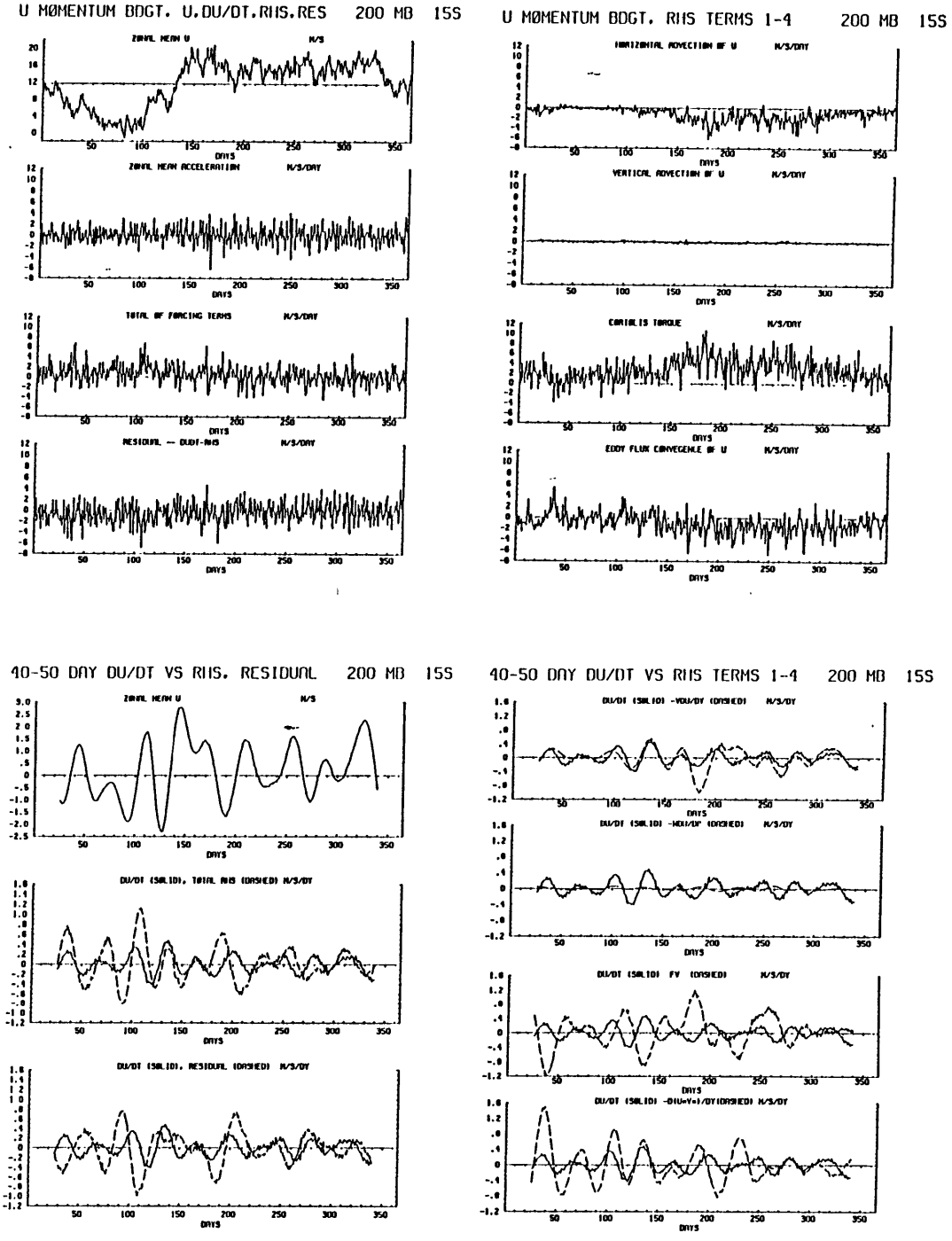

Fig. 6.20 As in Fig. 6.15 but for 15°S.

Table 6.3 Average Amplitudes of [u] and Components of Momentum Budget at 200 mb 12/1/78 - 11/30/79

(Individual terms are numbered as in Eq. 6.3)

Unfiltered

Term:	22.5°N	15°N	7.5°N	EQTR	7.5°S	15°S	Units
[u]	13.13	9.69	6.17	4.06	2.80	5.37	m/s
∂[u]/∂t	1.55	1.36	1.18	1.28	1.26	1.38	m/s/day
(1)	0.60	1.33	1.21	0.55	1.03	1.21	"
(2)	0.16	0.15	0.11	0.10	0.10	0.11	"
(3)	2.75	3.28	2.50	----	1.71	2.18	"
(4)	2.19	1.76	1.18	0.99	1.23	1.66	"
RHS	2.43	1.96	1.35	0.98	1.15	1.64	"
RES	2.38	1.96	1.51	1.33	1.41	1.70	"

Filtered

12/26/78 - 11/5/79

Term:	22.5°N	15°N	7.5°N	EQTR	7.5°S	15°S	
[u]	2.21	2.14	1.12	1.17	1.56	1.14	m/s
∂[u]/∂t	0.31	0.29	0.15	0.15	0.21	0.17	m/s/day
(1)	0.16	0.23	0.24	0.22	0.18	0.28	"
(2)	0.06	0.05	0.04	0.04	0.03	0.03	"
(3)	0.71	0.41	0.30	----	0.28	0.43	"
(4)	0.43	0.45	0.24	0.34	0.37	0.45	"
RHS	0.64	0.43	0.24	0.32	0.30	0.36	"
RES	0.55	0.33	0.24	0.27	0.22	0.33	"

overturnings peak in mid-troposphere, the divergence is roughly equal to 2×10^{-4} mb/s at 500 mb. With a divergent u anomaly near 3 m/s, the vertical eddy flux divergence could be as large as 0.2 m/s/day. It would appear then that this omitted term ought to be considered before any final conclusions are drawn.

With this in mind, the correlation results make it clear that the Hadley momentum advection as well as the Coriolis torque are not in phase with the acceleration of the zonal circulation, although they are important in RHS. In contrast, the unfiltered horizontal eddy flux convergence is significantly correlated to $\partial[u]/\partial t$ at each of the six latitudes; the 40-50 day correlations are significant in four cases. While conclusions as to a major role for the horizontal eddy flux convergence cannot be drawn without the benefit of information on the convergence of the vertical flux $[u^*\omega^*]$, it is quite clear that along with the mean horizontal and vertical advection terms, it is not the Hadley circulation which is driving the 40-50 day oscillation in the zonal circulation over the tropics. Furthermore, if it could be shown that the vertical eddy flux convergence does not completely cancel the horizontal convergence (or vice versa), we could speculate that a necessary condition for the oscillation is the presence of zonally asymmetric diabatic heating connected with the eastward propagating modulation of the Walker circulation.

Chen (1985) has examined the time dependence of the enstrophy budget for the northern summer season during FGGE. (Enstrophy is the vorticity squared and as such it represents the intensity of deviations from uniform horizontal flow.) Some of his findings have bearing on the results here. In the tropics he found that the vertical average

Table 6.4 Correlations of Momentum Equation Components to $\partial[u]/\partial t$ at 200 mb (in hundredths)

(Individual terms are numbered as in Eq. 6.3)

Unfiltered

Term:	22.5°N	15°N	7.5°N	EQTR	7.5°S	15°S
(1)	-3	2	5	3	2	0
(2)	2	-4	2	4	-6	4
(3)	3	1	0	---	-0	-0
(4)	35	36	27	30	30	38
RHS	34	35	28	32	32	38
RES	30	35	53	72	63	45

95% Significance Level (d.f.=729) 0.096
99% 0.070

Filtered

Term:	22.5°N	15°N	7.5°N	EQTR	7.5°S	15°S
(1)	-0	22	24	2	17	59
(2)	25	32	-7	19	-29	7
(3)	28	-23	-15	---	-26	-51
(4)	26	68	27	46	66	44
RHS	50	64	27	53	65	39
RES	-3	6	34	-6	9	10

95% Significance Level (d.f.=18) = 0.444
99% 0.561

enstrophy, which primarily reflects activity in the upper troposphere, the 200 mb level in particular, had a clear modulation at the 40-50 day time scale during the period. He notes 40-50 day variations in the generation of enstrophy due to correlations between vorticity and divergence (at both 200 mb and the surface) and in the vertical flux of enstrophy from the surface. Both of these would suggest a significant role for vertical eddy fluxes in the zonal momentum budget.

In Chen's time mean budget, the most important contribution to the zonally averaged enstrophy was the "beta" effect, expressed as the product of three factors: the gradient of planetary vorticity β, the meridional circulation [v] and the zonal mean relative vorticity. Since the latter is equal to minus the gradient of the zonal mean zonal wind, the entire term is directly proportional to the Hadley advective term in the zonal momentum budget. We have shown that the advection is of some importance in both the time mean and time dependent momentum budget, although with the exception of 15°S, it is not strongly correlated to the time tendency at 40-50 days. Similarly, Chen found little 40-50 day signal in the zonal mean beta term in the enstrophy budget.

Chen also determined that the beta effect in the eddy enstrophy budget, due to the eddy flux of relative vorticity ($[v^*\zeta^*]$ in our notation) is not important either at 40-50 days. If we assume that the divergence is somewhat smaller than the vorticity, the zonal mean of the eddy flux of vorticity is equivalent to the convergence of the horizontal eddy flux of zonal momentum. As we did find a substantial relationship between this flux convergence term and the zonal mean momentum time tendency at 40-50 days, our results are somewhat

contradictory. Some of the difference may be due to the fact that his calculations were summed over the entire tropical zone.

Several considerations suggest possible avenues for further investigation of the zonal momentum budget of the 40-50 day oscillation but which are beyond the scope of this study. In the present Eulerian frame, imbalance between the Coriolis torque and the eddy flux convergence (including the vertical eddy flux convergence if it could be reliably estimated) would indicate violation of the conditions of noninteraction between the waves and the mean flow (see e.g. Edmon et al., 1980) One important condition for noninteraction is diabatic heating; we suggest that one interpretation of an apparent lack of cancellation between the Coriolis torque and the eddy flux term is the presence of significant zonally asymmetric diabatic heating at the latitude of consideration. In the HRC data we have, in principle, a means of independently specifying regions of strong latent heating.

Chapter 7. Summary and Conclusions

In this work we have described the spatial structure and temporal evolution of the 40-50 day oscillation in the large scale divergent circulation of the tropical troposphere. Previous work had established the oscillation as a significant feature of the variability of the asymmetric tropical zonal wind field (Madden and Julian, 1971, 1972) and of the zonally averaged zonal wind in the upper troposphere (Anderson and Rosen, 1983). In this work we have considerably expanded upon the study by Lorenc (1984) who established that the 40-50 day oscillation is the dominant mode of variability at intraseasonal time scales of the large scale divergent circulation in the tropics. This oscillation appears prominently in the tropical zonal divergent wind field; we have referred to this aspect of the phenomenon as a modulation of the Walker circulation. There is also evidence for the oscillation in the zonally asymmetric divergent meridional winds as well as a somewhat weaker and longer period oscillation in the Hadley circulation as a whole. Using instantaneous momentum budgets we have investigated interrelationships of the zonally symmetric and asymmetric components of the oscillation.

In this final chapter we summarize our findings in the context of the expanding observational literature on the 40-50 day oscillation and the implications for theoretical understanding of the phenomenon. This discussion will point toward possible avenues for further diagnostic and theoretical investigations.

7.1 Some Methodological Considerations

We began this work as an attempt to utilize the superior data coverage and density of the FGGE observing systems to identify the day-to-day variability in the divergent wind fields over the tropics. Our primary data for this study were the wind fields from the 15-level FGGE III-b global analysis from the European Centre for Medium Range Weather Forecasts. From these data we derived two levels of velocity potential fields and 15 of zonally averaged winds.

Previous to this work global fields of velocity potential had been used to characterize the seasonal as well as interannual variability of diabatically-forced circulation systems in the tropics; in this work we have addressed the variability in the individual analyses rather than time averages. Our hope was that, at least in the European Centre's analysis procedure, the analysis of the divergent circulation in the tropics was of high enough quality to reveal coherent variations in space and in time. We have shown that it is certainly capable of preserving the gross characteristics of a diabatically forced planetary-scale phenomenon, albeit relatively slowly fluctuating. These characteristics include the collocation of convergence in the lower levels with divergence in the upper troposphere. Indeed, results from investigations of the properties of the ECMWF analysis procedure which we reviewed would suggest that the analysis would have difficulty establishing even the proper sign of the divergent wind field near the equator.

Empirical orthogonal function (EOF) analysis has been used to extract the primary modes of variability over the tropics and subtropics

in both the velocity potential and the meridional streamfunction. Since the leading modes of the velocity potential analyses tend to be highly coherent in both space and time, we have used fields of velocity potential reconstructed from just a few modes in order to examine the behavior of the 40-50 day oscillation during the year. Time series of divergent winds derived from these reconstructions have been employed here as well.

The results from four different EOF analyses of the velocity potential have been presented. Each of them takes as its spatial domain a set of zonal wavenumbers at the 25 latitudes from 45°S to 45°N, although we have found that these poleward limits are not critical for the structure of the leading modes.

The interpretation of empirical orthogonal function analysis applied to the time behavior of a dynamical system is fraught with certain hazards, some of which we have already discussed in Chapter 4. We make some additional comments here. First, one assumes statistical stationarity of the system in question. Then, because the EOFs derived from a particular set of data (realization of the system) are merely estimates of the "true" EOF's, one must ascertain that the derived EOFs can be identified with individual "true" modes. Finally, physical interpretation of individual EOF modes is easiest when there is a clear relationship between the "true" EOF's of the dynamical system and its normal modes. North (1984) has found that EOF-normal mode parallelism breaks down in the case of systems in which the physical modes of variability are not orthogonal. This is commonly the case with climate systems which have complex interrelationships of decay and growth modes. Horel (1981, 1984) has argued further that the use of EOF's should be

restricted to truly global phenomena, regionally confined phenomena being better represented by rotated eigenvectors. Finally, the question remains as to the usefulness of standard EOF analysis in the examination of wave phenomena. In the case of a purely progressive wave of a well-defined frequency Horel (1984) finds that conventional and complex EOF analysis are equally well-suited to the analysis of a dynamical system; conventional analysis simply uses two (real) modes for the single (complex) mode in the latter analysis. He finds however that complex EOF analysis has the potential to discriminate between standing and propagating waves which conventional analysis does not.

In the case of the velocity potential, especially at 200 mb, our results with a conventional EOF analysis show a progressive wave with generally global characteristics. In particular, the association of localized poleward meridional winds reconstructed from the leading modes in the EOF analyses with an index of diabatic heating certainly lends physical meaning to the pairs of EOFs which describe the propagating velocity potential wave.

7.2 Variability of the Walker Circulation

The FGGE time mean as well as seasonal characteristics of the zonally asymmetric divergent circulation have been described in Chapter 4. We have represented the Walker circulation by means of equatorial band profiles of velocity potential, the divergent zonal wind and the divergence, and each demonstrates the strong coherence between lower and upper tropospheric divergent flows. Furthermore, the excellent correspondence between the profile of highly reflective cloud and the upper

level divergence further strengthens the connection between the Walker circulation and the longitudinal variability of latent heating. The seasonal cycle in the divergent circulation is distinguished by a northwest-southeast shifts of the centers of divergence and velocity potential over the maritime continent/western Pacific region and the Americas. These are accompanied by corresponding changes in the HRC fields.

In the first velocity potential EOF analysis (C201025, Fig. 4.20) the "semi-spectral" spatial domain consists of waves 0-10 at 200 mb . Nearly 75% of the variance in these waves is contained in the first three EOF modes. In the first mode, which alone explains nearly a third of the variance, most of the variability is related to the seasonal movement of the Hadley cell between the Northern and Southern Hemispheres. Although there is some 40-50 day variability in the first mode, it is small in comparison to the amplitude of the seasonal cycle. 40-50 variability dominates in the second (22.3%) and third (14.5%) modes. As the gross structures of both the eigenvectors and principal components in each mode are essentially similar, these two modes are best treated as a pair, the differences between them being primarily a quarter-cycle phase shift in time and in space. With this relationship the 40-50 day variance accounted for by these modes appears in the form of anomalies which propagate eastward across the equatorial zone. We have presented (Fig. 5.8) time series of divergent zonal wind derived from reconstructions of the velocity potential from the time mean and the first seven modes of this EOF analysis. The strongest 40-50 day fluctuations in the divergent zonal wind field at the equator have

amplitudes on the order of 2 m/s and appear in the region between ~60° E and the dateline.

A second EOF analysis (C201025W, Fig. 4.23) was performed in which we did not include the zonally symmetric (wave 0) variance at each of the latitudes. This essentially eliminates the seasonal variance that comprised the first mode in the first analysis. Thus, despite some minor differences in detail, the first two modes of the second analysis are practically identical to the second and third modes of the first. It appears that some of the zonally asymmetric variance from the first mode in C201025 is carried in the third mode of C201025W.

A strong inverse relationship between the divergent flow in the upper and lower troposphere can be seen by comparing C201025 with the results from the third EOF analysis (C851025, Fig. 4.24) which is of the 850 mb velocity potential, waves 0-10. As in C201025, the dominant variance in C851025 is both seasonal and zonally symmetric, although in this case it appears to be split between modes 1 and 2 instead of simply the first. Although the principal components are somewhat noisier at this level, the contributions to 850 mb anomalies from these modes are generally in opposition to 200 mb anomalies from the first mode of C201025. This property is even more characteristic of variations in the divergent zonal wind contributed by the third and fourth modes which are analogous to the primary zonally asymmetric modes of the 200 mb analyses. For example, in the case of mode 2 of C201025 and mode 3 of C851025, the principal components are nearly indistinguishable and the extrema in the eigenvectors are nearly perfectly opposed.

We combined variance in waves 1-5 at 850 mb with the same at 200 mb in our final velocity potential EOF analysis (C820525W, Fig. 4.27).

Because it eliminates the zonally symmetric components of the velocity potential from consideration, the eigenvectors of the leading two modes describe a Walker circulation, i.e. easterly divergent winds in the lower levels are contrasted at the same longitude with westerlies in the upper levels and vice versa. As the previous analyses strongly suggested, extrema of one sign at one level are very nearly collocated with those of the opposite sign at the other.

This strong opposition of velocity potential anomalies is consistent with the simplified concept of tropical convection as essentially a two-layer phenomenon with inflow in the lower levels and outflow at higher levels. We note that the results of C820525W indicate that the amplitude of collocated anomalies of velocity potential are somewhat larger at 200 mb than at 850 mb. Until the vertical structure of variations in the divergence is studied with several more levels this question may not be fully answered. However the discrepancy may be due to the 850 mb level lying somewhat higher than the level of maximum low level convergence on the convective scale (see e.g. Houze and Betts, 1981). This suggests that it might be useful to include in further work a velocity potential analysis at 1000 mb or some other suitable level within the planetary boundary layer. In any case the physical plausibility of the 200/850 mb relationship is further indication that the European Centre's analysis is correctly assimilating the divergent circulation at large scales.

As an independent indicator of the changes in convection we have presented time series of an index of highly reflective cloud at a number of locations around the equatorial belt. There is evidence for significant 40-50 day variability in convection over the eastern Indian

Ocean; this is the same region in which the divergent wind anomalies presented in Chapter 5 are largest. In fact, we have shown that positive divergent zonal wind anomalies at 200 mb lead increases of highly reflective cloudiness over the eastern hemisphere region where the anomalies are the strongest. Eastward propagation of divergent wind anomalies over a large portion of the western hemisphere appears to be inhibited by westward propagation of cloudiness anomalies.

7.3 Variability of the Meridional Circulation

We have examined the variability of the meridional circulation in terms of both the zonal average of the meridional wind field and the streamfunction calculated therefrom. The seasonal variability reflects the north-south excursions of zonally symmetric rising motion; this is in fact the dominant variability as it explains over 75% of the variance in the meridional streamfunction. During the FGGE northern winter season the Hadley circulation derived from the ECMWF analysis is comparable in magnitude and form to results from station-based analyses. However in the northern summer, there appears a two-layer equatorial Hadley overturning reminiscent of theoretical results by Schneider and Lindzen (1977).

That the 40-50 day oscillation is in part a modulation of the global complex of Walker cells was first suggested in the original work on the oscillation by Madden and Julian (1971, 1972), and is entirely borne out here. In particular our statistical analysis of changes of the tropical velocity potential field shows an unmistakable west to east progression of the Walker cell modulation. We have also examined the

temporal variability of an index of the highly reflective clouds which characterize deep convection and have found an excellent correspondence with the local divergent wind anomalies. Thus the wind changes we have described are accompanied by eastward moving fluctuations in diabatic heating.

The velocity potential anomalies revealed in our analyses involve substantial localized changes in the divergent meridional wind as well as in the zonal wind. Furthermore, these anomalies in the meridional flow accompany the modulations of the Walker circulation in their eastward passage through the equatorial zone. The most prominent meridional wind changes have amplitudes on the order of 2 m/s at 200 mb and appear in the poleward edges of the Hadley cells (15-20^{o} of latitude) where the seasonal cycle in the divergent meridional wind is less marked than it is closer to the equator. In addition, at all latitudes the most significant meridional wind anomalies tend to occur in the longitudinal band extending from 60^{o}E to the dateline, which is generally the region of strongest time average divergent meridional wind. Despite this association of the strongest changes with the strongest mean field, little of the 40-50 day variability in the local meridional winds shows up in reconstructions of zonal averages of the divergent meridional wind (in other words the Hadley cell). This is due to a 180^{o} phase change in 40-50 day anomalies across the 60^{o}-180^{o} region; thus the region provides only a small net contribution to the zonal average divergent meridional wind.

Evidence for intraseasonal variability in the Hadley circulation comes from direct analysis of the meridional circulation itself. We have examined time series of the zonal average of the meridional wind

and found a certain degree of intraseasonal variability. Although the signal-to-noise ratio in the meridional winds is not as high as in the other indices so far discussed, there is unmistakable evidence of intraseasonal variability in the near equatorial meridional circulation. This intraseasonal variability shows a tendency to be phase-locked to the annual cycle with largest amplitudes near the modes of the seasonal cycle and smallest when the mean meridional wind passes through zero twice a year.

The variability of the streamfunction of the meridional circulation reflects the variability of the meridional wind as the largest fluctuations occur in the equatorial troposphere. This variability in the Hadley circulation has a discernible intraseasonal component which emerges in EOF analysis of the Hadley portions of the streamfunction field (30°S-30°N). These results depended upon the removal of the strong seasonal cycle in the streamfunction; as in the case of the zonally averaged meridional wind field, the signal-to-noise ratio in the principal component is not large. Furthermore, the intraseasonal variance is not clearly confined to one clearly independent mode or pair of modes; it seems to be spread over at least three. However, the leading nonseasonal mode (26.6%) possesses a very simple, equatorially symmetric structure. Thus anomalies due to this mode would produce intensification of the rising motion in one hemisphere and increasing sinking motion in the other. The eigenvectors for the second (19.9%) and third (12.7%) nonseasonal modes are more confined than the first to the equatorial zone. The second mode represents variations of rising motion centered between 5° and 10°S, the third between the equator and $\sim 8^{\circ}$N.

The high degree of noise in both the zonally averaged meridional wind field and the streamfunction of the meridional circulation is not unexpected considering the changes of sign in the meridional wind along latitude circles, even in the equatorial zone. A further handicap is the previously noted tendency for the European Centre's analysis scheme to suppress the Hadley circulation.

Proper identification of the intraseasonal variability in the meridional circulation will require some filtering of the short time scale noise. A longer data set, perhaps three to four years, would also be helpful. This would give us the luxury of longer impulse response filters and thus a less drastic filtering of the seasonal cycle and high frequency noise.

With regard to a longer series of data for study of the meridional circulation, we note that since the FGGE year, the European Centre has been continually modifying and improving their forecast model as well as the analysis scheme. Most of the changes likely have had only minor impacts upon the meridional circulation. Others, most significantly the introduction of a diabatic initialization procedure in 1982, should show up quite clearly in the data. Although this might be considered as an impediment to obtaining reliable statistics on the meridional circulation, it will be interesting to compare the intensity of the 40-50 day signals in the meridional circulation before and after the change to diabatic initialization.

7.4 Linkage Between the Zonal and Meridional Circulations

Our instantaneous zonally averaged zonal momentum budgets suggest that there is a degree of coherence at intraseasonal time scales between the horizontal eddy flux convergence and the acceleration of the zonal circulation that is not present in the remaining calculated forcing terms, including, most significantly, the Coriolis torque. Typically, however, the amplitude of the imbalance between the terms we have calculated and the time tendency is comparable to the net calculated forcing. We have not included in this calculation the divergence of the vertical eddy momentum flux. As suggested by Chen (1985), vertical eddy enstrophy fluxes are important in the maintenance of 40-50 day upper level disturbances; scale analysis from the results in this study would also suggest an important role of vertical eddy momentum fluxes.

If the eddy terms are indeed important in the maintenance of the 40-50 day oscillation of the zonal circulation, the phenomenon must be viewed as a wave-mean flow interaction and fundamentally different from the free wave phenomenon proposed by Anderson (1984). The truth may lie somewhere between these two extremes and certainly the brief analysis presented in this work suggests that a more thorough investigation is warranted. Among the avenues that might be explored is the calculation of a zonal momentum budget based not upon the terms in 6.4, but rather the divergence of the Eliassen-Palm flux. This quantity can be intepreted as the direct wave forcing upon the mean flow. The calculation of the Eliassen-Palm flux requires estimates of the eddy heat flux, which in the time average are small in the Hadley regime, but likely to be of some importance in the subtropics.

A wave-mean flow theory for the 40-50 day oscillation in the zonal circulation however still begs the question of the origin of the time scale. In this respect the advective effect of the Hadley circulation on the convective instability of the equatorial zone as a whole or in part could play an important role.

7.5 Comparisons with Recent Observational Work

Since the completion of the observational phase of FGGE, which seems to have been a particularly strong year for the 40-50 day oscillation, there have been an ever increasing number of publications dealing with this subject. We make an attempt in this section to place our work in the context of the developing literature on the oscillation.

We have already remarked in the discussion at the end of Chapter 4 how our velocity potential EOF results recapitulate those of Lorenc (1984) who chose a different method of EOF analysis but arrived at almost the identical results. In our work, we have shown that his initial time filtering of the velocity potential data was not necessary in order to isolate the 40-50 day signal. Moreover, our close examination of the divergent wind fields associated with the 40-50 day changes in velocity potential, has underlined the strong vertical coherence in the divergent circulation. Finally, it is clear from the present study that the eastward propagation of divergent zonal wind anomalies is accompanied by anomalies in the meridional divergent wind field. In contrast, the studies of the oscillation in total wind fields by Madden and Julian (1971,1972), Murakami et al. (1984) and others have

emphasized the Kelvin wave character of the oscillation, i.e. the lack of significant meridional wind anomalies.

Murakami et al. (1984) and Murakami and Nakazawa (1985) have examined the total wind fields at 200 and 850 mb during the northern summer of the FGGE year. They identified disturbances in the wind fields at 850 and 200 mb which propagate primarily eastward and northward across the Indian Ocean and maritime continent regions. They obtained speeds of 500 km/day or ~6 m/s. This speed is comparable to the speeds of anomalies in outgoing longwave radiation propagating across the same region during northern winter found by Weickmann (1983), Weickmann et al. (1985) and Lau and Chan (1985). Our divergent wind anomalies appear to move rather more quickly, around 8-15 m/s. Furthermore the wind anomalies, particularly the meridional wind anomalies, maintain a rather tight phase locking to the variations in highly reflective cloud. In fact, our work differs from the above investigations in that the relationship between changes in the circulation and convection are examined on a case-by-case basis; we thus have demonstrated a remarkable consistency in the connection between divergent zonal and meridional wind anomalies and changes in forcing due to convection.

It appears from our examination of the streamfunction of the meridional circulation that although there is coherent intraseasonal variability in the Hadley circulation, such changes are not strongly related to the more sharply defined intraseasonal variability in the zonal circulation and in the global angular momentum. This is supported as well by the results from time dependent zonal momentum budgets. These results do not provide support for a role of a zonally symmetric

oscillation in the meridional overturning suggested by Anderson and Rosen (1983) and Anderson (1984) in the maintenance of the 40-50 day oscillation in the zonal circulation. In addition, the lack of a clearly defined intraseasonal variation in the zonally symmetric meridional wind field suggests that the mechanisms for the generation of intraseasonal frequencies in the zonally symmetric models of Webster (1983) and Goswami and Shukla (1984) may be important only in local monsoon circulations. Indeed, Murakami et al. (1984) suggest a feedback between the localized zonal mean of the meridional wind over the Indian monsoon region and the generation of disturbances on the zonal wind field in the same region.

7.6 Critical Properties of the 40-50 Day Oscillation: Conclusions and Suggestions for Further Research

This investigation of the divergent circulation in the tropical atmosphere during a single year of enhanced observations has established that aside from the seasonal cycle connected to the meridional movement of solar forcing, the primary modes of coherent variability are intraseasonal in time scale. In the zonally asymmetric modes of the large-scale divergent circulation, as represented by the velocity potential, the dominant variance is centered near 45 days.

We have defined the Walker circulation as a vertically coherent system in the zonally asymmetric divergent zonal wind field in which westerly (easterly) flow in the upper levels (200 mb) flow is paired with easterly (westerly) flow in the lower levels (850 mb). The Walker

circulation consists of a complex of individual cells spanning the equatorial belt, although 2/3 of the belt is occupied in the time mean by a westward overturning cell over the Indian Ocean and an eastward overturning cell over the Pacific.

The intraseasonal variability of the velocity potential takes the form of an eastward propagating modulation of the time mean Walker cells. The largest velocity potential anomalies are coincident with the time mean Indian and Pacific Walker cells. In many respects the 40-50 day changes in the Walker circulation appear as in-place variations in intensity. However, the anomalies in the divergent zonal wind field can be seen to propagate eastward in the equatorial zone. These anomalies of the Walker circulation can be as large as several meters per second over the maritime continent.

We have examined an index of the highly reflective clouds (HRC) associated with deep convection and found excellent correspondence between it and the upper level divergent winds, both in the time mean and in the 40-50 day frequency band. It is clear from this study that the eastward propagation of the divergent wind anomalies across the Indian Ocean and maritime continent regions requires a similar propagation of forcing anomalies due to convection. These results broadly support the Madden and Julian empirical model of the oscillation in the Walker circulation (Fig. 1.1).

We have calculated three significant terms from the zonal momentum equation on an instantaneous basis: the Coriolis torque associated with the zonal mean of the meridional wind, the advection of zonal momentum by the meridional circulation and the convergence of eddy momentum. (The vertical advection by the Hadley circulation proved to be of

negligible importance.) The prominent changes at 40-50 days in the zonal circulation and the relative angular momentum seem to be linked to changes in horizontal eddy flux convergences and, we might also speculate, in vertical eddy flux convergences as well. It is likely that both forms of eddy flux convergences are related to the large scale 40-50 day changes in the Walker circulation. In contrast, the Hadley circulation is often times out of phase with the acceleration of the zonal circulation and its effect is usually opposed by the advection term.

This relationship suggests that the 40-50 day modulation in the Walker circulation and in the zonal circulation are connected through the enhancement of rising motion in the maritime continent region which gives rise to changes in the eddy momentum flux convergence in this region. This quasi-geostrophic process might well be accentuated by concomitant local changes in divergent meridional wind; these represent local ageostrophic imbalances and would also lead to local accelerations of the zonal wind field poleward of the convective disturbance. This latter mechanism has been shown to be an important acceleration mechanism in the East Asian jet by Lau et al. (1983) and Chang and Lum (1985). Along these lines a simple exercise to establish a physical relationship would be to calculate correlation coefficients between the longitudinally varying divergent wind series at 200 mb with the zonal averages of the zonal wind.

The problem of the time scale selection for the 40-50 day oscillation still remains. The presence of the oscillation year round, if not at a constant amplitude, points to a generating mechanism that is applicable to more than one specific season or land-ocean region. One

possibility that has not yet been ruled out is an interaction between the ocean and the atmosphere in the equatorial basins of the three tropical oceans. The dynamics of the equatorial ocean could induce changes in upwelling and advection with time scales controlled by the density structure of the upper ocean layers and the dimensions of the basin. Furthermore, the Indian Ocean might be a potentially fruitful location to look for 40-50 day changes of sea surface temperature. Mysak and Mertz (1984) have already shown that the Somali current during northern summer is susceptible to zonal wind stress forcing at 40-50 days. The Indian Ocean equatorial current system has been shown to undergo drastic current changes at the seasonal time scale (Wyrtki, 1973) and it is possible that higher frequency coherent variability may appear in the sea surface temperature fields.

Appendix A. Weighted Covariance Spectral Estimator

There are a great number of approaches to the estimation of the power spectrum of a discrete stochastic process. For the purposes of this study we wanted an estimator that was simple to apply and which possessed known confidence intervals. A common class of estimators which have these characteristics employ some form of the periodogram or sample spectrum which, following Koopmans (1974) is defined

$$I_{N,n} = |Z_n^{(N)}|^2 = \frac{1}{2\pi N} |EX(t) \exp(-i\omega_n t)|^2$$

where $Z_n^{(N)}$ is the component at frequency $\omega_n = 2 \quad n/N$ of the (complex) finite Fourier transform of the time series X(t) of length N, $-[(N-1)/2] \leq n \leq [N/2]$ (where [(x)] indicates the largest integer less than or equal to x) and vertical bars denote the complex amplitude. To obtain a consistent estimate of the theoretical spectrum, $I_{N,n}$ is usually smoothed with some form of spectral window such as non-overlapping running means (the Daniell estimator).

A second class of estimators are the weighted covariance estimators which are based upon the autocovariance function. In this approach, estimates of the autocovariance function are passed through a filter called a lag window and then transformed to yield a (windowed) spectral estimate. Before the advent of the Fast Fourier Transform (FFT) in the late 1960's, this method was cheaper computationally than periodogram methods.

Since the periodogram and sample autocovariance have the transform relationship

$$\hat{C}(k) = \frac{2}{N-1} \sum_{n=-N+1}^{N} \exp(i\omega_n k)\, I_{N,n}$$

where $\hat{C}(k)$ is the sample autocovariance at lag k, the sample autocovariance function can be obtained from the original time series by two discrete Fourier transforms: the first into frequency space and the second to lag space. At this point the sample autocovariance can be lag windowed as in the direct method and transformed back to frequency space to obtain the spectral estimate, viz.

$$\hat{f}(\omega) = \frac{\Delta t}{2} \sum_{k=-\infty}^{\infty} \exp(-i\omega k) w_M(k) \hat{C}(k)$$

where $\hat{f}(\omega)$ is the estimate of the power spectrum at frequency ω and $w_M(k)$ is the lag window length $M<N$.

The weighted covariance spectral estimate obtained in this manner is at least as computationally efficient as a smoothed periodogram estimator of equal resolution and degrees of freedom. In addition, the wide variety of lag windows that have been developed since the 1950's present a more flexible set of spectral windows than those applicable to the sample spectrum. The detailed steps for the construction of a weighted covariance spectral estimation program are outlined in Oppenheim and Schafer (1975, pp. 556-562).

The spectral estimates shown in this work were designed to distinguish 40-50 day variance from possible power in neighboring bands such as the 3-month and semiannual bands. The bandwidth then should be

at least as small as $(0.025\ d^{-1})/2 \leq 0.01$. For lag windows of the form $w_M(k) = w(k/M)$ the equivalent bandwidth (EBW) (Koopmans, op. cit., p. 312) is approximately

$$EBW = 2\pi/(c_w M \Delta t)$$

where c_w is a function of the shape of the lag window

$$c_w = \int_{-1}^{1} w^2(v)dv$$

(Koopmans, loc. cit.). (For twice-daily time series $\Delta t = 0.5$ day.) Thus in order that EBW be at least as small as 0.01, M should be at least as large as $400\pi/c_w$. Decreased bandwidth also decreases the degrees of freedom in the estimate which increases the uncertainty. For a fixed maximum bandwidth, the equivalent degrees of freedom $r = 2N/c_w M$ will increase with N. Koopmans provides a table of confidence intervals for the log of the spectral density, given a value for r.

The only remaining choice is that of the lag window. To certain degree, this is a matter of taste, since the properties of many of the lag windows are quite similar. For this study we have chosen the Papoulis(2) window which has a value for c_w of 0.587, giving an EDF of $r=3.41N/M$ and an EBW of $6.81\pi/M$. For the three spectral estimates shown in Fig. 4.21, we chose a value of EBW = 0.0075π. This is a moderately high resolution choice, as a band centered at 0.022π (45 days) would encompass frequencies from $0.01472\ \pi$ (67.9 days) to 0.02972π (33.6 days). To achieve this bandwidth using this window, the lag window width M required was 454, giving an equivalent degrees of freedom of 5.48.

Appendix B. Figure List

Fig. 1.1 Empirical model of the 40-50 day oscillation from Madden and Julian (1972).

Fig. 1.2 40-day filtered and raw time series of FGGE year global relative angular momentum. Details of calculation in Chapter 6.

Fig. 1.3 Four stages in an idealized half-cycle of the 40-50 day oscillation in the 200 mb velocity potential and divergence during northern summer. From Lorenc (1984).

Fig. 2.1 Time average meridional-height cross-sections of ψ_{MMC} from Oort(1983), contour interval 10^{10} kg/s. December-February 1963-1973 (upper) and June-August 1963-1973.

Fig. 2.2 As in 2.1, but for $[\bar{v}]$, contour intervals 1 m/s.

Fig. 2.3 Latitude-height fields of components in the time mean zonal momentum budgets for the seasons December - February and June - August taken from the study of Newell et al. (1972). The components displayed are (a) the advection of mean zonal momentum by the mean meridional circulation, (b) the vertical advection of zonal momentum, (c) the mean Coriolis torque, (d) the eddy flux convergence of zonal momentum by both standing and transient eddies and (e) the turbulent vertical transfer of momentum.

Fig. 2.4 Streamfunctions of the isentropic mean meridional circulation computed from NMC FGGE III-a data by Townsend and Johnson (1985): December 1978 - February 1979 (upper) and June - August 1979. Contour intervals 10^{10} kg/s.

Fig. 2.5 Longitudinal-height profiles of the east-west circulations in the 10 belts centered at 5°N (upper panels) and 5°S. Derived by Newell et al. (1974) from their time average zonal winds for the period 1957-1963 and kinematically-derived vertical velocities, December - January (top); June - August (bottom).

Fig. 3.1 Distributions of data assimilated into the ECMWF FGGE III-b 0Z analyses for January 18 (upper left); April 18 (upper right); June 18 (lower left); and October 18 (lower right). From Bjorheim et al. (1981).

Fig. 3.2 Flow chart for the ECMWF forecast-analysis-initialization procedure (top) and tabulation of typical observational errors for FGGE II-b data. From Bengtsson et al. (1982).

Fig. 3.3 Summary of the European Centre's 15-level grid point model used in the production of the ECMWF FGGE III-b analyses. From Bengtsson et al. (1982).

Fig. 3.4 Spherical harmonic spectrum of divergent wind energy at 200 mb in the ECMWF III-b analyses for the month of January. From Hollingsworth and Cats (1981).

Fig. 3.5 Wind and geopotential height patterns of individual wavenumber one Hough modes (lefthand panels) input to the ECMWF optimum interpolation and the analyses that result (righthand panels), given "perfect" observations: first symmetric Rossby wave (upper left); Kelvin wave (upper right); mixed Rossby-gravity wave (lower left); and gravest symmetric westward gravity wave (lower right). From Daley (1983).

Fig. 3.6 Meridional height cross-sections of the zonally averaged meridional wind at 24 hours from an initialized control run (top) of the ECMWF model and an experimental run in which only the first two internal gravity modes were initialized (instead of five), contour intervals 1m/s. From Hollingsworth and Cats (1981).

Fig. 3.7 Velocity potential at 150 mb in the control run of 3.5 (top) and the experiment after one day of assimilation, contour intervals 1×10^6 m^2/s.

Fig. 3.8 March 1981 averages of 200 mb velocity potential. From top, uninitialized 12Z analyses, initialized 12Z analyses, 1-day forecasts, and 10-day forecasts, contour intervals 1×10^6 m2/s. From Heckley (1982).

Fig. 3.9 200 mb velocity potential distributions from the FGGE III-b analyses by GFDL and ECMWF: January 1979 (upper panel) and June 1979, contour intervals 2×10^6 m^2/s. From Lau (1985a).

Fig. 3.10 Meridional height cross-sections of the zonally-averaged meridional wind from the the FGGE III-b analyses by GFDL and ECMWF for the months of January 1979 (left panels) and June 1979, contour intervals 1 m/s. From Lau (1985a).

Fig. 4.1 FGGE time averages, 12/1/78-11/30/79, 200 mb stream function, contour interval 10×10^6 m^2/s (top); zonal wind from ECMWF III-b analysis, contour interval 10 m/s (center); and standard deviation of zonal wind, contour interval 5 m/s (bottom).

Fig. 4.2 FGGE time averages, 850 mb stream function, contour interval 50×10^5 m^2/s (top); zonal wind, contour interval 5 m/s (center); and standard deviation of zonal wind, contour interval 2.5 m/s (bottom).

Fig. 4.3 FGGE time averages of 200 mb velocity potential (top), divergent zonal wind and divergent meridional wind.

Fig. 4.4 As in 4.3 but for 850 mb.

Fig. 4.5 Longitudinal profiles of FGGE time average Walker circulation components at 200 mb (solid) and 850 mb (broken) meridionally averaged from 15°S-15°N. Velocity potential (top), divergent zonal wind (center) and area-weighted divergence (bottom).

Fig. 4.6 FGGE year mean HRC profile along the equator for the latitude band 22.5°S - 22.5°N (top) and FGGE year mean HRC in average number of days of highly reflective cloud coverage per 1° x1° grid square per 31-day month.

Fig. 4.7 January 1979 (top) and July 1979 average 200 mb velocity potential, contour interval, 10×10^5 m^2/s.

Fig. 4.8 January 1979 (top) and July 1979 average 850 mb velocity potential, contour interval 100×10^4 m^2/s.

Fig. 4.9 Intersection of the earth's surface with the 850 mb level. From Oort (1983).

Fig. 4.10 As in Fig. 4.6 (lower) but for January 1979 (top) and July 1979 HRC.

Fig. 4.11 January 1979 200 mb (top) and 850 mb divergent zonal wind fields, contour interval 1 m/s.

Fig. 4.12 As in Fig. 4.11, but for July 1979.

Fig. 4.13 As in Fig. 4.11, but for the divergent meridional wind.

Fig. 4.14 As in Fig. 4.13, but for July 1979.

Fig. 4.15 January 1979 Walker circulation components at 200 mb (solid) and 850 mb (broken). Divergent zonal winds averaged across 0°-30°N (top) and 0°-30°S (upper middle); area-weighted divergence 0°-30°N (lower middle) and 0°-30°S.

Fig. 4.16 As in 4.15 but for July 1979.

Fig. 4.17 HRC profiles for January 1979 (upper half) and July 1979 (lower half). Each month is represented by separate profiles for each of the latitude bands 22.5°N - 0° and 0° - 22.5°S.

Fig. 4.18 Flow chart for semi-spectral empirical orthogonal analyses performed in Chapter 4. (1) Input flow.

Fig. 4.18 Flow chart for semi-spectral empirical orthogonal analyses in Chapter 4. (2) Singular value decomposition.

Fig. 4.18 Flow chart for semi-spectral empirical orthogonal analyses in Chapter 4. (3) Normalization and backtransformation to grid space.

Fig. 4.19 FGGE period standard deviation of velocity potential at 200 mb, contour interval 50×10^4 m/s (top); and 850 mb, same contour interval.

Fig. 4.20a Results of empirical orthogonal analysis C201025: 200 mb velocity potential 45°S-45°N, zonal wavenumbers 0-10. Grid-point eigenvectors for modes 1-5, contour intervals 100×10^4 m^2/s.

Fig. 4.20b Results of empirical orthogonal analysis C201025: 200 mb velocity potential 45°S-45°N, zonal wavenumbers 0-10. Normalized principal components, modes 1-5.

Fig. 4.20c Results of empirical orthogonal analysis C201025: 200 mb velocity potential 45°S-45°N, zonal wavenumbers 0-10. Divergent wind fields derived from eigenvectors 1-3, contour intervals 0.25 m/s.

Fig. 4.20d Results of empirical orthogonal analysis C201025: 200 mb velocity potential 45°S-45°N, zonal wavenumbers 0-10. Meridional wind fields for eigenvectors 1-3, contour intervals 0.5, 0.25 and 0.25 m/s.

Fig. 4.21 Weighted covariance spectral estimates for C201025 mode 1 (top), mode 2 (middle) and mode 3 (bottom).

Fig. 4.22 Reconstruction of annual and semi-annual cycle of velocity potential using first and second harmonics of first five principal components from C201025. Panels (from top) correspond to January 31, April 1, June 1, August 1 and September 30 from the FGGE year. Contour intervals 100×10^4 m^2/s.

Fig. 4.23a Results of empirical orthogonal analysis C201025W: zonally asymmetric 200 mb velocity potential 45 S-45 N, zonal wavenumbers 1-10, Eigenvectors for modes 1-3, contour intervals 100×10^4 m^2/s; modes 4-5, contour interval 50×10^4 m^2/s.

Fig. 4.23b Results of empirical orthogonal analysis C201025W: zonally asymmetric 200 mb velocity potential 45°S-45°N, zonal wavenumbers 1-10. Normalized principal components, modes 1-5.

Fig. 4.24a As in 4.23a but for EOF C851025: 850 mb velocity potential, 45°S-45°N, zonal wavenumbers 0-10. Contour intervals 50×10^4 m^2/s.

Fig. 4.24b As in 4.23b but for EOF C851025: 850 mb velocity potential, 45°S-45°N, zonal wavenumbers 0-10.

Fig. 4.25 Eigenvalues of C201025 and C851025. Error bars extend $\pm \Delta d_i$ (see text for explanation).

Fig. 4.26a As in 4.24a but for EOF C851025W: 850 mb velocity potential, 45°S-45°N, asymmetric zonal wavenumbers 1-10. Contour intervals 25×10^4 m^2/s.

Fig. 4.26b As in 4.23b but for EOF C851025W: 850 mb velocity potential, 45°S-45°N, zonal wavenumbers 1-10.

Fig. 4.27a Results of two-level empirical orthogonal analysis C820525W: combined 850 and 200 mb velocity potential 45°S-45°N, zonal wavenumbers 1-5. 200 mb components of eigenvectors for modes 1-5,contour intervals 100×10^4 m^2/s.

Fig. 4.27b Results of two-level empirical orthogonal analysis C820525W: combined 850 and 200 mb velocity potential 45°S-45°N, zonal wavenumbers 1-5. 850 mb components of eigenvectors for modes 1-5, contour interval 100×10^4 m^2/s.

Fig. 4.27c Results of two-level empirical orthogonal analysis C820525W: combined 850 and 200 mb velocity potential 45°S-45°N, zonal wavenumbers 1-5. Normalized principal components, modes 1-5.

Fig. 5.1 As in Fig. 4.25 but for C201025W and C851025W and modes 1-7.

Fig. 5.2 Impulse response (top) and frequency response (in units of = 1/day) of 40 day bandpass filter.

Fig. 5.3a Principal components of the first(left) and second eigenmodes from EOF analysis C201025W filtered with the bandpass filter of 5.2, superimposed upon their unfiltered versions. Filtered principal components are used in reconstruction of anomalies in Figures 5.4 and 5.6.

Fig. 5.3b As in 5.3a but for C851025W.

Fig. 5.4 Time lapse sequence of longitudinal profiles of velocity potential anomalies, reconstructed from modes 1 and 2 of C201025W and C851025W, filtered at 40 days and averaged across the latitudes 15°S-15°N. Sampling every 11 days. 200 mb profiles solid lines; 850 mb broken.

Fig. 5.5 Time lapse sequence of longitudinal profiles of total velocity potential (anomalies plus mean), reconstructed from modes 1-7 of C201025W and C851025W and averaged as in Figure 5.4. These profiles are not time filtered.

Fig. 5.6 As in 5.4 but for Walker circulation (divergent zonal winds) anomalies. Winds are derived from reconstructed velocity potential anomalies in 5.4.

Fig. 5.7 As in 5.5 but for total Walker circulation. Winds derived from total velocity potential in 5.5.

Fig. 5.8 FGGE year (12/1/78 - 11/30/79) time series of 200 mb divergent zonal winds at the equator reconstructed from modes 1-5 of C201025 added to the mean at 6 longitudes: (from top) 0°, 60°E, 120°E, 180°, 120°, 60°W and 0° (repeated). In m/s.

Fig. 5.9 As in Fig. 5.8 but for divergent meridional winds along 15°N.

Fig. 5.10 As in Fig. 5.9 but for 15°S.

Fig. 5.11a Time series of total HRC in equatorially-centered regions 30° degrees wide in longitude and covering the latitudes 22.5°S - 22.5°N; 4 longitudes at intervals of 60° from 0° eastward to 180°. Units: number of 1°x1° grid squares covered by highly reflective cloud.

Fig. 5.11b As in (a) but for the western hemisphere 180° - 0°.

Fig. 5.12 As in Fig. 5.2 but for a 44-day bandpass filter used for filtering daily data.

Fig. 5.13a As in Fig. 5.11a but for 44-day filtered HRC time series at 7 longitudes at 30° intervals.

Fig. 5.13b As in (a) but for the western hemisphere.

Fig. 5.14 As in Fig. 5.13 but for regions between the equator and 22.5°N at intervals of 60° eastward from 0° through 180° and back to 0°.

Fig. 5.15 As in Fig. 5.14 but for regions between 22.5°S and the equator.

Fig. 6.1 Latitude-height fields of the amplitude (upper panel) and phase of the first eigenmode in complex EOF analysis of 5 years of daily values of [u]. Taken from Anderson and Rosen (1983).

Fig. 6.2 40-day filtered and unfiltered time series of [u] derived from the ECMWF III-b analysis at 200 mb for the latitude bands 22.5°S - 7.5°S (downward on left), 22.5°N - 7.5°N (downward on right) and the equator (bottom). Values in m/s.

Fig. 6.3 40-day filtered and unfiltered time series of [u] at the equator at 10, 20, 50, 100 and 200 mb (downward on left) and 200, 300, 500, 700 and 850 mb (downward on right) in m/s. Filtered time series are scaled up by a factor of 2.

Fig. 6.4 Latitude-height fields of FGGE-year time averages (top) and standard deviations of [v] derived from the ECMWF III-b analysis. Values in m/s.

Fig. 6.5 January (top) and July averages of [v] derived from the ECMWF III-b analysis. Values in m/s.

Fig. 6.6 Amplitude (in m/s) of 40-day bandpassed anomalies of [v] (top) and percentage of total variance in 40-day passband.

Fig. 6.7 40-day filtered and unfiltered time series of [v] (in m/s) at 150 mb between 15°S and 15°N. As in Fig. 6.3, filtered anomalies are scaled up by a factor of 2.

Fig. 6.8 As in Fig. 6.7 but for 850 mb.

Fig. 6.9 As in Fig. 6.4 but for the streamfunction of the meridional circulation Ψ_{MC}. Values in 10^{12} g/s.

Fig. 6.10 As in Fig. 6.5 but for the streamfunction of the meridional circulation Ψ_{MC}. Values in 10^{12} g/s.

Fig. 6.11a Eigenvectors of the first 3 modes from EOF analysis of the meridional streamfunction for the 25 latitudes 45°N - 45°S and the 9 pressure layers between 100 mb and the surface. Values in 10^{12} g/s.

Fig. 6.11b Principal components for the eigenvectors in (a).

Fig. 6.12a Eigenvectors of the first 3 modes form EOF analysis of the nonseasonal variance of the meridional streamfunction for the 17 latitudes 30°N - 30°S and the 9 pressure layers between 100 mb and the surface. Values in 10^{12} g/s.

Fig. 6.12b Principal components for the eigenvectors in (a).

Fig. 6.13 Time series of zonal totals of highly reflective cloud (HRC) in the band from 22.5°N (top) to 22.5°S (bottom). Ordinate is the number of 1° x1° grid squares each day covered by HRC in strips 3.75° wide centered on the respective latitudes.

Fig. 6.14 As in Fig. 6.13 but for 44-day filtered values of HRC.

Fig. 6.15 Results from instantaneous zonal momentum budget calculations at 22.5°N. Upper left: unfiltered time series of [u], $\partial[u]/\partial t$, RHS, RES. Upper right: the four righthand side terms from (6.5) in order, i.e. the meridional advection of zonal momentum, the vertical advection, the Coriolis torque and the convergence of the horizontal eddy momentum flux. Lower left: 40-day filtered time series of [u], RHS and RES, the latter two (dashed) are superposed by the 40-day filtered time tendency (solid.) Lower right: 40-day filtered series for the four righthand side terms (dashed) also superposed by the time tendency.

Fig. 6.16 As in Fig. 6.15 but for 15°N.

Fig. 6.17 As in Fig. 6.15 but for 7.5°N.

Fig. 6.18 As in Fig. 6.15 but for the equator.

Fig. 6.19 As in Fig. 6.15 but for 7.5°S.

Fig. 6.20 As in Fig. 6.15 but for 15°S.

Appendix C: Table of Commonly Used Symbols
(roughly in order of appearance)

$[x]$	zonal average of x
x^*	deviation from zonal average of x
(x)	time average of x
a	mean radius of the earth, 6371 km
λ	longitude
ϕ	latitude
χ	velocity potential
ψ	stream function
Ω	earth's rotation rate, 2π/day
f	Coriolis parameter, $2\Omega\sin\phi$
u	zonal wind
v	meridional wind
ω	vertical wind speed, in Pa/s or mb/s
p	pressure
g	gravitational acceleration, 9.81 m/s^2
F	vertically integrated mass flux across latitude circle due to mean meridional circulation
Ψ_{MC}	Eulerian mass streamfunction for the mean meridional circulation
ζ	vertical component of vorticity
D	divergence of the horizontal wind
Φ	geopotential
u_d^r, v_d^r	rotational components of the horizontal wind
u_d, v_d	divergent components of the horizontal wind
Δ	horizontal grid spacing, 3.75°
d_k	eigenvalue for mode k of EOF analysis
z_k	unnormalized principal component time series for mode k
$\hat{z}_k$	normalized principal component time series for mode k
$\tilde{y}_k$	semi-spectral eigenvector of zonal wave coefficients at grid latitudes for EOF mode k
$\hat{y}_k$	semi-spectral eigenvector of zonal wave coefficients at grid latitudes for EOF mode k scaled by standard deviation of z_k.
y_k	grid point eigenvector loading for point i,j, i.e transform of $\hat{y}_k$ from latitude-zonal wavenumber space to geographic space.
$\chi^R_{i,j,k}$	grid point value of χ at i,j and time k reconstructed from leading modes in EOF analysis

References

Ahlquist, J.E., 1982: Normal-mode global Rossby waves: Theory and observations, J. Atmos. Sci., **39**, 193-202.

Anderson, J.R., 1984: Slow motions in the tropical troposphere, Atmospheric Science Paper No.381, Colorado State University, 142 pp.

Anderson, J.R. and R.D. Rosen, 1983: The latitude-height structure of 40-50 day variation in atmospheric angular momentum, J. Atmos. Sci., **40**, 1584-1591.

Anderson, J.R., D.E. Stevens and P.R. Julian, 1984: Temporal variations of the tropical 40-50 day oscillation, Mon. Wea. Rev., **112**, 2431-2438.

Arkin, P.A., 1979: The relationship between fractional coverage of high cloud and rainfall accumulation during GATE over the B-scale array, Mon. Wea. Rev., **107**, 1382-1387.

Arkin, P.A., J.E. Janowiak and W. Replane, 1985: Large-scale variability in Indian monsoon rainfall inferred from satellite data, in Proceedings of the Ninth Annual Climate Diagnostics Workshop, Corvallis, Oregon, October 1984, pp. 265-273. NOAA/U.S. Department of Commerce, Washington, D.C. 436 pp.

Arpe, K., 1985a: Comparison of FGGE level III-b analyses by ECMWF and by GFDL for the period 27 February to 7 March 1979 taking recent improvements of the ECMWF analysis scheme into account, in Report of the Seminar on Progress in Diagnostic Studies of the Global Atmospheric Circulation as a Result of the Global Weather Experiment -- Helsinki, August 1984. GARP Special Report No. 42, World Meteorological Organization.

Arpe, K., 1985b: Fit of FGGE level III-b analyses by ECMWF and by GFDL to observational data during the period 27 February to 7 March 1979, in Report of the Seminar on Progress in Tropical Meteorology as a Result of the Global Weather Experiment -- Tallahassee, October 1984. GARP Special Report No. 44, World Meteorological Organization.

Barwell, B.R., and A.C. Lorenc, 1984: A study of the impact of aircraft wind observations on a large-scale analysis and numerical weather prediction system, Quart. J. Roy. Meteor. Soc., **111**, 103-129.

Bengtsson, L., M. Kanamitsu, P. Kallberg, S. Uppala, 1982: FGGE 4-dimensional data assimilation at ECMWF, Bull. Amer. Meteor. Soc., **63**, 29-43.

Bjerknes, J., 1966: A possible response of the atmospheric Hadley circulation to equatorial anomalies of ocean temperature, Tellus, **18**, 820-829.

Bjerknes, J., 1969: Atmospheric teleconnections from the equatorial Pacific, Mon. Wea. Rev., **97**, 163-172.

Bjorheim, K., P. Julian, M. Kanamitsu, P. Kallberg, P. Price, S. Tracton and S. Uppala, 1981: FGGE III-b Daily Global Analyses. Part 1: December 1978 - February 1979. Part 2: March 1979 - May 1979. Part 3: June 1979 - August 1979. Part 4: September 1979 - November 1979. European Center for Medium Range Weather Forecasts, Reading, England.

Branstator, G., 1983: Horizontal energy propagation in a barotropic atmosphere with meridional and zonal structure, J. Atmos. Sci., **40**, 1689-1708.

Businger,S. and G.H. Golub, 1969: Singular value decomposition of a complex matrix, Commun. ACM., **12**, 564-565.

Cats, G.J. and W. Wergen, 1982: Analysis of large scale normal modes by the ECMWF analysis scheme, in Workshop on Current Problems in Data Assimilation, 8-10 November 1982, European Centre for Medium Range Weather Forecasts, Reading, England, pp. 343-371.

Chang, C.-P., 1977: Viscous internal gravity waves and low-frequency oscillations in the tropics. J. Atmos. Sci., **34**, 901-910.

Chang, C.-P. and K.G. Lum, 1985: Tropical-midlatitude interactions over Asia and the western Pacific Ocean during the 1983/1984 northern winter, Mon. Wea. Rev., **113**, 1345-1358.

Chen, T.-C., 1985: On the maintenance of enstrophy in the tropics during the FGGE Northern Hemisphere summer, Mon. Wea. Rev., **113**, 624-640.

Cornejo-Garrido, A. and P.H. Stone, 1977: On the heat balance of the Walker circulation, J. Atmos. Sci., **34**, 1155-1164.

Daley, R., 1983: Spectral characteristics of the ECMWF objective analysis system, Technical Report No. 40, European Centre for Medium Range Weather Forecasts, Reading, England, 119 pp.

Daley, R., 1985: The analysis of synoptic scale divergence by a statistical interpolation procedure, Mon. Wea. Rev., **113**, 1066-1079.

Dey, C.H. and Brown, J.A., 1976: Decomposition of a wind field on the sphere, NOAA Technical Memorandum NWS NMC-59, U.S. Department of Commerce.

Edmon, H.J., B.J. Hoskins and M.E. McIntyre, 1980: Eliassen-Palm cross sections for the troposphere, J. Atmos. Sci., **37**, 2600-2616.

Garcia, O., 1981: A comparison of two satellite rainfall estimates for GATE, J. Appl. Meteor., **20**, 430-438.

Goswami, B.N. and J. Shukla, 1984: Quasi-periodic oscillations in a symmetric general circulation model, J. Atmos. Sci, **41**, 20-37.

Gill, A.E., 1980: Some simple solutions for heat-induced tropical circulation, Quart. J. Roy. Meteor. Soc., **106**, 407-462.

Griffith, C.G., W.L. Woodley, P.G. Grube, D.W. Martin, J. Stout and D.N. Sikdar, 1978: Rain estimation from geosynchronous satellite imagery - Visible and infrared studies, Mon. Wea. Rev., **106**, 1153-1171.

Gruber, A. and J.S. Winston, 1978: Earth-atmosphere radiative heating based on NOAA scanning radiometer measurements, Bull. Amer. Meteor. Soc., **59**, 1570-1573.

Gutzler, D.S., 1985: The structure of annual and interannual wind variability in the tropics. Ph.D. thesis, Massachusetts Institute of Technology, Cambridge, Massachusetts. 224 pp.

Guymer, L.B., and J.F. Le Marshall, 1981: Impact of FGGE buoy data on Southern Hemisphere analysis, Bull. Amer. Meteor. Soc., **62**, 38-47.

Heckley, W.A., 1982: Adjustment in numerical weather prediction models in the tropics, in Workshop on Current Problems in Data Assimilation, 8-10 November 1982, European Centre for Medium Range Weather Forecasts, Reading, England, pp. 299-342.

Heckley, W.A., 1985: Systematic errors of the ECMWF operational forecasting model in tropical regions, Quart. J. Roy. Meteor. Soc., **111**, 709-738.

Heddinghaus, T.R. and A.F. Krueger, 1981: Annual and interannual variations in outgoing longwave radiation over the tropics, Mon. Wea. Rev., **109**, 1208-1218.

Held, I.M., and B.J. Hoskins, 1985: Large-scale eddies and the general circulation of the troposphere, in Advances in Geophysics, **28**, 3-31, Barry Saltzman (ed.). Academic Press, New York, 585 pp.

Hollingsworth, A. and G. Cats, 1981: Initialization in the tropics, in Workshop on Tropical Meteorology and its Effects on Medium Range Weather Prediction at Middle Latitudes, at European Centre for Medium Range Weather Forecasts, 11-13 March 1981.

Holton, J.R., and R.S. Lindzen, 1968: A note on "Kelvin" waves in the atmosphere, Mon. Wea. Rev., **96**, 385-386.

Horel, J.D., 1981: A rotated principal component analysis of the interannual variability of the Northern Hemisphere 500 mb height field, Mon. Wea. Rev., **109**, 2080-2092.

Horel, J.D., 1984: Complex principal component analysis: Theory and examples, J. Climat. Appl. Meteor., **23**, 1660-1673.

Hoskins, B.J., and D.J. Karoly, 1981: The steady linear response of a spherical atmosphere to thermal and orographic forcing, J. Atmos. Sci., **38**, 1179-1196.

Houze, R.A., and A.K. Betts, 1981: Convection in GATE, Rev. Geophys. Space Phys., **19**, 541-576.

Houze, R.A., S.G. Geotis, F.D. Marks and A.K. West, 1981: Winter monsoon conveciton in the vicinity of North Borneo. Part I: Structure and time variations of the clouds and precipiation, Mon. Wea. Rev., **109**, 1595-1614.

Hsiung, J. and R.E. Newell, 1983: The principal nonseasonal modes of variation of global sea surface temperature, J. Phys. Oceanogr., **13**, 1957-1967.

Julian, P.R., 1984: Objective analysis in the tropics: A proposed scheme, Mon. Wea. Rev., **112**, 1752-1767.

Julian, P.R., 1985: Some comparisons of ECMWF IIIb and GFDL IIIb analyses in the tropics, in Proceedings of the First National Workshop on the Global Weather Experiment, Woods Hole, July 9-20, 1984, U.S. Committee for GARP, National Academy of Sciences, pp. 211-216. National Academy Press, Washington, D.C.

Julian, P.R., and Madden, R.A., 1981: Comments on a paper by T. Yasunari, J. Meteor. Soc., **59**, 336-354.

Kallberg, S. Uppala, N. Gustafsson and J. Pailleux, 1982: The impact of cloud track wind data on global analyses and medium range forecasts. Technical Report No. 34, European Centre for Medium Range Weather Forecasts, Reading, England.

Kendall, M., 1980: Multivariate Analysis. Charles Griffin, 210 pp.

Kilonsky, B.J. and C.S. Ramage, 1976, A technique for estimating tropical open-ocean rainfall from satellite observations, J. Appl. Meteor., **15**, 972-975.

Koopmans, L.H., The Spectral Analysis of Time Series, Academic Press, New York, 366 pp.

Krishnamurti, T.N., 1971: Tropical east-west circulations during the northern summer, J. Atmos. Sci., **28**, 1342-1347.

Krishnamurti, T.N., M. Kanamitsu, W.J. Koss and J.D. Lee, 1973: Tropical east-west circulations during the northern winter, J. Atmos. Sci., **30**, 780-787.

Krishnamurti, T.N., P. K. Jayakumar, J. Sheng, N. Surgi, and A. Kumar, 1985: Divergent circulations on the 30 to 50 day time scale, J. Atmos. Sci., **42**, 364-375.

Krishnamurti, T.N., Y. Ramanathan, P. Ardanuy, R. Pasch and P. Greiman, 1980: Quick look Summer MONEX atlas. Part III: Monsoon depression phase, Florida State University Report No. 80-8.

Krishnamurti, T.N., and D. Subrahmanyam, 1982: The 30-50 day mode at 850 mb during MONEX. J. Atmos. Sci., **39**, 2088-2095.

Lau, K.-M., and P.H. Chan, 1983a: Short-term climate variability and atmospheric teleconnections as inferred from satellite-derived outgoing longwave radiation I: Simultaneous relationships, J. Atmos. Sci., **40**, 2735-2750.

Lau, K.-M., and P.H. Chan, 1983b: Short-term climate variability and atmospheric teleconnections as inferred from satellite-derived outgoing longwave radiation II: Lagged relationships, J. Atmos. Sci., **40**, 2751-2767.

Lau, K.-M., and P.H. Chan, 1985, Aspects of the 40-50 day oscillation during the northern winter as inferred from outgoing longwave radiation, Mon. Wea. Rev., **113**, 1889-1909.

Lau, K.-M., C.-P. Chang and P.H. Chan, 1983: Short-term planetary scale interactions over the tropics and midlatitudes. Part II: Winter-MONEX period, Mon. Wea. Rev., **111**, 1372-1388.

Lau, N.-C., 1985a: A comparison of circulation statistics based on FGGE Level III-b analyses produced by GFDL and ECMWF for the Special Observing Periods. NOAA Data Report ERL GFDL-6, U.S. Department of Commerce. 237 pp.

Lau, N.-C., 1985b: Circulation statistics based on FGGE Level III-b analyses produced by GFDL. NOAA Data Report ERL GFDL-5. U.S. Department of Commerce. 427 pp.

Lindzen, R.S., 1967: Planetary waves on beta-planes, Mon. Wea. Rev., **95**, 441-451.

Lorenc, A.C., 1981: A global three-dimensional multivariate statistical interpolation scheme, Mon. Wea. Rev., **109**, 701-721.

Lorenc, A.C., 1984: The evolution of planetary-scale 200 mb divergent flow during the FGGE year, Quart. J. Roy. Meteor. Soc., **110**, 427-441.

Lorenc, A.C., and R. Swinbank, 1984: On the accuracy of general circulation statistics calculated from FGGE data--a comparison of results from two sets of analyses, Quart. J. Roy. Meteor. Soc., **110**, 915-942.

Lorenz, E.N, 1967: The Nature and Theory of the General Circulation of the Atmosphere, World Meteorological Organization, Geneva. 161 pp.

Machenhauer, B., 1977: On the dynamics of gravity oscillations in a shallow water model, Contrib. Atmos. Phys., **50**, 253-271.

Madden, R.A., 1978: Further evidence of traveling planetary waves, J. Atmos. Sci., **35**, 1605-1618.

Madden, R.A., 1985: The annual variation in the vertical structure of the 40-50 day oscillation. In the Proceedings of the Ninth Annual Climate Diagnostics Workshop - Corvallis, Oregon, October 1984, pp. 123-127. NOAA/U.S. Department of Commerce, Washington D.C. 436 pp.

Madden, R.A., and P.R. Julian, 1971: Detection of a 40-50 day oscillation in the zonal wind in the tropical Pacific, J. Atmos. Sci., **28**, 702-708.

Madden, R.A., and P.R. Julian, 1972: Description of global-scale circulation cells in the tropics with a 40-50 day period. J. Atmos. Sci., **29**, 1109-1123.

McClellan, J.H., T.W. Parks and L.W. Rabiner, 1979: FIR linear phase filter design program, Chapter 5.1 in Programs for Digital Signal Processing. Edited by Digital Signal Processing Committee, IEEE Acoustics, Speech and Signal Processing Society. IEEE Press, New York.

McGuirk, J.P., A.H. Thompson, L.L. Anderson,Jr. and N.R. Smith, 1984: Reliability of circulation statistics over the tropical Pacific Ocean based upon FGGE data. In the Proceedings of the Eighth Annual Climate Diagnostics Workshop -- Toronto, October 1983, p. 247-257. Published by the NOAA/U.S. Dept. of Commerce.

Montgomery, R.B., 1940: Report on the work of G.T. Walker, Mon. Wea. Rev., Supplement No. 39.

Murakami, T. and T. Nakazawa, 1985: Tropical 45 day oscillations during the 1979 Northern Hemisphere summer, J. Atmos. Sci., **42**, 1107-1122.

Murakami, T., T. Nakazawa and J. He, 1984, On the 40-50 day oscillation during the 1979 Northern Hemisphere summer, J. Meteor. Soc., **62**, 440-468.

Mysak, L.A. and G.J. Mertz, 1984: A 40 to 60 day oscillation in the source region of the Somali Current during 1976, J. Geophys. Res., **89**, 711-715.

Newell, R.E., J.W. Kidson, D.G. Vincent and G.J. Boer, 1972, The General Circulation of the Tropical Atmosphere and Interactions with Extratropical Latitudes, Vol. 1. MIT Press, Cambridge, Massachusetts, 258 pp.

Newell, R.E., J.W. Kidson, D.G. Vincent and G.J. Boer, 1974, The General Circulation of the Tropical Atmosphere and Interactions with Extratropical Latitudes, Vol. 2. MIT Press, Cambridge, Massachusetts, 371 pp.

Norquist, D.C., E.E Recker, and R.J. Reed, 1982: The energetics of African wave disturbances observed during Phase III of GATE., Mon. Wea. Rev., **105**, 334-342.

North, G.R., 1984: Empirical orthogonal functions and normal modes, J. Atmos. Sci., **41**, 879-887.

North, G.R., T. Bell, F. Modeng, and R.F. Cahalan, 1982: Sampling errors in the estimation of empirical orthogonal functions, Mon. Wea. Rev., **110**, 699-706.

Oort, A.H., 1983: Global Atmospheric Circulation Statistics, 1958-1973. NOAA Professional Paper 14. NOAA/U.S. Department of Commerce, Rockville, Maryland, 180 pp.

Oort, A.H., and J.P. Peixoto, 1983: Global angular momentum and energy balance requirements from observations, pp. 355-490 in Advances in Geophysics, **25**, Barry Saltzman, ed. Academic Press, New York.

Oppenheim, A.V. and R.W. Schafer, Digital Signal Processing, Prentice-Hall, Englewood Cliffs, New Jersey, 585 pp.

Phillips, N.A., L.M. McMillin, A. Gruber and D.Q. Wark, 1979: An evaluation of early operational temperature soundings from TIROS-N, Bull. Amer. Meteor. Soc., **60**, 1188-1197.

Puri, K., 1983: The relationship between convective adjustment, Hadley circulation and normal modes of the ANMRC spectral model. Mon. Wea. Rev., **111**, 23-33.

Quah, L.-C., 1984, On the 30-50 day tropospheric oscillation during the 1978-79 northern winter, J. Meteor. Soc., **62**, 261-272.

Ramage, C.S., 1968: Role of a tropical "maritime continent" in the atmospheric circulation, Mon. Wea. Rev., **96**, 365-369.

Rosen, R.D., and D.A. Salstein, 1982: General circulation statistics on short time scales, Mon. Wea. Rev., **110**, 683-698.

Rosen, R.D., and D.A. Salstein, 1983: Variations in atmospheric angular momentum on global and regional scales and the length of day, J. Geophys. Res., **88**, 5451-5470.

Rosen, R.D., and D.A. Salstein, 1985: Effect of initialization on diagnoses of NMC large-scale circulation statistics, Mon. Wea. Rev., **113**, 1321-1337.

Rosen, R.D., D.A. Salstein, J.P. Peixoto, A.H. Oort and N.-C. Lau, 1985: Circulation statistics derived from level III-b and station-based analyses during FGGE, Mon. Wea. Rev., **113**, 65-88.

Sardeshmukh, P.D. and B.J. Hoskins, 1985: Vorticity balances during the 1982-1983 El Niño-Southern Oscillation event, Quart. J. Roy. Meteor. Soc., **111**, 261-278.

Schlatter, T.W., 1981: An assessment of operational TIROS-N temperature retrievals over the United States, Mon. Wea. Rev., **109**, 110-119.

Schneider, E.K., 1977: Axially symmetric steady-state models of the basic state for instability and climate studies. Part II. Nonlinear calculations, J. Atmos. Sci., 34, 280-296.

Schneider, E.K., and R.S. Lindzen, 1977: Axially symmetric steady-state models of the basic state for instability and climate studies. Part I. Linearized calculations, J. Atmos. Sci., **34**, 264-279.

Selkirk, R., 1984: Seasonally stratified correlations of the 200 mb tropical wind field to the Southern Oscillation, J. Climat., 4, 365-382.

Sikka, D.R, and S. Gadgil, 1980: On the maximum cloud zone and the ITCZ over Indian longitudes during the Southwest Monsoon, Mon. Wea. Rev., **108**, 1840-1853.

Stevens, D.E., 1979: Vorticity, momentum and divergence budgets of synoptic-scale wave disturbances in the tropical eastern Atlantic, Mon. Wea. Rev., **107**, 535-558.

Stevens, D.E., and G.H. White, 1979: Comments on "Viscous internal gravity waves and low-frequency oscillations in the tropics," J. Atmos. Sci., **36**, 545-546.

Stout, J.E., D.W. Martin and D.N. Sikdar, 1978: Estimating GATE rainfall with geosynchronous satellite images, Mon. Wea. Rev., **107**, 595-598.

Temperton, C. and D.L. Williamson, 1981: Normal mode initialization for a multi-level grid-point model. Part I: Linear aspects. Mon. Wea. Rev., **109**, 729-743.

Townsend, R.D. and D.R. Johnson, 1985: A diagnostic study of the isentropic zonally averaged mass circulation during the First GARP Global Experiment, J. Atmos. Sci., **42**, 1565-1579.

Trenberth, K.E., 1981: Seasonal variations in global sea level pressure and the total mass of the atmosphere, J. Geophys. Res., **86**, 5238-5246.

Trenberth, K.E. and H. van Loon, 1981: Comment on 'Impact of FGGE buoy data on Southern Hemisphere analysis', Bull. Amer. Meteor. Soc., **62**, 1486-1488.

Troup, A.J., 1965: The 'southern oscillation', Quart. J. Roy. Meteor. Soc., **91**, 490-506.

van Loon, H., 1980: Transfer of sensible heat by transient eddies in the atmosphere of the Southern Hemisphere: An appraisal of the data before and after FGGE, Mon. Wea. Rev., **108**, 1774-1781.

Webster, P.J., 1983: Mechanisms of low-frequency variability: Surface hydrological effects, J. Atmos. Sci., **40**, 2110-2124.

Webster, P.J., and J.R. Holton, 1982: Cross-equatorial response to middle-latitude forcing in a zonally varying basic state, J. Atmos. Sci., **39**, 722-733.

Weickmann, K. M., 1983: Intraseasonal circulation and outgoing longwave radiation modes during Northern Hemsiphere winter, Mon. Wea. Rev., **111**, 1838-1858.

Weickmann, K.M. and J.E. Kutzbach, 1985: Life cycle of a 28-72 day atmospheric oscillation during northern winter, in Proceedings of the Ninth Annual Climate Diagnostics Workshop -- Corvallis, Oregon, October 1984, pp. 128-140. NOAA/U.S. Department of Commerce, Washington, D.C. 436 pp.

Weickmann, K.M., G.R. Lussky and J.E. Kutzbach, 1985: Intraseasonal (30-60 day) fluctuations of outgoing longwave radiation and 250 mb streamfunction during northern winter, Mon. Wea. Rev., **113**, 941-961.

World Meteorological Organization, 1981a: Winter MONEX Field Phase Report, Vol. 7, FGGE Operations Report Series.

World Meteorological Organization, 1981b: Summer MONEX Field Phase Report, Vol. 8, FGGE Operations Report Series.

Williamson, D.L. and C. Temperton, 1981: Normal mode initialization for a multi-level grid-point model. Part II: Nonlinear aspects. Mon. Wea. Rev., **109**, 744-757.

Wyrtki, K., 1973: An equatorial jet in the Indian Ocean, Science, **181**, 262-264.

Yasunari, T., 1979: Cloudiness fluctuations associated with the Northern Hemisphere summer monsoon, J. Meteor. Soc. Japan, **57**, 227-242.

Yasunari, T., 1980: A quasi-stationary appearance of 30 to 40 day period in the cloudiness fluctuations during the summer monsoon over India, J. Meteor. Soc. Japan, **58**, 225-229.

Yasunari, T., 1981: Structure of an Indian summer monsoon system with around 40-day period, J. Meteor. Soc. Japan, **59**, 336-354.

Zebiak, S.E., 1985: Tropical atmosphere-ocean interaction and the El Niño/Southern Oscillation phenomenon, Ph.D. thesis, Massachusetts Institute of Technology, Cambridge, Massachusetts. 261 pp.